

Dissertation

submitted to the
Combined Faculty of Mathematics, Engineering and Natural Sciences
of Heidelberg University, Germany
for the degree of
Doctor of Natural Sciences

Put forward by

Patrick Binder

born in Tübingen

Oral examination: 15 December 2022

Optimal Design Principles in Pathogen Replication and Immune Response

Patrick Binder

Referees: Prof. Dr. Ulrich S. Schwarz
Prof. Dr. Frauke Gräter

To Miriam

Summary

Optimality is a cornerstone of biology, as evolutionary forces drive biological systems towards optimal performance. In this work, I develop theoretical models to reveal optimality principles in two biological systems: ligand discrimination by immune receptors and nuclear multiplication by parasites.

In multicellular organisms, antiviral defense is mediated by signaling molecules. They are usually characterized by highly inhomogeneous distributions due to scarcity of producer cells, diffusion and localized degradation. And yet, a molecular hub of antiviral response, the type I interferon receptor (IFNAR), discriminates between ligand types by their affinity regardless of concentration. In the first part of this work, I address the long-standing question of how a single receptor can robustly decode different ligand types. I frame ligand discrimination as an information-theoretic problem and systematically compare the major classes of receptor architectures: allosteric, homodimerizing, and heterodimerizing. As a result, the architecture of IFNAR—namely asymmetric heterodimers—achieve the best discrimination power over the entire physiological range of local ligand concentrations, enabling sensing of ligand presence and type. Here, receptor turnover, which drives the receptor system out of thermodynamic equilibrium, enables buffering against even high concentration fluctuation. Overall, these findings suggest that IFNAR is optimized for detecting and separating the presence of different ligand types in a noisy environment.

The malaria-causing pathogen *Plasmodium falciparum* is a eukaryotic parasite with a complex life cycle that includes proliferation within red blood cells. During the blood stage, the parasite invades a red blood cell, undergoes several rounds of asynchronous nuclear division, becoming multinucleated, and eventually forms and releases around 20 daughter parasites. Although clinical symptoms of malaria are manifest during this stage, a true understanding of the nuclear multiplication and its asynchrony remains missing. In the second part of this work, I address this topic by modeling the nuclear multiplication with various concepts of theoretical physics. The theoretical models are complemented by live-cell microscopy experiments, tracking nuclei and DNA replication. Our findings suggest that *Plasmodium falciparum* has evolved optimal resource utilization by exploiting a sequential sharing of replication machinery, a general mechanism for efficient and fast proliferation. This result was achieved by first investigating nuclear multiplication, showing that the number of daughter parasites is regulated by a counter mechanism. Second, we demonstrate that the nuclei are coupled by a shared resource that limits DNA replication and thereby actively generates asynchrony. In order to address the question in what way this asynchrony might be beneficial for the parasite, I introduce a minimal biophysical model for allocation of a shared enzyme to individual nuclei. The model captures parallel and sequential DNA replication mode, the latter being able to describe the observed asynchrony of the parasite. When the shared enzyme is limiting, a sequential replication utilizes resources more efficiently, resulting in faster completion of nuclear multiplication.

Zusammenfassung

Optimalität stellt ein grundlegendes Prinzip in der Biologie dar, da evolutionäre Kräfte in biologischen Systemen zu optimaler Leistung führen. In dieser Arbeit entwickle ich theoretische Modelle, um Optimalitätsprinzipien zweier biologischer Systeme aufzuzeigen: Ligandendiskriminierung durch Immunrezeptoren und Kernvermehrung von Parasiten.

In multizellulären Organismen wird die antivirale Immunantwort durch Signalmoleküle vermittelt. Diese Signalmoleküle sind in der Regel durch eine sehr inhomogene Verteilung im Gewebe gekennzeichnet, die auf die geringe Anzahl produzierender Zellen, Diffusion und lokalen Abbau zurückzuführen ist. Und dennoch ist ein essenzieller molekularer Bestandteil der antiviralen Immunantwort, der Typ-I-Interferonrezeptor (IFNAR), in der Lage konzentrationsunabhängig zwischen den Ligandentypen anhand ihrer Affinität zu unterscheiden. Im ersten Teil dieser Arbeit widme ich mich der Frage, welche biochemischen Eigenschaften Rezeptoren in die Lage versetzen, zuverlässig zwischen verschiedenen Ligandentypen zu unterscheiden. Hierzu formuliere ich die Ligandendiskriminierung als informationstheoretisches Problem und vergleiche systematisch die wichtigsten Klassen von Rezeptorarchitekturen: allosterische, homo- und heterodimerisierende Rezeptoren. Es zeigt sich, dass die Architektur von IFNAR — also asymmetrische Heterodimere — die beste Unterscheidungsfähigkeit innerhalb des gesamten physiologischen Bereiches lokaler Ligandenkonzentrationen bietet und sowohl die Präsenz als auch die Art des Liganden zu erkennen vermag. Dabei ermöglicht der stetige Austausch von Rezeptoren, der das Rezeptorsystem aus dem thermodynamischen Gleichgewicht bringt, eine Pufferwirkung gegenüber starken Konzentrationsschwankungen. Insgesamt deuten diese Ergebnisse darauf hin, dass IFNAR für die Erkennung und Unterscheidung der Anwesenheit verschiedener Ligandentypen in einer verrauschten Umgebung optimiert ist.

Der Malariaerreger *Plasmodium falciparum* ist ein eukaryotischer Parasit mit einem komplexen Lebenszyklus, welcher die Vermehrung in roten Blutkörperchen einschließt. Während des Blutstadiums befällt der Parasit ein rotes Blutkörperchen, durchläuft dort mehrere Runden asynchroner Kernteilung, wodurch er ein mehrkerniges Stadium erreicht und bildet letztlich circa 20 neue Tochterparasiten. Im Blutstadium manifestieren sich die klinischen Symptome, dennoch ist die Kernvermehrung und deren Asynchronität in ihren Details bislang noch weitestgehend unverstanden. Im zweiten Teil dieser Arbeit widme ich mich diesem Thema, indem ich die Kernvermehrung anhand verschiedener Konzepte der theoretischen Physik modelliere. Die theoretischen Modelle werden durch mikroskopische Experimente an lebenden Zellen ergänzt, in welchen die Kerne und die DNA-Replikation beobachtet werden. Unsere Ergebnisse deuten darauf hin, dass *Plasmodium falciparum* eine optimale Ressourcennutzung entwickelt hat, indem es die Replikationsmaschinerie nicht gleichzeitig sondern sequenziell auf die vorhandenen Kerne verteilt. Diese sequenzielle Nutzung stellt einen allgemeinen Mechanismus für eine effiziente und schnelle Vermehrung dar. Im Detail wird in dieser Arbeit zunächst die Kernvermehrung untersucht, wobei gezeigt

werden kann, dass die Anzahl der Tochterparasiten durch einen Zähler-Mechanismus reguliert wird. Danach zeigen wir auf, dass die Zellkerne durch eine geteilte Ressource, welche die DNA-Replikation limitiert und dadurch Asynchronität erzeugt, gekoppelt sind. Zur Beantwortung der Frage, inwiefern der Parasit durch diese Asynchronität profitieren könnte, entwickle ich ein minimales biophysikalisches Modell für die Verteilung eines geteilten Enzyms. Das Modell umfasst sowohl parallele als auch sequenzielle Replikation, wobei letztere die beobachtete Asynchronität des Parasiten zu beschreiben vermag. Wenn das gemeinsam genutzte Enzym limitierend ist, nutzt eine sequentielle Replikation die Ressourcen effizienter, was zu einer schnelleren Kernvermehrung führt.

Contents

Summary	vii
Zusammenfassung	ix
Contents	xi
List of Figures	xv
List of Tables	xvi
1 Introduction	1
I CELL-CELL COMMUNICATION IN INFLAMMATORY TISSUE	5
2 An Introduction to Cell Signaling	7
2.1 The Main Principles of Cell Signaling	7
2.2 Extracellular Signals	8
2.3 The Role of Receptors	10
2.4 The Interferon System	11
3 Physiological Cytokine Ligand Distribution	13
3.1 Maximum-Entropy Distribution	13
3.2 Production-Diffusion-Consumption Model	14
3.3 Concluding Remarks	16
4 Modeling Ligand-Receptor Binding	17
4.1 Allosteric Receptor Activation	18
4.2 Receptor Dimerization	20
4.3 Receptor Turnover	26
4.4 Receptor Readout	29
5 An Introduction to Information Theory	31
5.1 What is Information?	31
5.2 Transmission of Information	32
6 An Information-Theoretic Analysis of Optimal Ligand Discrimination	35
6.1 Ligand Discrimination as Information-Processing Task	36
6.2 Receptor Architectures and Their Ligand Discrimination Power	39
6.3 Effect of Additional Noise Sources	45
6.4 Ligand Discrimination for Different Input Distributions	48
6.5 Receptor Turnover	52
6.6 Does the Interferon Operate in the Optimal Regime?	54
6.7 Conclusion	54
7 Discussion - Ligand Discrimination by Interferon Receptors	57

II	PROLIFERATION OF MULTINUCLEATED PARASITES	61
8	An Introduction to the Malaria-Causing Parasite <i>Plasmodium Falciparum</i>	63
8.1	In a Nutshell: The History of Malaria and <i>Plasmodium</i> . . .	63
8.2	The Complex Life Cycle of <i>Plasmodium Falciparum</i>	64
8.3	Blood Stage of <i>Plasmodium Falciparum</i>	65
8.4	Eukaryotic Cell Cycle	65
9	An Introduction to Branching Processes	69
9.1	Galton-Watson Process	69
9.2	Bellman-Harris Process	72
9.3	Controlled Branching Process	74
10	Nuclear Multiplication Dynamics of <i>Plasmodium Falciparum</i>	75
10.1	Experimental Setup and Results	76
10.2	Is the Parasite Counting or Waiting?	80
10.3	Nuclear Multiplication as Branching Processes	83
10.4	Nuclear Multiplication as Biphasic Branching Process . . .	87
10.5	Conclusion	90
11	What Causes Asynchrony in <i>Plasmodium falciparum</i>?	91
11.1	DNA-Replication Antibunching	91
11.2	Nuclei Share a Resource Limiting DNA Replication	95
11.3	Conclusion	96
12	Optimal Resource Allocation in Multinucleated Cells	99
12.1	Mechanism for Allocation of a Shared Enzymatic Resource	100
12.2	Nuclear Multiplication as Resource-Limited Branching Process	102
12.3	Asymptotic Growth of Resource-Limited Branching Process	106
12.4	Sequential Resource-Sharing Enables Rapid Nuclear Mul- tiplication	113
12.5	Does <i>P. Falciparum</i> Operate in the Optimal Regime?	115
12.6	Conclusion	116
13	Discussion - Nuclear Multiplication of <i>Plasmodium Falci- parum</i>	117
	APPENDIX	121
A	Author's Contribution	123
B	Physiological Cytokine Ligand Distribution in Higher Di- mensions	125
B.1	Two-Dimensional Profiles	125
B.2	Three-Dimensional Profiles	126
B.3	Concluding Remark	127
C	Physical Aspects of Ligand-Receptor Binding	129

D Mutual Information Decomposes for Hierarchical Probability Distributions	131
E Parameter Values for Response Curves Optimally Discriminating Ligands	133
F Summary of all Lineage Trees of <i>Plasmodium Falciparum</i> Nuclei	135
G Binding Timescale of the Resource Allocation Model	137
List of Manuscripts	139
Bibliography	141

List of Figures

Figure 2.1	The main principles of cell signaling.	7
Figure 2.2	Overview of different types of chemical signaling in intercellular communication.	9
Figure 2.3	A good signal must be specific.	10
Figure 2.4	Main types of cell-membrane receptors.	11
Figure 2.5	Type I interferon signaling pathway.	12
Figure 3.1	Schematic illustration of the relevant length scales in the tissue, determining the ligand distribution.	13
Figure 3.2	Schematic illustration of a typical early-stage viral infection within a tissue.	15
Figure 4.1	Schematic illustrations of the receptor architectures, turnover and readout.	17
Figure 4.2	Response repertoire of allosteric receptors.	19
Figure 4.3	Response curves of homodimerizing receptors.	21
Figure 4.4	Schematic illustration of the diamond-shaped kinetic topology for heterodimerization receptors.	22
Figure 4.5	Response curves of heterodimerizing receptors.	23
Figure 4.6	Response repertoire of dimerizing receptors.	26
Figure 5.1	Binary entropy function.	32
Figure 5.2	Relationship between entropy and mutual information.	34
Figure 6.1	Interferon receptor act as a bottleneck in signal transduction.	36
Figure 6.2	Signal processing by membrane receptors.	37
Figure 6.3	Optimal ligand discrimination in basic receptor architectures.	42
Figure 6.4	Discrimination power <i>vs.</i> concentration range and readout number.	44
Figure 6.5	Effect of additional noise sources on the readout distribution.	47
Figure 6.6	Ligand discrimination for different input distributions.	50
Figure 6.7	Optimal activation curves for different input distributions.	51
Figure 6.8	Ligand discrimination by dimerizing receptors including receptor turnover.	53
Figure 6.9	Ligand discrimination by the IFN receptor system.	54
Figure 6.10	Overall discrimination power of all considered receptor architectures.	55
Figure 8.1	Life cycle of the malaria-causing parasite <i>P. falciparum</i>	64
Figure 8.2	Eukaryotic cell cycle.	65
Figure 9.1	Schematic lineage tree of a Galton-Watson process.	70
Figure 9.2	Schematic lineage tree of a Bellman-Harris tree.	72

Figure 10.1	<i>P. falciparum</i> proliferates through consecutive rounds of asynchronous DNA replications and nuclear divisions.	77
Figure 10.2	Heterogeneous accumulation of PCNA1 among nuclei permits development of a nuclear cycle sensor system.	78
Figure 10.3	Single cell dynamics of nuclear multiplication.	79
Figure 10.4	Overview of the timer model.	81
Figure 10.5	Overview of the counter model.	81
Figure 10.6	<i>P. falciparum</i> is counting its nuclei.	82
Figure 10.7	Nuclear replication dynamics initially accelerates and then slows down as nuclear multiplication progresses.	84
Figure 10.8	Simulation of <i>P. falciparum</i> proliferation predicts a slowdown of the nuclear cycle dynamics at later stage.	88
Figure 11.1	The nuclei of <i>P. falciparum</i> are coupled.	92
Figure 11.2	Asynchrony facilitate fast nuclear cycles.	96
Figure 12.1	Schematic illustration of resource allocation in a multinucleated cell.	100
Figure 12.2	Overview of the resource-dependent branching process with its resource allocation.	103
Figure 12.3	Lifetime of active complex determines the resource-sharing mode.	106
Figure 12.4	Schematic illustration of fully synchronized and shifted toy models.	107
Figure 12.5	Asymptotic behavior of resource-limited branching process.	111
Figure 12.6	Sequential allocation of a shared resource is a general mechanism for efficient and fast replication.	113
Figure 12.7	The sequential resource-sharing mode enables rapid nuclear multiplication.	114
Figure 12.8	The parasite <i>P. falciparum</i> seems to exploit a sequential resource-sharing mode.	115
Figure B.1	Spatial ligand profiles and concentration distributions.	127
Figure F.1	Summary of all lineage trees of lineage trees of <i>P. falciparum</i> nuclei.	135

List of Tables

Table 4.1	Binding length scales λ in the IFN receptor system.	25
Table 4.2	Response curves f for the equilibrium receptor-ligand binding motifs.	26
Table 6.1	Parameter bounds and fixed parameter values used for optimizing the ligand discrimination power I .	40
Table 10.1	Parameters used in the branching process models.	87

Table E.1	Dissociation constants and unbinding rates for activation curves shown in Fig. 6.3.	133
Table E.2	Dissociation constants for activation curves shown in Fig. 6.7.	133
Table E.3	Dissociation constants and unbinding rates for activation curves shown in Fig. 6.8.	134
Table E.4	Kinetic rates for IFN α 2 and IFN β	134

Mankind is in a constant struggle with pathogens, such as viruses and parasites. The current COVID-19 pandemic, caused by the SARS-CoV-2 virus, for example, is having a major impact on almost all aspects of our lives, including social and economic impacts [4–6]. However, COVID-19 is far from the most severe global health issue. Among parasites, the malaria-causing parasite is probably the greatest global health challenge. It is estimated to have killed not only half of all the people that ever lived [7] and despite decades of effort, it still causes around 240 million cases and more than half a million of fatalities each year [8]. The current COVID-19 pandemic and the ongoing fight against malaria highlight that we lack both a predictive understanding of the human immune response to viruses and of the malaria-causing parasites in humans, respectively. In this thesis, I apply concepts from theoretical physics to two biological systems to reveal the underlying biological processes. Accordingly, this thesis is a contribution to the body of work that shows how applying tools from physics, such as the question of optimality, can contribute to the goal of deciphering biological mechanisms, enabling for example the development of more efficient drugs.

The concept of optimality clearly is a cornerstone of physics [9, 10]. Indeed, there are numerous examples which were of great importance for the development of theoretical physics, such as Fermat’s principle or Hamilton’s principle.¹

The main principles of optimality can be discussed very well by means of Fermat’s principle, which states that a ray of light, traveling between two given points, takes the path for which the transit time is the least [12, 13]. First, the problem must be well-defined. Regarding Fermat’s principle, it is defined as moving the light from an initial point to a terminal point. Second, the problem must have a well-defined set of competing solutions. For the ray of light the set of solutions corresponds to all physically possible paths which join the two points. Third, a cost must be assigned to each solution so that they can be compared with each other. The function associating the cost is typically referred as cost functional. For Fermat’s principle, the cost is given by the transit time of the ray for the given path. The optimal path for the ray light is then the path with the least cost, i.e. the shortest transit time. Fermat’s principle states that nature exhibits this optimal path.

As a second illustrative example, it is worth mentioning the Hamilton’s principle of least action², which is probably the most important optimality principle in theoretical physics [9, 15]. This principle asserts that a system will move along that path which minimizes the so-called action functional. The solutions considered by the Hamilton’s principle are the paths which result from the process of virtual displacement, in which the time is held fixed and only the spatial coordinates of the system are varied. Here, this variational problem is equivalent to the differential equations of motion of the physical system, as they can be derived from the variational problem. The importance of defining a set of competing solutions, can be

1: Besides Fermat’s principle or Hamilton’s principle, there are many other examples in physics which are no less important, e.g. the principle of maximal entropy in thermodynamics. This principle arises from the second law of thermodynamics, which states that the total entropy cannot decrease in general, thus entropy effectively describes the thermodynamic direction in which a system can evolve [11].

2: In many cases the action turns out not to be minimal, but only stationary. Therefore, this principle is often referred to as principle of stationary action [14]. The same holds true for Fermat’s principle.

illustrated by comparing Hamilton's principle with the historically older Maupertuis's principle. The latter principle is one of the first formulated principles of least action in the context of classical mechanics, also stating that a system will move along the path, which minimizes the action. In contrast to Hamilton's principle, the set of solutions is restricted to those paths that satisfy conservation of energy. Since the virtual displacement in general does not fulfill the conservation of energy, the sets of solutions differ and therefore the principles differ in their application. It should be noted that the definition of the cost is of course equally important, and a change of this definition can be expected to alter the solution as well.

"Nothing makes sense in biology except in the light of evolution" [16], and evolution can be expressed quantitatively within the framework of optimality. Here, the so-called natural selection is the reason why concepts of optimality play an important role not only in physical systems, but also in biological systems [9].³ In simple terms, the idea of natural selection is that individuals who compete more efficiently have a higher probability of surviving the competition, resulting in an increased frequency of more efficiently competing individuals, or in the words of Charles Darwin [17]:

"The vigorous, the healthy, and the happy survive and multiply."

Indeed, there are myriad examples of biological systems that exploit optimality such as the quantum efficiency of photosynthesis [25] and photoreceptors [26], the frequently observed optimal surface receptor densities in cells for sensing diffusing signals [27, 28], and the optimal resource allocation in the chemotaxis network of *Escherichia coli* [29]. Natural selection is based on two assumptions. On the one hand, the advantage of the individual can be passed on, at least to some extent, to its descendants. In other words, the adaptation of populations is driven by heritable differences in reproductive success. On the other hand, the environment remains unchanged for a sufficient amount of time, such that the population is able to adapt to the environment by evolving optimal features. Although both assumptions apply in most cases, especially the latter assumption is not always fulfilled, and therefore it should not be expected that every trait is optimally adapted [30, 31]. Furthermore, finding both the cost functional and the set of competing solutions in biological systems is often a very difficult if not impossible task. Therefore, the determined degree of optimality of the traits is also subject to uncertainty. Nevertheless, even in the case of negative results [32], the question of optimality is an important tool, enabling a better understanding of biological systems [33–44].

Despite these caveats in regard to biological systems, this thesis explores how far one can get using principles of optimality to explain important biological processes in the context of infections. First, I dedicate myself to gaining a better understanding of the human immune response to viral infections. In particular, I address the long-standing question of how the immune system can evoke a quick and reliable response in the face of uncertainty about the concentrations of the myriad of different interferon ligands that mediate the antiviral response in tissues. Here, it is particularly perplexing that a single protein complex, the type I interferon receptor, can robustly multiplex the information of its different

3: The concept of evolution by natural selection was originally proposed in the theory of Charles Darwin [17]. In the 20th-century, the theory was replaced by the modern synthesis which combines natural selection, Mendelian genetics, and population genetics [18–23]. In recent years, new syntheses coming from different fields, e.g. molecular biology, were proposed [24]. However, the fundamental idea of evolution by natural selection remains in all theories, and with it the important role of optimality in biological systems.

ligands, despite the highly inhomogeneous and noisy ligand distributions. Therefore, this thesis addresses the question of what generic features enable a receptor to discriminate ligands directly at the membrane, overcoming the challenges of a tissue environment where local ligand concentrations can vary over several orders of magnitude.

Second, I study the proliferation of the predominant malaria-causing pathogen *Plasmodium falciparum* in red blood cells. *Plasmodium falciparum* is a eukaryotic parasite with a complex life cycle that includes proliferation within red blood cells. During the blood stage, the parasite invades a red blood cell, undergoes several rounds of nuclear division, becoming multinucleated before cellularization, and eventually releases around 20 daughter parasites [45–47]. Here, frequently observed odd numbers of nuclei indicate that nuclei divide asynchronously. Although all clinical symptoms of malaria are caused by the rapid multiplication of parasites in the blood of patients [48, 49], it remains unknown how this asynchronous nuclear multiplication is orchestrated. Therefore, I investigate the dynamics of nuclear proliferation and reveal how this asynchronous process is controlled to yield nevertheless a well-controlled final outcome. Furthermore, I address the question of what mechanism could cause the asynchrony, and in particular in what way the asynchrony might be beneficial for the parasite.

Outline

This thesis is made up of two parts, namely

Part I is devoted to the immune response and addresses the question of how a single receptor can distinguish between different ligands, while

Part II is dedicated to decipher how the malaria-causing parasite *Plasmodium falciparum* orchestrate its nuclear multiplication.

Part I: Cell-Cell Communication in Inflammatory Tissue

In multicellular organisms, antiviral defense mechanisms evoke a reliable collective immune response despite the noisy nature of biochemical communication between tissue cells. A molecular hub of this response, the type I interferon receptor, discriminates between different ligand types. Part I addresses this long-standing question of how ligand type can be decoded robustly by a single receptor complex directly at the membrane stage.

Chapter 2 provides a general introduction into cell signaling and discusses what makes a good signal as well as what makes a good receiver. Using a production-diffusion-consumption model, **Chapter 3** demonstrates that cytokine signaling encodes the information in the ligand type and not in the ligand concentration by addressing the question of what local ligand concentration is experienced by a random receiving cell in the tissue. Thus, the specificity of the signal relies on the specificity of the ligand-receptor interaction. In **Chapter 4**, a mathematical description of how to model this ligand-receptor interaction and signal

transduction is provided. To quantitatively evaluate the ligand discrimination performance of the different receptor architectures, **Chapter 5** provides a brief introduction into the framework of information theory. To understand how ligand type can be decoded robustly by a single receptor, **Chapter 6** frames ligand discrimination as an information-theoretic problem and systematically compares the discrimination power of the major classes of receptor architectures: allosteric, homodimerizing, and heterodimerizing.

Part I is based on Ref. [1] and advanced earlier work by Nikolas Schnellbacher [50]. For a detailed listing of author contributions see Appendix A.

Part II: Proliferation of Multinucleated Parasites

Despite decades of effort to combat malaria, even fundamental questions about the nuclear multiplication of the parasite at the blood stage remain unanswered. Part II aims to shed light on some of these fundamental questions and thus take an important step towards deciphering nuclear multiplication.

Chapter 8 gives an overview of the biology needed to understand the process of nuclear multiplication of the malaria-causing parasite *Plasmodium falciparum*. In **Chapter 9**, the mathematical framework of branching processes are introduced, the most natural way to model and study growing population such as the nuclear multiplication of the parasite. **Chapter 10** is devoted to gain a better understanding of the nuclear multiplication of the parasite. The question of how the nuclear multiplication is controlled to yield nevertheless a well-controlled final outcome, is addressed by examining different mechanisms of regulation. In addition, by using branching processes, the nuclear dynamics are further investigated. Revising the data and including mother-daughter and sister correlations to the branching processes, **Chapter 11** seeks to understand the observed asynchrony. Using resource-limited branching processes that are based on a minimal biophysical model for the allocation of a shared enzyme to individual nuclei, **Chapter 12** then addresses the question of what mechanism could cause the asynchrony, and in particular in what way the asynchrony might be beneficial for the parasite *Plasmodium falciparum*.

Part II is based on a collaboration Ref. [2] and an unpublished manuscript Ref. [3], see Appendix A for a detailed listing of author contributions.

Part I

**CELL-CELL COMMUNICATION IN
INFLAMMATORY TISSUE**

All cells are constantly exposed to signals in many forms. Whether a cell lives individually or in a multicellular organism, the ability of a cell to communicate with its environment is crucial and is called cell signaling.

The aim of this chapter is to give a concise overview of the principles of cell signaling. For a more comprehensive treatment, I recommend the two excellent textbooks: a specialist reference [51] and the classic reference in cell biology [52].

2.1 The Main Principles of Cell Signaling

Cell signaling comprises three fundamental parts, namely the perception, the signal transduction, and the cellular response, see Fig. 2.1.

It all starts with the arrival of the signal at the cell. For instance, in the case of the so-called photoreceptor cells in the retina, the signal may be photons. In the context of cell-cell communication, the signal may be a chemical signal consisting of small molecules. As illustrated in Fig. 2.1, most signals are detected at the extracellular side of the cell membrane. Here, the detection of the signal and its transmission into the cell is realized by dedicated protein complexes called receptors. Receptors then process¹ the signal and pass its message to the interior of the cell, activating a signaling cascade, which is designed to transport the message to its final destination inside the cell. For instance, in the case of a chemical signal, the binding of a signaling molecule to the receptor may induce a change in conformation in the intracellular side, resulting in an activation of an enzymatic domain. It should be noted that in most cases, the signaling molecule does not pass the membrane, but only its message is transmitted by the receptor. Eventually, the message

- 2.1 The Main Principles of Cell Signaling 7
- 2.2 Extracellular Signals 8
 - 2.2.1 Ways of Chemical Signaling 8
 - 2.2.2 What Makes a Good Signal? 9
- 2.3 The Role of Receptors 10
 - 2.3.1 What Makes a Good Receptor? 10
 - 2.3.2 Types of Receptors 10
- 2.4 The Interferon System 11

1: At this step, receptors often already integrate, filter and shape the signals, exploiting nonlinear activation [53] or temporal [54–56] and spatiotemporal activation dynamics [57, 58].

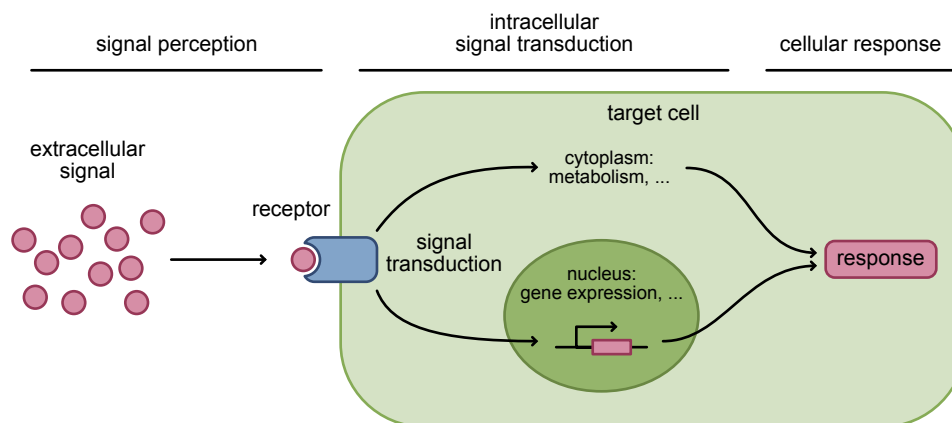


Figure 2.1 | The main principles of cell signaling comprises three fundamental parts: the perception, the signal transduction and the cellular response.

of the signal arrives at its final destination, where it provokes a cellular response. The final destination inside the cell depends on the signal and could be for example in the nucleus to control gene expression or in the cytoplasm to control metabolism.

Three things should be noted. First, these main principles of the signaling mechanisms are conserved across most cells, ranging from animals and plants down to bacteria. Second, cells are not fortunate enough to process the signals one after the other, but rather must process and respond to many signals at the same time. A single signal can activate more than one cascade and also result in more than one cellular response. Third, during the signaling cascade the message may not only cross several barriers, like the nuclear membrane, and travel some distance, but also may get amplified. Therefore, signaling cascades often involve many components and mechanisms.

2.2 Extracellular Signals

Extracellular signals can be roughly classified into two major categories. On the one hand, there are environmental signals. This could be such things as small molecules (chemical signals, ions, etc.) or physical agents like temperature, light, voltage, mechanical stress, etc. On the other hand, in multicellular organisms there are also signals originating from the organism itself, corresponding to cell-cell signaling. This intercellular communication is mostly realized by chemical signaling, i.e. by releasing and detecting extracellular signaling molecules referred to as ligands. Depending on their function, the ligands are often loosely divided into hormones, cytokines and growth factors. Hormones refer to substances produced and released in dedicated tissue, carried to distant tissues, where they provoke specific responses like stimulating or inhibiting proliferation. By contrast, cytokines are produced by many cell types and their effect is only of short distance. Growth factors comprise ligands that regulate growth and differentiation of cells.

2.2.1 Ways of Chemical Signaling

In multicellular organisms, cell-cell signaling is categorized by the distance of the signaling cell to the target cell, namely a cell may target itself (autocrine), an adjacent cell connected by gap junctions (juxtacrine), a nearby cell within the tissue (paracrine), or a distant cell (endocrine), see Fig. 2.2.

Autocrine signaling describes a local effect of diffusible signaling molecules, where the signaling cell targets itself, see Fig. 2.2A. One example in which this type of signaling is commonly found are tumor cells. Here, autocrine signaling is used to stimulate the own cell to uncontrolled growth and proliferation with self-produced growth hormones.

Juxtacrine signaling summarizes different types of contact-dependent signaling. One type of juxtacrine signaling is the signaling across gap junctions, see Fig. 2.2B. Gap junctions connect two adjacent cells and enable small molecules to move directly between these cells. Another type

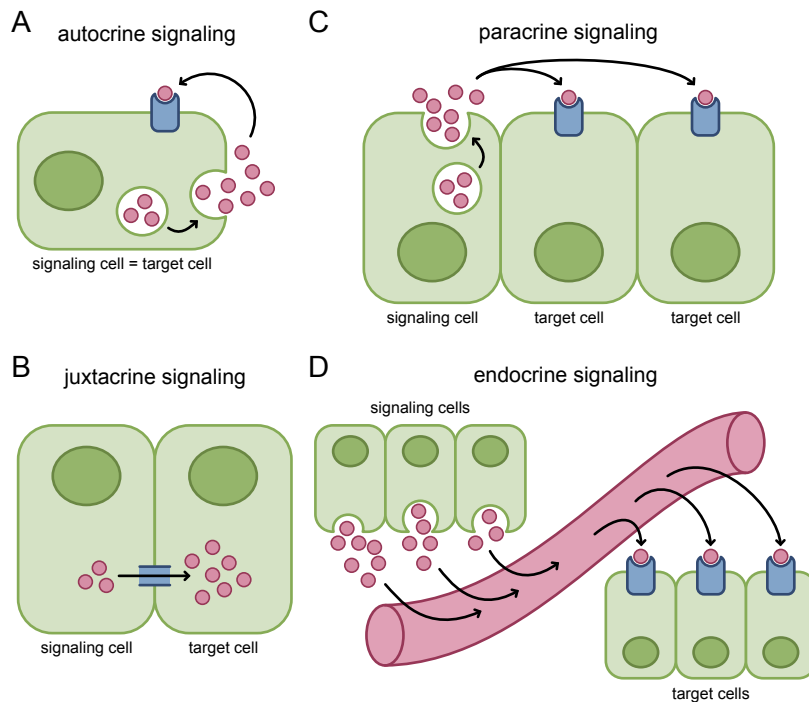


Figure 2.2 | Overview of different types of chemical signaling in intercellular communication. A cell may target (A) itself (autocrine), (B) an adjacent cell connected by gap junctions (juxtacrine), (C) a nearby cell within the tissue (paracrine) or (D) a distant cell (endocrine).

is the interaction of a fixed membrane ligand and a membrane receptor of two adjacent cells, as it is used for example by T cell receptors. Even though the ligand is not released, the main principles of ligand-receptor signal transduction are the same as for soluble ligands.

In paracrine signaling, cells communicate by releasing ligands, which diffuse to and are detected by other cells, see Fig. 2.2C. The main difference to autocrine signaling is that the producing and the consuming cell are distinct. Since the ligands are effected by uptake and degradation, paracrine signaling mainly occurs within a local area, see Chapter 3 for a mathematical description. An example of paracrine signaling can be found in the immune response during a viral attack, where cells release cytokines to evoke antiviral response in their neighboring cells.

In endocrine signaling, the signaling cell and the target cells are located in different tissues, see Fig. 2.2D. To be able to travel vast distances, the ligands use the circulatory system. By doing so, their distribution within the organism is unspecific. For example, many hormones uses the bloodstream to travel to distant organs.

2.2.2 What Makes a Good Signal?

Specificity is probably the most important and most fundamental property of a good signal. First, a signal must affect only its target cell. Second, a signal must be specific enough to elicit a well-defined cellular response in its target cell. In other words, a signal that is too unspecific to either provoke the right cellular response or to address only the defined target cells, fails to deliver its message. Fig. 2.3 summarizes this idea.

To achieve specific signals, organisms have evolved a myriad of ligands and receptors with associated signaling cascades. One should keep in mind that a signaling cell cannot send the signal specifically to a defined

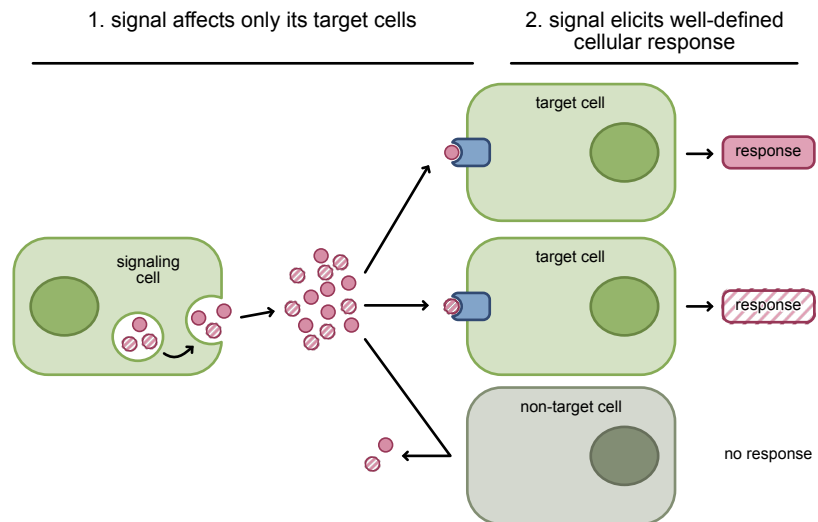


Figure 2.3 | A good signal must be specific, i.e. it affects only its target cells and elicits a well-defined cellular response.

target cell, except in the case of autocrine and juxtacrine signaling. Instead, most signaling molecules are relatively small and rely on diffusion. In addition, endocrine signaling uses the vascular system which is even more unspecific. Therefore, the specificity of the signals is largely due to the specificity of the ligand-receptor interaction.

2.3 The Role of Receptors

Regardless of how many or what kind of signals a cell is exposed to, without the ability to perceive the signals, the cell cannot respond to any of them. Since most signals are perceived at the cell membrane by receptors, they play a crucial role in cell signaling.

2.3.1 What Makes a Good Receptor?

The necessary specificity for ligands discussed in the previous section is based on the need for a specific ligand-receptor recognition and thus also applies to the receptor itself. A good receptor must only detect the specific ligands. Further, signals often occur at extremely low concentrations such as 10 pM, although the cell should perceive the message. This means that depending on the typical concentration of a signal, the corresponding receptor must have the needed sensitivity. Further, receptors must fulfill two more criteria. First, the receptor must be able to transduce the signal to the cell. Second, the receptor should be able to be turned off after the message is received and acted on.

2.3.2 Types of Receptors

Usually, a functional transmembrane receptor comprises three main parts: an extracellular domain where the ligand binds, a hydrophobic transmembrane domain and an intracellular domain, relaying the signal to the inside of the cell. Transmembrane receptors can be grouped by structure and function. The three largest classes are ligand-gated ion

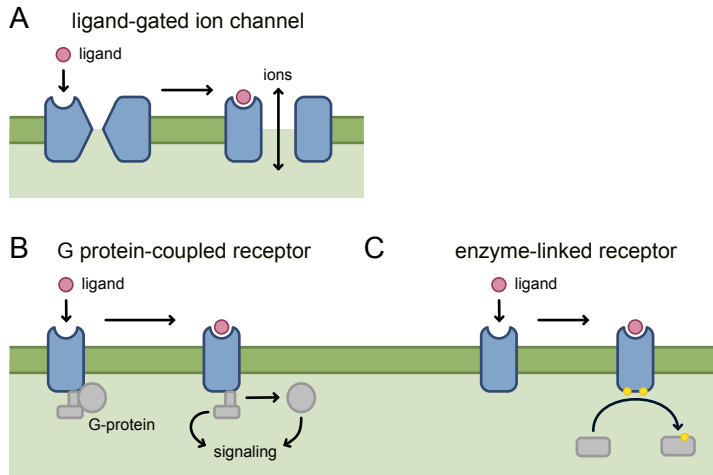


Figure 2.4 | Main types of cell-membrane receptors: (A) Ligand-gated ion channel, (B) G protein-coupled receptor, and (C) enzyme-linked receptor.

channels, G protein-coupled receptors and enzyme-linked receptors, see Fig. 2.4. Upon binding of a ligand, ion channel linked receptors open or close an ion channel, effectively changing the permeability of the cell membrane for specific ions. G protein-coupled receptors have seven transmembrane domains and activate a membrane protein called G protein upon ligand binding. The activated G Protein then interacts with either an ion channel or an enzyme in the membrane. For enzyme-linked receptors, the binding of a ligand to the extracellular domain translates into an activation (see Fig. 2.4, yellow points) of an intracellular enzyme, mainly protein kinases. Here, either the intracellular domain of the receptor itself is an enzyme or the intracellular domain interacts directly with an enzyme.

2.4 The Interferon System

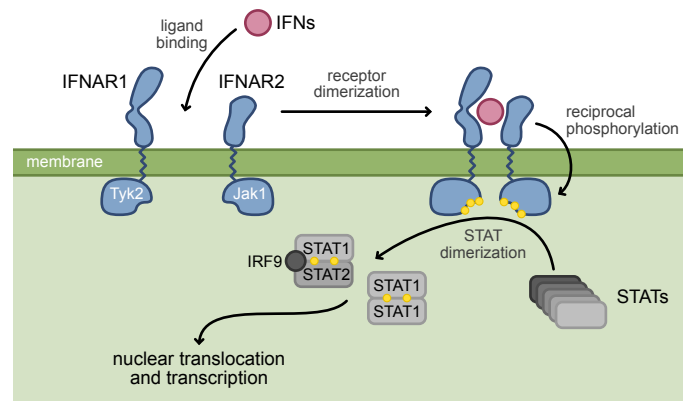
As an example of a cytokine, the signal transduction by the type I interferon (IFN) system is discussed in the following. IFNs act as immunomodulatory signaling molecules, playing an important role in the innate immune response. Often IFNs are referred to as the first line of defense against viral infections [59]. Cells infected with virus secrete IFNs to alert neighboring cells, which then respond by antiviral or antiproliferative behavior. As IFNs interfere with viral replication within host cells [60], they were named interferons. However, the interferon system plays an important role not only in antiviral responses, but in immune defense in general, including malaria [61]. In addition, IFNs are crucial in other immunologically relevant scenarios, including bacterial infections, shock, autoimmunity, and cancer [62, 63]. For a comprehensive overview covering the biological aspects of IFN and their importance in the immune system, I refer to the following reviews [64–67]. Recent studies showed that IFNs is also contributing critically in the pathogenesis and treatment of COVID-19 [68–72].

In humans, most cells both express the IFN receptors and produce IFN ligands. The family of IFN comprises seventeen signaling molecules, namely thirteen IFN α subtypes and IFN β , IFN ϵ , IFN κ and IFN ω , all binding to a single dimeric receptor composed of two receptor subunits, the so-called IFNAR1 and IFNAR2 [73]. The signaling pathway of IFN is

shown in Fig. 2.5. The associated tyrosine kinases of IFNAR1 and IFNAR2 are Tyk2 and Jak1, respectively, thus IFNAR are enzyme-linked receptors. Following ternary complex assembly by ligand binding, both tyrosine kinases are activated by reciprocal transphosphorylation (yellow dots in Fig. 2.5) [74]. Upon activation, the signal is propagated to so-called transducers and activators of transcription (STAT) factors, which are phosphorylated by the receptor-complex. The phosphorylated STATs dimerize and translocate into the nucleus, where they directly regulate gene transcription. Fig. 2.5 summarizes the signaling pathway of the IFN system.

Beside type I interferons, there are two more classes of interferons: type II and type III. The former contains one ligand called IFN γ , which activates type II receptors by homodimerization [75]. The latter comprises four IFN λ subtypes, which bind all to two distinct receptor chains like type I interferons [76].

Figure 2.5 | Type I interferon (IFN) signaling pathway. IFNs form a ternary complex with a dimeric receptor (IFNAR1 and IFNAR2), resulting in a reciprocal transphosphorylation of both tyrosine kinases Tyk2 and Jak1 [59]. Upon activation, the signal is propagated by phosphorylation and dimerization of STATs, which translocate into the nucleus, where they directly regulate gene transcription.



Physiological Cytokine Ligand Distribution

3

This chapter is based on Ref. [1]. For a detailed listing of author contributions see Appendix A.

3.1 Maximum-Entropy Distribution	13
3.2 Production-Diffusion-Consumption Model	14
3.3 Concluding Remarks	16

In multicellular organisms, intercellular communication mostly relies on chemical signaling, which uses ligands to transfer information. Here, the information can be encoded into the ligand concentration or the ligand type [77]. To demonstrate that cytokine signaling encodes the information in the ligand type and not in the ligand concentration, this chapter addresses the question which local ligand concentration is experienced by a random receiving cell in the tissue.

In general, the expected spatial ligand distribution strongly depends on the length scales of communication ν compared to the overall tissue size l , Fig. 3.1. For length scales in the order of the tissue size and beyond, i.e. $\nu \gtrsim l$, the tissue can be considered as well-mixed, resulting in a homogeneous concentration distribution [78]. By contrast, for concentration length scales much shorter than the tissue size and sparse producing cells placed with a distance η , i.e. $\nu \ll l$, the resulting ligand concentration is expected to be heterogeneous with local domains with higher concentration, termed niches [79–85]. An example for the latter would be the cytokine-based communication in the early-stage of viral infection. Here, production, diffusion and degradation of cytokines result in cytokine niches of size $\nu \simeq 100 \mu\text{m}$ [86].

This chapter presents two estimates for such a local cytokine concentration experienced by a random receiving cell. First, the most uninformative prior distribution is derived in Section 3.1. To get a more thorough estimate of physiological distributions, a reaction-diffusion model is discussed in Section 3.2.

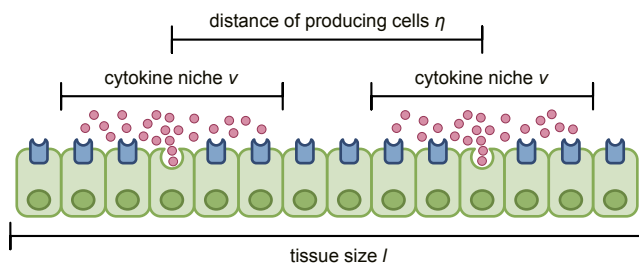


Figure 3.1 | Schematic illustration of the relevant length scales in the tissue, determining the ligand distribution.

3.1 Maximum-Entropy Distribution

Having no knowledge about the real distribution, one can ask what is the most uninformative prior distribution. For a location parameter, the prior distribution should be location invariant, i.e. the natural choice would be a uniform distribution [87]. However, ligand concentration distributions $p(L)$ typically span a broad concentration range $\mathcal{L} = \{L_{lo}, L_{hi}\}$, ligand

concentration can therefore be seen as a scale parameter. For example, receptor systems can be exceptionally sensitive, achieving detection threshold in the pM range [59, 81], i.e. $L_{lo} \approx 1$ pM. At the same time, in tissues with highly-secreting cells, ligand levels can locally reach high μ M concentrations, i.e. $L_{hi} \approx 1$ μ M. Without further information, no concentration scale other than these approximate limits L_{lo}, L_{hi} should be imposed. This implies that the distribution $p(L)$ should be invariant under rescaling transformations $L \rightarrow \alpha L$, except for adjusting the lower and upper bounds of its support, see e.g. Ref. [88]. The unique such scale-free distribution reads

$$p_{sf}(L) = \begin{cases} \frac{1}{\log(L_{hi}/L_{lo})} \frac{1}{L} & \text{for } L_{lo} < L < L_{hi}, \\ 0 & \text{otherwise.} \end{cases} \quad (3.1)$$

Note that the $1/L$ distribution is uninformative in the sense that it weights each decade in concentration with the same probability. This can be seen by transforming the distribution into the log-concentration space $\ell \equiv \log L$, where the distribution is constant, i.e.

$$\tilde{p}_{sf}(\ell) = \begin{cases} \frac{1}{\ell_{hi} - \ell_{lo}} & \text{for } \ell_{lo} < \ell < \ell_{hi}, \\ 0 & \text{otherwise.} \end{cases} \quad (3.2)$$

Moreover, it should be noted that there are many frameworks to determine good priors, since the choice of priors is of great importance in many areas, such as in Bayesian statistics [89]. In particular, if there is no information available about the prior, like in the case considered here, an uninformative prior can be used to avoid a biased outcome. Uninformative priors are, for example, the *maximum-entropy prior*, the *reference prior* and the *Jeffreys prior*. While the maximum-entropy prior applies the principle of maximum entropy, the reference prior maximizes the expected Kullback-Leibler divergence of the posterior distributions [90]. The idea of the Jeffreys prior is that it should be invariant under a change of parameters and is therefore found to be proportional to the square root of the determinant of the Fisher information matrix [91]. Intriguingly, in the one parametric case considered here, all three methods result in the same $1/L$ distribution as found in Eq. (3.1). A more general and detailed discussion on how to choose an appropriate prior distribution can be found in the following excellent textbooks [88] and [92].

3.2 Production-Diffusion-Consumption Model

Next, by considering the processes of ligand production, diffusion, and consumption, as proposed by Oyler-Yaniv et al. [1, 79–81], a more accurate estimate of physiological ligand distributions is provided. As depicted in Fig. 3.2, in a typical early-stage viral infection, a small subset of infected cells produce and secrete inflammatory cytokine ligands. The ligands then spread effectively diffusively within the tissue until they are degraded, typically by being taken up by receiving cells. Further, as a simple model, it is assumed that the degradation rate is linearly to the ligand concentration $L(\mathbf{x}, t)$. On spatial scales much larger than a cell diameter, the production-diffusion-consumption equation for the spatial

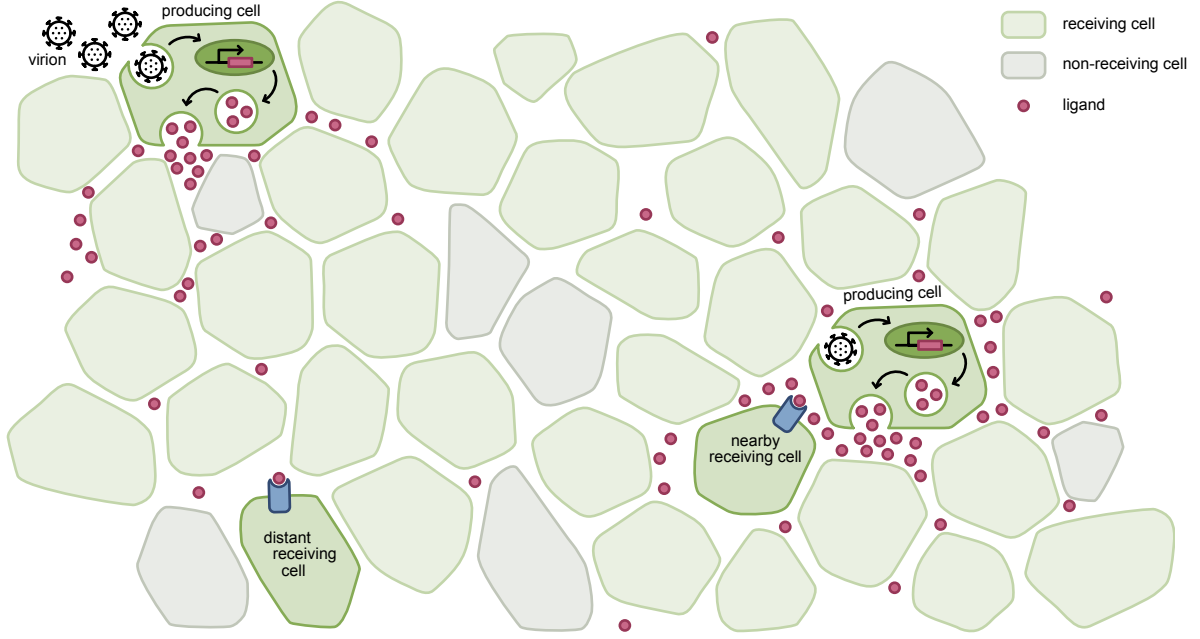


Figure 3.2 | Schematic illustration of a typical early-stage viral infection within a tissue. A small percentage of infected cells produce and secrete inflammatory cytokine ligands (red circles), which are perceived by a majority of receiving cells (green). With increasing distance to the producing cell, the ligand concentration decreases strongly.

concentration profile reads:

$$\frac{\partial L(\mathbf{x}, t)}{\partial t} = \underbrace{k_s \sum_i \delta(\mathbf{x} - \mathbf{x}_i)}_{\text{production}} + \underbrace{D \Delta L(\mathbf{x}, t)}_{\text{diffusion}} - \underbrace{\mu L(\mathbf{x}, t)}_{\text{consumption}}, \quad (3.3)$$

where the source term $s(\mathbf{x}) = \sum_i \delta(\mathbf{x} - \mathbf{x}_i)$ is the local density of producer cells at positions $\{\mathbf{x}_i\}$, k_s is the ligand production rate per cell, D is the effective diffusion coefficient, and μ the total degradation rate. In the stationary state, this equation predicts that sparse producing cells are surrounded by niches of elevated cytokine concentration [79] with a characteristic size $\nu = \sqrt{D/\mu}$.

For the sake of clarity, the following discussion is restricted to one spatial dimension, a discussion of higher dimensions $d = 2$ and 3 is provided in Appendix B. The well-known stationary solution of Eq. (3.3) for a single producing cell in one dimension at $x_0 = 0$ reads

$$L(x) = L_{\text{hi}} e^{-\frac{|x|}{\nu}}, \quad (3.4)$$

where the maximal concentration is attained directly at the position of the producing cell, and it is defined by the ratio of the production rate with the total degradation rate and the characteristic niche size, namely

$$L_{\text{hi}} = \frac{k_s}{2\mu\nu}. \quad (3.5)$$

The ligand concentration distribution $p(L)$ is obtained by randomly selecting a tissue cell within a region of size S around the producer and determining the distribution of concentration values the tissue cell is

exposed to, i.e.

$$p(L) = \frac{1}{S} \int_{-S/2}^{S/2} \delta [L(x) - L] dx = \frac{2\nu}{SL}, \quad (3.6)$$

where δ is the Dirac delta distribution. Interestingly, the production rate k_s only enters the support, it does not affect the shape of the distribution. By choosing the minimal concentration such that $\log L_{hi}/L_{lo} = S/(2\nu)$ is fulfilled, $p(L)$ coincide with the scale-free distribution Eq. (3.1), that is

$$p(L) = p_{sf}(L). \quad (3.7)$$

In a tissue with multiple producing cells, the profiles superimpose, changing the concentration distribution. However, in the relevant limit of sparse producers of density $\rho_s \ll 1/\nu$, the cytokine profile can be well approximated by Eq. (3.5) relative to the nearest producer. By doing so, the tissue is assumed to be effectively composed of individual, well separated niches. Then Eq. (3.7) still holds when setting the spatial range of integration equal to the spacing of producers $\sigma \simeq 1/\rho_s$.

3.3 Concluding Remarks

In one dimension, the production-diffusion-consumption model of cytokine spreading generates exponential ligand profiles with niches of characteristic size ν set by diffusion coefficient and degradation rate exclusively. Assuming sparse producers, this leads to the least informative ligand concentration distribution p_{sf} , see Eq. (3.1).

In Appendix B, the effect of higher dimensions $d = 2$ and 3 on the physiological ligand distribution is discussed. The characteristic niche size remains ν , but within the niche, the ligand profiles get steeper, reaching higher concentrations at the producer cells. However, since this only affects a small fraction $\rho_s \nu^d$ of tissue cells, Eq. (3.1) remains a good approximation.

In Chapter 6, the physiological cytokine distributions are approximated by the scale-free distribution p_{sf} , since this gives a simple and good approximation for small, sparse producers in any dimension.

Modeling Ligand-Receptor Binding

4

This chapter is based on Ref. [1]. For a detailed listing of author contributions see Appendix A.

What is a good ligand receptor in the context of cytokine-based communication in the early-stage of viral infection? In general, a good receptor must only detect the specific ligands, see Chapter 2. Since cytokines are produced by a small subset, the cytokine ligand concentration within a tissue spans a broad concentration range, although all cells should receive the same message, see Chapter 3. Therefore, the information is encoded in the ligand type and not in the ligand concentration. In other words, the specificity of the signal relies on the specificity of the ligand-receptor interaction.

This chapter provides a mathematical description of how to model the receptor activation and signal transduction through the cell membrane upon ligand-receptor binding. First, the equilibrium response curves for different ligand-receptor binding motifs are derived: allosteric transmission in Section 4.1 and receptor dimerization in Section 4.2, see Fig. 4.1A-C. Section 4.3 investigates the effect of receptor turnover on these response curves, see Fig. 4.1D. The chapter concludes by providing a description of how to model the readout of activated enzyme-linked receptors in Section 4.4, see Fig. 4.1E.

The foundational papers by Perelson on modeling ligand-receptor binding are wonderfully readable [93–96]. In addition, for a more comprehensive overview, I recommend the excellent textbook [97].

- 4.1 Allosteric Receptor Activation 18
- 4.2 Receptor Dimerization 20
 - 4.2.1 Homodimerization 20
 - 4.2.2 Heterodimerization 21
 - 4.2.3 Ligand-Independent Binding Length Scale 23
- 4.3 Receptor Turnover 26
 - 4.3.1 Allosteric Transmission 27
 - 4.3.2 Homodimerization 28
 - 4.3.3 Heterodimerization 29
- 4.4 Receptor Readout 29

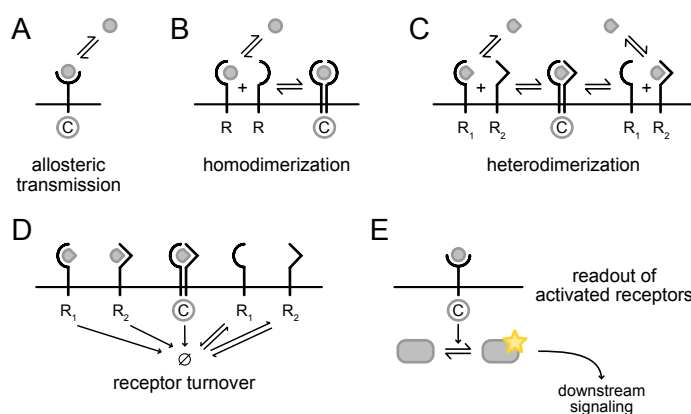


Figure 4.1 | Schematic illustrations (A-C) of the three receptor architectures considered in this chapter, (D) of the receptor turnover, and (E) of the readout of activated receptors.

Response Curve

To quantify how the receptor architecture determines the receptor activation and thereby the signal transduction at the cell membrane, the fraction f of activated receptor complexes C as a function of the ligand

concentration L is used, i.e.

$$f(L) = \frac{C(L)}{C_{\max}}, \quad (4.1)$$

where $C_{(\max)}$ is the (maximal) concentration of activated receptors C . Here and in the following, upright symbols, such as L and C , denote species themselves and italic symbols, such as L and C , denote their concentrations. The fraction of activated receptors f as a function of the ligand concentration L is called *response curve* or equivalently *activation curve*. In the literature, *binding curve* and *dose response curve* are also commonly used.

For the derivation of the response curves it is assumed that the ligand binding does not deplete the ligand concentration. This is equivalent to the assumption that the total ligand number exceeds the number of receptors, i.e. $VL \gg AR$, where R denotes the receptor concentration and A is the size of the membrane patch and V describes the respective volume of the ligand reservoir. Since the IFN receptor system has a low copy number of only around 1000 receptors [98], this assumption is well justified.

4.1 Allosteric Receptor Activation

As a first activation mechanism I consider transmembrane receptors that transduce the signal by allosteric regulation, see Fig. 4.1A. Here, a monovalent ligand binds to a monovalent receptor. Upon binding, the ligand elicits a conformational change in an extracellular ligand-binding domain. This change then propagates through the membrane, triggering a modification in a cytosolic effector domain, changing enzymatic rates, activating further downstream signaling. In this thesis, different activation mechanisms are compared, therefore I refer to this kind of ligand-receptor binding motif as allosteric transmission in the following. For allosteric transmission it is crucial that the receptor acts as a single unit. However, from a molecular perspective it may exist as a monomer (e.g. the G-protein coupled receptors β_2AR and CXCR1 [99]) or as a preformed oligomer (e.g. CXCR2 [99] and other chemokine receptors [100]).

In allosteric transmission, a free monovalent ligand L binds reversibly to a monovalent receptor R , forming a ligand-receptor complex $C = RL$ according to



where the receptor is activated whenever a ligand is bound and inactivated whenever a ligand unbinds. As both the receptor and ligand are monovalent, no additional receptor or ligand can bind to the binary complex and the system is fully described by L , R and C . Using the principles of *mass action kinetics* and assuming that both, the receptors and ligands are well-mixed, the change in time of the concentration for activated receptor complexes C reads¹

$$\frac{dC}{dt} = k_b R \times L - k_u C. \quad (4.3)$$

1: Here, the notation $R \times L$ is used to describe the product of the receptor and the ligand concentration, i.e. to avoid confusion with the concentration of the ligand-receptor complex RL .

The binding rate constant k_b and the unbinding rate constant k_u characterize the velocity of the second-order binding and first-order breakdown of the ligand-receptor complex, respectively. By imposing receptor conservation, i.e. $R(t) + C(t) = R_{\text{tot}} = \text{const.}$, and introducing the equilibrium dissociation constant K ,

$$K = \frac{R \times L}{C} = \frac{k_u}{k_b}, \quad (4.4)$$

the equilibrium concentration of activated receptors ($dC/dt = 0$) can be written as

$$C = R_{\text{tot}} \frac{L}{K + L}. \quad (4.5)$$

Since the maximal concentration of activated receptors is $C_{\text{max}} = R_{\text{tot}}$, the activation curve f , as defined in Eq. (4.1), results to be the well-known hyperbolic curve

$$f(L) = \frac{L}{K + L}, \quad (4.6)$$

corresponding to the standard *Hill-Langmuir equation* with Hill coefficient $n = 1$. The response curve for allosteric transmission is depicted in Fig. 4.2. The half activation point L_{act} , i.e. the ligand concentration with receptor occupancy $f(L_{\text{act}}) = 1/2$, coincides with the dissociation constant $L_{\text{act}} = K$. In addition, f is symmetric about the half activation point ($L = L_{\text{act}}, f = 1/2$) in log-concentration, i.e. $f(cL_{\text{act}}) + f(c^{-1}L_{\text{act}}) = 1$. Increasing or decreasing the dissociation constant shifts the whole function in log space to higher or lower concentrations, respectively. Both can be seen directly by rescaling the ligand concentration L by K , i.e.

$$f(L) = \Phi(L/K) \quad \text{with} \quad \Phi(x) \equiv \frac{x}{1 + x}, \quad (4.7)$$

onto which all binding curves for different ligand affinities collapse. In particular, this means that irrespectively of the ligand-receptor binding affinity, the fraction of activated receptors always saturates for sufficiently high ligand concentration $L \gg K$. As will be shown in Chapter 6, this feature is one of the reasons why allosteric receptors are unable to properly discriminate between different ligands. In the case that lateral allostery between subunits makes binding cooperative, the saturation feature persists [101, 102]. Therefore, cooperativity is not considered in the following.

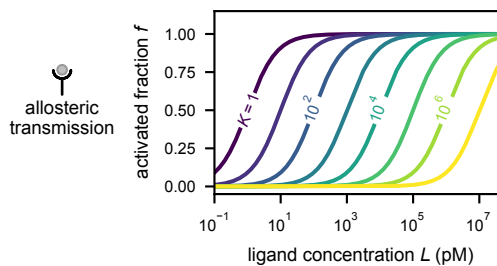


Figure 4.2 | Response repertoire of allosteric receptors Eq. (4.6). Increasing or decreasing K shifts the whole function to higher or lower concentrations, respectively. Dissociation constants K given in pM.

4.2 Receptor Dimerization

Besides allosteric receptors, another large class of receptors, discussed in this section, are receptors activated via ligand-induced oligomerization. This class includes the type I and type II cytokine receptor families [103]. In ligand-induced oligomerization, a multivalent ligand binds to a receptor, inducing cross-linking with other receptor units within the membrane. This receptor cross-linking is then accompanied by cytosolic receptor cross-activation and downstream signaling [51]. Although there are receptor systems using both mechanisms for signaling [104–109], allosteric transmission together with ligand-induced oligomerization, in the following only pure oligomerization is considered. As two of the simplest oligomerization motifs, I consider homo- and heterodimerization, see Fig. 4.1BC. In homodimerization a symmetric bivalent ligand binds to a monovalent receptor, followed by cross-linking to another identical receptor unit. By contrast, in heterodimerization, the receptor architecture used by the IFN system (see Section 2.4), binding of an asymmetric bivalent ligand results in the formation of a ligand-receptor complex comprising two different receptor chains. The receptor activation in the IFN system is based on ligand-induced heterodimerization.

4.2.1 Homodimerization

Ligand-induced homodimerization, the simplest scenario of oligomerization, comprises a symmetric bivalent ligand L and a monovalent receptor R , see Fig. 4.1B. The activated ligand-receptor ternary complex $C = RLR$ is formed according to the following scheme:



where all four reaction rate constants correspond to one binding site. The binary complex RL in Eq. (4.8a) denotes a free receptor R bound to either of the two binding sites from the ligand L . To account for this fact, the additional factor of two in Eq. (4.8a) is introduced. The factor of two in Eq. (4.8b) occurs since C can break down by dissociation of either bound receptor R . I denote the equilibrium dissociation constant for the ligand binding from bulk solution by $K^B = k_u/k_b$ and for the receptor cross-linking within the membrane by $K^X = k_d/k_a$. In equilibrium, applying the *law of mass action* to Eq. (4.8) results in

$$K^B = \frac{2R \times L}{RL}, \quad (4.9a)$$

$$K^X = \frac{R \times RL}{2C}. \quad (4.9b)$$

Resolving Eq. (4.9) for $RL = 2(L/K^B)R$ and $C = R^2L/(K^BK^X)$, the receptor conservation $R(t) + RL(t) + 2C(t) = 2R_{\text{tot}} = \text{const.}$ can be rewritten as

$$R^2 + \left(1 + \frac{K^B}{2L}\right)K^XR - \frac{K^B}{L}K^XR_{\text{tot}} = 0. \quad (4.10)$$

Solving this equation and using $C = R^2L/(K^B K^X)$ the concentration of active receptor complexes is

$$C = R_{\text{tot}} \left[1 - (\sqrt{\Delta^2 + 2\Delta} - \Delta) \right], \quad (4.11)$$

where

$$\Delta = \frac{K^X}{R_{\text{tot}}} \frac{(2L + K^B)^2}{8LK^B} > 0. \quad (4.12)$$

Since the maximal number of active receptor complexes is $C_{\text{max}} = R_{\text{tot}}$, the response curve for homodimerization reads [93, 96, 97, 110, 111]

$$f(L) = F(\Delta) = 1 - (\sqrt{\Delta^2 + 2\Delta} - \Delta), \quad (4.13)$$

where the auxiliary function F decreases from 1 to 0 as Δ increases from 0 to ∞ . This result was found first by Perelson while studying receptor aggregation of immunoglobulins and is also termed *cross-linking curve* [93]. The response curve Eq. (4.13) is bell-shaped as shown in Fig. 4.3. The concentration of active ternary receptor complexes first increases with increasing ligand concentration. At $L_{\text{max}} = K^B/2$, the maximal activation level is attained, i.e.

$$f_{\text{max}} = f(L_{\text{max}}) = F(K^X/R_{\text{tot}}). \quad (4.14)$$

For even higher concentration, the presence of more ligand results in a competition for free receptors, resulting in a decrease in f . Eventually, all receptors are bound in a ligand-receptor complex RL , which effectively blocks receptor dimerization as no free receptors are left to cross-link. The ligand concentration L_{max} depends on the bulk equilibrium dissociation constant K^B , whereas f_{max} solely depends on the ratio R_{tot}/K^X . In particular, this means that unlike the case of allosteric transmission Eq. (4.6), a low affinity ligand cannot fully activate the receptors, irrespectively of the ligand concentration. Since Eq. (4.12) is symmetric in log space with respect to L_{max} , i.e. $\Delta(cL_{\text{max}}) = \Delta(c^{-1}L_{\text{max}})$, the activation curve Eq. (4.13) is also symmetric.

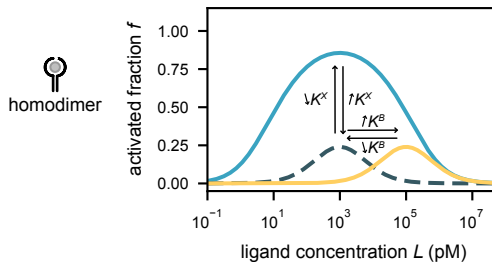


Figure 4.3 | Response curves of homodimerizing receptors Eq. (4.13), for a high (blue) and low (yellow) affinity ligand. The maximal activation level solely depends on the ratio R_{tot}/K^X , whereas its position solely depends on the bulk equilibrium dissociation constant K^B . Dissociation constants: blue, $K^B = 2$ nM; yellow, $K^B = 200$ nM. Binding length scale $K^X/K^B = 5$ nm and total receptor density $2R_0 = 2 \mu\text{m}^{-2}$.

4.2.2 Heterodimerization

A heterodimerizing receptor system is made up of two distinct monovalent receptor chains R_1 and R_2 , each binding reversibly to one of two distinct binding sites of a bivalent ligand L , see Fig. 4.1C and Fig. 4.4. Hence, the activated receptor complex $C \equiv R_1LR_2 = R_2LR_1$ can either be formed by a ligand binding to R_1 followed by cross-linking with R_2 , or

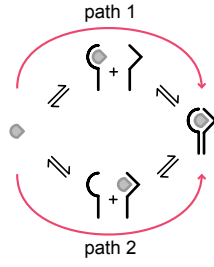
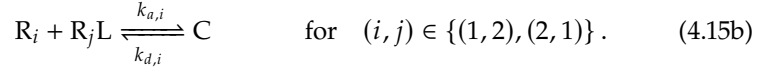
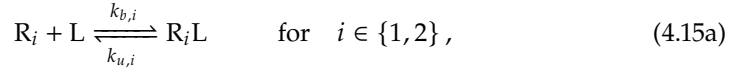


Figure 4.4 | Schematic illustration of ligand-induced receptor heterodimerization. The two pathways forming the ternary complex give rise to a diamond-shaped kinetic topology.

vice versa. These two competing dimerization pathways are described by



Eq. (4.15) lacks the factor two compared to Eq. (4.8), since a receptor R_i can only bind to one specific ligand binding site. In particular, this means that a symmetric heterodimerizing receptor system, in the sense that the ligand binds both receptors chains with the same affinity, but the chains are still specific for only one of the binding sites of the ligand, differs from a homodimerizing receptor system. As in the homodimerizing receptor system, the equilibrium dissociation constants for the ligand binding to the receptor chain R_i from bulk solution is denoted by $K_i^B = k_{u,i}/k_{b,i}$, the receptor cross-linking of a free receptor R_i within the membrane is referred to as $K_i^X = k_{d,i}/k_{a,i}$. Applying the law of mass action to Eq. (4.15), the equilibrium dissociation constants must obey the following equations:

$$R_1 L = \frac{R_1 \times L}{K_1^B}, \quad R_2 L = \frac{R_2 \times L}{K_2^B}, \quad (4.16a)$$

$$C = \frac{R_2 \times R_1 L}{K_2^X}, \quad C = \frac{R_1 \times R_2 L}{K_1^X}. \quad (4.16b)$$

Here, each binding process is in equilibrium with its reverse process. This principle is called *detailed balance* and connects the equilibrium constants by

$$K_1^B K_2^X = K_2^B K_1^X. \quad (4.17)$$

Combining the receptor conservation laws for both receptor chains R_1 and R_2 , i.e. $R_i(t) + R_i L(t) + C(t) = R_{\text{tot},i} = \text{const.}$, with Eq. (4.16), the equilibrium concentration of active receptor complexes reads

$$C = \frac{R_{\text{tot},1} + R_{\text{tot},2}}{2} \left[1 - \left(\sqrt{\tilde{\Delta}^2 + 2\tilde{\Delta} + 1 - \frac{4R_{\text{tot},1}R_{\text{tot},2}}{(R_{\text{tot},1} + R_{\text{tot},2})^2}} - \tilde{\Delta} \right) \right], \quad (4.18)$$

where

$$\tilde{\Delta} \equiv \frac{K_1^X}{R_{\text{tot},1} + R_{\text{tot},2}} \frac{(L + K_1^B)(L + K_2^B)}{LK_1^B}. \quad (4.19)$$

For the case of equally abundant receptor chains, i.e. $R_{\text{tot},1} = R_{\text{tot},2} = R_{\text{tot}}$, the response curve reduces to [94, 96, 97, 111]

$$f(L) = \frac{C}{R_{\text{tot}}} = F(\tilde{\Delta}), \quad (4.20)$$

corresponding to the response curve of homodimerization Eq. (4.13), but Δ replaced by $\tilde{\Delta}$, given by

$$\tilde{\Delta} = \frac{K_1^X}{R_{\text{tot}}} \frac{(L + K_1^B)(L + K_2^B)}{2LK_1^B}. \quad (4.21)$$

This result was achieved first by Perelson studying histamine release by mast cells and basophils [94]. Using the detailed balance condition Eq. (4.17), Eq. (4.21) can be rewritten to

$$\tilde{\Delta} = \frac{K_2^X}{R_{\text{tot}}} \frac{(L + K_1^B)(L + K_2^B)}{2LK_2^B}, \quad (4.22)$$

emphasizing the overall symmetry of both pathways, see Fig. 4.4. The activation point is set by the receptor chain that binds the ligand with high affinity, whereas the deactivation point is determined by the low-affinity receptor chain. Thus, a ligand binding both receptor chains with highly different affinities, results in a broad activation plateau, see Fig. 4.5. The maximal activation level solely depends on both cross-linking equilibrium constants,

$$f_{\text{max}} = F \left(\frac{[\sqrt{K_1^X} + \sqrt{K_2^X}]^2}{2R_{\text{tot}}} \right), \quad (4.23)$$

and is attained for a ligand concentration coinciding to the geometric mean of both bulk equilibrium constants, i.e. $L_{\text{max}}^2 = K_1^B K_2^B$. As for the homodimerizing system, the heterodimeric response curve [see Eq. (4.20)] is symmetric in log space with respect to L_{max} , since $\tilde{\Delta}(cL_{\text{max}}) = \tilde{\Delta}(c^{-1}L_{\text{max}})$.

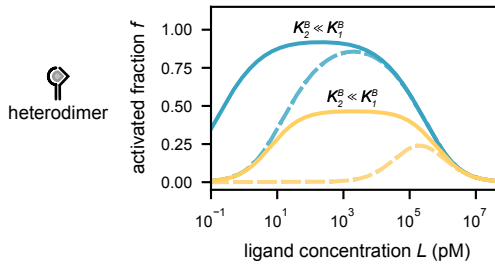


Figure 4.5 | Response curves of heterodimerizing receptors Eq. (4.20), for a high (blue) and low (yellow) affinity ligand. Asymmetric binding affinities result in broad activation plateaus. Dissociation constants: blue, $K_1^B = 2$ nM, $K_2^B = 20$ pM; yellow, $K_1^B = 200$ nM, $K_2^B = 20$ pM. Dashed lines indicate the corresponding symmetric response curve with increased K_2^B such that $K_2^B = K_1^B$. Binding length scale $K^X/K^B = 5$ nm and total receptor density $2R_0 = 2 \mu\text{m}^{-2}$.

4.2.3 Ligand-Independent Binding Length Scale

The formation of an activated receptor complex in ligand-induced dimerization comprises two steps, cf. Eq. (4.8) or Eq. (4.15). The first step is the ligand binding from bulk solution, i.e. $R + L \rightleftharpoons RL$, and the second step the receptor cross-linking within the membrane, i.e. $RL + R \rightleftharpoons RLR$. The equilibrium dissociation constants for both binding reactions are referred to K^B and K^X , respectively. Although both reactions describe different processes and thus differ in their binding free energies, both share the feature that the same new $R \cdot L$ non-covalent bond is formed. Keeping the similarity in mind, the binding free energy is decomposed into two parts, i.e.

$$\Delta G = \Delta G_{\text{struct}} + \Delta G_{\text{bond}}, \quad (4.24)$$

where G_{struct} introduces the binding free energy arising on the scale of the entire molecule and G_{bond} describes the part of the binding free energy originating from local residue-residue interactions at the ligand-receptor binding interface. Here, the former energy contains a conformational internal energy due to overall structural deformations in the complex and the configurational entropy of the complex partners while the latter includes energies due to the formation of hydrogen bonds, salt bridges or local nonpolar interactions.

Focusing on ΔG_{struct} , the overall structural changes and the configurational entropy losses differ for both reactions. In the first step of ligand binding from the bulk solution, overall structural changes correspond to the transition of a free ligand-receptor pair to a ligand-receptor complex RL. In contrast, upon cross-linking the conformation of a free receptor R and a ligand-receptor complex RL is changed into that of an activated receptor complex RLR. Furthermore, upon ligand binding from the bulk solution, the ligand loses the entropy of its three-dimensional degrees of freedom, whereas upon cross-linking the receptor chain pair loses two-dimensional configuration entropy. Thus, in general, the molecular-scale binding free energy change differs between the two reactions, i.e.

$$\Delta\Delta G_{\text{struct}} \equiv \Delta G_{\text{struct}}^B - \Delta G_{\text{struct}}^X \neq 0. \quad (4.25)$$

Next, for the binding free energy G_{bond} , I make the simplifying assumption that the binding mode of ligand and receptor is independent of the overall structural changes occurring between RL and RLR. In particular, this plausible assumption implies that the residue-residue contacts in RL and at both interfaces of RLR are the same, i.e.

$$\Delta\Delta G_{\text{bond}} \equiv \Delta G_{\text{bond}}^B - \Delta G_{\text{bond}}^X = 0. \quad (4.26)$$

In the interferon system, ligands with different affinities form structurally highly similar activated receptor complexes [59]. In other words, ligands of different affinities differ in their local residue-residue contacts but not the overall structure of the RL and RLR complexes. Thus, it is plausible to assume that only ΔG_{bond} but not ΔG_{struct} depends on the ligand type. Using the standard thermodynamic relation for the dissociation constant,

$$K = c^0 e^{\beta\Delta G^0}, \quad (4.27)$$

where β is the inverse thermal energy and ΔG^0 the free energy corresponding to the reference concentration c^0 , the binding length scale $\lambda = K^X/K^B$ reads

$$\lambda = \frac{K^X}{K^B} = \frac{c_{2d}^0 e^{\beta\Delta G^{X,0}}}{c_{3d}^0 e^{\beta\Delta G^{B,0}}} = \frac{c_{2d}^0}{c_{3d}^0} e^{-\beta\Delta\Delta G_{\text{struct}}^0}, \quad (4.28)$$

where c_{2d}^0 and c_{3d}^0 denote the reference concentration corresponding to K^X and K^B , respectively. The assumption of an unchanged binding mode therefore results in a binding length scale $\lambda = K^X/K^B$ independent of the ligand. In the case of heterodimerization, the presented arguments carry through for each of the binding sites, resulting in a ligand-independent binding length scale λ for each receptor chain R_i . Furthermore, applying the detailed balance condition [see Eq. (4.17)] yields a common λ for both

IFN ligand	receptor chain	binding length scale λ (nm)	reference
$\alpha 2$ wt	IFNAR1	5.1; 12.2; 4.8; 11.1	[112–115]
	IFNAR2	5.6; 18.6	[112, 114]
$\alpha 2$ YNS	IFNAR1	5.5	[112]
	IFNAR2	4.5	[112]
$\alpha 2$ R144A	IFNAR1	22.0; 8.8	[113, 114]
	IFNAR2	8.7	[114]
$\alpha 2$ M148A	IFNAR1	11.2	[113]
$\alpha 2$ R120E	IFNAR1	< 40	[115]

Table 4.1 | Overview of the binding length scales λ in the IFN receptor system for IFN $\alpha 2$ and several IFN $\alpha 2$ mutants. Here, all binding length scales are extracted from Refs. [112–115].

receptor chains R_1 and R_2 , i.e.

$$\lambda = \frac{K_1^X}{K_1^B} = \frac{K_2^X}{K_2^B}. \quad (4.29)$$

In the interferon system, a ligand-independent λ is supported within experimental error in the data from independent biochemical experiments [112–115]. Table 4.1 gives an overview of measured K^B and K^X , with their ratios, for a range of different ligands.

Finally, two points should be remarked. First, a ligand-independent length scale has already been applied in a similar context in Ref. [111], although the relation to the underlying assumptions about the binding model was not given there. Second, the ligand-independent length scale is a consequence of simplifying, albeit plausible, assumptions and is therefore not a thermodynamic identity. Dimerizing receptors other than IFNAR may deviate this behavior.

Ligand-Independent Binding Length Scale Sets Global Deactivation Point

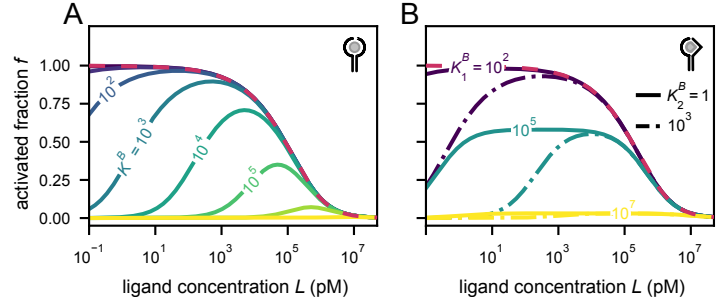
A ligand-independent binding mode on the response curves for dimerizing receptor systems is investigated. For both, homo- and heterodimerizing receptor systems, the maximal activation is solely dependent on the cross-linking dissociation constant(s) $K_{(i)}^X$, and the concentration of maximal activation depends only on the dissociation constant(s) for the ligand binding from the bulk $K_{(i)}^B$, see Eq. (4.14) and Eq. (4.23). Applying Eq. (4.28), i.e. $\lambda = K^X/K^B = \text{const.}$, couples the maximal activation level with its position, see Fig. 4.6. In particular, shifting the maximal activation to higher concentration, results in a decrease of activation.

Both response curves Eq. (4.13) for homodimerizing and Eq. (4.20) for heterodimerizing receptors are decreasing functions with respect to K^B and K_i^B , respectively. Therefore, maximizing the response curve for a given ligand concentration L , corresponds to the high affinity limit. Applying this limit, i.e. $K^B \rightarrow 0$ and $K_i^B \rightarrow 0$, to Eq. (4.12) and Eq. (4.21), respectively,

Table 4.2 | Overview of the response curves f for the three equilibrium receptor-ligand binding motifs: allosteric transmission, homo- and heterodimerizing. While the allosteric response function follows hyperbolic saturation kinetics (monotonic increase), the two dimerization motifs show a characteristic bell-shape response in log-space. For the dimerization, a ligand-independent binding length $\lambda = K^X/K^B$ is assumed. $F(\Delta)$ is defined in Eq. (4.13) and the result for heterodimerizing case assumes $R_{1,\text{tot}} = R_{2,\text{tot}} = R_{\text{tot}}$.

receptor topology	activation curve f	parameters
allosteric transmission	$f = L/(K + L)$	K
homodimerization	$f = F(\Delta)$ $\Delta = \frac{\lambda(2L+K^B)^2}{8LR_{\text{tot}}}$	$K^B, \lambda, R_{\text{tot}}$
heterodimerization	$f = F(\tilde{\Delta})$ $\tilde{\Delta} = \frac{\lambda(L+K_1^B)(L+K_2^B)}{2LR_{\text{tot}}}$	$K_1^B, K_2^B, \lambda, R_{\text{tot}}$

Figure 4.6 | Response repertoire of dimerizing receptors: (A) homodimerizing and (B) heterodimerizing. Limiting curves at high affinities are shown dashed and in red, and total receptor density $2R_0 = 2\mu\text{m}^{-2}$. Dissociation constants K is given in pM.



directly results in a common envelope function (see Fig. 4.6)

$$f_{\text{envelope}}(L) = F\left(\frac{\lambda L}{2R_{\text{tot}}}\right), \quad (4.30)$$

with a global half-deactivation point at

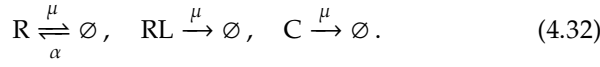
$$L_{\text{deact}} = \frac{R_{\text{tot}}}{2\lambda}. \quad (4.31)$$

In summary, dimerizing receptors with a ligand-independent binding mode have a repertoire of response curves that are constrained to remain below a common envelope response curve. The activation curves for all three equilibrium receptor-ligand binding motifs are summarized in Table 4.2.

4.3 Receptor Turnover

Membrane receptors are exposed to receptor internalization, which is followed by either degradation or recycling. This kind of receptor turnover fulfills many important functions [116], such as replacement of defective receptors, sensitization by reducing receptor densities [117] and degradation of ligands to enable a better gradient sensing [118]. Therefore, I revisit the previously discussed ligand-receptor activation curves and investigate the effect of receptor turnover, see Fig. 4.1D. The essential features of turnover are captured by two additive reactions. First, by a first order process describing the receptor internalization followed by degradation. Since there is no evidence for targeted degradation in the IFN receptor system, I assume that all stages of receptor complex R, RL, C are internalized and degraded with the common degradation rate μ . Second, to ensure a constant overall receptor concentration in

steady state, a zeroth order receptor production process reintegrates free receptors R into the membrane with a rate α . Combining both processes, the receptor turnover scheme reads



In steady state, the overall number of receptor chains is determined by the ratio of production and degradation rate:²

$$\left. \begin{array}{l} \text{allosteric transmission: } R + C \\ \text{homodimerization: } \frac{R+RL}{2} + C \\ \text{heterodimerization: } R_i + R_iL + C \end{array} \right\} = \frac{\alpha}{\mu} \equiv R_{\text{tot}}, \quad (4.33)$$

2: The response of dimerizing receptors depends on the receptor concentration. Here, the factor of 1/2 ensures that both dimerizing receptor systems have the same overall concentration of receptors given by $2R_{\text{tot}}$.

where the equation for the heterodimerizing receptor holds true for each $i = 1, 2$ separately. Here, the ratio α/μ is set to R_{tot} , i.e. $\alpha = \mu R_{\text{tot}}$, such that the response curves are consistent with the previously discussed equilibrium response curves.

In the following, I derive closed form expressions for the binding curves in the case of allosteric transmission and homodimerization. For the case of heterodimerization, binding curves are obtained numerically.

4.3.1 Allosteric Transmission

To investigate the effect of receptor turnover on the allosteric response curve Eq. (4.6), I apply the law of mass action to the reaction scheme for allosteric transmission Eq. (4.2) combined with the turnover scheme Eq. (4.32), yielding a system of ordinary differential equations (ODEs),

$$\frac{dR}{dt} = -k_b R \times L + k_u C + \mu(R_{\text{tot}} - R), \quad (4.34a)$$

$$\frac{dC}{dt} = k_b R \times L - (k_u + \mu)C, \quad (4.34b)$$

where the production rate was replaced by $\alpha = \mu R_{\text{tot}}$, see Eq. (4.33). In steady state, adding both equations, Eq. (4.34a) and Eq. (4.34b), results in the receptor conservation law $R_{\text{tot}} = R + C$. Using this conservation law with the fact that Eq. (4.34b) corresponds to the equation without receptor turnover Eq. (4.3) with $k_u \rightarrow k_u + \mu$, the steady state response curve reads

$$f(L) = \Phi\left(\frac{L}{(1 + \tau_u)K}\right), \quad (4.35)$$

where $\tau_u = \mu/k_u$ introduces a dimensionless binding time, $K = k_u/k_b$ denotes the equilibrium dissociation constant, see Eq. (4.4), and $\Phi(x)$ is the collapsed response curve for allosteric transmission defined in Eq. (4.7). Comparing Eq. (4.35) with the response curve without turnover Eq. (4.7), the turnover shifts the whole curve to higher concentrations, i.e. $L_{\text{act}} = (1 + \tau_u)K$. The overall shape of the activation curve is not affected by the process of receptor turnover. In the limit of slow turnover, i.e. $\tau_u \rightarrow 0$, the case without turnover is recovered. Overall, including the effect of turnover to the response curve of allosteric transmission

corresponds to an effectively increased dissociation constant. Because receptor turnover is ligand independent, the effect of the turnover on the response curves corresponds to effectively lowering the affinity of all ligands by the factor $(1 + \tau_u)$.

4.3.2 Homodimerization

Next, I consider a homodimerizing receptor system including receptor turnover. Incorporating turnover Eq. (4.32) into Eq. (4.8) results in

$$\frac{dR}{dt} = -(2k_b L + \mu)R + k_u RL - k_a R \times RL + 2k_d C + \mu R_{\text{tot}}, \quad (4.36a)$$

$$\frac{dRL}{dt} = 2k_b L \times R - (k_u + \mu)RL - k_a R \times RL + 2k_d C, \quad (4.36b)$$

$$\frac{dC}{dt} = k_a R \times RL - (2k_d + \mu)C. \quad (4.36c)$$

Using Eq. (4.1) with $C_{\text{max}} = R_{\text{tot}}$, the steady state response curve can be found after some straightforward calculations and reads [1]

$$f(L) = 1 - (\sqrt{\Delta_1^2 + 2\Delta_2} - \Delta_1), \quad (4.37)$$

where

$$\Delta_1 = \Delta_0 + \frac{\tau_u(2L - K^B)}{(2 + \tau_u)(4L + \tau_u K^B)}, \quad (4.38a)$$

$$\Delta_2 = \Delta_0 + \frac{\tau_u^2 K^B}{2(2 + \tau_u)(4L + \tau_u K^B)}, \quad (4.38b)$$

$$\Delta_0 = \frac{K^X(2 + \tau_d) [K^B(2 + \tau_u) + 4L + \tau_u K^B]^2}{8R_{\text{tot}} K^B(2 + \tau_u)(4L + \tau_u K^B)}. \quad (4.38c)$$

$K^B = k_u/k_b$ and $K^X = k_d/k_a$ denote the equilibrium dissociation constants for the ligand binding from bulk and for the receptor cross-linking within the membrane respectively as previously. In addition, $\tau_u = \mu/k_u$ and $\tau_d = \mu/k_d$ introduce two dimensionless binding times. In the limit of no turnover, i.e. $\tau_u, \tau_d \rightarrow 0$, Eq. (4.37) simplifies to the homodimerizing response curve without turnover Eq. (4.13), as required.

One observes that receptor turnover breaks the symmetry of the response curve in log space. Further it decreases the maximal activation cf. Eq. (4.14)

$$f_{\text{max}} = F \left(\frac{(2 + \tau_d)K^X}{2R_{\text{tot}}} \right) \quad (4.39)$$

and shifts it to higher concentration

$$L_{\text{max}} = \frac{K^B}{2} \left[1 + \frac{\tau_u}{2} \left(1 + \sqrt{1 + \frac{4R_{\text{tot}}}{K^X(2 + \tau_d)}} \right) \right]. \quad (4.40)$$

Taking into account that all ligand-receptor complexes share a common binding mode [see Eq. (4.28)], maximizing Eq. (4.37) with respect to K^B

results in the half-deactivation point

$$L_{\text{deact}} = \frac{R_{\text{tot}}}{2\lambda} \frac{2 + 3\tau_u}{2 + \tau_d}. \quad (4.41)$$

Comparing Eq. (4.41) with Eq. (4.31) illustrates that the turnover can shift the global deactivation point to higher (lower) concentrations for $3\tau_u > \tau_d$ ($3\tau_u < \tau_d$). Intuitively, slow τ_u means bulk ligand unbinding is slower relative to the turnover, so that at high ligand concentration, excess binary complexes are removed by turnover and thereby supporting ternary complex formation. Counteracting this effect, slow complex dissociation τ_d means some active complexes are removed before reforming. In combination, whether the deactivation point is shifted to higher (lower) concentration is fully determined by the ratio $k_d/k_u < (>) 3$.

4.3.3 Heterodimerization

Including the effect of receptor turnover Eq. (4.32) and Eq. (4.33), in a heterodimerizing system with two distinct receptor chains R_1 and R_2 as in Eq. (4.15), results in the following ODEs:

$$\frac{dR_i}{dt} = -(k_{b,i}L + \mu)R_i + k_{u,i}R_iL - k_{a,i}R_i \times R_jL + k_{d,i}C + \mu R_{\text{tot}}, \quad (4.42a)$$

$$\frac{dR_iL}{dt} = k_{b,i}R_i \times L - (k_{u,i} + \mu)R_iL - k_{a,j}R_j \times R_iL + k_{d,j}C, \quad (4.42b)$$

$$\frac{dC}{dt} = k_{a,1}R_1 \times R_2L + k_{a,2}R_2 \times R_1L - (k_{d,1} + k_{d,2} + \mu)C, \quad (4.42c)$$

where $(i, j) \in \{(1, 2), (2, 1)\}$. Here, $K_i^B = k_{u,i}/k_{b,i}$ and $K_i^X = k_{d,i}/k_{a,i}$ introduce the equilibrium dissociation constants and $\tau_{u,i} = \mu/k_{u,i}$ and $\tau_{d,i} = \mu/k_{d,i}$ the dimensionless timescales, as previously. As for the homodimerizing case, including turnover increases the allowed design space of the response curves. In particular, it includes broad plateaus with distinct low and high activation levels and common activation and deactivation point.

Because Eq. (4.42) does not have a straightforward closed-form steady state, I calculate the response curves numerically. These will be discussed in Chapter 6.

4.4 Receptor Readout

After the signal has been detected by the cell in the form of receptor activation in the first step, the signal is passed on to the intracellular side in the next step. In many signal transduction pathways, activated receptor complexes C are read out by phosphorylation of intracellular signaling molecules M , i.e. $M \rightleftharpoons M_p$, see Fig. 4.1E. The rate of phosphorylation is proportional to the total number of activated complexes. Since I consider a fixed total receptor number R_{tot} in the context of ligand discrimination, the rate of phosphorylation is also proportional to the activated receptor fraction f . Assuming constitutive dephosphorylation with the rate ω_u

and absorbing the receptor number R_{tot} in the phosphorylation rate ω_p , yields



The master equation corresponding to Eq. (4.43) reads

$$\begin{aligned} \frac{\partial p(n;t)}{\partial t} = & f\omega_p (N - n + 1) p(n - 1;t) + \omega_u (n + 1) p(n + 1;t) \\ & - [\omega_u n + f\omega_p (N - n)] p(n;t), \end{aligned} \quad (4.44)$$

where, $p(n;t)$ introduces the probability that n out of N readout molecules M are phosphorylated at time t . Next, as simplifying assumption, I consider a linear regime where only a small fraction of M is phosphorylated and therefore neglect effects of readout molecule depletion. Mathematically, this assumption corresponds to a large reservoir of unphosphorylated readout molecules, i.e. $N \rightarrow \infty$ with $N\omega_p \rightarrow \text{const}$. The reaction then simplifies to



where $\tilde{\omega}_p \equiv \omega_p N$ introduces an effective phosphorylation rate. Applying the assumption of a reservoir to the master equation, i.e. applying the limit of $N \rightarrow \infty$ with $N\omega_p \rightarrow \tilde{\omega}_p = \text{const}$, yields

$$\begin{aligned} \frac{\partial p(n;t)}{\partial t} = & f\tilde{\omega}_p p(n - 1;t) + \omega_u (n + 1) p(n + 1;t) \\ & - [\omega_u n + \tilde{\omega}_p] p(n;t). \end{aligned} \quad (4.46)$$

Solving Eq. (4.46) for steady state distribution $p(n)$ yields the well-known Poisson distribution with mean $f\bar{n}$ [119],

$$p(n) = \frac{(\bar{n}f)^n}{n!} e^{-\bar{n}f}, \quad (4.47)$$

where the readout number $\bar{n} = \tilde{\omega}_p / \omega_u$ introduces the mean phosphorylated readout molecule number at full receptor activation $f = 1$. This parameter thus characterizes the *noise level* of the readout, i.e. the readout noise coefficient of variation is $c_v = \langle n \rangle / \text{Var}(n) = 1 / \sqrt{\bar{n}f}$.

An Introduction to Information Theory

5

Although most of us have a vague intuitive idea of what information is, a mathematical precise formulation for it has been missing for a long time until Claude Shannon introduced it in the 1940s [120]. Information theory address this question by formalizing this intuition into something mathematically precise. Here, I give a brief introduction to information theory, focusing on the concepts relevant for this thesis. For a more comprehensive introduction into information theory, I recommend the excellent textbooks [92, 121, 122] and the original work by Shannon [120]. In addition, two reviews should be mentioned: Ref. [123] stands out for its intuitive introduction to the foundation of information theory. Ref. [124] provides an overview of information theory combined with the physics of living systems.

5.1 What is Information? . . .	31
5.1.1 Entropy	32
5.2 Transmission of Information	32
5.2.1 Mutual Information	33
5.2.2 Joint Entropy and Conditional Entropy	34
5.2.3 Relation Between Entropy and Mutual Information	34

5.1 What is Information?

Let us assume that Alice and Bob are having a conversation and Alice is about to ask Bob a question. Before hearing Bob's answer, Alice cannot tell for sure which answer Bob will give. From her perspective, the answer is random, and Alice is therefore uncertain about it. Upon hearing the answer, the uncertainty and randomness are eliminated, therefore Alice has obtained information. However, even though it is intuitively clear that Alice has obtained information, the question of how much information Alice has obtained is much more difficult to answer. Claude Shannon addressed this open question and derived the measure of information by proposing that it must obey the following properties [120]: First, he started with the implicit assumption that the information gained is a function of the probability distribution over all possible answers to the question. In the case of Alice and Bob, this corresponds to the assumption that Alice knows her interlocutor Bob very well. Therefore, Alice knows all possible answers $n = 1, 2, \dots, N$ and assigns to each of them a probability p_n . Second, he proposed that the information must grow with the total number N of possible answers, in the case of equally likely answers, i.e. $p_n = p$. Third, if the question can be broken down into independent parts, then the information gained on hearing the answer to each part should add to the total. Fourth, if the question can be decomposed into a tree of choices, then the total information should be the weighted sum along the paths through the tree. Strikingly, Shannon proved that the entropy is a unique solution as a measure of information, fulfilling these postulates [120].

Statistical mechanics textbooks typically teach the statement that the entropy of a gas should be understood as a measure of our lack of information about the microscopic state of the molecules. Thus, in contrast to the textbooks which mostly left the connection between entropy and information a bit vague, Shannon's theorem formalizes this connection. The entropy of a gas¹ can therefore be also viewed as the information one would gain upon learning the full microscopic state [124].

1: If starting with a classical formulation, estimating the entropy of a gas results in the problem of defining the entropy for continuous variables, i.e. taking the logarithm of a quantity with dimensions. This problem can be circumvented by using the quantum version, as here the problem has a discrete set of states. A detailed discussion on this subject can be found for example in Ref.[122].

5.1.1 Entropy

Let X be a discrete random variable and x a particular outcome of it. The set of possible outcomes of X is then denoted by \mathcal{X} , i.e. $x \in \mathcal{X}$. The entropy of X is defined as

$$H(X) = - \sum_{x \in \mathcal{X}} p(x) \log_2 p(x), \quad (5.1)$$

where $p(x) = \Pr\{X = x\}$ introduces the probability that X has the outcome x . By choosing the base-2 logarithm, the unit of information is called bit.

By introducing the expectation value of a random variable $f(X)$

$$\langle f(X) \rangle = \sum_{x \in \mathcal{X}} p(x) f(x), \quad (5.2)$$

the entropy can be rewritten to

$$H(X) = -\langle \log_2 p(X) \rangle. \quad (5.3)$$

Thus, the entropy can be interpreted as the expected value of the random variable $-\log_2 p(X)$, and therefore a measure for how surprising the random event is on average. Here, an outcome with low probability is more surprising and contains more information. Therefore, one might think that a random variable containing many extremely rare outcomes and a few likely ones will have the highest entropy. In fact, the opposite is the case: The maximal entropy for a given number of possible outcomes is given by equally likely outcomes. The reason is that as the event becomes rarer, the probability $p(x)$ that this rare event occurs decreases more quickly, effectively outweighing the gains in information, i.e. $-p(x) \log_2 p(x) \rightarrow 0$ for $x \rightarrow 0$. To illustrate this behavior, let us consider a Bernoulli process, where a random variable X can take the values $x = 0, 1$ with probability $p(0) = q$, $p(1) = 1 - q$. The entropy then reads

$$H(X) = -q \log_2 q - (1 - q) \log_2 (1 - q). \quad (5.4)$$

For the case of $q = 0$ or $q = 1$ the outcome is certain and therefore the entropy vanishes, see Fig. 5.1. By contrast, for $q = 1/2$ the uncertainty of the outcome is maximal and so the entropy.

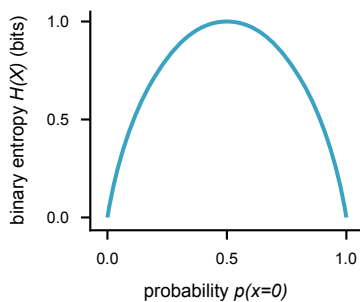


Figure 5.1 | Binary entropy function $H(X)$ as defined in Eq. (5.4).

5.2 Transmission of Information

The previous section addressed how the information of a random variable can be quantified. Next, the more general case of how information can be shared among multiple random variables is considered. Here, the shared information means how much the uncertainty of one random variable will be reduced by knowing the outcome of another random variable.

5.2.1 Mutual Information

The *mutual information* $I(X; Y)$ quantifies the mutual dependence between the two variables X and Y and is defined by

$$I(X; Y) = \sum_{x \in \mathcal{X}} \sum_{y \in \mathcal{Y}} p(x, y) \log_2 \frac{p(x, y)}{p(x)p(y)} \quad (5.5a)$$

$$= \left\langle \log_2 \frac{p(x, y)}{p(x)p(y)} \right\rangle. \quad (5.5b)$$

In other words, the mutual information $I(X; Y)$ corresponds to taking a probability-weighted average of the point-wise mutual information $\log_2 p(x, y) - \log_2 p(x)p(y)$. Here, one bit of information corresponds to be able to rule out half of the probability mass. In the case of equally likely outcomes, one bit also corresponds to be able to rule out half of the possible outcomes. For independent variables, both the mutual information and the correlation vanish. However, the mutual information can capture highly informative relation between X, Y that are not linear and is therefore a more general version of correlation.

By using Jensen's inequality, it can be shown that $I(X; Y)$ is non-negative, i.e. $I(X; Y) \geq 0$. The minimum value $I(X; Y) = 0$, corresponds to the case of independent X and Y , i.e. $p(x, y) = p(x)p(y)$. The upper bound of the mutual information is set by the random variable containing less information, i.e. the lesser of $H(X)$ and $H(Y)$. Intuitively, this bound means that a random variable can neither convey more information about another random variable as it contains itself, nor than the other random variable contains.

The mutual information can be considered in terms of a signal transduction, which is employed in Chapter 6. Here, X describes the input. The input is then processed, producing the outcome Y . In this context the mutual information can be interpreted in two ways. From the perspective of the sender, the mutual information quantifies how well the outcomes of Y can be distinguished for different input of X . Whereas from the perspective of the receiver, the mutual information measures how well the input X can be inferred from the measured output Y .

Data Processing Inequality

Another important property of the mutual information is described by the *data processing inequality*, which states that the information about a signal cannot be increased by any local physical operation. For example, let the three random variables A, B, C form the Markov chain $A \rightarrow B \rightarrow C$, i.e. the signal is mapped first from A to B and then further processed from B to C . The theorem then states that no post-processing of B can increase, but only preserve or reduce the information [121], i.e.

$$I(A; B) \geq I(A; C). \quad (5.6)$$

In other words this means that the information about A can only be preserved or lost at each step ($A \rightarrow B$ and $B \rightarrow C$). In particular, the theorem states that information lost at the first stage, can not be recovered latter on.

5.2.2 Joint Entropy and Conditional Entropy

The mutual information is a measure for the information obtained about one random variable by observing another random variable. By contrast, the *conditional entropy* quantifies how much uncertainty remains having observed another random variable. Let (X, Y) be a pair of discrete random variables with a joint distribution $p(x, y)$. The conditional entropy $H(Y|X)$ of this pair is then defined as

$$\begin{aligned} H(Y|X) &= \sum_{x \in \mathcal{X}} p(x)H(Y|X = x) \\ &= -\langle \log_2 p(Y|X) \rangle. \end{aligned} \tag{5.7}$$

The *joint entropy* $H(X, Y)$ extends the entropy to two random variables considered together $(X, Y) \sim p(x, y)$:

$$\begin{aligned} H(X, Y) &= \sum_{x \in \mathcal{X}} \sum_{y \in \mathcal{Y}} p(x, y) \log_2 p(x, y) \\ &= -\langle \log_2 p(X, Y) \rangle. \end{aligned} \tag{5.8}$$

In the case that X and Y are independent, observing X does not reduce the uncertainty about Y , and vice versa. Thus, the joint entropy is given by the sum of the entropy of each random variable, i.e. $H(X, Y) = H(X) + H(Y)$, as a direct consequence of $p(x, y) = p(x)p(y)$.

The relation between entropy, joint entropy and conditional entropy is given by:

$$H(X, Y) = H(X) + H(Y|X) \tag{5.9a}$$

$$= H(Y) + H(X|Y). \tag{5.9b}$$

This chain rule directly follows from $p(x, y) = p(x)p(y|x)$.

5.2.3 Relation Between Entropy and Mutual Information

Using the joint entropy and conditional entropy, the mutual information can be rewritten in different forms:

$$I(X; Y) = H(X) - H(X|Y) \tag{5.10a}$$

$$= H(Y) - H(Y|X) \tag{5.10b}$$

$$= H(X) + H(Y) - H(X, Y). \tag{5.10c}$$

In the first two rows, the mutual information can be interpreted as the difference of the average uncertainty in the random variable X (Y) with the uncertainty that remains in X (Y) having observed another random variable Y (X), respectively. Here, the symmetry in both random variables X and Y emphasize that X says as much about Y as Y says about X . In addition, Eq. (5.10a) implies that $I(X; X) = H(X)$, which is the reason why the entropy is sometimes also referred to as *self-information*. In the third row Eq. (5.10c), the mutual information can be interpreted as the sum of the average uncertainty of two random variables X, Y minus the uncertainty of both considered together. The relation between the mutual information and the entropy is visualized in Fig. 5.2.

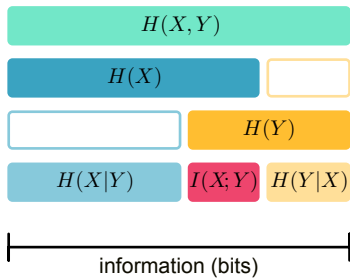


Figure 5.2 | Relationship between entropy $H(X)$, $H(Y)$, joint entropy $H(X, Y)$, conditional entropy $H(X|Y)$, $H(Y|X)$ and mutual information $I(X; Y)$. The width of each bar encodes the corresponding information in bits [92, 123].

An Information-Theoretic Analysis of Optimal Ligand Discrimination

6

This chapter is based on Ref. [1]. For a detailed listing of author contributions see Appendix A.

The cell-cell communication in tissue cells is mostly realized by chemical signaling, i.e. by releasing and detecting extracellular ligands including hormones, growth factors and cytokines, see Chapter 2. At the receiving cell, the message of the incoming signal must first cross the membrane, which is typically achieved through activation of membrane receptors. This initial step in signal transduction is decisive because intracellular signaling cascades may process, amplify and integrate signals [125–127], but cannot recover information lost at the receptor stage [121, 128, 129]. Furthermore, as membrane receptor systems often already process signals¹, this suggests that information processing at the membrane enables cells to transmit relevant signals but reject noise and thereby to establish a robust communication channel. Understanding the information-theoretic properties of receptor systems [130–132] is instrumental for clarifying the biological function of signaling pathways.

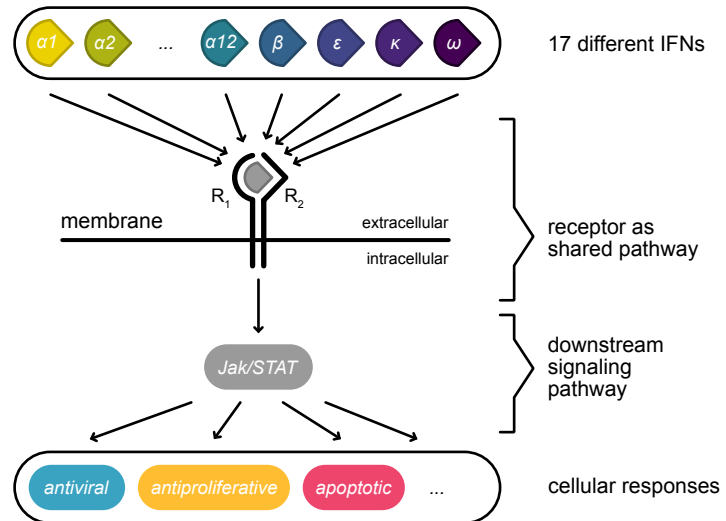
This chapter is dedicated to ligand discrimination at the membrane stage, where the relevant signal is the type of ligand present in the cellular environment, rather than its concentration, motivated by the phenomenon of affinity sensing in the type I interferon (IFN) system. In the case of viral infections, tissue cells can alert cells in vicinity by secreting interferons, to which these respond by antiviral or antiproliferative behavior. In humans, 17 different IFN ligands are known (13 IFN α subtypes and IFN β , ϵ , κ and ω), which bind to a single dimeric receptor (IFNAR) with widely varying affinities [59, 73, 133], see Section 2.4. As all ligands form structurally highly similar activated receptor complexes [59], the evolutionary advantages of this diversity are not fully understood. Therefore, it has been a puzzling finding that different IFN types elicit different cellular responses, for example, IFN β can inhibit cell proliferation while saturating concentrations of a lower-affinity IFN variant cannot [134]. Ultimately, it has been an open question how the single receptor complex IFNAR can robustly multiplex information [135] from its diverse ligands despite the inhomogeneous and noisy ligand distributions, see Fig. 6.1. For this kind of affinity sensing, several possible mechanisms have been proposed, including effects of downstream gene expression feedback [133], bistability [136], corraling of receptors on the membrane [137] and the kinetics of dimer-receptor activation [111]. A related and widely studied topic is foreign vs. self-peptide discrimination in adaptive immunity in T-cells [138–142]. It has been predicted theoretically and shown experimentally that signaling pathways operating by kinetic-proofreading schemes downstream of T-cell receptors can read out the dwell times of ligands to optimally separate multiple self and foreign antigens in heterogeneous environments [143–146].

Here, I ask what generic features enable a receptor system to discriminate between ligand types directly at the membrane, overcoming the

6.1 Ligand Discrimination as Information-Processing Task	36
6.1.1 Input Distribution	38
6.1.2 Input-Output Relation	38
6.1.3 Ligand Concentration Distribution	39
6.2 Receptor Architectures and Their Ligand Discrimination Power	39
6.3 Effect of Additional Noise Sources	45
6.3.1 Cell-to-Cell Variability in Receptor Number	45
6.3.2 Molecular Noise in Receptor Activation	46
6.3.3 Optimal Responses Including all Additional Noise Sources	47
6.4 Ligand Discrimination for Different Input Distributions	48
6.4.1 Rare Inflammation	48
6.4.2 Unequal Ligand Abundance	49
6.5 Receptor Turnover	52
6.6 Does the Interferon Operate in the Optimal Regime?	54
6.7 Conclusion	54

1: Receptors often integrate, filter and shape the signals, exploiting nonlinear activation [53] or temporal [54–56] and spatiotemporal activation dynamics [57, 58].

Figure 6.1 | Schematic overview of the signal transduction of interferon type I (IFN) receptors. Although all 17 distinct ligands bind to a single dimeric receptor (R1 and R2), forming highly similar receptor complexes, different IFN types elicit different cellular responses, effectively multiplexing different signals through the shared pathway component [59, 134]. In this way the receptor acts as an information bottleneck.



2: As discussed in Chapter 3, the highly variable local ligand concentrations at receiving cells are caused due to the scarcity of producer cells, diffusion and consumption.

challenges of a tissue environment, where local ligand concentrations can vary over several orders of magnitude.² To address the question quantitatively, Section 6.1 formulates the combined tasks of detecting the presence of ligands and discriminating between different ligands as an information-processing problem and Section 6.2 compares the respective performance of the three most important membrane receptor architectures. Section 6.3 and Section 6.4 investigate the effect of additional noise sources and different input distributions, respectively. The effect of receptor turnover on the ligand discrimination is discussed in Section 6.5. Finally, Section 6.6 addresses the question if IFNAR exploits optimality.

6.1 Ligand Discrimination as Information-Processing Task

Fig. 6.2A schematically depicts the situation of interest. Upon viral infection, single cells in the tissue produce a variety of cytokine ligands that are subject to diffusion and degradation in the tissue. The signal of these ligands is sensed by the receiving cells through a shared receptor, where it elicits an intracellular response in the form of phosphorylated readout molecules. Here, adopting the perspective of information theory [147–151], ligand discrimination is viewed as an inference problem to be solved by the cell:

*Given the number of intracellular readout molecules,
determine if extracellular ligand is present and decide on its type.*

To formalize this notion, I characterize the receptor input by a random variable X with outcomes $x \in \mathcal{X} = \{\alpha, \beta, \emptyset\}$, corresponding to steady states with presence of ligand of type α, β or no ligand, respectively. In particular, the input $x = \emptyset$ that no ligand is present enables addressing the sensing of ligand presence regardless of type. Discrimination of true signal from subthreshold or unspecific ligand is an essential requirement for any receptor system and hence is a constitutive feature of the theory presented here. As receptor output I take the fluctuating intracellular

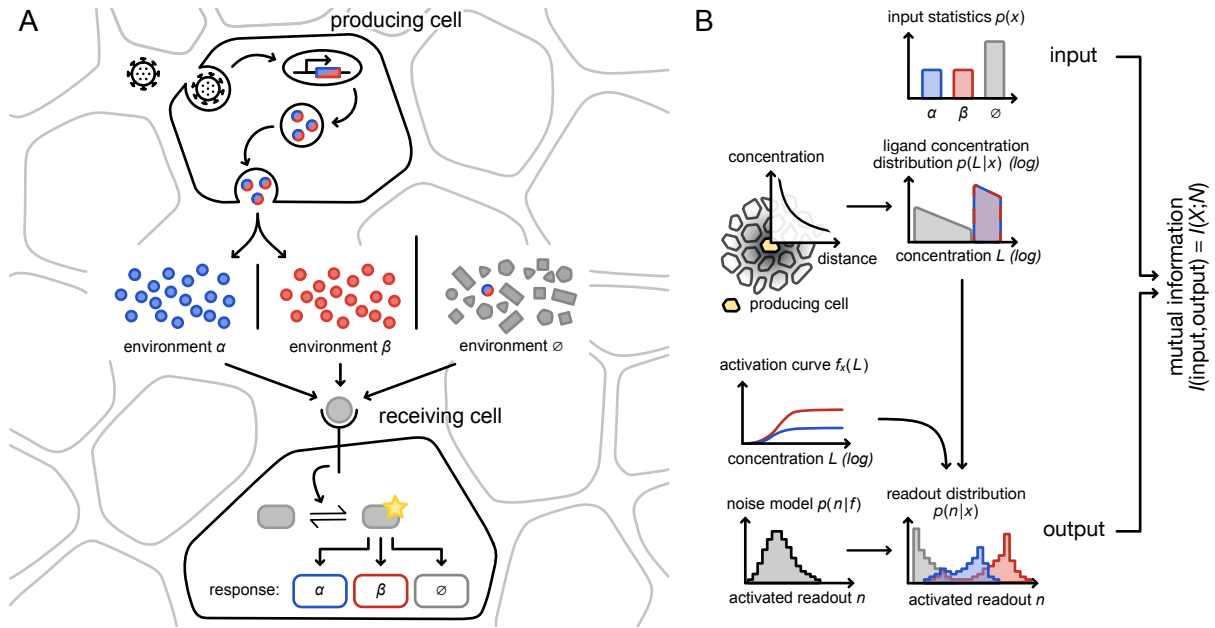


Figure 6.2 | Signal processing by membrane receptors. (A) From top to bottom: Viral infection leads to cytokine secretion by infected host cells. Extracellular environments with ligand α , β or sub-threshold ligand (\emptyset) are sensed by receptors at the membrane of receiving cells. Activated receptors phosphorylate readout molecules, which effect appropriate cellular responses. (B) Probability distributions involved in the signaling processing depicted in A: Probabilities of ligand environments; ligand concentration distribution for a given environment; average receptor activation depending on receptor architecture; distribution of activated readout molecules for given receptor activation and finally, the distributions of activated readout molecules that determine how well the shared receptor can discriminate between different ligands. Overall system performance is quantified by mutual information I , which is measured in bits and in our context is interpreted as discrimination power. Taken and adapted from Ref. [1].

number N of activated readout molecules. The performance of a receptor system regarding this inference problem is measured in bits by the mutual information (see Chapter 5), i.e.

$$I(X; N) = \left\langle \log_2 \frac{p(x, n)}{p(x)p(n)} \right\rangle = \left\langle \log_2 \frac{p(n|x)}{\sum_{x'} p(n|x')p(x')} \right\rangle, \quad (6.1)$$

which is the average reduction in uncertainty about the input X when the output N is known. By the data processing inequality [121], in the absence of feedback, the information available after further processing downstream, for example by pSTAT dimers binding to distinct classes of regulatory sites on DNA [134], is bounded by Eq. (6.1). Thus, I quantifies the ability of a cell with input-output relation $p(n|x)$ to adapt to the environment x characterized by $p(x)$. In the following, I is referred to as the discrimination power of the system. I could be measured experimentally by targeted induction of ligand secretion from sparse producer cells followed by flow cytometry of tissue cells for phosphorylated readout molecules [79, 146].

In order to calculate the discrimination power I for different receptor architectures of interest, the flow of information by a sequence of probability distributions as shown in Fig. 6.2B is tracked.

6.1.1 Input Distribution

The point of departure for the information flow is the input distribution, see Fig. 6.2B top. First I decompose the input distribution as

$$p(x) = \begin{cases} 1 - p_\pi & \text{for } x = \emptyset, \\ p_\pi p_\tau(x) & \text{for } x \in \{\alpha, \beta\}, \end{cases} \quad (6.2)$$

which assigns probability p_π to ligand being present, and if so, $p_\tau(\alpha)$ to type α and $p_\tau(\beta) = 1 - p_\tau(\alpha)$ to type β . By introducing I_π as the information contained in the readout N about ligand presence and I_τ as the information in the readout N about ligand type, the discrimination power decomposes accordingly (see Appendix D for a detailed discussion),

$$I(X; N) = I_\pi(X; N) + p_\pi I_\tau(X; N). \quad (6.3)$$

As is biologically plausible, for good discrimination power a system needs to both detect ligand and distinguish the ligand types, a requirement that would not be captured by measuring performance as the concentration range over which activation levels are different, known as absolute discrimination window [141].

To proceed a specific input distribution is required. As a parsimonious choice, I allow equal chances of ligand being absent or present, and of types α and β , i.e. $p_\pi = p_\tau(\alpha) = p_\tau(\beta) = 1/2$ (Fig. 6.2B). Because I_π and I_τ reflect binary inputs, the total discrimination power is then bounded by $I \leq 1.5$ bits. Alternative scenarios of rare inflammation ($p_\pi \ll 1/2$) and unequal ligand abundances ($p_\tau(\beta) < 1/2$) are treated in Section 6.4.

6.1.2 Input-Output Relation

The input-output relation $p(n|x)$ decomposes according to the stages of information propagation in the system, Fig. 6.2B:

$$p(n|x) = \int p(n|L, x) p(L|x) dL. \quad (6.4)$$

Here, $p(L|x)$ is the distribution of the ligand concentration L for given ligand type, discussed in the following subsection. The distribution $p(n|L, x)$ of activated readout molecules is a property of the receiving cell, determined by the activation curve and by molecular noise. The activation curve is the fraction $f_x(L)$ of activated receptors for given ligand type $x = \alpha, \beta$. It depends on the receptor architecture as discussed below. Activated receptors phosphorylate intracellular readout molecules at a rate proportional to $f = f_x(L)$, which entails molecular readout noise. As derived in Section 4.4, in a linear regime with weakly phosphorylated readout molecules, the steady state distribution of phosphorylated molecules n is given by the Poisson distribution [see Eq. (4.47)],

$$p(n|f) = \frac{(\bar{n}f)^n}{n!} e^{-\bar{n}f}. \quad (6.5)$$

The readout number \bar{n} is the mean number of phosphorylated readout molecules at full activation, which sets the level of intrinsic molecular noise in the receptor system. Other sources of noise in a receptor system

include cell-to-cell variability of receptor numbers and molecular noise in receptor activation. Here, I consider constitutively expressed receptors with unimodal copy number distributions. This allows to summarily treat additional noise sources by adjusting \bar{n} (see Section 6.3). From activation curve and noise model, I calculate the transfer functions as $p(n|L, x) = p(n|f_x(L))$ for each ligand, and finally, the non-Poissonian output distributions via Eq. (6.4). From Eq. (6.1), I then obtain the desired mutual information I as depicted in Fig. 6.2B.

6.1.3 Ligand Concentration Distribution

As discussed in Chapter 3, the ligand concentration distribution $p(L|x)$ in a typical early-stage virally infected tissue can be approximated by the scale-free $1/L$ distribution:

$$p(L|x) = \begin{cases} [\log(L_{\max}/L_{\min}) L]^{-1} & \text{for } L \in \mathcal{L} = [L_{\min}, L_{\max}], \\ 0 & \text{else.} \end{cases} \quad (6.6)$$

For the cases of either ligand α or β being present, i.e. $x = \alpha, \beta$, the lower concentration limit L_{\min} is set by the average spacing of producer cells and corresponds to the threshold concentration L_{thr} at which the ligand can still be sensed by the receptor system, cf. Fig. 6.2B, red and blue. The upper concentration limit L_{\max} is set to L_{hi} , the concentration attained in the immediate vicinity of producer cells.

Absence of ligand ($x = \emptyset$) is represented by placing producer cells of both α and β outside the relevant tissue region. This produces concentration distributions given by Eq. (6.6), but this time limited to variable sub-threshold ligand concentrations by setting $L_{\max} \equiv L_{\text{thr}}$ and $L_{\min} \equiv L_{\text{lo}}$, cf. Fig. 6.2B, gray. Nonspecific binding of other ligands is not represented explicitly but would result in a similar baseline of spurious low-level activation.

Summing up, $p(L|x)$ is modelled by the scale free distribution Eq. (6.6) and its support depends on the input x , i.e.

$$[L_{\min}, L_{\max}] = \begin{cases} [L_{\text{lo}}, L_{\text{thr}}] & \text{for } x = \emptyset, \\ [L_{\text{thr}}, L_{\text{hi}}] & \text{for } x \in \{\alpha, \beta\}. \end{cases} \quad (6.7)$$

6.2 Receptor Architectures and Their Ligand Discrimination Power

Using the information-theoretic framework introduced in the previous section, the question of what generic features enable a receptor system to detect the presence and type of ligands can be addressed quantitatively. To compare the three equilibrium ligand-receptor binding motifs, allosteric transmission (see Section 4.1), homo- and heterodimerization (see Section 4.2), their maximal achievable discrimination powers I , as introduced in Eq. (6.1), are compared. Here, the optimization of I , is with respect to the dissociation equilibrium constants for both ligands, i.e.

$$I_{\max} = \max_{K \in \mathcal{K}} I(X; N), \quad (6.8)$$

where

$$\mathcal{K} = \begin{cases} \{K_\alpha, K_\beta\} & \text{for allosteric transmission,} \\ \{K_\alpha^B, K_\beta^B\} & \text{for homodimerization,} \\ \{K_{\alpha,1}^B, K_{\alpha,2}^B, K_{\beta,1}^B, K_{\beta,2}^B\} & \text{for heterodimerization.} \end{cases} \quad (6.9)$$

The discrimination power is optimized with constrained bounds using dual annealing [152] as implemented in the function `dual_annealing` in the package `Scipy 1.5.0` [153]. The bounds for the dissociation constant are $K^B \in [1 \text{ pM}, 10^7 \text{ pM}]$, roughly corresponding to the biological range of IFN binding affinities [154]. The remaining parameters $L_{\text{thr}}, L_{\text{lo}}, L_{\text{hi}}, R_{\text{tot}}, \lambda, \bar{n}$ are held fixed during optimization. As for the affinities, the fixed parameters are set to values, reflecting the physiological range of the IFN system and basic biophysical constraints. The detection threshold $L_{\text{thr}} = 10 \text{ pM}$ is within the range of measured detection thresholds for IFNs [154]. The minimum concentration is set to $L_{\text{lo}} = 10^{-7} \text{ pM}$, preventing generating optimal solutions with inverted responses, where the receptors are only activated at low concentrations $L < L_{\text{thr}}$ and deactivating for higher concentrations. The maximal concentration L_{hi} is varied over the range $10^2 L_{\text{thr}} - 10^6 L_{\text{thr}}$, reflecting the fact that physiologically relevant cytokine concentration distributions span many orders of magnitude. These ranges correspond to an average spacing 2σ between producing cells of $2\sigma \approx 9\nu - 28\nu$, respectively, where ν describes the domain size of a cytokine niche, see Chapter 3.

For the dimerizing receptor system, the receptor density and the ligand-independent binding mode are set to measured values for IFN, i.e. $R_{\text{tot}} = 1 \mu\text{m}^{-2}$ [59] and $\lambda = K^X / K^B = 5 \text{ nm}$ [112–115, see Subsection 4.2.3], respectively.

To study the performance of receptor architectures for conditions of different difficulty, the range of concentration fluctuations $L_{\text{hi}}/L_{\text{thr}}$ is varied from 10^2 to 10^6 fold and the readout number \bar{n} is varied from 1500 to 10. Table 6.1 summarizes the allowed parameter ranges as well as the fixed parameter values.

Table 6.1 | Parameter bounds and fixed parameter values used for optimizing the ligand discrimination power I in Eq. (6.8).

parameter	unit	value / range	reference
K^B	pM	1– 10^7	[154]
L_{thr}	pM	10	[154]
L_{lo}	pM	10^{-7}	
R_{tot}	μm^{-2}	1	[59]
λ	nm	5	see Table 4.1
$L_{\text{hi}}/L_{\text{thr}}$	-	10^2 – 10^6	[154]
\bar{n}	-	10–1500	

Paradigmatic Cases

To discuss the optimal equilibrium response functions for the different receptor architectures, I consider four paradigmatic cases labeled I–IV, see Fig. 6.3AB. Case I introduces the simplest task, combining low readout noise, i.e. a high readout number $\bar{n} = 1000$, and narrow ligand range

($\log_{10}(L_{\text{hi}}/L_{\text{thr}}) = 3.25$). The two more challenging cases II and III, are like case I but with increased readout noise ($\bar{n} = 20$) or broader ligand range ($\log_{10}(L_{\text{hi}}/L_{\text{thr}}) = 5.44$), respectively. The last case IV combines both, high readout noise and broad ligand range, and thus represents the most challenging situation.

Optimal Sensor

To provide a clearer picture, before discussing the optimal response curves of the three receptor architectures, I first address the question of how an optimal sensor looks like. In the considered ligand discrimination scenario, the signal is encoded in the ligand type and not its concentration. Therefore, an optimal sensor should have distinct and concentration-fluctuation independent activation levels for the three different environments x , respectively. Thus, an ideal step-like response function $f_{\text{optimal}}(L)$, where all three inputs x provoke different receptor activation levels f_x , can be seen as an optimal sensor system:

$$f_{\text{optimal}}(L) = \begin{cases} f_{\emptyset} & \text{for } x = \emptyset, \\ f_{\alpha} & \text{for } x = \alpha, \\ f_{\beta} & \text{for } x = \beta. \end{cases} \quad (6.10)$$

The optimal sensor successfully decodes the ligand presence and type, even when challenged with the most difficult case IV, see Fig. 6.3CD.

Allosteric Transmission

The results for receptors with allosteric transmission, challenged by the cases I-III, are shown in Fig. 6.3EF. Here, the optimization of I is with respect to the dissociation constants for both ligands K_{α} and K_{β} , see Eq. (6.9). For the simplest discrimination task case I, optimal discrimination is achieved by setting the activation points K_{α} and K_{β} slightly below the threshold concentration L_{thr} and maximal concentration L_{hi} , respectively, see Fig. 6.3E, case I, red and blue curves. The separation of the activation points results in high type sensing $I_{\tau} = 0.97$ bits due to the small overlap of the corresponding readout distributions $p(n|\alpha)$ and $p(n|\beta)$, see Fig. 6.3F, case I, red and blue curves. The type sensing could be further improved somewhat by choosing K_{α} as high and K_{β} as low as possible within the optimization range, separating the output distributions $p(n|\alpha)$ and $p(n|\beta)$ even better. However, since the ligand discrimination task Eq. (6.3) also incorporates presence sensing, the optimal response curves do not show this pathological behavior. Instead, the maximal mutual information $I_{\text{max}} = 1.14$ bits reflects a compromise of presence and type sensing, keeping the overlap between the ligands, $p(n|\alpha)$ and $p(n|\beta)$, small while reducing the overlap between ligand α and no ligand, gray curve, ($I_{\pi} = 0.66$ bits).

Broadening the ligand range aggravates the overlap of $p(n|\alpha)$ and $p(n|\emptyset)$, reducing the type presence sensing I_{π} . Increasing the ligand range even further, eventually results in an optimal strategy with equal affinities $K_{\alpha} = K_{\beta}$, see Fig. 6.3EF, case II. Choosing the same affinity for both ligands, means that the optimal strategy disregards the type information

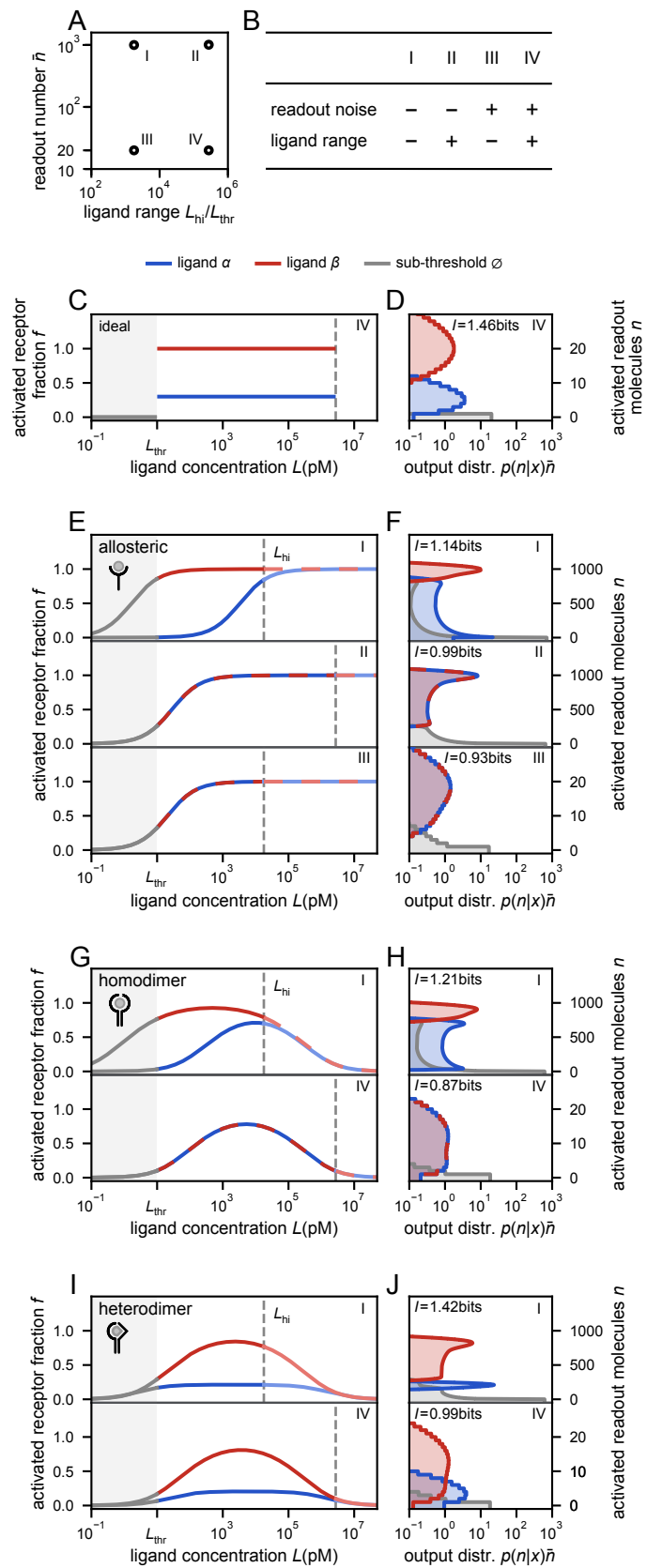


Figure 6.3 | Optimal ligand discrimination in basic receptor architectures. (A) Parameter space of readout noise and ligand concentration fluctuations with parameter points for example cases I-IV. (B) Definition of four paradigmatic test cases. (C) Activation curves of an optimal sensor. Here $f_\alpha = 0.3$, $f_\beta = 1$ and $f_\emptyset = 0$. (D) Corresponding readout distributions with excellent separation of α , β and \emptyset . (E) Optimal activation curves for allosteric receptors. Ligands are separated but α overlaps with no ligand (\emptyset). II and III, ligands α and β superimpose (dashed curves) but are separated from \emptyset , indicating pure presence sensing. (F) Readout distributions corresponding to E. Case I, ligands α and β are separated but α overlaps with no ligand (\emptyset). II and III, ligands α and β superimpose (dashed curves) but are separated from \emptyset , indicating pure presence sensing. (G) Optimal activation curves for homodimerizing receptors. (H) Readout distributions corresponding to G. Case I, α and β are separated but α overlaps with \emptyset . IV, pure presence sensing. (I) Optimal activation curves for heterodimerizing receptors. (J) Readout distributions corresponding to I. Case I, α , β and \emptyset are well separated. IV, all distributions are distinct but still overlap somewhat due to readout noise and deactivation at high concentration. Optimal parameter values are detailed in Table E.1. Taken and adapted from Ref. [1].

entirely ($I_\tau = 0$ bits), solely focusing on the ligand presence. In this regime, the performance is limited to $I_{\max} < 1$ bit.

Like for increasing L_{hi} , decreasing the readout number \bar{n} eventually leads to a presence sensing only strategy with equal affinities for both ligands, see Fig. 6.3EF, case III. The increased readout noise results in noisier readout distribution, creating a tiling problem: Separating $p(n|\alpha)$ and $p(n|\beta)$ necessarily increases the overlap of $p(n|\alpha)$ and $p(n|\emptyset)$.

Homodimerization

The results for homodimerizing receptors are shown in Fig. 6.3GH. The discrimination power I is now optimized with respect to K_α^B and K_β^B , see Eq. (6.9). In the low readout noise and narrow concentration range regime, exemplified by case I, the optimal strategy can decode the ligand type by choosing different peak activation levels for the two ligands α and β , see Fig. 6.3GH, case I, $I_\tau = 0.97$ bits. However, since the peak activation level and the onset point are coupled, the high peak of ligand β inevitably implies an early activation, resulting in a reduced presence information of $I_\pi = 0.73$ bits

As for the allosteric transmission, increasing readout noise or broadening concentration range, reduces the performance. In particular, increasing L_{hi} beyond the deactivation point L_{deact} , as defined in Eq. (4.31), inevitably leads to additional overlap of the readout distributions $p(n|\alpha)$ and $p(n|\beta)$, impeding accurate type sensing. In both cases, increasing the difficulty eventually results in a strategy solely focusing on presence sensing, completely abandoning type sensing, see Fig. 6.3GH, case IV.

Heterodimerization

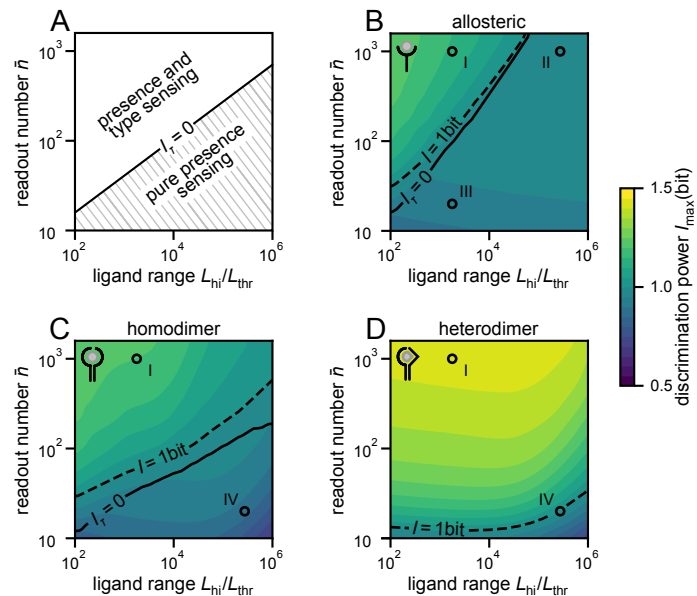
Finally, Fig. 6.3IJ depicts the results for heterodimerizing receptors. The discrimination power is optimized with respect to the four dissociation constants for the ligand binding of both ligands to the receptor chains from bulk solution, see Eq. (6.9). As asymmetric dimerization leads to broad activation plateaus, the receptor system can separate the output distributions well for low concentration range and low noise, see Fig. 6.3IJ, case I. For case I, the heterodimerizing receptor system achieves a discrimination performance of $I_{\max} = 1.42$ bits, consisting of a perfect type sensing $I_\tau = 1.00$ bits and good presence sensing $I_\pi = 0.92$ bits.

In contrast to allosteric and homodimerizing receptor, increasing the difficulty of the discrimination task only requires minor changes to the optimal sensing strategy. Even for case IV, corresponding to high readout noise and broad concentration range, the optimal discrimination strategy is unchanged and in particular not collapsed to the presence only regime, see Fig. 6.3IJ, case IV. However, challenging the system by even broader concentration range with L_{hi} beyond the deactivation point L_{deact} and high readout noise results in overlap of the distribution, reduces the performance to $I_{\max} = 0.99$ bits.

Robust Ligand Discrimination Requires Asymmetric Dimerization of Receptors

The discrimination power of the three ligand-receptor binding motifs for the whole range of concentration fluctuations L_{hi}/L_{thr} and readout number \bar{n} are summarized in Fig. 6.4. To illustrate the different optimal strategies, the contour line with $I_\tau = 0$ is added, marking the transition from presence and type sensing to pure presence sensing, Fig. 6.4A.

Figure 6.4 | Discrimination power *vs.* concentration range and readout number. (A) Pure presence sensing is optimal below the solid line $I_\tau = 0$. (B) Allosteric receptors achieve type sensing only in a regime of low readout noise and well-controlled concentrations, upper left corner. (C) Homodimerizing receptors moderately improve discrimination power and enlarge the type sensing regime. (D) Heterodimerizing receptors accommodate type sensing even for high noise and broad concentration ranges. Cases I-IV as in Fig. 6.3AB. Taken and adapted from Ref. [1].



In the regime of well-controlled ligand concentrations and low readout noise level, receptors using allosteric transmission prioritize type sensing and thereby achieve some discrimination power, Fig. 6.4B, upper left region. However, for more challenging discrimination tasks, the optimal strategy is to redundantly sensing ligand presence, entirely abandoning type sensing, Fig. 6.4B, lower right region. In conclusion, signal transduction by allosteric transmission with readout of the activated fraction f cannot achieve robust ligand discrimination. Discrimination with allosteric receptors would require other mechanisms such as readout of ligand dwell-times by nonequilibrium post-processing.

By encoding the ligand type in their peak activation level, homodimerizing receptor system can separate ligand type in a slightly expanded regime of moderate difficulty, Fig. 6.4C, upper left. However, for more difficult discrimination tasks, i.e. broader ligand concentration ranges and higher readout noise, the optimal strategy forgoes type detection, along with an overall performance reduction. Due to false negative detection at high concentrations, the overall performance can fall below that of allosteric receptors.

By contrast, asymmetric binding allows type sensing even for broad concentration ranges, improving greatly on the performance of homodimerizing systems (Fig. 6.4D). Discrimination is still somewhat limited by the constraint that high activation levels require early activation, by the finite slope of the activation curves and by possible deactivation at very high concentrations.

6.3 Effect of Additional Noise Sources

So far, for the estimation of discrimination power Eq. (6.1), two kinds of noise sources were included: The variation of ligand concentration the cell is exposed to as extrinsic noise and the low copy-number effect of readout molecules Eq. (6.5) as intrinsic noise. Thinking of ligand-receptor binding, fluctuations in receptor number due to cell-to-cell variability or low copy-number noise in receptor activation could additively affect the readout distributions. Nevertheless, to demonstrate that the simplified low copy-number noise model for the readout molecule Eq. (6.5) provides an appropriate effective description for the case of ligand discrimination, I will investigate the effect of these additional noise sources.

6.3.1 Cell-to-Cell Variability in Receptor Number

In general, distributions describing cell-to-cell variability in protein numbers can be of diverse shapes, including bimodal and long-tailed distributions. For simplicity here, I consider only constitutive genes, i.e. genes that are transcribed continually, which exhibit unimodal number distributions. In this case, the cell-to-cell variability in protein numbers can be approximated well by a Gamma distribution [155]. Therefore, the variability in the total number of receptors r is set to

$$p(r) = \frac{r^{k-1}}{\Gamma(k)\theta^k} e^{-r/\theta}. \quad (6.11)$$

To include this additional noise source to the discrimination power, the input-output relation Eq. (6.4) is generalized by introducing an additional sum over the total receptor number r :

$$p(n|x) = \int \left[\sum_{r=0}^{\infty} p(r) p\left(n \left| \frac{r}{r_{\text{tot}}} f_x(L)\right.\right) \right] p(L|x) dL, \quad (6.12)$$

where $r_{\text{tot}} = k\theta$ is the mean total receptor number and $p(n|r f_x(L)/r_{\text{tot}})$ is Eq. (6.5) as before. Notice, the phosphorylation rate of readout molecules is proportional to the number of activated receptors complexes. Thus, by considering cell-to-cell variability in receptor number, i.e. by giving up the assumption of a fixed total receptor number, the phosphorylation rate of readout molecules is now proportional to the fluctuating number $r f$, as reflected by the ratio r/r_{tot} in Eq. (6.12).

Next, the question of how the ligand discrimination power I is affected by receptor number fluctuation Eq. (6.12) is addressed. As starting point serves the optimal activation curves and corresponding readout distributions of allosteric receptors without the additional receptor noise, computed as in Section 6.2 with $\bar{n} = 100$ and $L_{\text{hi}} = 18$ nM, Fig. 6.5A. This parameter set defines a new paradigmatic case V, similar to case I and III but with intermediate readout noise. As a next step, I recalculate the readout distribution for the same activation curves, but this time including cell-to-cell variability in receptor number, i.e. replacing Eq. (6.5) by Eq. (6.12), Fig. 6.5B, top. Here, I assumed a mean total receptor number of $r_{\text{tot}} = 100$ and a coefficient of variation of 25% for the distribution of the variability in receptor number $p(r)$ [156], corresponding to $k = 16$ and

$\theta = 6.25$. As expected, the additional noise source of cell-to-cell variability in receptor number broadens the readout distribution. Remarkably, comparable broadening and nearly identical output distribution shape can be obtained by reducing the readout number \bar{n} from 100 to 20 and keeping $r = r_{\text{tot}}$ fixed, Fig. 6.5B, bottom.

Repeating this procedure for homodimerizing receptors confirms the previous finding, i.e. the cell-to-cell variability can be approximated well by reducing the readout number \bar{n} to 20, Fig. 6.5CD without accounting for protein fluctuations. As a technical point, I remark that by leaving the response curves unchanged, cell-to-cell variability is effectively incorporated for changes in cell size at constant receptor density and not from changes in receptor density at constant cell size. By doing so, further complication of the calculation of Eq. (6.12) are avoid, since the total receptor number r and the receptor density are independent. In particular, the fraction of activated receptors f is independent on r and only depends on R_{tot} , i.e. $f_x(L) = f_x(L, R_{\text{tot}})$.

6.3.2 Molecular Noise in Receptor Activation

Beside cell-to-cell variability, the low copy-number noise in receptor activation is the other noise source affecting the readout distributions. Therefore, I next consider the effect of molecular noise in receptor activation on the input-output distribution. By introducing $p(a|f, r_{\text{tot}})$ as the probability that a out of a fixed number r_{tot} of receptors are activated for a given mean activation of $f \times r_{\text{tot}}$, the input-output relation Eq. (6.4) becomes

$$p(n|x) = \int \left[\sum_{a=0}^{r_{\text{tot}}} p(a|f_x(L), r_{\text{tot}}) p(n|\frac{a}{r_{\text{tot}}}) \right] p(L|x) dL. \quad (6.13)$$

In general, estimating the probability distribution $p(a|f, r_{\text{tot}})$ is a difficult task, since it corresponds to solving the master equation of the reaction scheme for the specific receptor architecture at steady state. However, for the simple reaction scheme Eq. (4.2) of allosteric receptors, the master equation results in the binomial distribution [119]

$$p(a|f, r_{\text{tot}}) = \binom{r_{\text{tot}}}{a} f^a (1-f)^{r_{\text{tot}}-a}. \quad (6.14)$$

To demonstrate the effect of the molecular noise in receptor activation, the optimal activation curves and readout distributions are estimated for case V, again first without the receptor activation noise, Fig. 6.5E. Next, using these receptor activation curves, the readout distribution including the receptor activation noise is estimated. Typical numbers of IFN receptors are in the range of a few hundred copies per cell [98]. However, even for low receptor numbers of $r_{\text{tot}} = 100$, the effect on the readout distribution is only modest, Fig. 6.5EF. Overall, the effect of receptor activation noise is negligible next to typical amounts of cell-to-cell variability (cf. Fig. 6.5B).

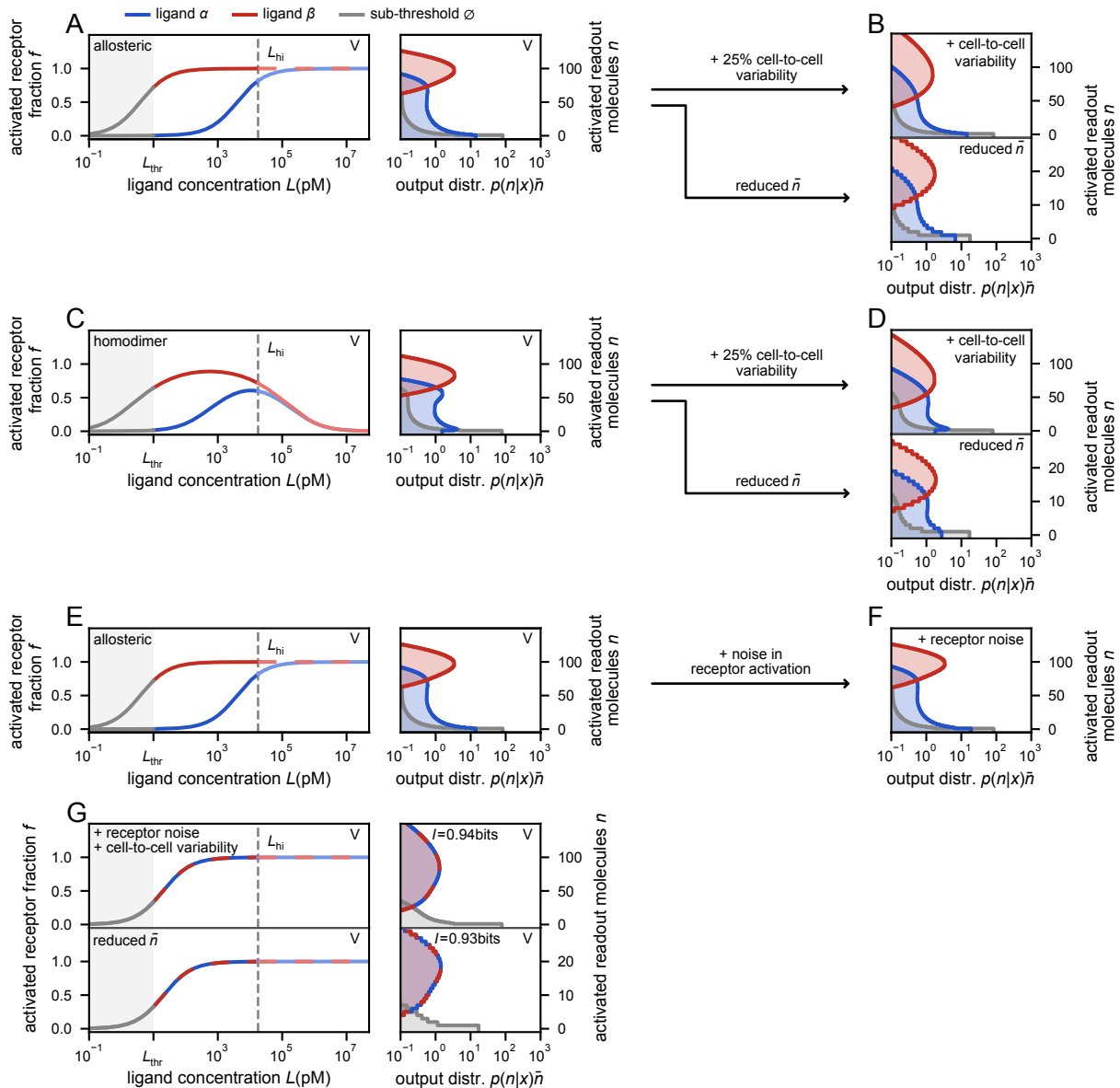


Figure 6.5 | Effect of additional noise sources in form of cell-to-cell variability in receptor numbers and molecular noise in receptor activation on the readout distribution. (A) Optimal activation curves and corresponding readout distributions for allosteric receptors without additional noise source. Case V (like case I and III in main but with intermediate readout number $\bar{n} = 100$), $K_\alpha = 4.0$ nM, $K_\beta = 3.9$ pM. (B) Readout distribution corresponding to A. Top, including 25% cell-to-cell variability in receptor numbers broadens the readout distributions. Bottom, reducing the readout number to $\bar{n} = 20$ reproduces a similar effect on the readout distributions. (C) Optimal activation curves and corresponding readout distributions for homodimerizing receptors. Case V, $K_\alpha = 21$ nM, $K_\beta = 1.1$ nM. (D) Readout distribution corresponding to C. Effect of including 25% cell-to-cell variability in receptor numbers on the readout distributions (top) can be approximated well by reducing the readout number to $\bar{n} = 20$ (bottom). (E) same as A. (F) Readout distributions for allosteric receptors including molecular noise in receptor activation corresponding to E. (G) Optimal activation curves and corresponding readout distributions for allosteric receptors considering receptor activation noise and 25% cell-to-cell variability (top, $K_\alpha = K_\beta = 20$ pM) almost coincide with optimal solutions for reduced readout number $\bar{n} = 20$ (bottom, $K_\alpha = K_\beta = 21$ pM). Both results in superimposed ligands α and β (dashed curves) with good separation from \emptyset , indicating pure presence sensing. Here, $r_{\text{tot}} = 100$ is used. Taken and adapted from Ref. [1].

6.3.3 Optimal Responses Including Readout Noise, Activation Noise and Cell-to-Cell Variability

To confirm the initial statement that the readout noise provides an appropriate effective description for ligand discrimination, I optimize the ligand discrimination power of an allosteric receptor like in Section 6.2 but this time including both additional noise sources. The input-output

relation Eq. (6.4) then reads

$$p(n|x) = \int \left[\sum_{r=0}^{\infty} \sum_{a=0}^r p(r) p(a|f_x(L), r) p(n|\frac{a}{r_{\text{tot}}}) \right] p(L|x) dL. \quad (6.15)$$

Fig. 6.5G (top) shows the result for optimizing the ligand discrimination power for case V, comprising well-controlled concentration range and intermediate readout number. Including the additional noise sources moves the system to the regime of pure presence sensing, where both dissociation constants coincide $K_\alpha = K_\beta$. Interestingly, the result obtained is very similar to the previously obtain result excluding the two noises but with reduced readout number $\bar{n} = 20$, Fig. 6.5G (bottom) and Fig. 6.3F, case III.

In conclusion, pure readout noise, tuned in strength by setting an appropriate effective \bar{n} , provides a convenient effective description for the relevant noise sources in ligand discrimination and is sufficient at the level of detail of the present study.

6.4 Ligand Discrimination for Different Input Distributions

The comparison of the three receptor architectures presented in Section 6.2 is based on the assumption of equal chances of ligand being absent or present, and of being type α and β , i.e. $p(\emptyset) = 2p(\alpha) = 2p(\beta) = 1/2$. Because the discrimination power $I(X; N)$ depends on the chosen input distribution $p(x)$, in the following, I will consider two plausible alternative choices for $p(x)$, corresponding to rare inflammation and unequal ligand abundances, respectively. To explore how these choices for $p(x)$ affect the optimal sensing strategy, the ligand discrimination is re-optimized.

6.4.1 Rare Inflammation

In the scenario of IFN considered here, ligands are produced in response to inflammation. Therefore, the case of rare inflammation corresponds to a reduction of p_π , the probability of the ligand being present, i.e. $p_\pi = 1 - p(\emptyset) \ll 1/2$.

The effect of changing the input distribution can be understood by considering the upper bound for the discrimination power. By decomposing the discrimination power into the presence information I_π and the weighted type information $p_\pi I_\tau$, i.e. $I = I_\pi + p_\pi I_\tau$, see Eq. (6.3), both variables, presence and type, are binary. The upper bound for the information of a binary variable Y which can take two outcomes $y \in \{y_0, y_1\}$ with probability

$$p(y) = \begin{cases} p & \text{for } y = y_0, \\ 1 - p & \text{for } y = y_1, \end{cases} \quad (6.16)$$

is given by the binary entropy function (see Fig. 5.1)

$$I(Y) \leq H(Y) = -p \log_2 p - (1 - p) \log_2 (1 - p). \quad (6.17)$$

Keeping the ligand type stoichiometry unchanged ($p_\tau = 1/2$), the upper bound for I_τ is unchanged, but its contribution to the discrimination power is decreasing linearly, since it is weighted with p_π . The upper bound for I_π decreases, but sub-linearly according to Eq. (6.17), see Fig. 5.1. Thus, decreasing the probability of ligand being present p_π reduces the type sensing more strongly, and puts more importance on achieving a good presence sensing.

The results for the re-optimized discrimination power are shown in Fig. 6.6BC. Here, the reduced upper bounds for the discrimination power for the two exemplary cases $p_\pi = 0.25$ and $p_\pi = 0.1$ are $I \leq 1.06$ bits and $I \leq 0.57$ bits, respectively. As expected, the regime of pure presence sensing extends to lower readout noise and narrower concentration ranges for allosteric and homodimerizing receptors, compare Fig. 6.6A,1-2 and Fig. 6.6BC,1-2. For even rarer inflammation ($p_\pi = 0.1$), the regime extends over the full parameter range tested, Fig. 6.6C,1-2. By contrast, the heterodimerizing system can reconcile presence and type sensing also for lower p_π , as activation curves can exploit distinct activation plateaus Fig. 6.6BC,3.

6.4.2 Unequal Ligand Abundance

The case of unequal ligand abundance corresponds to a change of p_τ . As example, the weaker ligand α is assumed to occur more frequently than the stronger ligand β . In the inflammatory scenario this is a plausible assumption, as the more drastic response of the high affinity ligand β is required only in the most extreme cases. To not conflate the effect of changed stoichiometry and rare inflammation, the probability of a ligand being present is kept unchanged, $p_\pi = 1/2$.

Lowering $p_\tau(\beta) < 0.5$ results in a reduced upper bound for type information I_τ , see Eq. (6.17). Whereas, keeping $p_\pi = 1/2$ unchanged, the upper bound for the presence information I_π and the weight for the type information p_π are unchanged. Thus, as for the case of rare inflammation, unequal ligand abundance reduces the ratio of type and presence information I_τ/I_π , putting more importance on presence sensing.

The results for re-optimizing the discrimination power for the two input distributions with $p_\tau(\beta) = 0.25, 0.1$ are shown in Fig. 6.6DE. Here, the upper bound of the discrimination power is $I \leq 1.41$ bits for $p_\tau(\beta) = 0.25$ and $I \leq 1.23$ bits for $p_\tau(\beta) = 0.1$. As expected, for allosteric and homodimerizing receptors, the reduced maximal-achievable type information leads to a change in the optimal strategy. For $p_\tau(\beta) = 0.25$, the region of pure presence sensing increases towards simpler discrimination tasks (upper left corner), compare Fig. 6.6A,1-2 and Fig. 6.6D,1-2. Eventually, increasing the inequality of ligand abundance to $p_\tau(\beta) = 0.1$, pure presence sensing is optimal for the whole parameter range, Fig. 6.6E,1-2. As before, the heterodimerizing system can reconcile presence and type sensing Fig. 6.6D-E,3.

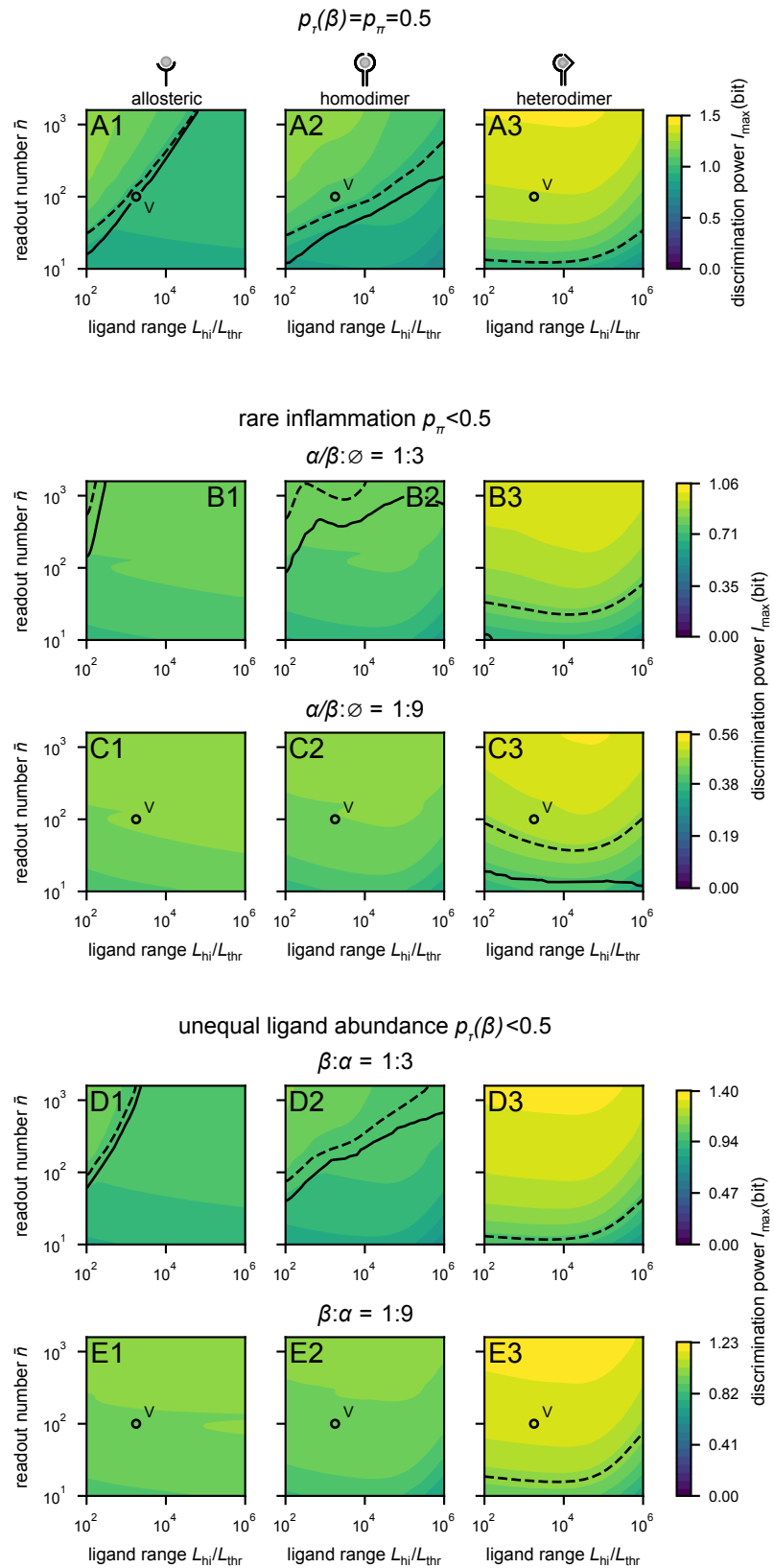


Figure 6.6 | Ligand discrimination in allosteric (1), homodimerizing (2) and heterodimerizing (3) receptors for different input distributions. (A) Optimal discrimination power vs. concentration range and readout number as in Fig. 4B-D. (BC) Optimal discrimination power vs. concentration range and readout number for rare inflammation: $p_\pi = 0.25$ (B) and $p_\pi = 0.1$ (C). (DE) Optimal discrimination power vs. concentration range and readout number for unequal ligand abundance: $p_r(\beta) = 0.25$ (D) and $p_r(\beta) = 0.1$ (E). Taken and adapted from Ref. [1].

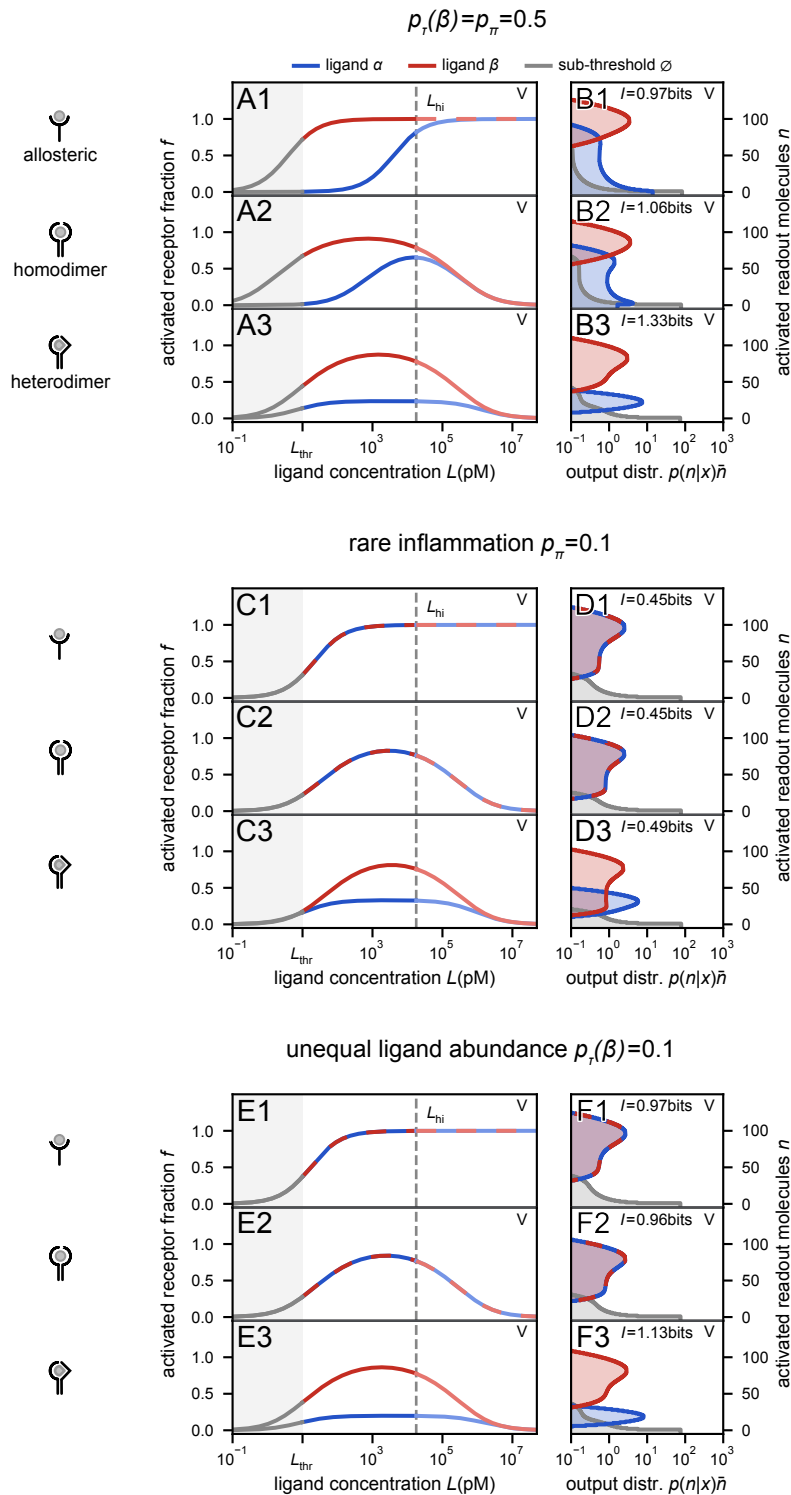


Figure 6.7 | Optimal activation curves for the ligand discrimination task case V in allosteric (1), homodimerizing (2) and heterodimerizing (3) receptors for different input distributions. (A) Optimal activation curves for case V, cf. Fig. 6.6A. Ligands are separated for all basic receptors. (B) Readout distributions corresponding to A. Receptor 1 and 2, α and β are separated but α overlaps with \emptyset . 3, α , β and \emptyset are well separated. (C) Optimal activation curves for rare inflammation, cf. Fig. 6.6C. Equal affinities for ligands are optimal in receptor 1 and 2, but ligands are separated in 3. (D) Readout distributions corresponding to C. Receptor 1 and 2, pure presence sensing. 3, α , β and \emptyset are well separated. (E) Optimal activation curves for rare inflammation, cf. Fig. 6.6E. Equal affinities for ligands are optimal in receptor 1 and 2, but ligands are separated in 3. (F) Readout distributions corresponding to E. Receptor 1 and 2, pure presence sensing. 3, α , β and \emptyset are well separated. The optimal resulting dissociation constants are given in Table E.2. Taken and adapted from Ref. [1].

A Change in Input Distribution Does not Affect the Performance Ranking of Different Receptor Architectures

Both rare inflammation and unequal ligand abundance lead to an increased pure presence sensing regime, in which type information is omitted completely. As the only receptor architecture, heterodimerizing receptors retain type sensing and remain superior to the allosteric and homodimerizing receptors. Interestingly, within each regime, the optimal

activation curves are almost unaffected, Fig. 6.7. Thus, the main effect of the input distribution is a redistribution of importance between presence and type sensing, which does not affect the performance ranking of different receptor architectures. The optimal resulting dissociation constants are given in Table E.2.

6.5 Receptor Turnover

Next, I revisit the discrimination power and discuss the effect of non-equilibrium receptor turnover, see Section 4.3. The receptor turnover is modelled by a first order degradation process of all stages of receptor complex (R, RL, C) with the common degradation rate μ and a zeroth order receptor production process, reintegrating free receptors R to ensure a constant overall receptor concentration in steady state, see Eq. (4.32). The effect of non-equilibrium receptor turnover on the equilibrium response curves is discussed in detail in Section 4.3.

Allosteric Transmission

Accounting for receptor turnover to allosteric receptors, simply shifts the activation point to higher concentration, effectively lowering the affinity of all ligands, see Subsection 4.3.1. In particular, the shape of the response curve is not affected and therefore turnover neither helps nor hurts ligand discrimination. In other words, ligand discrimination in allosteric receptors is unaffected by turnover.

Homodimerization

By contrast, turnover has a strong effect in dimerizing receptor systems. Including the non-equilibrium receptor turnover, the steady-state for homodimerizing receptors is now controlled by the dissociation constant K^B and two new time scales $\tau_u = \mu/k_u$ and $\tau_d = \mu/k_d$, set by the degradation rate and the bulk and in-membrane dissociation rate, see Subsection 4.3.2. Turnover breaks the symmetry of the response curve f in log-concentration space, see Eq. (4.37), and shifts the limiting deactivation point, see Eq. (4.41), towards higher (lower) concentrations for $3k_d > (<) k_u$, respectively, reflecting a competition of internalization of binary vs. ternary complexes. In addition, the maximal activation level Eq. (4.39) is decreased when turnover is faster than in-membrane dissociation.

To quantify how the larger design space affects the achievable ligand discrimination power, I optimize I with respect to K^B , k_u and k_d for ligand α and β , respectively. The optimization range of the bulk and in-membrane dissociation rates are set to

$$k_u \in \left[10^{-9} \text{s}^{-1}, 0.06 \frac{K^B}{\text{pM s}} \right], \quad (6.18a)$$

$$k_d \in \left[10^{-9} \text{s}^{-1}, 2 \times 10^{-6} \frac{\lambda K^B}{\text{nm pM s}} \right]. \quad (6.18b)$$

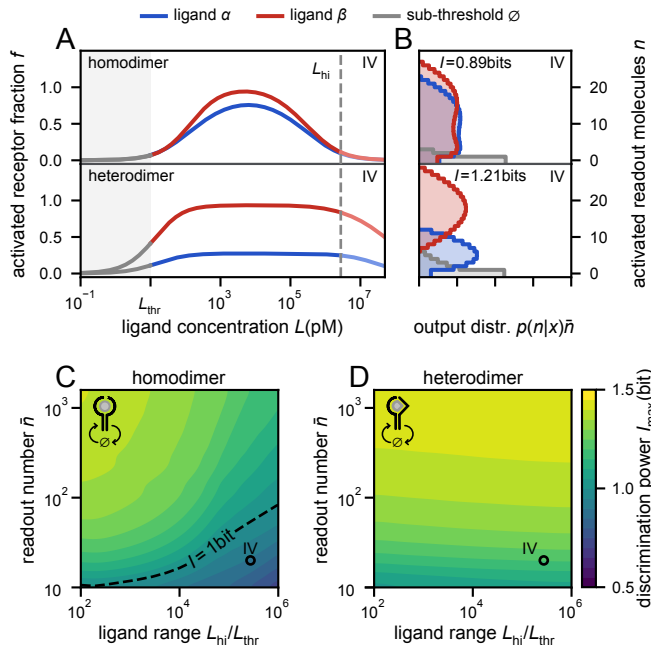


Figure 6.8 | Ligand discrimination by dimerizing receptors including receptor turnover. (A) Optimal activation curves for homodimer and heterodimer case IV (B) Corresponding readout distributions. Homodimer, poor separation of α and β ; heterodimer and ideal, excellent separation of α , β and \emptyset ; Optimal parameter values are detailed in Table E.3. (CD) Optimal discrimination power *vs.* concentration range and readout number, cf. Fig. 6.4CD. Turnover improves performance in the well-controlled regime for homodimerizing (C), and in all conditions for heterodimerizing (D) receptor systems. Taken and adapted from Ref. [1].

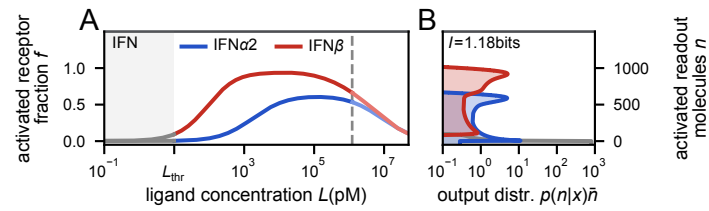
Here, both upper bounds depend on the equilibrium dissociation constant to ensure that the effective binding rate do not exceed the diffusion-limited case, respectively, see Appendix C. The lower bound of both rates, are constrained to ensure numerical stability. The turnover rate is fixed at $\mu = 10^{-3}\text{s}^{-1}$, a typical value for cytokine receptors [157, 158]. The remaining parameters are set to the same ranges and fixed values as in Section 6.2, see Table 6.1.

In contrast to the equilibrium homodimerizing system without turnover, homodimerizing receptors with turnover can still resolve some ligand type information, even for the most challenging case IV, comprising broad ligand range and high readout noise, see Fig. 6.8AB, upper row. The improvement is mainly due to the ability of the system to align activation points of weak and strong ligands to the threshold concentration L_{thr} , reducing ligand presence ambiguity. Overall, including receptor turnover generally improves the discrimination power over the equilibrium homodimerizing case but not the equilibrium heterodimerizing case, Fig. 6.8C, cf. Fig. 6.4CD.

Heterodimerization

Finally, I consider heterodimerizing receptor systems with receptor turnover, an architecture that closely resembles the IFNAR system. Having two receptor chains $i = 1, 2$, the response curves are now controlled by a total of six parameters: K_i^B , $\tau_{u,i}$, $\tau_{d,i}$, see Subsection 4.3.3. The discrimination power I is optimized with respect to these parameters for each ligand α and β , using the same bounds and fixed values as for the previous case. Including turnover, the optimal response curves now feature broad plateaus with distinct low and high activation levels, Fig. 6.8A, bottom row. Furthermore, the increased design space allows aligned activation points at the threshold concentration L_{thr} in combination with a deactivation point shifted beyond L_{hi} . Combining these features results in good type and presence sensing, even for the most

Figure 6.9 | Ligand discrimination by the IFN receptor system. (A) Optimal activation curves of IFN α 2 and IFN β at lower readout noise. (B) Corresponding readout distributions: good separation at lower noise. Optimal parameter values are $R_0 = 20$ and $L_{hi}/L_{thr} = 1.2 \times 10^5$. As optimization range $R_0 = 0.1 - 10^3 \mu\text{m}^{-2}$ and $L_{hi}/L_{thr} = 10^2 - 10^6$ was used. Taken and adapted from Ref. [1].



difficult discrimination task case IV ($I_\tau = 0.83$ bits, $I_\tau = 0.79$ bits). Overall, the discrimination power becomes essentially independent of the ligand range Fig. 6.8D, achieving robust buffering of strong concentration fluctuations.

6.6 Does the Interferon Operate in the Optimal Regime?

Does IFNAR actually exploit the possibilities of its architecture outlined above for ligand discrimination? Literature values of IFNAR kinetic rates show that IFNs bind chain IFNAR2 with much higher affinity than IFNAR1, and IFN β binds both with higher affinity than IFN α 2, see Table E.4. This ordering agrees with that of the optimal rates for heterodimerizing receptors with turnover, cf. Table E.1. More concretely, Fig. 6.9AB, shows activation curves corresponding to fixed literature rate values in the IFNAR system, where optimization was carried out only with respect to the receptor density R_{tot} and the upper cutoff L_{hi} . As optimization range $R_0 = 0.1 - 10^3 \mu\text{m}^{-2}$ and $L_{hi}/L_{thr} = 10^2 - 10^6$ was used. Although they lack alignment of the activation points, these unmodified activation curves are similar in shape to the optimal solutions, cf. Fig. 6.3C. The discrimination performance of these unmodified natural response curves is remarkable at $I_{max} = 1.18$ bits, demonstrating the ability of IFNAR to detect and discriminate ligands at fluctuating concentrations.

6.7 Conclusion

The main findings of this chapter are summarized in Fig. 6.10. First, single-unit receptors, which transmit information across the membrane by an allosteric mechanism, cannot reliably discriminate ligand type. Second, receptors that transmit information by ligand-induced oligomerization however can enable ligand discrimination. While homodimerizing receptors resolve ligand presence and type only in well-controlled environments, heterodimerizing receptors discriminate ligands very robustly, through efficient buffering of concentration fluctuations. Third, active turnover of receptors can improve performance further by independently setting activation point and level of the response curve.

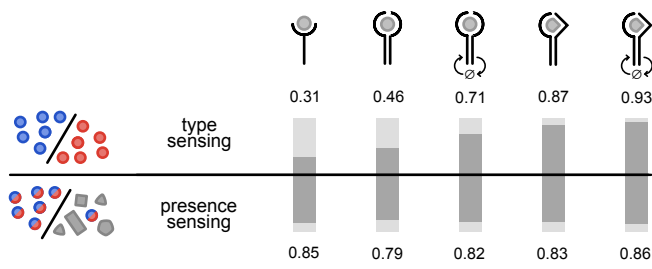


Figure 6.10 | Overall discrimination power of all considered receptor architectures. Type information I_τ (upper row) and presence information I_π (lower row) averaged over the parameter range $L_{\text{hi}}/L_{\text{thr}} = 10^2 - 10^6$ and $\bar{n} = 10 - 1500$ (cf. Fig. 6.3A) is indicated as a fraction of the maximum 1 bit. Taken and adapted from Ref. [1].

Discussion - Ligand Discrimination by Interferon Receptors

7

Cells in multicellular organisms communicate through a wide variety of chemical signals. For example, in the case of viral infections, as first line of defense infected cells secrete interferons to warn tissue cells in the vicinity. Here, the cell-cell communication is challenged by highly variable local ligand concentrations at receiving cells that are caused due to the scarcity of producer cells, diffusion and consumption. Therefore, it has been an open question how the single receptor complex IFNAR can robustly multiplex information from its diverse ligands despite the inhomogeneous and noisy ligand distributions. To circumvent this fundamental uncertainty, the signal can be encoded digitally in the chemical properties of the ligands rather than in the ligand concentration. Reliable communication then rests on the receptors' ability to discriminate between different ligands in presence of large concentration fluctuations.

Using information theory, this thesis quantified how well different receptor architectures, namely allosteric, homo- and heterodimerizing receptors, discriminate ligands at the membrane. The discrimination power has been measured via the mutual information that incorporates ligand presence and type sensing, as both are required for a fully functional ligand sensor. Then, based on the cytokine concentration model and a simple but reasonable model for readout noise, the discrimination power achievable by the three most important cytokine receptor architectures was calculated. As a result, this thesis reveals the generic features that enable ligand discrimination. While all architectures can sense ligand presence well, allosteric receptors cannot achieve robust type sensing, see Fig. 6.10. In homodimerizing receptors, the maximal activation level encodes the affinity which is a well-known and important mechanism to generate ligand discrimination [111]. However, this thesis shows that this mechanism offers only a partial solution for robust ligand discrimination as concentration fluctuations confound ligand types. Robust type sensing is achieved only by a heterodimerizing receptor with strongly asymmetric binding of ligands to the two receptor chains, a receptor architecture that allows both ligand-dependent and concentration-independent receptor activation. When receptor turnover drives the system out of equilibrium, the activation curves can come close to a theoretically perfect discriminator. The fact that actual biochemical parameters realized by IFNAR [59] come close to this ideal supports the hypothesis that ligand discrimination is at the core of the biological function of this system. These results further suggest that ligand-discriminating receptors should favor an asymmetrically dimerizing architecture, while single-ligand receptors have no need for asymmetry. In accordance with this prediction, type-I and type-III IFN receptors feature multiple ligands and asymmetry, whereas type-II receptors bind only IFN γ via homodimerization [75].

For the estimation of the discrimination power, two kinds of noise sources were included. The variation of ligand concentration as extrinsic noise and low copy-number effect of readout molecules as intrinsic noise. However, the signal transduction is also compromised by fluctuations in receptor number due to cell-to-cell variability or low copy-number noise

in receptor activation. Here, it was shown that when considering only constitutive genes, pure readout noise provides a convenient effective description for these additional noise sources that is sufficient at the level of detail of the present study. Including both a typical fluctuation in protein number of about 25% and a low copy-number noise in receptor with only 100 receptors [156], it has a similar effect as reducing the readout number \bar{n} from 100 to 20.

As a parsimonious choice, the input distribution was chosen to reflect equal chances for ligand being absent or present, and of either type. Effectively, this choice results in a maximal discrimination power of 1.5 bits, where presence sensing contributes 1 bit and type sensing the remaining 0.5 bits. In the scenario of IFN considered here, ligands are produced in response to inflammation. Therefore, one could argue that to describe rare inflammation, ligands should be present only in rare situations. Furthermore, one could also reason that the weaker ligand α occurs more frequently than the stronger ligand β . By re-optimizing the discrimination power for these alternative scenarios, it was shown that both rare inflammation and unequal ligand abundance lead to an increased pure presence sensing regime, in which type information is omitted completely. This was to be expected, as both rare inflammation or unequal ligand abundance reduces the total information encoded in ligand type, putting more importance on presence sensing. As the only receptor architecture, heterodimerizing receptors can still accommodate type sensing. For all three considered architectures, the optimal activation curves within each regime are almost unchanged. Thus, changing the input distribution results in a redistribution of importance between presence and type sensing, which does not affect the performance ranking of different receptor architectures. In particular, a balance of presence and type sensing emerges as a generic feature of ligand discrimination. As the task of information-processing is defined, detecting a rarely occurring ligand contributes less information to the discrimination power than detecting a more frequently occurring ligand. In general, this does not always reflect the biological system, as detecting a rarely occurring ligand can still be important for survival. Therefore, by accounting for the relative value of certain information compared to others, the work presented may be further refined. Assignment of fitness values to certain ligands using the tools of decision theory remains an interesting approach for further study.

By investigating basics equilibrium ligand-receptor binding motifs, this thesis shows that asymmetric ligand-induced heterodimerizing enables robust ligand discrimination. In the future it would be interesting to extend this analysis, as ligand-induced oligomerization may occur in combination with other mechanisms for ligand discrimination. For instance, the ability to discriminate between different ligands in T-cells is realized through nonequilibrium dwell-time sensing via modified kinetic proofreading schemes [142, 146]. Consequently, also nonequilibrium receptor phosphorylation kinetics could contribute to ligand discrimination in ligand-induced oligomerizing receptor systems. In the IFNAR system, slow negative feedback via USP18 [59, 73] could be a possible candidate for such a nonequilibrium function of the downstream reaction, further improving ligand discrimination. Furthermore, an interesting question to be addressed is whether by comparing the modified kinetic proofreading

schemes with the receptor dimerization schemes, universal properties of system with ligand discrimination can be found.

In general, cells do not have the luxury of receiving and responding to one signal after another, but they are usually bombarded with a variety of signals simultaneously. The interaction of multiple ligands at once leads to combinatorial responses including antagonism [145] and combinatorial signal integration [159, 160]. In the future, it would be interesting to extend the study to capture the interaction of multiple ligands. This could provide a mechanistic understanding of which feature enables a receptor to decode the information encoded in combinations of different ligands.

In conclusion, by combining rigorous mathematical analysis with detailed biological knowledge, this thesis reveals laws of digital signal processing at the receptor level. Therefore, this thesis demonstrates how applying the concepts of optimality on biological systems can help to decipher how these systems really work. In particular, it demonstrates that information theoretic methods as used here may help elucidate the specific advantages of membrane receptor architectures and eventually full pathways.

Part II

PROLIFERATION OF MULTINUCLEATED PARASITES

An Introduction to the Malaria-Causing Parasite *Plasmodium Falciparum*

8

Malaria is a life-threatening human infectious disease that is caused by parasites of the genus *Plasmodium* and is widespread in the tropical and subtropical regions [8]. Typical symptoms of malaria include but are not limited to high periodic fever, chills, tiredness and headaches.

In the battle against malaria, which has been going on for centuries, there have been many successes, such as the development of drugs [161] and the elimination of malaria from Europe and the United States [162]. However, the battle is also marked by numerous drawbacks, such as the rapidly developing resistance of the parasite to antimalarial drugs [161]. In 2021 the first malaria vaccine was approved, but it has only a low protection rate [163]. Overall, despite all these efforts of fighting malaria, it still causes around 240 million cases and more than half a million of fatalities each year, the latter mainly attributed to children under the age of five [8].

Plasmodium parasites alternate between a vertebrate host and an insect host. Humans are not the only vertebrate host of *Plasmodium* parasites, but the variety of *Plasmodium* species have evolved to infect a wide range of vertebrate hosts, including reptiles, birds and mammals [162]. In humans, Malaria is caused by five *Plasmodium* species [49]: *P. falciparum*, *P. malariae*, *P. vivax*, *P. ovale*¹ and *P. knowlesi*. However, *P. falciparum* is responsible for the majority of infections and deaths worldwide [8].

The aim of this chapter is to give a concise overview of the cell biology of the malaria-causing parasite *P. falciparum* with a focus on its nuclear replication during blood stage which will be studied more in detail in the following chapters. For a more comprehensive treatment, I recommend the following reviews Refs. [49, 165, 166].

8.1 In a Nutshell: The History of Malaria and *Plasmodium*

Malaria is an ancient disease and its unique periodic fevers are documented throughout history [166, 167]. For instance, Hippocrates already distinguished periodic fevers according to their periodicity [168]. The name of malaria originates from the Medieval Italian words bad (mal) and air (aria), as it was believed that the disease is caused by harmful swamp vapors [169, 170]. This belief was further strengthened by the subsequent decline in malaria cases after the swamps were drained [171].

The modern understanding of malaria as a disease caused by a parasite started in 1880, when Alphonse Laveran first discovered the parasite in the blood of malaria patients [166]. However, it took until 1898 to prove that the parasite was transmitted by mosquitoes, thus disproving the myth of harmful swamp vapors [166, 170].

8.1 In a Nutshell: The History of Malaria and <i>Plasmodium</i>	63
8.2 The Complex Life Cycle of <i>Plasmodium Falciparum</i>	64
8.3 Blood Stage of <i>Plasmodium Falciparum</i>	65
8.4 Eukaryotic Cell Cycle	65

1: Actually, six species are known since *P. ovale* comprises two species, namely *P. ovale curtisi* and *P. ovale wallikeri* since both are genetically distinct [164]. However, as both show the same morphology they are often referred to as one species [164].

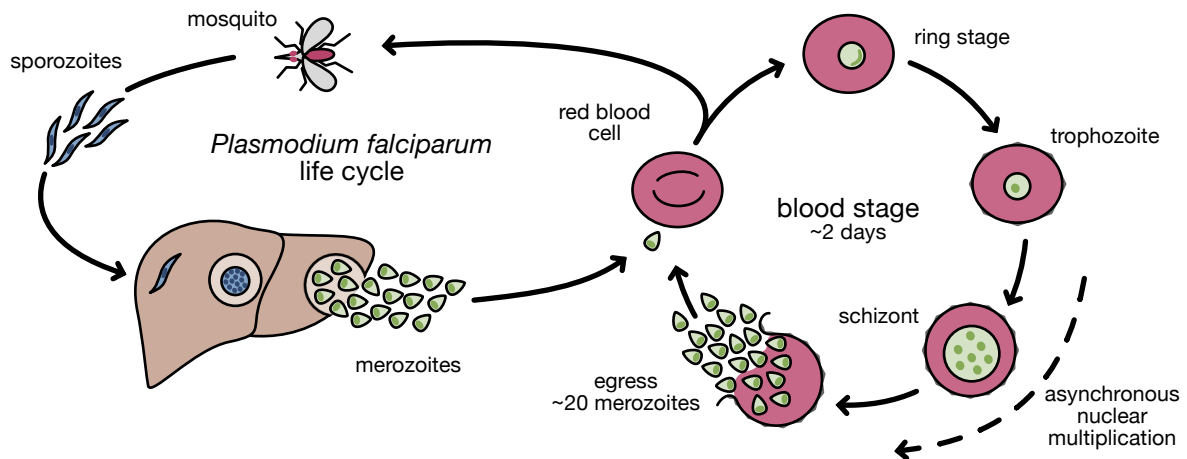


Figure 8.1 | Life cycle of the malaria-causing parasite *P. falciparum*. The parasite alternates between the human host and female *Anopheles* mosquito host.

8.2 The Complex Life Cycle of *Plasmodium Falciparum*

Today, there is a very detailed picture of the complex life cycle of *P. falciparum* in which parasites alternate between a female *Anopheles* mosquito host and a human host, see Fig. 8.1. Following the bite of an infected *Anopheles* mosquito, *P. falciparum* parasites enter the human host, in the form of sporozoites² (see Fig. 8.1, blue), and travel into the liver via the bloodstream. After the invasion of liver cells, the sporozoites multiply asexually for about one week via schizogony³. The liver stage concludes with cytokinesis, during which up to 10^5 daughter parasites are formed and released into the bloodstream [165, 172–174].

The release of the daughter parasites in the form of merozoites⁴ (see Fig. 8.1, green) into the bloodstream marks the onset of clinical symptoms [48, 49]. During the blood stage, merozoites invade red blood cells, where they asexually multiply via schizogony. After 48 h, one parasite gives rise to approximately 20 ± 3 daughter merozoites [45–47]. Merozoites enter the bloodstream again to invade other red blood cells, starting the proliferative cycle anew. Here, a few merozoites switch to the sexual development, differentiating into gametocytes. The mature gametocytes can then infect a mosquito during a blood meal. The transmission from the human host to the mosquito host is followed by the so-called sporogonic cycle, which describes the multiplication of the parasite in the mosquito. After the mosquito bites another human, the life cycle of the parasite begins anew.

During the life cycle, *P. falciparum* faces two bottlenecks, in which a few parasites replicate massively to establish a stable population size. One bottleneck is the transmission from the mosquito host to the human host, as the liver stage starts with only a few sporozoites ($1-10^2$) [165]. To overcome this, the parasite passes through two stages characterized by rapid multiplication: the liver stage and the blood stage. The liver stage establishes a population size of 10^4-10^5 , whereas the blood stage further increase the number of parasites to $10^{10}-10^{12}$ [165]. Another bottleneck

2: The sporozoite is a motile form of the *P. falciparum* parasite transmitted by the mosquito.

3: The schizogony is an atypical form of cell division, where the occurrence of multiple rounds of nuclear division without cell division results in a multinucleated stage.

4: The merozoite is a motile form of the parasite *P. falciparum* that originates from the first schizogony in the human host during the liver stage.

is the retransmission from the human host to the mosquito host, which is again overcome by a period of rapid growth [165].

8.3 Blood Stage of *Plasmodium Falciparum*

Among all the different stages in the human host, only the blood stage, see Fig. 8.1, is of clinical relevance. After the initial invasion of a red blood cell, the parasite develops first into a so-called ring stage. Over time, it transitions to a feeding stage, the so-called trophozoite stage. Within both stages, *P. falciparum* remodels the red blood cell, starting from a terminally differentiated cell that lacks most organelles, the parasite remodels the red blood cell such that the parasite can grow and hide from host immune responses [175–177]. During the trophozoite stage, the parasite takes up hemoglobin from the host cell. To neutralize the toxic by-product heme, it is stored in a biocrystal known as hemozoin [178].

Around 30–36 hours post invasion, with the first nuclear division, the parasite transitions into its last stage, the schizont stage, where it multiplies via schizogony. In detail, the parasite undergoes several rounds of nuclear divisions without cytokinesis, becoming multinucleated. During the blood stage, the nuclear membrane stays intact, no breakdown or chromosome condensation can be seen [179, 180]. Interestingly, although all nuclei reside in a shared cytoplasm, odd numbers of nuclei are frequent and nuclear microtubule structures often differ between nuclei, indicating that nuclei divide asynchronously [179, 181–183]. Nuclear multiplication concludes with a relatively synchronous final round of division, which coincides with cellularization [180, 184]. The daughter cells are subsequently released during egress and can then invade other red blood cells. It should be noted that the egress at the blood stage of all parasites is—to a non-negligible extent—synchronized in the human host and that this synchronous egress is associated with the periodic fever in patients [185, 186].

8.4 Eukaryotic Cell Cycle

To address the question of how the blood-stage schizogony of *P. falciparum* might be regulated, the concept of the cell cycle and its regulation in eukaryotic cells is explained first. The cell cycle describes the series of events, required for cell division. In eukaryotic cells, i.e. cells with nuclei, the cell cycle is commonly divided into four different phases: G₁-phase, S-phase, G₂-phase and M-phase [187], see Fig. 8.2A.

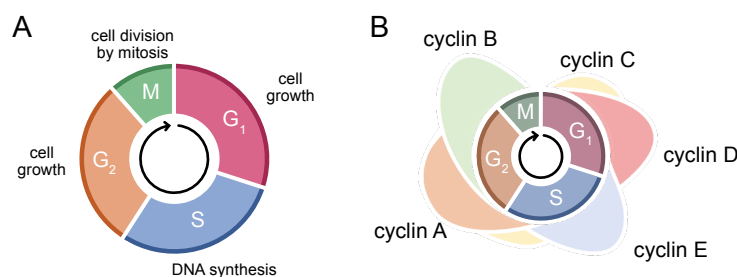


Figure 8.2 | Schematic illustration of the eukaryotic cell cycle and its regulation. (A) The cell cycle comprises four subsequent phases: G₁-phase, S-phase, G₂-phase and M-phase. (B) Cell cycle regulation in humans: the progression throughout the cell cycle is dictated mainly by the expression level of five cyclins A, B, C, D and E [187, 188]. Here, the height of the waves indicates relative intra-cellular cyclin concentrations.

The G₁-phase describes the duration between the previous M-phase and the onset of DNA replication. During the G₁-phase, cells grow and prepare for the subsequent DNA replication, i.e. cells increase their supply of proteins and organelles such as ribosomes. Therefore, this phase is also referred to as growth phase. It should be noted that the duration of the G₁-phase is usually the most variable phase within the cell cycle, even among different cells of the same species. In the G₁-phase, a cell can either decide to divide and therefore proceed to S-phase or to leave the cell cycle. In the second case, the cell moves into the so-called G₀-phase, a state outside the replicative cell cycle.

Next up is the S-phase which describes the phase the DNA replication. As accurate genome duplication is critical for cells, the processes taking place during S-phase are tightly regulated and widely conserved.

After the S-phase, the cell enters the so-called G₂-phase, in which the cell prepares for cell division. The G₂-phase is characterized by rapid cell growth and rapid protein synthesis. Since the progression of a cell through the first three phases is not accompanied by visible changes under the microscope, the duration spanning G₁-, S-, and G₂-phases is also referred to as interphase.

Finally, the M-phase describes the phase of cell division by mitosis, i.e. the process in which the replicated chromosomes are segregated into separate nuclei and the cell divides into two identical daughter cells.

The regulation of the eukaryotic cell cycle plays an important role as it is essential for the survival of a cell [189, 190]. For example, uncontrolled cell division or unrepaired genetic damage can have lethal consequences. The cell cycle progression is regulated by diffusible cytoplasmic factors called cyclins and cyclin-dependent protein kinases, see Fig. 8.2B. The interplay between these regulatory and catalytic components leads to a sequential progression through the G₁-, S-, G₂-, and M-phases [191, 192].

Cell Cycle Regulation in *P. Falciparum*

The molecular details of cell cycle regulation in *P. falciparum* remain poorly understood [165], in part because the biology of *P. falciparum* is divergent to many model organisms. Therefore, many of the canonical proteins could not be identified by sequence homology, in particular no cyclins regulating the G₁-, S-, or M-phases have been found [193].

Given that the canonical cell cycle regulation is based on diffusible cytoplasmic factors, the observed asynchrony of nuclei in *P. falciparum* blood-stage parasites is surprising, as all nuclei reside in the same cytoplasm. Therefore, one might expect that all nuclei should get the same signal to progress in their proliferative cycle. Indeed, the nuclei of many multinucleated cells, such as the early *Drosophila* embryo, undergo cell cycle events synchronously [194–197]. In addition, experiments in which the nuclei of HeLa cells⁵ in different stages synchronized their cell cycle after fusion [199] further demonstrate that the cell cycle control is mediated by diffusible cytoplasmic factors.

5: The HeLa cell is the first human cell line and is commonly used in scientific research [198].

But asynchrony in nuclear multiplication is not unique and can be observed also in other species. For instance, in experiments with multinucleated mammalian cells, asynchronous nuclear division has been observed [200, 201]. Furthermore, asynchronous nuclear division can also be observed in the large multinucleated filamentous fungus *Ashbya gossypii* [202]. Here, the asynchrony was attributed to a combination of limited diffusion of cytoplasmic factors and nucleus-intrinsic mechanisms [203–205].

However, it is important to keep in mind that despite the frequently raised hypothesis that asynchronous nuclear proliferation is in contradiction to the regulation by diffusible cytoplasmic factors [206, 207], the lack of a mechanistic understanding of the process renders the hypothesis a mere speculation.

An Introduction to Branching Processes

9

A branching process is a stochastic process, consisting of a random collection of particles¹, each of which proliferate according to certain rules. Branching processes are a conceptually simple yet powerful tool for modeling proliferation of a population. Their applicability is not limited to demography, but includes many fields like cell biology, genetics, evolution theory and epidemiology, see for instance Refs. [208–212]. An excellent textbook focusing on branching processes and their application in biology is Ref. [209]. Besides reproduction in the biological sense, the processes can also describe other systems with similar dynamics like cascade process or particles which split in a physical sense, see for instance Ref. [213]. For example, branching processes were recently used to model oscillating neuronal avalanches [214].

In branching processes, each particle proliferates according to rules, involving various degrees of randomness of its lifetime and its number of offspring. The unifying principle is the so-called *branching property*, consisting of two assumptions. First, each particle in the process behaves independently of all other particles. Second, each particle behaves identically as all other particles. Even though these are basic assumptions, the consequences are far-reaching. For example, consider a branching process starting with a single ancestor. Then taking any particle at any time point give rise to a subprocess identical to the entire process. Mathematically, the branching property is a form of *self-recurrent* [215, 216] and allows to decompose a branching process to subprocesses, which are identically distributed to each other and to the entire process.

This chapter is devoted to the so-called classical process, in which the particle produces a random number of offspring at the moment of death. However, it should be noted that the concept of branching process is more general and processes allowing production of offspring during the lifetime are referred to as general or Crump-Mode-Jagers processes [210].

This chapter is based on the textbook [209] by Marek Kimmel and David Axelrod.

9.1 Galton-Watson Process

The Galton-Watson process is the simplest branching process and originally arose from addressing the concern of the extinction of family names [217].² The process starts with a single particle which lives for a predefined time τ , see Fig. 9.1. Without loss of generality, the lifetime is set to one unit of time ($\tau = 1$) such that the first particle is born at time $t = 0$ and dies at time $t = 1$. At death, the particle give birth to a random number of offspring according to the probability distribution $(p_k)_{k \geq 0}$. Each offspring behaves independently of each other and identically as the initial ancestor particle. In particular, this branching property implies that all particles live for one time unit and the process can therefore be

9.1 Galton-Watson Process . . .	69
9.1.1 The Probability Generating Function	70
9.1.2 Moments	71
9.2 Bellman-Harris Process . . .	72
9.2.1 Moments	73
9.2.2 Markov Age-Dependent Branching Process with Exponential Lifetimes . . .	73
9.3 Controlled Branching Process	74

1: Here, the particle is a representative for the respective system of interest. In the case of nuclear multiplication a particle corresponds to a nucleus and in the case of bacterial growth to a bacterial cell.

2: An enjoyable historical introduction can be found in Ref. [218].

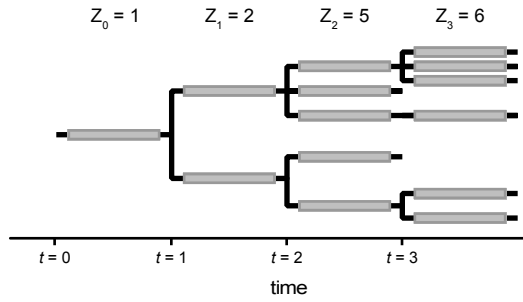


Figure 9.1 | Schematic lineage tree of a Galton-Watson process. In this step-like branching process, each particle (gray rectangle) life for one time unit and Z_i describes the number of particles at time i .

described using a discrete time index, corresponding to the number of successive generations. As a consequence, applying the Galton-Watson process to a system implies discrete non-overlapping generations.

Let Z_n denote the number of particle at time n and let $X_{i,n}$ be the number of offspring of the i -th particle existing at time n . Since a Galton-Watson process with m ancestors is just the sum of m independent Galton-Watson processes with one ancestor, one can assume $Z_0 = 1$, without loss of generality. The Galton-Watson process $(Z_n)_{n \geq 0}$ can then be recursively defined by

$$Z_{n+1} = \sum_{i=1}^{Z_n} X_{i,n}, \tag{9.1}$$

where $(X_{i,n})_{i \geq 1, n \geq 0}$ form a family of independent and identically distributed random variables with common family size distribution $(p_k)_{k \geq 0}$. This formulation is often referred to as forward construction, since it is based on the fact that the number of particles in the $(n + 1)$ -th generation is equal to the number of offspring of all particles in the previous generation n .

Typically, the Galton-Watson process is used to addresses two fundamental questions. First, what is the mean and the variance of the number of particle at time n . Second, what is the probability that the population becomes extinct. Within the scope of this thesis, the concept of branching processes is used to model nuclear multiplication. Since the case of death for an individual particle is not considered ($p_0 = 0$), the second question is trivial and is therefore not discuss further.

9.1.1 The Probability Generating Function

A useful tool for handling random sums like in Eq. (9.1) is the probability generating function (pgf). The pgf f_n of Z_n is defined as

$$f_n(s) = \langle s^{Z_n} \rangle = \sum_{k=0}^{\infty} s^k P(Z_n = k), \tag{9.2}$$

3: Restricting the symbolic argument to $|s| \leq 1$ ensures that the power series converges absolutely.

where s introduces a symbolic argument with $|s| \leq 1$.³ As the name suggests, the probability $P(Z_n = k)$ to find k particles at time n is recovered by taking derivatives of f ,

$$P(Z_n = k) = \frac{1}{k!} \left. \frac{d^k f_n(s)}{d(s^k)^k} \right|_{s=0}. \tag{9.3}$$

Since the process starts with a single ancestor ($Z_0 = 1$), the pgf of the typical family size reads

$$f(s) = f_1(s) = \langle s^{X_{1,0}} \rangle = \sum_{i=0}^{\infty} s^i p_i. \quad (9.4)$$

By using Eq. (9.1), a recursion rule of the pgf can be derived, namely

$$f_{n+1}(s) = f_n[f(s)] = (f_n \circ f)(s). \quad (9.5)$$

In particular, by applying this recursive rule n times, the pgf can be rewritten to

$$f_n(s) = \underbrace{(f \circ f \circ \dots \circ f)}_{n \text{ times}}(s). \quad (9.6)$$

9.1.2 Moments

All moments of Z_n can be expressed in terms of the derivatives of f_n evaluated at $s = 1$. The first moment of Z_n reads

$$\langle Z_n \rangle = \left. \frac{df_n(s)}{ds} \right|_{s=1} \equiv f'_n(1). \quad (9.7)$$

Applying the recursion rule of f_n Eq. (9.5) $(n - 1)$ -times, the mean of Z_n Eq. (9.7) can be rewritten as

$$\begin{aligned} \langle Z_n \rangle &= f'_{n-1}(1)f'(1) \\ &= f'_{n-2}(1)[f'(1)]^2 \\ &= \dots \\ &= [f'(1)]^n = m^n, \end{aligned} \quad (9.8)$$

where m introduces the mean of the family size distribution, i.e. $m = \langle Z_1 \rangle$. Thus, whether the mean of the branching process grows, depends only on the mean of the family size distribution and not on the details of the distribution. The process grows geometrically for $m > 1$ (supercritical), stays constant for $m = 1$ (critical) and declines geometrically for $m < 1$ (subcritical).

The variance of Z_n can be written like

$$\text{Var}(Z_n) = f''_n(1) + f'_n(1)[1 - f'_n(1)]. \quad (9.9)$$

By using Eq. (9.5), a straight forward calculation yields

$$\text{Var}(Z_n) = \begin{cases} n\sigma^2 & \text{if } m = 1, \\ \frac{1-m^n}{1-m} m^{n-1} \sigma^2 & \text{if } m \neq 1, \end{cases} \quad (9.10)$$

where $\sigma^2 = \text{Var}(Z_1)$ introduces the variance of the family-size distribution. Thus, the variance of Z_n depends solely on m and σ^2 and not on the details of the family size distribution.

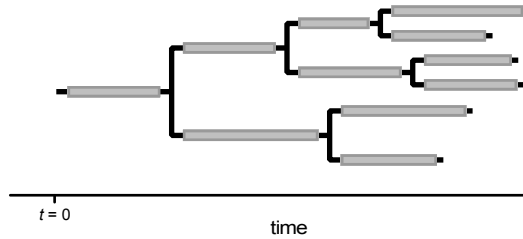


Figure 9.2 | Schematic lineage tree of a Bellman-Harris process. Here, each gray rectangle indicates a particle with a lifetime corresponding to the length of the rectangle.

9.2 Bellman-Harris Process

The Bellman-Harris process is a more general branching process, studied first by Richard Bellman and Theodore Harris [219]. In contrast to the Galton-Watson process, where all particles live exactly one unit of time, the lifetime τ of particles in the Bellman-Harris process are non-negative random variables with arbitrary distribution, see Fig. 9.2. The process starts with a single ancestor particle born at $t = 0$. The lifetime τ of the particle is a random variable with cumulative distribution function $G(\tau)$. After its lifetime, the particle is transformed into a random number of offspring particles according to a probability distribution with pgf $f(s)$. Each offspring behaves independently of each other and identically as the initial ancestor particle. In particular, this branching property assumption means that the lifetime and the number of offspring depends neither on the current number of particles nor on the absolute time of the process t . Any newborn particle at any time point gives rise to a subprocess identical to the entire process. Introducing $Z(t)$ to denote the particle count at time t , the Bellman-Harris process $(Z(t))_{t \geq 0}$ is called age-dependent branching process.

Let τ be the lifetime of the single ancestor particle. Then, for any time before the proliferation took place, i.e. $t < \tau$, the process consists of the ancestor particle only. At its death $t = \tau$, the particle produces a random number of the first-generation offspring denoted by X . At any time after its death $t \geq \tau$, the process can be described by the sum of all subprocesses $Z^{(i)}(t - \tau)$ started by the offspring at time $t = \tau$. The particle count conditional on τ reads

$$Z(t) = \begin{cases} 1 & \text{if } t < \tau, \\ \sum_{i=1}^X Z^{(i)}(t - \tau) & \text{if } t \geq \tau. \end{cases} \tag{9.11}$$

Here, the superscript $Z^{(i)}$ is introduced to emphasize that each subprocess is an independent and identically distributed realization of the initial process. Introducing the pgf of $Z(t)$ as $F(s, t)$ yields⁴

$$F(s, t) = \begin{cases} s & \text{if } t < \tau, \\ f[F(s, t - \tau)] & \text{if } t \geq \tau. \end{cases} \tag{9.12}$$

Integrating Eq. (9.12) with respect to the cumulative distribution of lifetime G yields [219]⁵

$$F(s, t) = s [1 - G(t)] + \int_0^t f[F(s, t - u)] dG(u). \tag{9.13}$$

A mathematical more rigorous derivation can be found for instance

4: In the Galton-Watson process the pgf of $Z_n = Z(t = n)$ is denoted by f_n , since latter was just the n -fold functional iterate of the pgf of the offspring number f , see Eq. (9.5).

5: The Galton-Watson process with a particle lifetime τ can be obtained by choosing the Heaviside step function as the cumulative distribution function, i.e. $G(t) = \theta(t - \tau)$.

in [209]. Eq. (9.13) illustrates the strong impact of the distribution of lifetime τ on the process. Whereas for Galton-Watson process with discrete time steps $\tau = 1$, the pgf of the number of offspring $Z(t)$ is simply the t -fold functional iterate of the pgf of the offspring number Eq. (9.5), for general distributions of lifetime, Eq. (9.13) can not be solved explicitly.

9.2.1 Moments

The moments can be expressed in terms of partial derivatives of F and letting $s \rightarrow 1$. Differentiating Eq. (9.13) results in the following equation

$$\langle Z(t) \rangle = \left. \frac{\partial F(s, t)}{\partial s} \right|_{s=1} = [1 - G(t)] + m \int_0^t \mu(t-u) dG(u). \quad (9.14)$$

Interestingly, just as in the Galton-Watson process [compare Eq. (9.8)], the equation for the mean does not depend on the actual offspring distribution, but only on its mean m . In general, Eq. (9.14) can not be solved explicitly. However, since it is of the renewal type, one can estimate the asymptotic behavior by using result from the renewal theory. In the supercritical case ($m > 1$), it can be shown that the mean particle count grows exponentially [219, 220]

$$\langle Z(t) \rangle \simeq e^{\alpha t} \quad \text{as } t \rightarrow \infty, \quad (9.15)$$

where α denotes the Malthusian parameter defined by the root of the equation

$$\int_0^\infty e^{-\alpha y} dG(y) = \frac{1}{m} \quad (9.16)$$

for a given m and G .

9.2.2 Markov Age-Dependent Branching Process with Exponential Lifetimes

Next, the special case of exponentially distributed lifetimes with parameter λ , i.e. $G(t) = 1 - \exp(-\lambda t)$, is considered. The advantage of this case is that it leads to some closed-form expression. However, one should keep in mind that the exponential distribution is not well justified to model lifetimes in biological systems. The reason therefore is that it admit arbitrarily short lifetimes, although for many biological processes like cell-cycle or nuclear multiplication the lifetime has a lower bound larger than zero. Since the process with exponentially distributed lifetimes and the Galton-Watson process are the only two Markov special cases of the Bellman-Harris processes, the former is also called Markov age-dependent branching process.

By using $G(t) = 1 - \exp(-\lambda t)$ and taking the derivative, Eq. (9.13) can be simplified to the following differential equation

$$\frac{dF(s, t)}{dt} = -\lambda \{F(s, t) - f[F(s, t)]\}. \quad (9.17)$$

The advantage of using the exponential distribution is that the mean and variance of $Z(t)$ can be solved explicitly [209]

$$\langle Z(t) \rangle = e^{\alpha t}, \quad (9.18a)$$

$$\text{Var}[Z(t)] = \begin{cases} \frac{(m-1)^2 + \sigma^2}{m-1} e^{\alpha t} (e^{\alpha t} - 1) & \text{if } \alpha \neq 0, \\ [m(m-1) + \sigma^2] \lambda t & \text{if } \alpha = 0. \end{cases} \quad (9.18b)$$

Further, the Malthusian parameter of population growth simplifies to $\alpha = \lambda(m-1)$.

9.3 Controlled Branching Process

So far, this chapter solely addressed branching processes with particles that are independent of each other, i.e. that fulfilled the branching property. However, it is clear that such processes are generally not appropriate to describe populations in which the growing dynamics are dominated by the interaction between particles. For example, a conceivable such interaction might be that the growth depends on the current population size, or in the context of multinucleated cells, such interaction might be a shared resource, limiting growth. Indeed, Chapter 12 shows that the nuclei of *P. falciparum* are coupled with each other during the blood stage, and this coupling can be well described by a shared limiting resource.

In the case of discrete time and single-type, such processes can be described by the so-called controlled branching processes, which are stochastic processes in which the number of reproductive individuals is affected by a control mechanism [210, 221, 222]. Furthermore, there are first successes to generalize the concept of controlled branching processes to continuous times [223]. However, since both continuous time and multi-type are necessary in order to appropriately describe the nuclear multiplication processes of the parasite, a more detailed introduction is not provided here.

Nuclear Multiplication Dynamics of *Plasmodium Falciparum*

10

This chapter is based on a collaboration with experimentalists [2].
For a detailed listing of author contributions see Appendix A.

The malaria-causing pathogen *P. falciparum* is a unicellular parasite with a complex life cycle, see Section 8.3. During the blood stage, the parasite invades a red blood cell and undergoes several rounds of nuclear division, forming a multinucleated cell before cellularization [184, 224]. Each blood-stage proliferative cycle takes roughly 48 hours and one parasite gives rise to approximately 20 ± 3 daughter parasites [45–47]. The stage with the presence of multiple nuclei is referred to as the schizont stage, and the nuclear multiplication is called schizogony. Even though the disease severity is directly related to the parasite burden and therefore also linked to the dynamics of nuclear multiplication at the blood-stage [48, 49], the dynamics of asynchronous nuclear division, its coordination with DNA replication and the mechanism for the regulation of the final number of daughter parasites are unknown [47].

Here, the blood-stage nuclear multiplication in *P. falciparum* is investigated by confronting data with two different theoretical frameworks. First, to unravel the mechanism that underlies the regulation of the progeny number, models originating from the rich history of theoretical approaches to the question of cell-size control [225, 226] are used. Second, the dynamics of nuclear multiplication are studied with branching processes, which are the most natural way to model growing population. As there is a plethora of publications devoted to modeling a variety of biological growth phenomena with branching processes, these have a well-developed theory [208, 209], see Chapter 9. Besides phenomena such as cell population growth or tissue proliferation, there is also considerable work on modeling the cell cycle using a Bellman-Harris process [208, 227–231].

Section 10.1 presents the main experimental results of my collaboration partners, which established a novel nuclear cycle sensor with single cell resolution. A more comprehensive treatment can be found in Ref. [2] and in the PhD thesis of Severina Klaus [232]. In Section 10.2–10.4, I present my own results on modeling nuclear multiplication at the blood stage. Section 10.2 addresses the question by what mechanism the final number of progeny is regulated. By modeling the nuclear multiplication as a branching process, Section 10.3 discovers a slowdown of the cycling dynamics as nuclear multiplication progress from the second cycle onwards. By simulating a more complex branching process, Section 10.4 confirms that the final number of daughter parasites can be well explained by a counter mechanism. In addition, it provides an estimate of the observed slowdown.

10.1 Experimental Setup and Results	76
10.1.1 Unravel the Nuclear Multiplication Mode . . .	76
10.1.2 A Nuclear Cycle Sensor System	77
10.1.3 Single Cell Dynamics of Nuclear Multiplication .	78
10.2 Is the Parasite Counting or Waiting?	80
10.2.1 Timer Model	80
10.2.2 Counter Model	81
10.2.3 The Parasite Counts its Number of Progeny . . .	81
10.3 Nuclear Multiplication as Branching Processes . . .	83
10.3.1 General Setup	83
10.3.2 Galton-Watson Process .	85
10.3.3 Bellman-Harris Process .	86
10.4 Nuclear Multiplication as Biphasic Branching Process	87
10.4.1 General Setup	87
10.4.2 Counter Model	88
10.4.3 Predictions for the Total Merozoite Count	89
10.5 Conclusion	90

10.1 Experimental Setup and Results

This section is based on the work of my collaboration partners Markus Ganter and Severina Klaus [2].

10.1.1 Unravel the Nuclear Multiplication Mode

Two distinct models have been proposed to describe the chronology of DNA replication and nuclear division events in *P. falciparum* during the blood stage, see Fig. 10.1A. The first model assumes several rounds of DNA replication, which precede a phase of nuclear division [206, 233]. This model predicts at first parasites with a single nucleus and varying DNA content and then parasites with varying number of nuclei and a relatively constant total DNA content. By contrast, model 2 proposes alternating rounds of DNA replication and nuclear divisions [206, 234, 235]. Thereby, it predicts a gradual increase of both number of separate nuclei per parasite and the total DNA content. To test the predictions of both models, the total DNA content and the apparent number of nuclei per parasite were quantified after staining the DNA. Here, the DNA content is normalized to the DNA content of a parasite in the early blood stage, so-called ring stage, where the parasite still has a single copy of its genome¹, corresponding to 1 C.² For the estimation of apparent number of nuclei it was assumed that every distinct DNA mass corresponds to an individual nucleus. As depicted in Fig. 10.1B, the DNA content and the number of nuclei per parasite were positively correlated, supporting model 2. Additionally, the total DNA content did not exceed a value of 2 C per nucleus of a given parasite. These observations suggest that the DNA content of individual nuclei alternates between 1 C and 2 C, i.e. between 1-2 copies.

1: A cell with a single copy of its genome is called haploid cell.

2: The C-value is typically used to denote the weight of the DNA contained within a haploid nucleus, i.e. the weight of a single copy of a genome. Here, it is used to normalize the DNA content.

To exclude the possibility that membranous connections still existed between the envelopes of nuclei that appeared separate in light microscopy, three-dimensional electron tomographic views of cell parts containing several entire nuclei were recorded, see Fig. 10.1CD. Although the nucleoplasm of some adjacent nuclei were only 75 nm apart (not shown here, see Ref. [2]), most nuclei appeared as separate compartments with clearly discernible nuclear envelopes and ribosomes filling the cytoplasmic gap. In only one out of eight analyzed cells, a narrow bridge interconnecting two nuclei was recorded, which appeared to be completing nuclear division, see Fig. 10.1E. Altogether these data support the second model. Thus, *P. falciparum* proliferates at the blood stage through alternating rounds of DNA replication and nuclear divisions before cellularization.

Although nuclear divisions lack synchronization [47, 179, 181, 206], it is unclear whether DNA replication in pairs of sister nuclei is synchronized. To address this question, the DNA content using a live-cell compatible DNA dye was quantified [236, 237], employing time-lapse live-cell microscopy of a cell line that expressed mCherry³ fused to a triple nuclear localization signal as a marker for nuclei. As a result, the DNA content of sister nuclei increased at different times, onset and end of DNA replication are not synchronized, see Fig. 10.1FG.

3: mCherry is a red fluorescent protein that is used to study components in the cell using fluorescence microscopy [238].

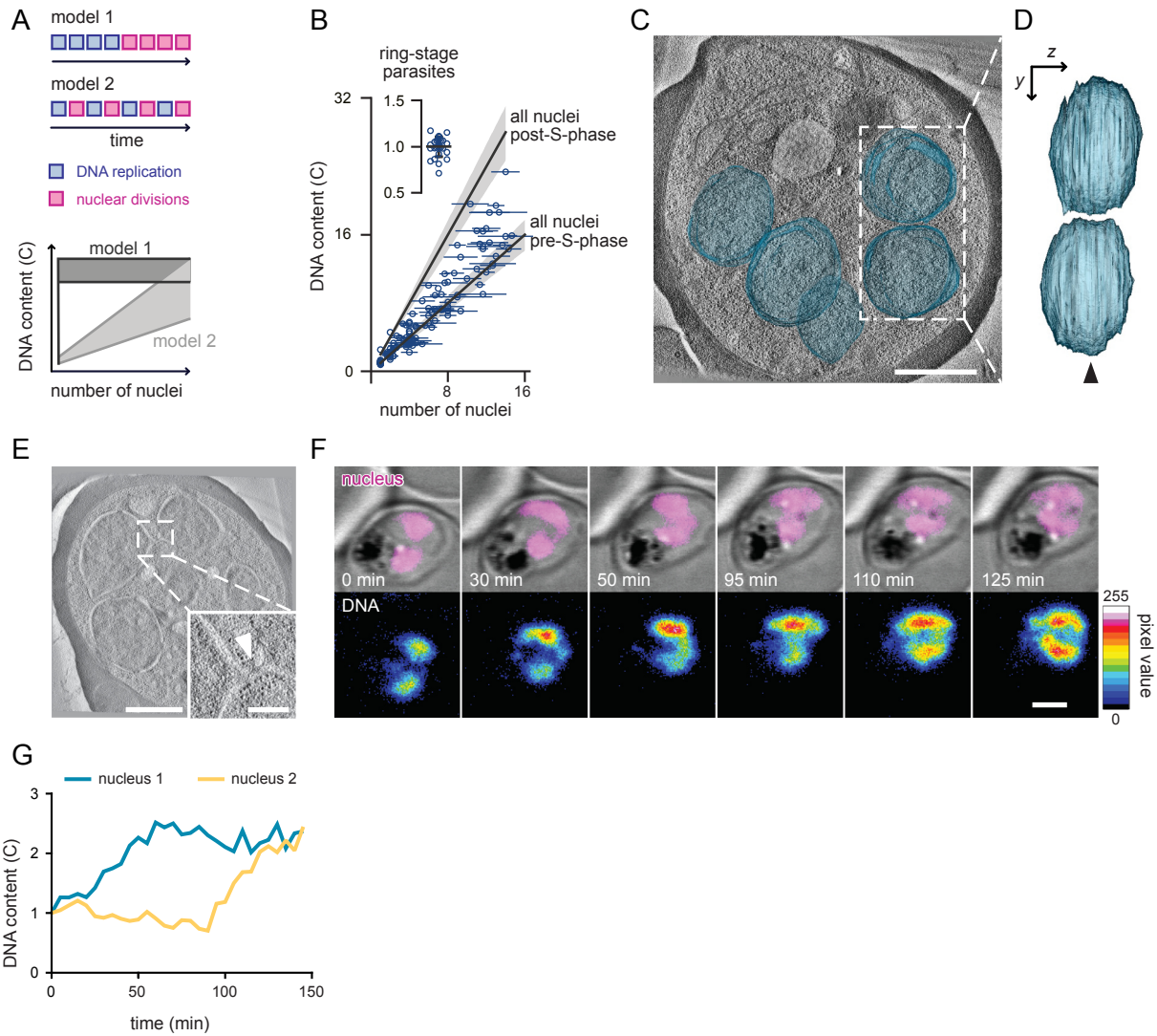


Figure 10.1 | *P. falciparum* proliferates through consecutive rounds of asynchronous DNA replications and nuclear divisions. (A) Schematic and predictions of two models proposing the mode of *P. falciparum* proliferation in the blood stage of infection. (B) Gradual increase of the total DNA content and the number of nuclei of *P. falciparum* supports model 2. The DNA content was normalized to haploid ring-stage parasites (insert), defined as 1 C. Horizontal bars, standard deviation; gray lines, expected DNA contents of parasites with all nuclei pre- or post-S-phase; gray bands, propagated error (standard deviation) of ring-stage measurements. (C) Electron tomogram, overlaid with 3D-segmented inner nuclear membranes (blue); bar, 1 μ m. (D) Side view of nuclear volumes showed no connection (90° rotation around the y-axis); arrowhead, tomogram plane shown in C. (E) Electron tomogram of connected nuclei; bar, 1 μ m; inset highlights the connection (arrowhead); bar, 250 nm. (F) Time-lapse microscopy of a reporter parasite stained with a far-red DNA stain, the DNA dye 5-SiR-Hoechst, showed asynchronous DNA replication in sister nuclei; bar, 2 μ m. (G) Quantification of the DNA content of the nuclei shown in F. Taken and adapted from Ref. [2].

10.1.2 A Nuclear Cycle Sensor System

To understand how asynchronous DNA replications are orchestrated, the localization of the DNA replication machinery was investigated, using the *P. falciparum* proliferating cell nuclear antigen (PCNA) 1 as a proxy. PCNA is a critical co-factor of DNA polymerases and serves as a hub for many other components of the replication fork [239]. As endogenous fusion of PCNA1 with the green fluorescent protein (GFP) failed, a PCNA1::GFP⁴ fusion protein was episomally expressed in the background of the nuclear marker line. Using correlative light and electron microscopy, it was found that in contrast to previous reports [241, 242], PCNA1::GFP localized unequally in nuclei of the same parasite,

4: Here the double colon (::) is used to describe the fusion protein of PCNA1 and GFP [240].

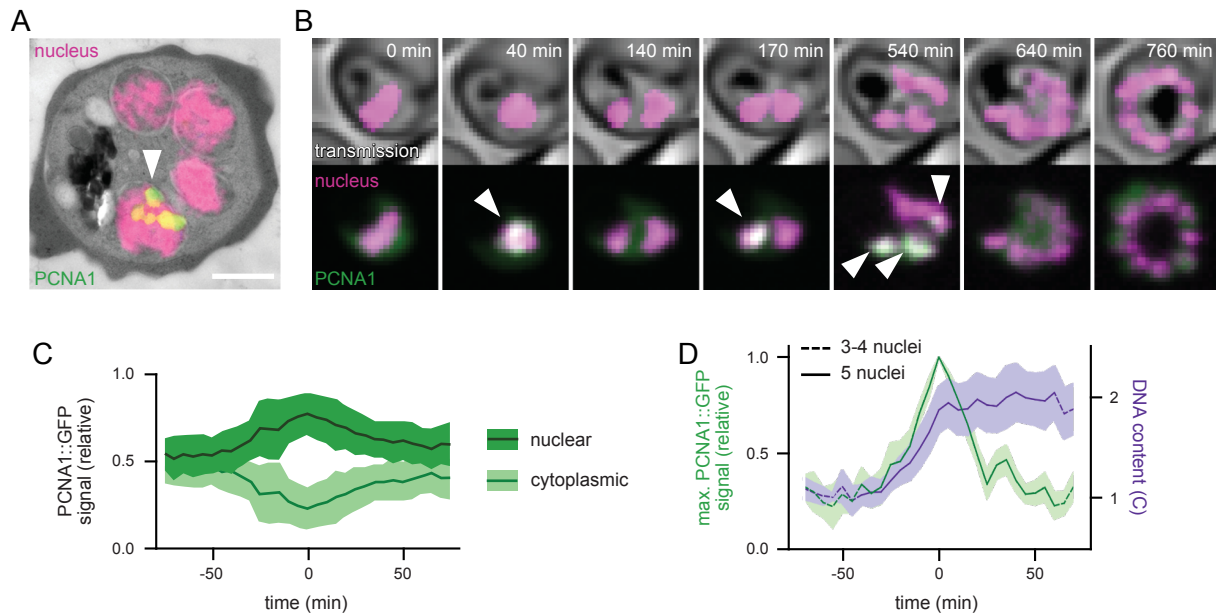


Figure 10.2 | Heterogeneous accumulation of PCNA1::GFP among nuclei permits development of a nuclear cycle sensor system. (A) Correlative light and electron microscopy showed heterogeneous accumulation of PCNA1::GFP among *P. falciparum* nuclei; bar, 1 μm ; arrowhead, PCNA1::GFP focus. (B) Time-lapse microscopy showed dynamic and transient accumulation of PCNA1::GFP; bar 2 μm ; arrowheads, nuclear PCNA1::GFP accumulation. (C) Nuclear accumulation of PCNA1::GFP coincided with a depletion of the cytosolic pool; lines, average ($n = 4$); bands, standard deviation. (D) Nuclear PCNA1::GFP accumulation caused a peak in the maximal pixel intensity, coinciding with DNA content duplication. DNA content was normalized to the average of ten or all available values prior to the nuclear accumulation of PCNA1::GFP, defined as 1C; solid lines, average; bands, standard deviation. Taken and adapted from Ref. [2].

with only some nuclei showing distinct PCNA1::GFP foci, see Fig. 10.2A. Additionally, time-lapse imaging revealed a dynamic localization and transient accumulation of PCNA1 in changing subsets of nuclei, see Fig. 10.2B. An increasing nuclear PCNA1::GFP signal was accompanied by a decreasing cytosolic signal and vice versa, see Fig. 10.2BC, suggesting that nuclei access a common cytoplasmic pool of PCNA1. Moreover, nuclear accumulation of PCNA1::GFP coincided with a duplication of the DNA content in the same nuclei, see Fig. 10.2D. This allowed tracking individual DNA replications and nuclear division events over time in a given cell, see Fig. 10.2B. Hence, the parasite line expressing PCNA1::GFP can be considered a nuclear cycle sensor system in analogy to the widely used FUCCI cell cycle sensor system for mammalian cells [243].

10.1.3 Single Cell Dynamics of Nuclear Multiplication

By using the PCNA1-based nuclear cycle sensor system, the timing of individual events during nuclear multiplication over several generations of nuclei are quantified. Here, the S-phase is defined as the time interval between the onset and the end of visible PCNA1::GFP accumulation in a nucleus, see Fig. 10.2AB. Completion of nuclear division is defined as the first time point where two separate nuclei can be observed. To enable the comparison of different events during nuclear multiplication, each event is labeled by its ancestor and in the order of S-phase initiation, e.g., 00 indicates a second generation nucleus entering the S-phase first.⁵ All 70 nuclear lineage trees are summarized in Fig. F.1. The resolution of the live-cell microscopy was set to 5 min. Strikingly, the timing of events and, thus, the resulting nuclear lineage trees varied markedly between

5: The initial S-phase in a parasite containing a single nucleus is labeled 0. Subsequent division of this nucleus resulted in two nuclei labelled 00 and 01, respectively; with 00 indicating the nucleus that entered S-phase first, see Fig. 10.3A. In other words, each new generation extends the name of the ancestor by appending 0 (1) for the earlier (later) S-phase initiation.

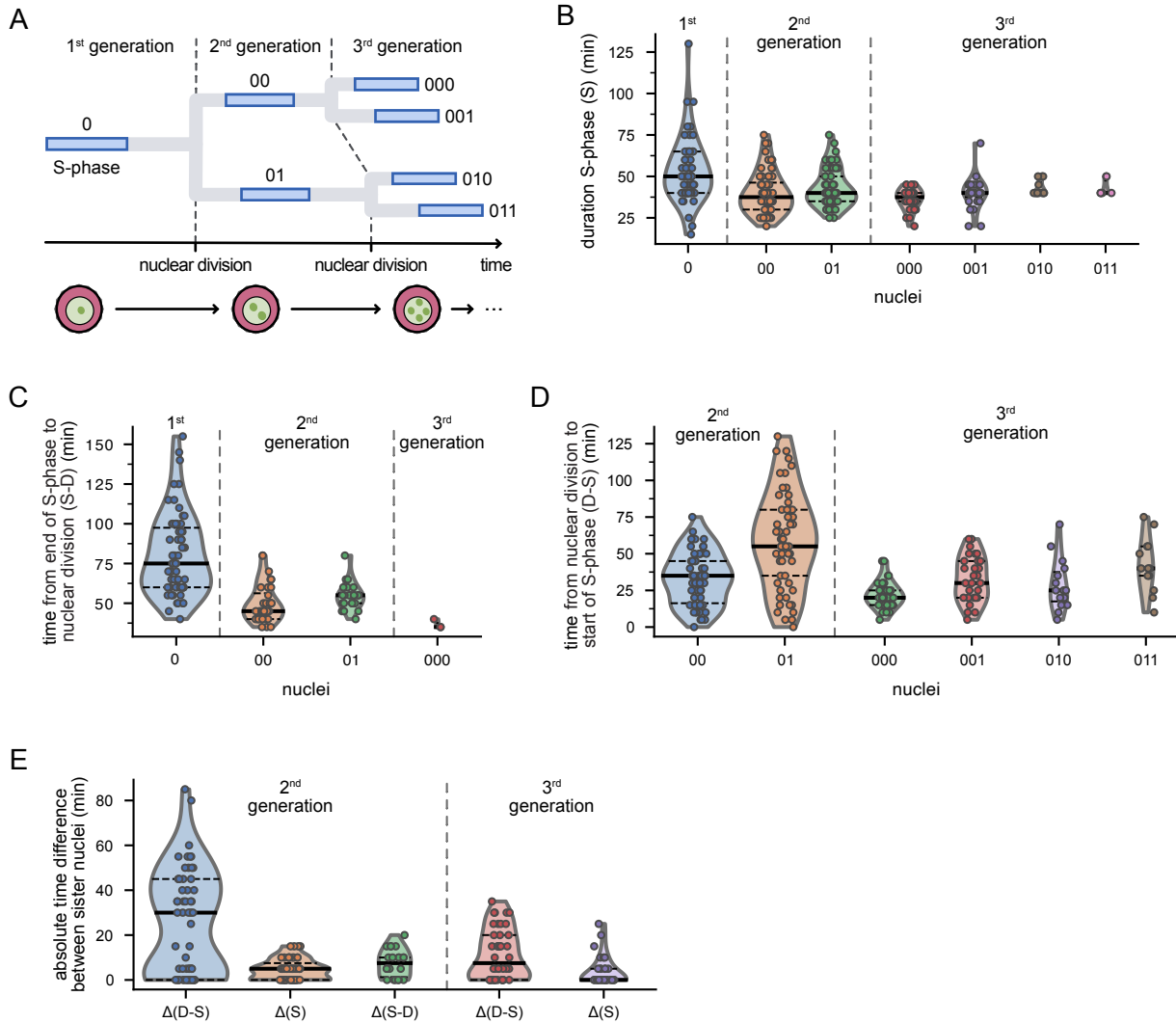


Figure 10.3 | Single cell dynamics of nuclear multiplication. (A) Nuclear lineage tree illustrating the three consecutive generations of nuclei quantified in B-E. Dashed lines, nuclear divisions demarcating generations and defined as the first time point where two separate daughter nuclei were observed; blue, S-phases (S) defined as the interval during which PCNA1::GFP accumulation was observed in a nucleus; nuclei are numbered by ancestor and in order of S-phase occurrence (e.g., 00: daughter of 0, second generation; first S-phase). (B) S-phase durations of three generations of nuclei. S_0 phases were longer than the pooled second-generation S-phases S_{0*} (two-sided Mann-Whitney U -test effect size $f = 0.72$, $n_1 = 54$, $n_2 = 117$, $p = 3.2 \times 10^{-6}$) and $S_{00,01}$ was the same as $S_{000,001,010,011}$ ($f = 0.51$, $n_1 = 117$, $n_2 = 75$, $p = 0.85$). (C) Time from end of S-phase to nuclear division (S-D) of two generations of nuclei. $(S-D)_0$ was longer than $(S-D)_{00,01}$ ($f = 0.87$, $n_1 = 63$, $n_2 = 60$, $p = 8.1 \times 10^{-13}$). (D) Time from nuclear division to start of S-phase (D-S) of two generations of nuclei. $(D-S)_{00,01}$ was longer than $(D-S)_{000,001,010,011}$ ($f = 0.66$, $n_1 = 119$, $n_2 = 91$, $p = 4.2 \times 10^{-5}$). Numbering of events in B-D as indicated in A; each dot represents an event occurring in a single nucleus of a single parasite out of 70 parasites analyzed. (E) Absolute time difference of nuclear cycle phases between sister nuclei shows that the interval between division and S-phase has the largest influence on synchrony. Solid lines, median; horizontal dashed lines, quartiles. Taken and adapted from Ref. [2].

individual parasites. This cannot be explained by variable expression of PCNA1::GFP, which had no effect on DNA replication dynamics.

Investigating all nuclear lineage trees show that the first S-phase S_0 is on average significantly longer than the S-phases of the second-generation nuclei $S_{00,01}$, while the duration of S-phases then remains similarly long in the third generation of nuclei ($S_{000,001,010,011}$), see Fig. 10.3B. Further, the time from the end of S-phase to nuclear division (S-D) was longer in the first generation than in the second generation, see Fig. 10.3C. The following interval between nuclear division and S-phase (D-S) in nuclei of the second generation was longer than in the third generation, see Fig. 10.3D. Hence, all initial phases of nuclear multiplication (i.e., duration

of the first S-phase, time from the end of first S-phase to first nuclear division, and time from first division to the start of the second S-phases) were slower than the corresponding phases in the ensuing cycle. These data are consistent with the duration of different microtubule stages, which were recently reported for the initial and the subsequent nuclear divisions [47].

The observed S-phases and the observed times from completed S-phase to nuclear division were similar in sister nuclei of the second and third generation. By contrast, the time from nuclear division to the start of the following S-phase varied markedly between sister nuclei, see Fig. 10.3E. Therefore, the interval between nuclear division and onset of S-phase predominantly introduces asynchrony during nuclear multiplication.

10.2 Is the Parasite Counting or Waiting?

Next, the long-standing question of which mechanism governs the final number of daughter parasites is addressed by confronting the single cell data with the prediction of two different mechanisms: a sizer model and a timer model. Both models have been originally proposed in the context of cell proliferation [225, 226]. Here, the rich history of theoretical approaches to the question of cell-size control comprises three fundamental classes of size regulation: sizer, adder and timer [225, 226]. Recently, these classes were also discussed in context of multicellular organisms [244–246].

In the context of cell proliferation, size homeostasis plays a central role. However, the timer is the only class not able to maintain size homeostasis. In biology, this fact is reflected by the finding that most biological system favor adder or sizer mechanisms for cell-size control [226]. By contrast, size homeostasis does not play a role in the case of nuclear multiplication of multinucleated cells, since the total growth only determines the number of progeny and not the cell size of an individual daughter cell. Therefore, it is not surprising that the (synchronous) nuclear multiplication in the unicellular organism *Sphaeroforma arctica* can be described by a timer model [247].

10.2.1 Timer Model

The *timer model* posits that a system grows for a fixed amount of time, irrespectively of the current system size, see Fig. 10.4A. Therefore, the model predicts that an initial delay of the growth phase, occurring after the onset of the timer, has no effect on the time point the growth process stops. An increase of the initial delay effectively decreases the duration of the growth phase. Thus, an increase of the initial delay results in a reduced final system size, see Fig. 10.4B. In addition, by setting the overall duration, the timer model predicts that the initial delay is uncorrelated with the overall duration, see Fig. 10.4C.

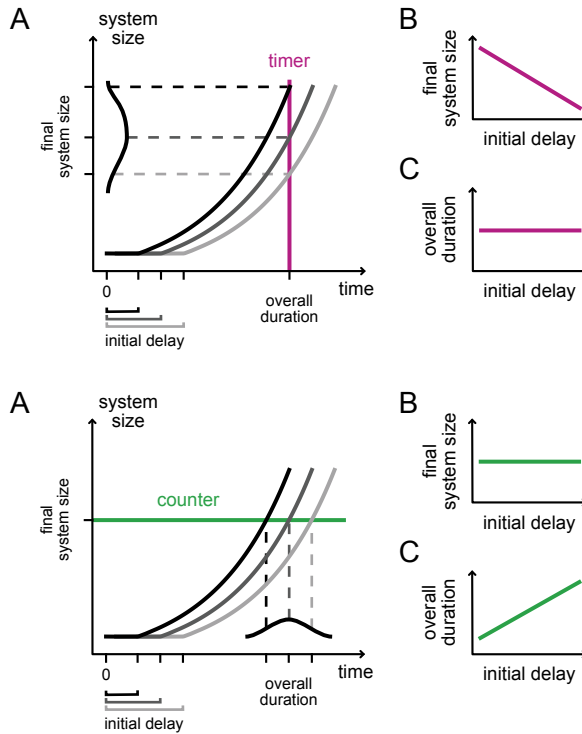


Figure 10.4 | Overview of the timer model. (A) Schematic illustrating how the duration of an initial delay affects the final system size. Timer model predicts (B) a negative correlation between the duration of initial delay and the final system size and (C) no correlation between the duration of initial delay and the overall duration. Taken and adapted from Ref. [2].

Figure 10.5 | Overview of the counter model. (A) Schematic illustrating how the duration of an initial delay affects the final system size. Counter model predicts (B) no correlation between the duration of initial delay and the final system size and (C) positive correlation between the duration of initial delay and the overall duration. Taken and adapted from Ref. [2].

10.2.2 Counter Model

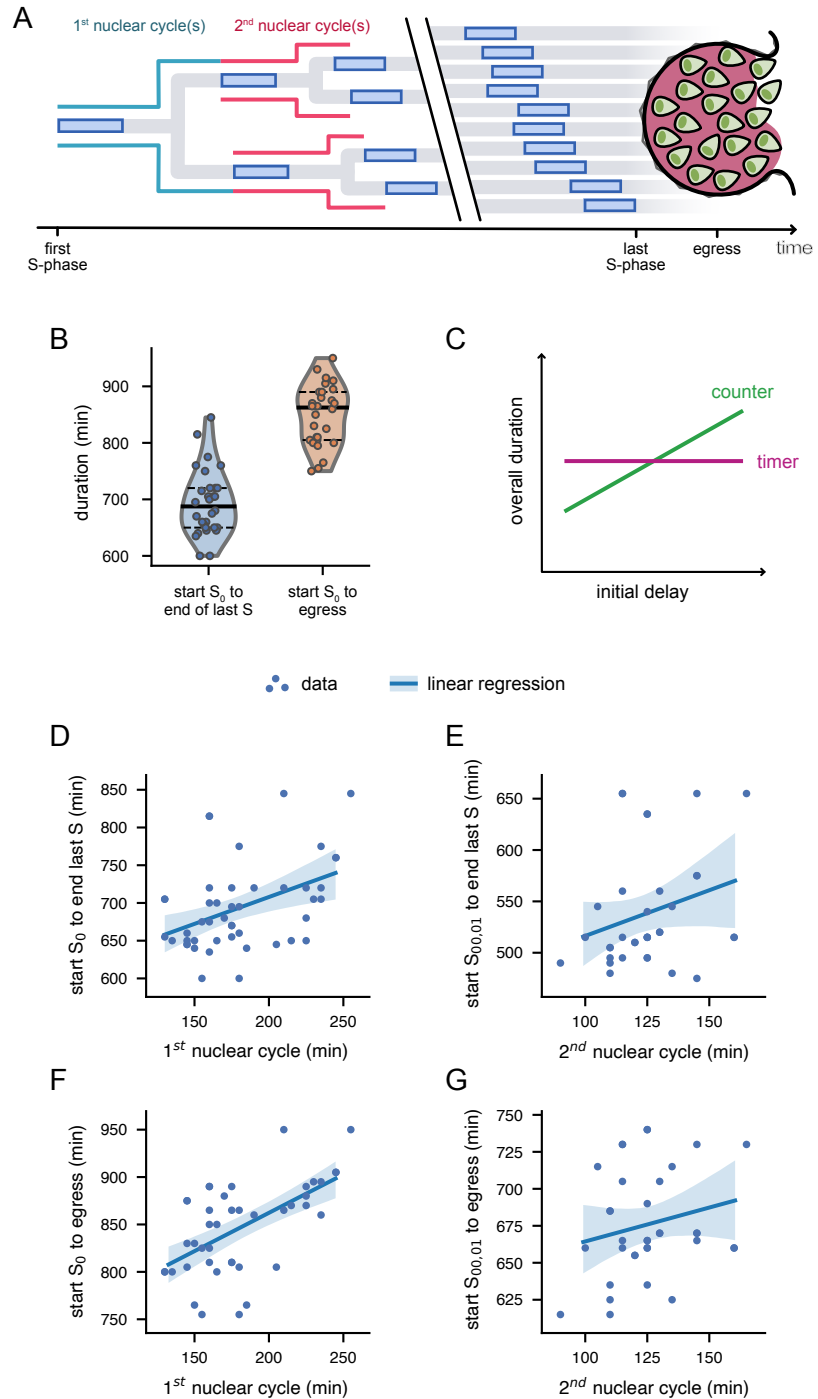
By contrast, the *sizer model* posits that a system must reach a predetermined system size before it is allowed to stop with its growth phase, see Fig. 10.5A. In contrast to the continuous cell size considered in the context of cell proliferation, the system size in the context of nuclear multiplication is represented by the number of nuclei and is therefore discrete. Furthermore, the initial system size in nuclear multiplication of the parasite is well-defined as the process always starts with exactly one nucleus. Therefore, a sizer model can not be distinguished from an adder model, where a system must grow a predetermined amount. To emphasize these differences, the model is referred to in the following as *counter model* rather than sizer model. A counter model predicts that an initial delay, effecting the whole process, is uncorrelated with the final system size, see Fig. 10.5B. Whereas, the initial delay translates into a delayed completion of the number of nuclei, see Fig. 10.5C.

10.2.3 The Parasite Counts its Number of Progeny

Next, to test whether either model can describe the regulation of the number of *P. falciparum* progeny, the model predictions are compared with experimental data. Here, the number of progeny is used as the system size. The overall duration of nuclear multiplication, defined as the duration spanning the start of the first S-phase to the end of last S-phase for each parasite is used to quantify the overall duration. The nuclear cycle, defined as the total time from the start of an S-phase until the start of an ensuing S-phases serves as the initial delay, see Fig. 10.6AB.

The data on the number of progeny and on the first nuclear cycle originate from separate experiments, and therefore no correlation between these

Figure 10.6 | *P. falciparum* is counting its nuclei. (A) Nuclear lineage tree illustrating events of *P. falciparum* proliferation that were quantified in single parasites. S-phases depicted blue; nuclear cycles are defined as the total time from the start of an S-phase until the start of ensuing S-phases. Break indicates events that could not be individually resolved in the experiments. (B) Quantification of key parameters of *P. falciparum* schizogony via long-term time-lapse microscopy; last DNA replication was defined as last detectable nuclear accumulation of PCNA1::GFP; solid lines, median; dashed lines, quartiles. (C) A counter model predicts a positive correlation between the initial delay and the overall duration, whereas a timer model predicts no correlation, cf. Fig. 10.4C and Fig. 10.5C. (D-G) Live-cell imaging data supports a counter model. Solid line, linear regression; band, bootstrapped 95% confidence interval. (D) Time-lapse imaging data showed a positive correlation between duration of first nuclear cycle and total time needed, i.e. time from start S_0 to end of last S-phase ($\rho = 0.42$, $n = 46$, $p = 0.0034$), supporting a counter model and contradicting a timer model; blue solid line and band, linear regression and bootstrapped 95% confidence interval; red solid line, timer prediction; green solid line; counter prediction if all events were synchronous. (E) Correlation of the duration from the start of $S_{0,11}$ to last S-phase with the duration of the second nuclear cycle is consistent with a counter model ($\rho = 0.33$, $n = 35$, $p = 0.054$). (F) Positive correlation of the duration from the start of S_0 to egress, i.e. parasite exit from the host erythrocyte, with the duration of the first nuclear cycle supports a counter model and contradicts a timer model ($\rho = 0.55$, $n = 42$, $p = 1.9 \times 10^{-4}$). (G) Correlation of the duration from the start of $S_{0,01}$ to egress with the duration of the second nuclear cycle is consistent with a counter model ($\rho = 0.23$, $n = 35$, $p = 0.18$). Taken and adapted from Ref. [2].



quantities can be estimated. Subsequently, the correlation between the duration of the first nuclear cycle and the overall duration of nuclear multiplication is considered and compared to the prediction of the counter and timer model, see Fig. 10.6C. By showing a significant positive correlation, the data contradict a timer model and favor the counter model, see Fig. 10.6CD. Using the branching property, the process after the first nuclear cycle can be understood as two subprocesses, each consisting of one daughter nucleus starting at this time with the process. Having this in mind, a similar analysis can be performed by decomposing the process into these two subprocesses, i.e. comparing the duration of the second nuclear cycle with the time, spanning the start of the second

S-phase and the last S-phase. These data also favor a counter model, see Fig. 10.6E. Redoing the analysis by using the time needed from the onset of the first and second S-phase to parasite egress, i.e. parasite exit from the host erythrocyte, respectively, yields the same results, see Fig. 10.6FG.

It should be noted that for the ideal case where an initial event act as a delay for the whole subsequent process, a counter model would predict a linear relation between the duration of the initial event and the overall time with slope one. The reason therefore is that the initial event is part of the overall time. Since for the counter model the remaining time is independent of the initial event, an initial prolonged event results on average in a prolongation of the same amount in the overall completion. For a synchronous branching process, the first nuclear cycle fulfills the requirements of such an initial event. However, the nuclear multiplication in the *P. falciparum* is not synchronized. Therefore, the first cycle measured for either sister cell does not simply delay the completion of the full nuclear multiplication process, as the other branch may partially compensate. As a consequence, using the nuclear cycle as the initial event, a regression slope of less than one should be expected. Indeed, later in Section 10.4, simulating the process as a branching process stopped by a counter model nicely reproduces the experimentally observed slope.

10.3 Nuclear Multiplication as Branching Processes

Due to nuclear crowding, only the first two nuclear cycles could be extracted with confidence from the experiments, cf. Fig. 10.3B-D and Fig. 10.6A. To investigate the unobserved second half of schizogony, the nuclear multiplication is modeled as a branching process in the following. Here, the branching process is inferred from the observed nuclear cycles. By comparing the model prediction of the final number of progeny which experimental data, the question of how the nuclear cycle dynamics behaves in the unobserved second half is addressed. This section focuses on simplistic branching processes, for which a closed-form expression of the mean population size for a given time can be derived, namely the Galton-Watson process and the Bellman-Harris process with exponential lifetimes, as introduced in Chapter 9.

10.3.1 General Setup

Since the nuclear multiplication of the parasites starts with a single nucleus, it is assumed that the branching process starts also with a single nucleus, see Fig. 10.7A. For the sake of simplicity, the nuclear divisions are assumed to occur between subsequent nuclear cycles, even though the actual nuclear division takes place within the nuclear cycle, cf. Fig. 10.3A. By doing so, the lifetime of the nucleus is approximated by the nuclear cycle duration.⁶

There is no experimental evidence that nuclear death or arrest plays a notable role [2]. Therefore, nuclear division is modeled as a pure birth process with binary fission, also known as the *Yule process* [212]. The

6: Strictly speaking, this process corresponds to a multitype process in which each type corresponds to a cell-cycle phase. However, due to its cyclic nature, the lifetime of a particle can be considered as the convolution of the duration of each successive cell cycle phase.

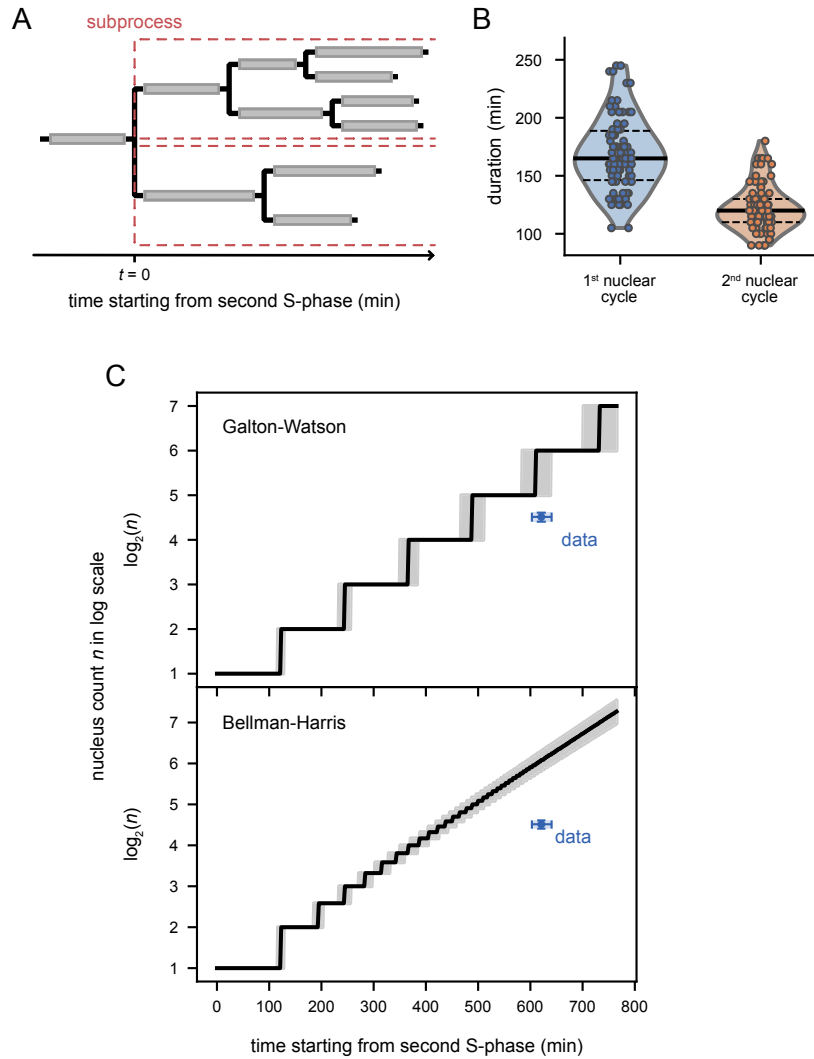


Figure 10.7 | Nuclear replication dynamics initially accelerates and then slows down as nuclear multiplication progress. (A) Schematic illustrating of a branching process with binary fission and a stochastic nucleus lifetime. Here, each gray rectangle indicates a nucleus with a lifetime corresponding to the length of the rectangle. (B) Experimental data show that the nuclear cycle initially speed up; solid lines, median; dashed lines, quartiles. (C) Model prediction of nucleus count as a function of time: Top, Galton-Watson process; bottom, Bellman-Harris process. The prediction of both models clearly overestimates the observed data (blue), predicting a slowdown of the nuclear cycle speed as multiplication progress further.

corresponding probability distribution $(p_k)_{k \geq 0}$ that a nucleus gives birth to k daughter nuclei reads

$$p_k = \begin{cases} 1 & \text{if } k = 2, \\ 0 & \text{otherwise.} \end{cases} \quad (10.1)$$

The corresponding probability generation function of the family size distribution Eq. (9.4) reads $f(s) = s^2$ and the mean family size is $m = 2$. Since the number of daughter nuclei is fully deterministic, all randomness in the nucleus count $Z(t)$ is introduced by the distribution of nucleus lifetimes.

Nuclear Cycle Dynamics Initially Accelerates

Comparing the first and the second nuclear cycle show that there is an initial speed up, see Fig. 10.7B and also Fig. 10.3B-D. Since the first nuclear cycle also marks the transition of the parasite from the feeding stage (trophozoite) to nuclear multiplication (schizont), it is reasonable to assume that the later nuclear cycles are better approximated by the duration of the second nuclear cycle τ_{cycle} . In other words, it is

assumed that all nuclear cycles starting from the second nuclear cycle onwards can be described by the dynamics of the second cycle. To keep the model simple, the initial change in speed is avoided by using the branching property and decomposing the process into two independent subprocesses, each starting with one daughter nucleus at $t = 0$ min, see Fig. 10.7A.

10.3.2 Galton-Watson Process

As a first rough estimate, the nuclear multiplication is modeled with the simplest branching process, the Galton-Watson process. Here, each nucleus live a predefined time τ , whereas the process is often described by using a discrete time index. The deterministic lifetime combined with a pure binary birth process [see Eq. (10.1)], results in a fully deterministic process with $\text{Var}(Z_t) = 0$, see Eq. (9.10). Adding the nucleus counts [see Eq. (9.8)] of both subprocesses, the total nucleus count, corresponding to the predicted number of nuclei at a given time t , reads

$$n_{\text{gw}}(t) = 2^{1+\lfloor t/\tau \rfloor}, \quad (10.2)$$

where the floor function $\lfloor t/\tau \rfloor$ is used to map the continuous time t to the step-like Galton-Watson process.

The nucleus lifetime τ can be estimated by asking what exponential growth rate α corresponds to the observed doubling time defined by the second nuclear cycle durations τ_{cycle} . Here, α corresponds to the Malthusian parameter of the exponential growth $n(t) = e^{\alpha t}$, and the nucleus lifetime is given by $\tau = \ln(2)/\alpha$. Inserting $m = 2$ into Eq. (9.16), α is defined by

$$2 \int_0^{\infty} e^{-\alpha t} dG(t) = 1, \quad (10.3)$$

where $G(t)$ is the cumulative distribution of the lifetime of a nucleus. Solving this equation numerically for α results in $\alpha = 0.0057 \pm 0.0001 \text{ min}^{-1}$ and

$$\tau = 176 \pm 4 \text{ min}. \quad (10.4)$$

Note, since the distribution of τ_{cycle} is relative narrow, τ deviates only slightly from the expectation value of the measured durations, i.e. $\tau \approx \langle \tau_{\text{cycle}} \rangle$.

The last nuclear division in the parasite takes place synchronously as a part of the formation of the daughter parasites and thus differs significantly from the previous ones [180, 184]. In particular, the time between the preceding S-phases and the last nuclear divisions are much longer than during the nuclear multiplication. Therefore, the time $T_{2^{\text{nd}} \text{ to last}}$ starting from the second nuclear cycle to the last S-phase is used as the overall duration. To account for the fact that for the last S-phase the second part of the nuclear cycle is missing, the overall duration is corrected by the term $\tau_{\text{cycle}} - S_{00,01}$, i.e.

$$T = T_{2^{\text{nd}} \text{ to last}} + (\tau_{\text{cycle}} - S_{00,01}) = 617 \pm 10 \text{ min}. \quad (10.5)$$

For a nuclear multiplication with the typical overall duration T , the model predicts the following number of generations:

$$\log_2[n_{\text{cw}}(T)] = 5.53 \pm 0.61. \quad (10.6)$$

Compared to the experimentally observed nuclei count n_{obs} with $\log_2(n_{\text{obs}}) = 4.51 \pm 0.24$, a constant cycling speed starting from the second nuclear cycle has one additional generation, effectively producing twice as much progeny as the data. Another way to put this is that the model reaches the measured number of nuclei faster than expected with a constant cycle speed, see Fig. 10.7C top. Consequently, the cycling speed of the unobserved half of the nuclear multiplication cannot be described by the dynamics of the second cycle, but seems to slow down.

10.3.3 Bellman-Harris Process

By modeling the nuclear multiplication as a Bellman-Harris process with exponential lifetimes with parameter λ , a more accurate estimate is made. The exponential distribution leads to a process with continuous time which can be considered an interpolation of the Galton-Watson process between integer time points. Furthermore, the stochastic nature of the lifetime introduces a dephasing of the individual nuclei. Therefore, the process is better suited to describe the asynchronous nuclear multiplication.

Considering the pure binary birth scenario [see Eq. (10.1)], the expectation value of $Z(t)$ [see Eq. (9.18a)] is given by $\langle Z(t) \rangle = e^{\lambda t}$. Here, the Malthusian parameter of population growth corresponds to λ , i.e. $\alpha = \lambda$. By describing the process as two subprocesses, the number of nuclei reads

$$n_{\text{BH}}(t) = 2 \times \lfloor e^{\alpha t} \rfloor = \lfloor 2^{1+t/\tau} \rfloor. \quad (10.7)$$

Here, the floor function is used, so that the estimate can be better compared to the experimental data.

As for the Galton-Watson process, modeling the nuclear multiplication based on the cycling speed of the second generation [see Eq. (10.4)] results at the typical overall duration [see Eq. (10.5)] in too many nuclei, see Fig. 10.7C bottom, i.e.

$$\log_2[n_{\text{BH}}(T)] = 6.08 \pm 0.49. \quad (10.8)$$

Summing up, both branching process models predict a slowdown of the cycling dynamics in the second half of nuclear multiplication.

It should be noted that the experimentally observed durations of the second nuclear cycles (see Fig. 10.7B) clearly do not follow an exponential distribution. In particular, since the shortest observed duration is 90 min, whereas the exponential distribution admit arbitrarily short lifetimes. However, since a general Bellman-Harris process can asymptotically be described by Eq. (10.7) (see Section 9.2), the equation is nevertheless a reasonable approximation for the nuclear multiplication.

nuclear cycle: parameters	first		second and higher	
	S_0	D_0	$S_{0\dots}$	$D_{0\dots}$
α	8.14	18.77	12.49	25.85
β	0.15	0.15	0.30	0.32
KS test p	0.24	0.033	0.013	0.17

Table 10.1 | Parameters of the gamma distribution used in the branching process models, based on time-lapse microscopy of the initial nuclear cycles. The shape and rate parameter of the gamma distributions, α and β , were estimated by maximizing a log-likelihood function. The KS test is performed as a one-sample test with a two-sided alternative hypothesis.

10.4 Nuclear Multiplication as Biphase Branching Process

Two main results were found in the previous sections. First, the number of progeny is described by a counter model, see Section 10.2. Second, the nuclear cycling speed decreases from the second cycle onwards as the nuclear multiplication progresses, see Section 10.3. In the following, a more detailed branching process is discussed to confirm these findings.

10.4.1 General Setup

The nuclear multiplication is again modeled as a branching process, where nuclei stochastically progress through nuclear cycles. In contrast to the previous section, this time each nuclear cycle resolves two subsequent phases: an S- and a D-phase, see Fig. 10.8AB. The S-phase, which spans the DNA replication, is followed by two parallel D-phases, one for each daughter nucleus. The D-phase describes the duration from the end of the DNA replication of the mother to the start of the replication of the daughter, spanning a nuclear division. By using this more detailed description of the nuclear multiplication, the model can resolve the individual S-phases, whereas the timings of the nuclear divisions can not be resolved.

For the sake of simplicity, it is imposed that each (S- and D-) phase duration is independent of each other. This assumption holds true for adjacent S- and D-phases, as well as D- and next-cycle D-phases which are not significantly correlated, see Fig. 10.8C. But it neglects the observed correlation between S- and subsequent S-phases (Fig. 10.8B) and between S- and D-phases in sister nuclei (Fig. 10.8C, diagonal). However, including these correlations had only a minor effect on the prediction of the model. Therefore, these details are not presented here. A detailed discussion, how these correlations can be integrated into the model, can be found in Section 11.1. In sum, each (S- or D-) phase duration is independently sampled from a gamma distribution with density

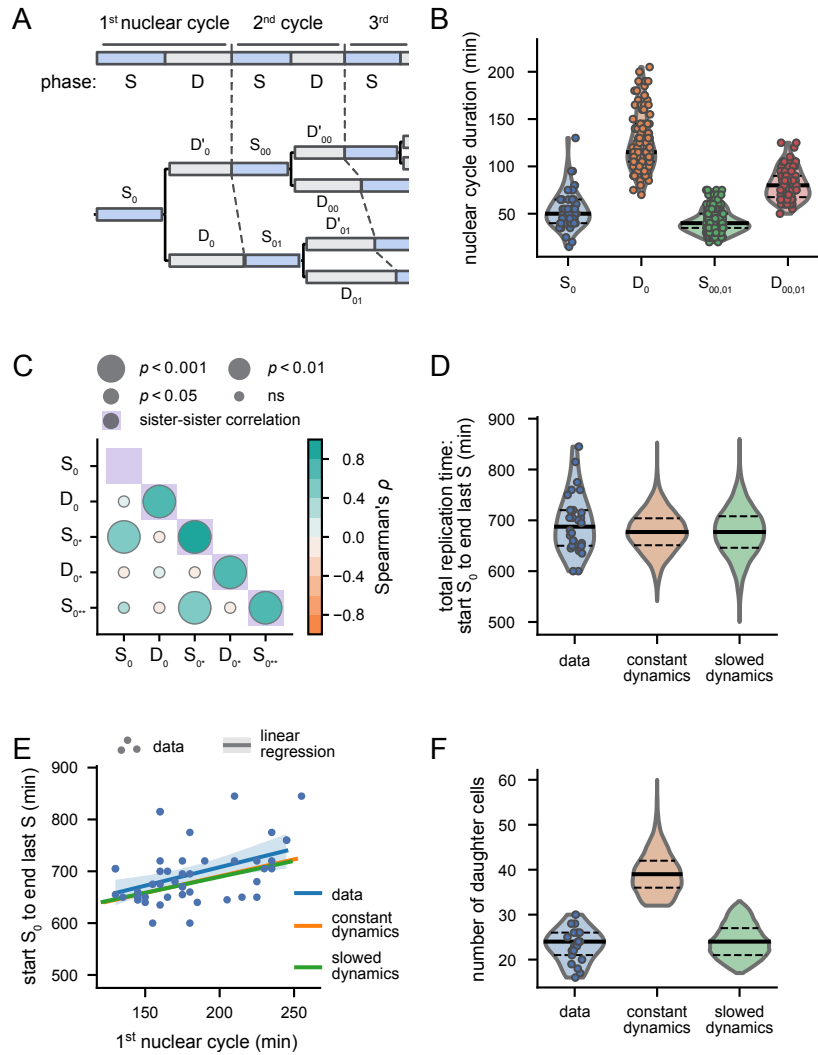
$$p(x; \alpha, \beta) = \beta^\alpha x^{\alpha-1} / \Gamma(\alpha), \quad (10.9)$$

where the shape and rate parameter α and β are parameterized by experimental data. All parameters are summarized in Table 10.1.

A realization of the nuclear branching process is generated as follows. At time $t = 0$ a single nucleus enters S-phase S_0 , with a duration drawn from the corresponding gamma distribution, see Table 10.1. The two subsequent D-phases D_0 and D'_0 are then sampled independently of the

corresponding distribution D_0 , see Table 10.1. For nuclei of all following generations, this procedure is repeated, the only difference being that the durations for S- and D-phases are somewhat faster, see Table 10.1. As a baseline, the hypothesis that all subsequent nuclear cycles share the statistics of the second cycle is again adopted. This constant dynamics approach is used to reproduce the results of the previous Section 10.3, i.e. to show that there must be a slowdown of the cycling speed. Thereafter, in order to quantify the extent of the slowdown, an approach with slowed dynamics is used.

Figure 10.8 | Simulation of *P. falciparum* proliferation predicts a slowdown of the nuclear cycle dynamics at later stage. (A) Scheme of the two-phase branching process model. Generations of nuclei are indicated above the tree; dashed lines connect the onset and conclusion of S-phases within the generations. (B) Experimentally observed S- and D-phase durations, cf. Fig. 10.3B-D. (C) Spearman rank correlation of the S- and D-phases; diagonal, sister-sister correlation. (D) Time needed to complete nuclear multiplication. Measured data were compared to optimized solutions based on our computational model with independent nuclei and a counter mechanism (with constant cycling-speed or 17% slowdown per nuclear cycle, respectively); solid lines, median; dashed lines, quartiles. (E) Simulations of the branching model using a counter stopping criterion with constant cycling-speed or 17% slowdown per nuclear cycle, respectively, reproduce the positive correlation between duration of first nuclear cycle and the interval from the start of S_0 to last S-phase (observed: $\rho = 0.42^{+0.22}_{-0.27}$; constant cycling: $\rho = 0.55$; slowing cycling: $\rho = 0.44$). They also reproduce the slope m of the linear regression (observed: $m = 0.71^{+0.46}_{-0.45}$, constant: $m = 0.65$; slowing: $m = 0.60$). Solid lines, linear regression; shaded bands and square brackets for m, ρ : bootstrapped 95% confidence intervals. (F) Mathematical model with slowing nuclear cycling dynamics (17% per cycle) fitted the experimental data best; solid lines, median; dashed lines, quartiles. Taken and adapted from Ref. [2].



10.4.2 Counter Model

Due to the positive correlation between initial cycle and total replication time, see Fig. 10.6, the stopping of the simulation is implemented as a counter model: After reaching a given number of nuclei n_{stop} , all running DNA replications are completed, but no further replications may be initiated. Thus, the final number of nuclei n is given by

$$n = n_{\text{stop}} + n_s, \quad (10.10)$$

where n_s is the number of running DNA replications, i.e. the number of nuclei in S-phase, at the time n_{stop} nuclei are reached. For example, the stopping criterion for $n_{\text{stop}} = 17$ triggers at the moment when the 16-th S-phase is completed in a nucleus. At this point in time, a certain number of nuclei n_s are currently in S-phase. Because the timing of cycles is stochastic in the model, n_s and therefore also n are random numbers.

To parameterize the stopping condition of our branching process, n_{stop} is adjusted to reproduce the total duration of replication. By simulating 10^4 nuclear multiplications with $n_{\text{stop}} = 32$, both median and interquartile range of the measured total duration of replication were recovered, see Fig. 10.8D. Furthermore, the counter model accurately reproduced the positive correlation and the slope of the linear regression between the first nuclear cycle and the overall time of replication, see Fig. 10.8E.

Interestingly, the way the counter is implemented generates the right amount of variability to reproduce the variance of n , see Fig. 10.8F. Here, this fact is exploited to keep the model minimal. Nonetheless, it should be noted that a more realistic description of a counter mechanism would need to involve a count threshold that is subject to noise. Such a more detailed description will be warranted when more detailed data becomes available in the future.

10.4.3 Predictions for the Total Merozoite Count

With the constant dynamics cycling parameters and $n_{\text{stop}} = 32$ the model predicts a progeny count of $n = 39$ (36, 42) [median (1st, 3rd quartiles)], whereas $n = 24$ (21, 26) were measured, see Fig. 10.8E. As no loss of nuclei that participated in multiplication by time-lapse microscopy was observed, this confirms the previous finding that the simulated third and later nuclear cycles are too fast on average. Overall, the nuclear cycling speed increases from first to second cycle, but then slows down again as nuclear multiplication continues.

Nuclear Dynamics Slows Down as Multiplication Progresses

To estimate the slowdown of the cycling speed after the second cycle, the previous branching model is modified in a parsimonious way by introducing one new parameter, a retardation factor γ . In the modified model, starting from the third nuclear cycle, each S- or D-phase is prolonged by a factor of γ per cycle, i.e. α remains unchanged whereas β is modified as follows

$$\beta_i = \begin{cases} \beta_1 & \text{for the first nuclear cycle } i = 1, \\ \beta_2/\gamma^{i-2} & \text{else,} \end{cases} \quad (10.11)$$

where β_1 and β_2 corresponds to the rate parameter of the first and higher nuclear cycles, respectively, see Table 10.1.⁷ Compared to an alternative model where all nuclear cycles $i \geq 3$ are statistically identical and slower than the second cycle, the gradual slowdown has the advantage of avoiding a step-like change in cycling speed.

Next, the model with the slowed dynamics is re-fitted.⁸ 10^4 simulated schizogonies with $\gamma = 1.17$ and $n_{\text{stop}} = 17$ show that both median

7: For example, the S-phase S_{0000} in cycle $i = 4$ is sampled from a gamma distribution with unchanged $\alpha = 12.49$ but reduced rate parameter $\beta = \beta/\gamma^{i-2} = \beta/\gamma^2$.

8: The optimization is performed by the traditional grid search. Using approximate Bayesian computation (ABC) results in a similar result.

and interquartile range of the total duration of nuclear multiplication (Fig. 10.8D), the final nucleus count n of (Fig. 10.8F), the positive correlation and the slope of the linear regression (Fig. 10.8E) are captured accurately by the branching process with slowdown. To illustrate the effect of $\gamma = 1.17$, the final S-phases in the nuclear cycle $i = 5$ are on average 60% longer than the S-phase in the second nuclear cycle $S_{00,01}$.

10.5 Conclusion

The main findings of this chapter can be summarized as follows. First, the single cell data, that were made possible by a novel PCNA1-based nuclear cycle sensor system, showed that the parasite proliferates through alternating, consecutive rounds of DNA replication and nuclear division. In particular, although nuclei reside in proximity in a shared cytoplasm, DNA replications and nuclear divisions occur asynchronously. Second, confronting the single cell data with two different regulation mechanisms revealed that the number of progeny is governed by a counter mechanism, i.e. the nuclear multiplication is stopped upon reaching a given number of nuclei. Third, the nuclear cycling speed increases initially from the first to second cycle. Finally, adapting branching processes to the single cell data, using a constant cycling speed for later cycles, resulted in an overestimation of the number of progeny and therefore revealed a slowdown of the cycling dynamics in the second half of nuclear multiplication. In summary, the nuclear cycling speed increases from first to second cycle, but then slows down again as nuclear multiplication continues.

What Causes Asynchrony in *Plasmodium falciparum*?

11

This chapter is based on an unpublished manuscript [3], with Section 11.2 based on the collaboration Ref. [2]. All experimental data shown originate from Ref. [2].

11.1 DNA-Replication Antibunching	91
11.2 Nuclei Share a Resource Limiting DNA Replication	95
11.3 Conclusion	96

In the previous Chapter 10, it was shown that the nuclear replication at the blood stage of the parasite *P. falciparum* is asynchronous. This is a surprising finding as the cell cycle of most eukaryotic cells is regulated by diffusible cytoplasmic factors, i.e. one might expect that all nuclei should get the same signals, resulting in a synchronized replication, see Chapter 8. Indeed, many other multinucleated cells, e.g. the early *Drosophila* embryo, have a synchronized nuclear replication [194–197]. This chapter investigates the asynchronous replication of *P. falciparum* and thereby addresses the question of what possible mechanism could introduce this asynchrony.

First, Section 11.1 addresses the question if the asynchrony can be described by the lack of the regulating factors, i.e. by the observed variability and correlations of the nuclear dynamics. Second, Section 11.2 revises the single cell data of the nuclear dynamics, discussed in Chapter 10, to propose a possible mechanism coupling nuclei.

11.1 DNA-Replication Antibunching

In Chapter 10, simple branching processes are used to investigate the dynamics of the unobserved second half of nuclear multiplication. Here, the branching processes inferred an expected number of progeny based on the data of the initial dynamics and the total nuclear multiplication duration. Comparing the inferred number of progeny with data predicts a slowdown of the cycling dynamics. However, although this approach already provides a lot of information about nuclear multiplication, the lack of longitudinal data of the second half of nuclear multiplication prevents a detailed study of asynchrony. Therefore, my collaboration partner Severina Klaus revisited the time-lapse microscopy videos acquired for Ref. [2] and extracted the number of nuclei in S-phase as a function of time. Since for this type of longitudinal data, neither nuclei have to be identified over time, nor do they have to be assigned to the corresponding nuclear lineage tree, the data could be extracted for the whole process of nuclear multiplication.¹

Figure 11.1A shows the longitudinal data of DNA replication, where all nuclear multiplications (each corresponding to a single parasite) are aligned to the end of the first S-phase S_0 . Strikingly, the data exhibit a strong dephasing, i.e. already the S-phases of the third and fourth generations cannot be confidently distinguished anymore. This is in clear contradiction to that in the case of a synchronized nuclear multiplication, where a step-like function describes the longitudinal number of nuclei

1: However, it should be noted that for later stages with many nuclei, it is difficult to distinguish individual nuclei from each other due to nuclear crowding, and thus the measured values at these late stages should be treated with caution.

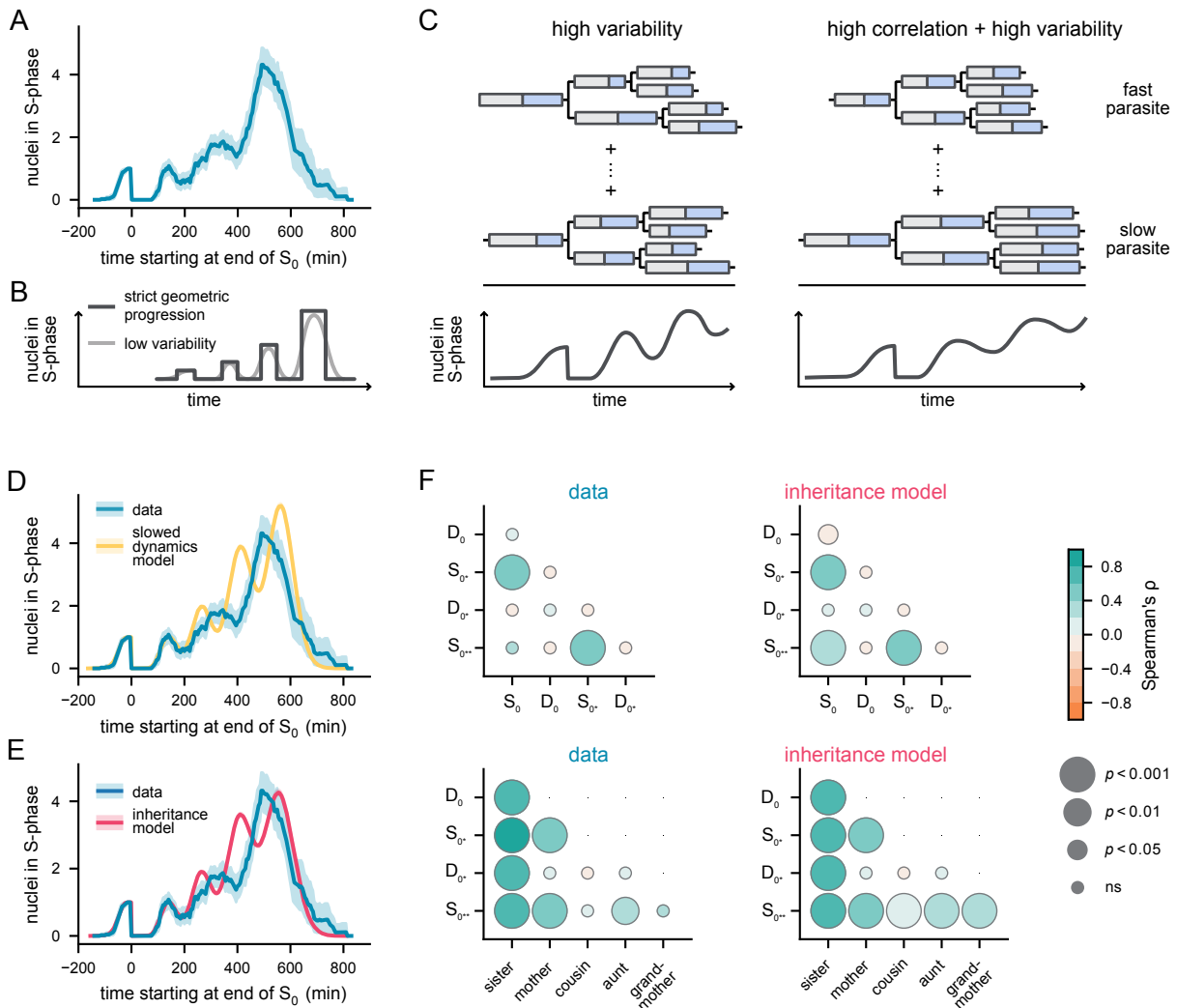


Figure 11.1 | The nuclei of *P. falciparum* are coupled. (A) Experimental data of number of nuclei in S-phase vs. time. Here, the longitudinal data of 49 parasites are aligned with respect to the end of the first S-phase S_0 , respectively. (B) Schematic illustration of a perfectly synchronous nuclear multiplication corresponding to a step-like Galton-Watson process. In addition, the effect of low variability in both phases is illustrated. (C) Schematic illustration of two major mechanisms that could produce dephasing in a branching process: left, high variability in individual phases; right, high variability with positive correlation. (D) The slowed dynamics model can not reproduce the experimentally observed dephasing. Thus, the measured variability of both phases is not sufficient to produce such DNA-replication antibunching. (E) The DNA-replication antibunching can also not be explained by including the mother-daughter and sister correlations. Here, the mother-daughter correlation is modelled by the Pearson correlation between S_0 and $S_{00,01}$ ($\rho = 0.81$), the sister correlation by the correlation between S_{00} and S_{01} ($\rho = 0.44$). (F) The simulated model can reproduce all observed Spearman correlation. In A,D and E: Solid line, mean; band, bootstrapped 95% confidence interval. For both models, 10^4 nuclear multiplications were simulated.

2: Photon antibunching describes the quantum mechanical effect of non-occurrence of temporal correlations of single photons from the same light source and arises as a single-photon emitter can only emit one photon at a time [248–251].

in S-phase, see Fig. 11.1B. In particular, even by adding moderate noise one would expect that the assignment of the individual generations should still be feasible. By contrast, the observed dephasing effectively corresponds to a non-occurrence of temporal correlations of S-phases, i.e. S-phases seem to avoiding each other in time. In analogy to photon antibunching², this effect is subsequently also referred to as DNA-replication antibunching.

Mechanisms for Dephasing

Under the assumption that the nuclei do not interact with each other, two mechanisms could cause S-phase dephasing: a high variability of the

phase durations or a high variability of the phase durations combined with strong correlation. First, high variability in individual phases can lead to overlap in the S-phases of subsequent generations, both within a parasite and between different parasites, see Fig. 11.1C left. Second, combining high variability with mother-daughter and sister correlations may amplify the effect of dephasing. However, one should keep in mind that correlation cannot only promote desynchronization but also synchronization. The S-phase dephasing is the superposition of two different effects: the dephasing within a single parasite and the dephasing between different parasites. A positive mother-daughter and sister-sister correlation effectively correspond to having parasites with different nuclear cycling speeds, see Fig. 11.1C right. Since the dephasing within a single parasite is solely caused by the difference of phase durations of sister nuclei, the positive correlation reduces the dephasing within a single parasite by effectively narrowing the distribution of the random variables. By contrast, having parasites with different nuclear cycling speeds promote desynchronization between different parasites.

Branching Process with Slowed Dynamics

To test whether the variability of S- and D-phases (see Fig. 10.8B) can explain the observed DNA-replication antibunching, nuclear multiplication is first modeled as a branching process without inheritance. Here each nucleus progresses stochastically through its nuclear cycles, comprising two subsequent phases: D- and S-phase. Upon completion of both phases, the nucleus divides into two daughter nuclei each of which progress through both phases anew. To account for the initial speed up from the first to second nuclear cycle, they are drawn from different gamma distribution, see Table 10.1. The overall slowdown for the second half of nuclear multiplication, is accounted for by the addition of a gradual slowdown starting from the third generation onwards. This model corresponds to the so-called *slowed dynamics model* already studied in Section 10.4 and for more details, the reader is referred to that section. By simulating 10^4 nuclear multiplications, the model predicts a much slower dephasing compared to the data, see Fig. 11.1D. Thus, the experimentally observed variability cannot describe the DNA-replication antibunching.

Branching Process with Inheritance

Next, to address whether the DNA-replication antibunching could be caused by the observed mother-daughter and sister correlations in the S-phase durations (see Fig. 10.8C), the slowed dynamics model is modified such that it also captures these correlations. From a mathematical point of view, this question could be rephrased as whether including local two-point correlations can predict the global feature of DNA-replication antibunching.

The correlations can be incorporated into the model using a multivariate Gaussian distribution. For a mean vector $\boldsymbol{\mu}$ and covariance matrix $\boldsymbol{\Sigma}$, the distribution is described by the probability density function

$$p(\mathbf{x}) = \frac{1}{\sqrt{\det(2\pi\boldsymbol{\Sigma})}} \exp\left[-\frac{1}{2}(\mathbf{x} - \boldsymbol{\mu})^\top \boldsymbol{\Sigma}^{-1}(\mathbf{x} - \boldsymbol{\mu})\right]. \quad (11.1)$$

As the branching process is simulated in the forward approach, incorporating the correlations corresponds to the task to draw the daughter S-phase durations dependent on their given mother S-phase duration. To estimate the conditional distribution, the multivariate Gaussian variable \mathbf{x} is partitioned as

$$\mathbf{x} = \begin{bmatrix} \mathbf{x}_1 \\ \mathbf{x}_2 \end{bmatrix}, \quad (11.2)$$

where \mathbf{x}_1 and \mathbf{x}_2 correspond to the daughter and mother durations, respectively. Accordingly, $\boldsymbol{\mu}$ and $\boldsymbol{\Sigma}$ decompose as follows

$$\boldsymbol{\mu} = \begin{bmatrix} \mu_1 \\ \mu_2 \end{bmatrix} \quad \text{and} \quad \boldsymbol{\Sigma} = \begin{bmatrix} \Sigma_{11} & \Sigma_{12} \\ \Sigma_{21} & \Sigma_{22} \end{bmatrix}. \quad (11.3)$$

The distribution of \mathbf{x}_1 conditioned on $\mathbf{x}_2 = \bar{\mathbf{x}}_2$ is again a multivariate Gaussian distribution with adjusted mean $\bar{\boldsymbol{\mu}}$ and adjusted covariance matrix $\bar{\boldsymbol{\Sigma}}$ [252], i.e.

$$\bar{\boldsymbol{\mu}} = \boldsymbol{\mu}_1 + \boldsymbol{\Sigma}_{12}\boldsymbol{\Sigma}_{22}^{-1}(\bar{\mathbf{x}}_2 - \boldsymbol{\mu}_2), \quad (11.4a)$$

$$\bar{\boldsymbol{\Sigma}} = \boldsymbol{\Sigma}_{11} - \boldsymbol{\Sigma}_{12}\boldsymbol{\Sigma}_{22}^{-1}\boldsymbol{\Sigma}_{21}. \quad (11.4b)$$

Since the S-phase distributions are gamma distributed (see Fig. 10.8B and Table 6.1), the multivariate Gaussian distribution cannot be applied directly. How the distribution can nevertheless be used to incorporate inheritance into the branching process is briefly described in the following. First, the mother S-phase duration T_s is transformed to a standard Gaussian variable x_2 , with a nonlinear transformation

$$x_2 = g(T_s) = c_{\text{gauss}}^{-1}[c_{\text{gamma}}(T_s)], \quad (11.5)$$

where c_{gauss} is the cumulative distribution function (CDF) of standard Gaussian distribution, and c_{gamma} introduces the CDF of the corresponding gamma distribution. It should be noted that in the case of nuclear multiplication, \mathbf{x}_1 from Eq. (11.2) describes the two-dimensional standard Gaussian variable corresponding to the daughter S-phase durations and x_2 introduces the one-dimensional standard Gaussian variable corresponding to the mother S-phase duration. Second, using Eq. (11.5) and Eq. (11.4), \mathbf{x}_1 can be drawn from the conditional multivariate Gaussian distribution. Here, the covariance matrix is chosen to match the experimentally observed Pearson correlation coefficient. Specifically, the mother-daughter correlation is modelled by the correlation between the first S-phase duration S_0 and the second-generation S-phase durations $S_{00,01}$. The sister correlation is modelled by the correlation between the second generation S-phase durations S_{00} and S_{01} . Finally, using the inverse transformation g^{-1} , the realization of two-dimensional standard Gaussian variable \mathbf{x}_1 can be transformed back to the corresponding S-phase duration.

It should be noted that the presented model here corresponds to the bifurcating autoregressive (BAR) model proposed by Richard Cowan and Robert Staudte and is frequently used to study cell lineages [253–255].

Incorporating the correlations introduces some additional desynchroniza-

tion, see Fig. 11.1E. In particular, although the model only incorporates the mother-daughter and sister correlations, it can nevertheless explain all other correlation and trends in ancestral lineage (grandmother) as well as first side-branch (cousin and aunt), see Fig. 11.1F. While the model can describe the data very well and the overall effect on the prediction is only minor, it cannot nearly explain the observed DNA-replication antibunching, the model is therefore not further tuned here. Overall, the branching processes with non-interacting nuclei cannot explain the observed DNA-replication antibunching, suggesting that the nuclei are coupled.

11.2 Nuclei Share a Resource Limiting DNA Replication

Since at the blood-stage, the parasite multiplies rapidly, a promising candidate for the coupling of nuclei is a shared limiting resource. In particular, having in mind that the nuclear cycling speed decreases in the later stages of nuclear multiplication, this may indicate that the number of nuclei grows faster than the available resource, which further exacerbates the scarcity. To test for this hypothesis, the experimental data discussed in Chapter 10 are revisited.

If nuclei share a limited resource that is needed for multiplication, then simultaneously multiplying nuclei should experience a stronger limitation than nuclei that multiply sequentially. To test this prediction, pairs of sister nuclei are compared for which the S-phases show a varying degree of temporal overlap, see Fig. 11.2AB. Depending on their temporal overlap, the S-phases are grouped into three categories: *Complete*, both nuclei start and end their S-phase simultaneously within the experimental temporal resolution; *Partial*, nuclei start their S-phase at different time points but still having a temporal overlap, i.e. the second nucleus starts its S-phase before the first nucleus finishes its S-phase; *No*, the S-phases of both nuclei have no temporal overlap, i.e. the first nucleus finishes before the second nucleus starts. The first generation consists only of one nucleus and the data for the third generation are sparse due to the limited resolution of the microscopy, see Fig. 10.3A-D. Therefore, the following analysis is restricted to the grouping of the S-phase of the second generation, where the parasite has two nuclei in total.

While the intervals between S-phases do not differ significantly, see Fig. 11.2CD and also Ref. [2] Fig. S7A-D, partially overlapping S-phases are significantly longer than non-overlapping S-phases, and completely overlapping S-phases are again markedly longer, see Fig. 11.2E. Interestingly, the increased duration of complete overlapping S-phases also translated into a longer nuclear cycle, suggesting that the delay caused by synchronous S-phases cannot be fully compensated, see Fig. 11.2F. By contrast, the partially overlapping S-phases had no effect on the nuclear cycle length. Summing up, the correlation between the S-phase duration with its temporal overlap shows that the nuclei are coupled.

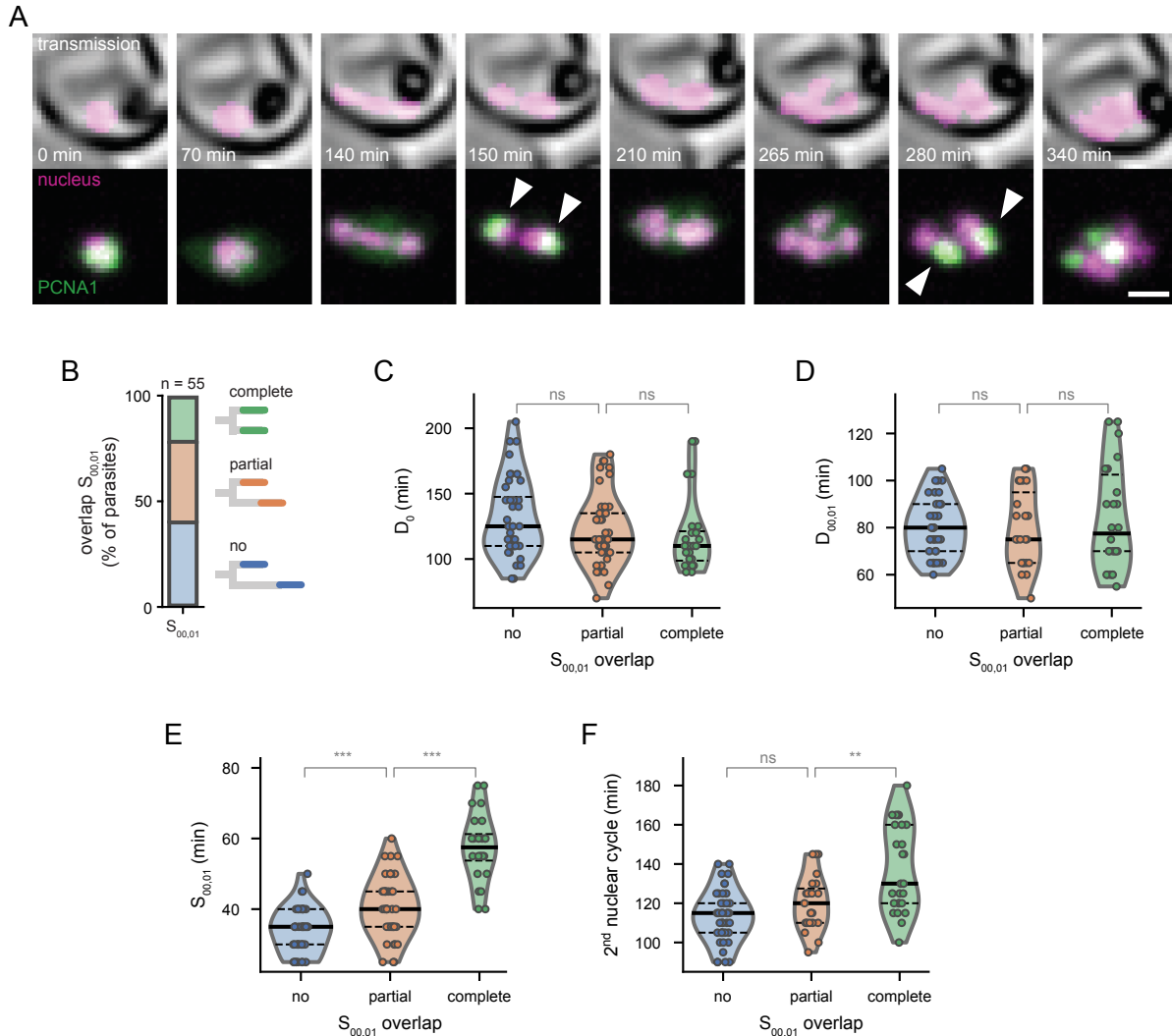


Figure 11.2 | Asynchrony facilitates fast nuclear cycles. (A) Time-lapse microscopy of a parasite with synchronous DNA replication events (arrowheads); scale bar, 2 μm . (B) Fraction of parasites with completely, partially, and not overlapping S_{00} and S_{01} . (C-D) Durations of D-phases are independent of their degree of temporal S-phase overlap. (C) Preceding D-phases D_0 : two-sided Mann-Whitney U test, no versus partial overlap, $f = 0.58$, $n_1 = 40$, $n_2 = 42$, $p = 0.22$; partial versus complete overlap, $f = 0.58$, $n_1 = 42$, $n_2 = 24$, $p = 0.26$. (D) Subsequent D-phases D_{00} and D_{01} : no versus partial overlap, $f = 0.52$, $n_1 = 41$, $n_2 = 23$, $p = 0.78$; partial versus complete overlap, $f = 0.46$, $n_1 = 23$, $n_2 = 26$, $p = 0.68$. (E) Durations of S-phases increased with the degree of temporal overlap; no versus partial overlap, $f = 0.28$, $n_1 = 44$, $n_2 = 42$, $p = 2.7 \times 10^{-4}$; partial versus complete overlap, $f = 0.10$, $n_1 = 42$, $n_2 = 24$, $p = 5.9 \times 10^{-3}$. (F) Nuclear cycles containing synchronous S-phases were longer; no versus partial overlap, $f = 0.36$, $n_1 = 41$, $n_2 = 23$, $p = 0.07$; partial versus complete overlap, $f = 0.27$, $n_1 = 23$, $n_2 = 26$, $p = 0.0067$. ns, not significant; **, $p < 0.01$; ***, $p < 0.001$. Solid lines, median; dashed lines, quartiles. Taken and adapted from Ref. [2].

11.3 Conclusion

Comparing the longitudinal data of replicating nuclei with branching processes reveals that nuclei desynchronize during multiplication more rapidly than expected for non-interacting nuclei. In particular, this result demonstrates that the observed asynchrony during the blood stage in *P. falciparum* is not caused by the lack of regulating factors, but rather actively arises from the coupling of nuclei. The experimental observation that the DNA replication speed of the pair of sister nuclei is correlated with their temporal overlap, i.e. synchronously occurring DNA replications are significantly prolonged, further stresses that nuclei are not independent of each other. Therefore, both findings suggest that the coupling of nuclei is caused by a shared resource. In particular, since only the speed

of DNA replication is affected, and not the D-phase duration between to subsequent S-phases, the coupling of the nuclei might be caused by a shared resource, limiting DNA replication. Overall, although the findings clearly indicate that the nuclei in *P. falciparum* interact through a shared resource that limits DNA replication, the question of exactly which resource we are dealing with remains unanswered and can only be answered by further detailed studies.

Optimal Resource Allocation in Multinucleated Cells

12

This chapter is based on an unpublished manuscript [3]. All experimental data shown originate from the Ref. [2].

In virtually all living organisms [256, 257], such as animals [258], plants [259], fungi [260], parasites [261] and bacteria [29, 262], the distribution of finite amounts of resources plays an important role in optimizing the fitness. The underlying principle in all cases is that the part of resource spent for something that confers no benefit to the organism cannot be spent elsewhere, thereby compromising fitness. For example in the well-studied model organism *Escherichia coli*, the allocation of a finite resource between metabolic network and ribosomes limits the growth rate [262]. In particular, producing proteins that are of no benefit can slow down the growth rate [263]. Another example is that the chemotaxis network of *Escherichia coli* exploits optimal resource allocation [29].

The parasite *P. falciparum* multiplies during the blood stage roughly 20-fold within two days [2, 45–47] despite the limited resource of nutrition of the red blood cell [264, 265]. As this rapid growth demands lots of resources, it is reasonable to assume that optimal resource allocation also plays an important role in *P. falciparum*. Furthermore, the fitness of the parasite can be expected to be largely determined by the final number of produced daughter parasites. Maximizing the fitness then corresponds to finding the optimal time to transition from the feeding stage, in which the resource is already produced, to the nuclear multiplication. Here, the trade is between a late start with enough resource but a short phase of nuclear multiplication, and an early start with a long phase of nuclear multiplication but resource scarcity. Indeed, the observed prolongation of synchronous S-phases together with the observed DNA-replication antibunching suggest that the nuclei of the parasite share a resource that limits DNA replication, see Chapter 11. This chapter is devoted to the resource allocation of replication machinery between nuclei and thus addresses the question of how nuclei are coupled to produce asynchrony, and in what way asynchrony might be beneficial for the parasite.

This chapter begins by introducing a biophysical model to describe allocation of a shared enzyme to individual nuclei, see Section 12.1. Next, Section 12.2 incorporates this model into a branching process. The asymptotic behavior of this resource-limited branching process is investigated in Section 12.3, whereas the scenario of nuclear multiplication is studied in Section 12.4. Finally, Section 12.5 addresses whether the parasite exploits the optimal resource allocation mode.

12.1 Mechanism for Allocation of a Shared Enzymatic Resource . . .	100
12.2 Nuclear Multiplication as Resource-Limited Branching Process . . .	102
12.2.1 Resource-Limited S*-Phase	103
12.2.2 Resource Independent D*-Phase	104
12.2.3 Relation Between Experimental and Model Frame.	105
12.2.4 Lifetime of Active Complex Determines Resource-Sharing Mode	105
12.3 Asymptotic Growth of Resource-Limited Branching Process . . .	106
12.3.1 Analytic Solutions of Simplified Processes . . .	107
12.3.2 Simulations	110
12.3.3 Mean-Field Growth Law	112
12.4 Sequential Resource-Sharing Enables Rapid Nuclear Multiplication	113
12.5 Does <i>P. Falciparum</i> Operate in the Optimal Regime?	115
12.6 Conclusion	116

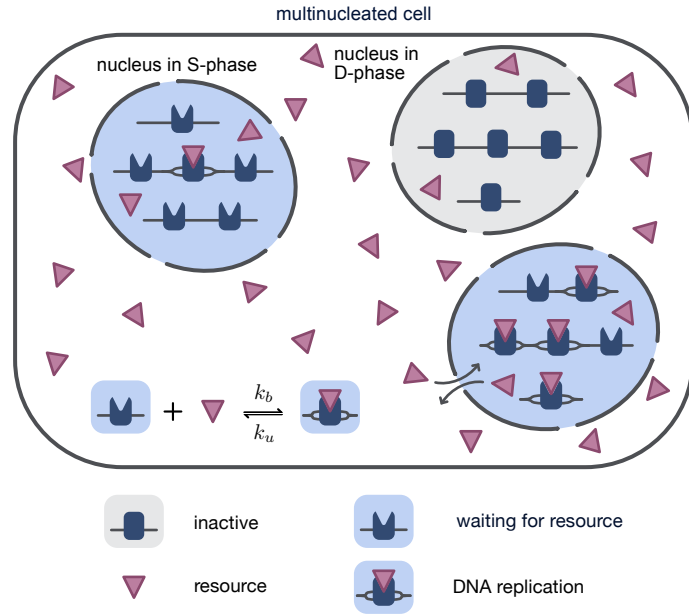


Figure 12.1 | Schematic illustration of resource allocation in a multinucleated cell, where two nuclei are in S-phase (blue), replicating their DNA, and one nucleus is in D-phase (gray). Here, the well-mixed resource can move freely between cytoplasm and nuclei.

12.1 Mechanism for Allocation of a Shared Enzymatic Resource

In the following, a simple mechanistic model for resource allocation is proposed and subsequently discussed mathematically. Despite its simplicity, the model is able to describe both observed effects, the prolongation of synchronous S-phases (see Section 11.2) and the DNA-replication antibunching (see Section 11.1). Since the resource limits DNA replication, it is referred to as replication machinery. As the name suggests, the class of replication machinery comprises factors involved in DNA replication, such as many replication enzymes, e.g. DNA polymerase, DNA helicases, DNA clamps and DNA topoisomerases [52, 266]. For instance, the previously discussed PCNA1 (see Chapter 10), which is used in the nuclear cycle sensor system to visualize the S-phase, is a component of the DNA clamp.

1: The reversible binding corresponds to a catalysis-like resource, as this means that the resource is not consumed during replication.

The enzymatic resource R can reversibly¹ bind to the complex F that replicates DNA in its active state $F^* \equiv RF$, i.e.



where k_b and k_u denote the binding and unbinding rate, respectively. In general, the details of molecular activation depend on the specific limiting resource. In the case of PCNA, F^* corresponds to forming the DNA clamp, which is composed of three molecules of PCNA [239]. However, since no such resource has been identified experimentally so far in the case of *P. falciparum*, the binding model here is kept simple as described in Eq. (12.1). Since replication occurs within the so-called replication fork, F will be referred to as the replication fork in the following. Furthermore, as the molecular details of the limiting resource remain missing, it is assumed that the resource travels diffusively and freely between cytoplasm and nuclei, see Fig. 12.1. Due to a clear timescale separation of the much faster diffusion compared to the duration of a

typical S-phase ($\tau \lesssim 1 \text{ s} \ll 10^3 \text{ s} \approx \langle S \rangle$), the resource can be assumed to be well-mixed.²

Single Nucleus in S-Phase

In the simplest case, a single nucleus is in S-phase. The active complex F^* is then described by the following ordinary differential equation:

$$\frac{dF^*}{dt} = k_b R F - k_u F^* , \quad (12.2)$$

where the concentrations are to be understood as concentrations over the entire parasitic volume V_{parasite} , i.e. $F^{(*)} = F^{(*)}/V_{\text{parasite}}$ and $R = R/V_{\text{parasite}}$. Therefore, upright symbols, such as F and R , denote again species themselves and italic symbols, such as F and R , denote their concentrations. By imposing conservation of possible replication forks³

$$F_{\text{tot}} = F + F^* , \quad (12.3)$$

and by expressing the part of unbound resource through the difference of the total amount of resource R_{tot} and the already bound resource, i.e. $R = R_{\text{tot}} - F^*$, Eq. (12.2) can be rewritten to

$$\frac{dF^*}{dt} = k_b (R_{\text{tot}} - F^*) (F_{\text{tot}} - F^*) - k_u F^* . \quad (12.4)$$

Here, it should be noted that Eq. (12.4) is similar to the ordinary differential equation for allosteric receptors [see Eq. (4.3)], i.e. the resource and the replication fork correspond to the ligand and the receptor. However, since the resource R is limiting here, the excess assumption (made for the ligand receptor binding) cannot be applied, i.e. $R_{\text{tot}} - F^*$ cannot be approximated by R_{tot} .

As all nuclei are identical, it is assumed that they all have the same number of possible replication forks F_{tot} . Accordingly, it is sufficient to consider the fraction of active complexes $f = F^*/F_{\text{tot}}$, i.e.

$$\frac{df}{dt} = k_b F_{\text{tot}} (r_{\text{tot}} - f)(1 - f) - k_u f , \quad (12.5)$$

where $r_{\text{tot}} = R_{\text{tot}}/F_{\text{tot}}$ introduces a dimensionless resource and $r_{\text{tot}} = 1$ corresponds to a 1:1 stoichiometry of R_{tot} and F_{tot} . The system is described by two timescales. On the one hand by the unbinding timescale $\tau_u = 1/k_u$. On the other hand by the binding timescale τ_b . In the regime of high affinity and resource abundance, the binding timescale can be approximated by (for further details see Appendix G)

$$\tau_b \approx \frac{\ln(2)}{k_b F_{\text{tot}} r_{\text{tot}}} . \quad (12.6)$$

The steady state fraction of active replication forks f_{eq} reads

$$f_{\text{eq}} = \rho - \sqrt{\rho^2 - r_{\text{tot}}} , \quad (12.7)$$

2: The timescale τ of diffusion, meaning the time for a resource R to transverse distance r is described by [267]

$$\tau = \frac{r^2}{6D} ,$$

where D denotes the diffusion coefficient. By using a typical diffusion coefficient for a protein in cytoplasm $D = 10 \mu\text{m}^2\text{s}^{-1}$ and a typical distance of $r = 5 \mu\text{m}$, the timescale is given by $\tau = 400 \text{ ms}$.

3: The replication of DNA is initiated at certain sequences in the genome, the so-called origin of replication (ORI). As two replication forks start from each ORI, one in each direction, F_{tot} corresponds to twice the number of ORI.

where the auxiliary parameter ρ is defined as

$$\rho = \frac{1}{2} \left(1 + r_{\text{tot}} + \frac{k_u}{k_b F_{\text{tot}}} \right). \quad (12.8)$$

Hence, f_{eq} solely depends on the dimensionless resource r_{tot} and the effective equilibrium dissociation constant $k_u/(k_b F_{\text{tot}})$.

Multiple Nuclei in S-phase

In general, as shown in Fig. 12.1, more than one nucleus can be in S-phase at the same time. By generalizing Eq. (12.5) to the multinucleated state with n_s nuclei in S-phase, the fraction of active complexes f_i^* of the i -th nucleus is described by⁴

$$\frac{df_i}{dt} = k_b F_{\text{tot}} \left(r_{\text{tot}} - \sum_{j=1}^{n_s} f_j \right) (1 - f_i) - k_u f_i. \quad (12.9)$$

Here, the nuclei are now no longer independent of each other, instead they are coupled through the shared resource. Vividly, this means that any resource used by one nucleus cannot be used by another nucleus at that time. Due to symmetry (all nuclei are identical), the steady state fraction of active complexes for all nuclei must be equal, i.e. $f_{\text{eq},i} = f_{\text{eq},j}$ for all $i = 1, \dots, n_s$ and $j = 1, \dots, n_s$. Using this symmetry, estimating the steady state of Eq. (12.9) yields

$$f_{\text{eq},i} = \rho_{n_s} - \sqrt{\rho_{n_s}^2 - r_{\text{tot}}/n_s} \quad (12.10)$$

with

$$\rho_{n_s} = \frac{1}{2} \left[1 + \frac{r_{\text{tot}} + k_u/(k_b F_{\text{tot}})}{n_s} \right]. \quad (12.11)$$

As expected, $f_{\text{eq},i}$ corresponds to the solution for a single nucleus f_{eq} [see Eq. (12.7)] with increased total concentration of available complexes $F_{\text{tot}} \rightarrow n_s F_{\text{tot}}$ and decreased (since equally shared) resource $r_{\text{tot}} \rightarrow r_{\text{tot}}/n_s$.

12.2 Nuclear Multiplication as Resource-Limited Branching Process

In order to model the nuclear multiplication with a shared resource, the previously discussed resource allocation model is incorporated into a branching process in which each nucleus progress through its nuclear cycle. Here, similar to Section 10.4 and 11.1, each nuclear cycle is composed of two subsequent phases, i.e. D*- and S*-phase, see Fig. 12.2AB. As nuclei share a resource that limits DNA replication (see Chapter 11 and Section 12.1), the S*-phase depends on the resource whereas the D*-phase is resource independent. In particular, in contrast to the previously discussed branching processes (Section 10.4 and 11.1), here the shared resource couples the nuclei with each other, see Fig. 12.2C. The phases of the model do not correspond one-to-one to the experimentally observed

4: As all nuclei are identical they all share the same total number of complexes and the same binding and unbinding rate, i.e.

$$\begin{aligned} F_{\text{tot},i} &= F_{\text{tot}}, \\ k_{u,i} &= k_u, \\ k_{b,i} &= k_b. \end{aligned}$$

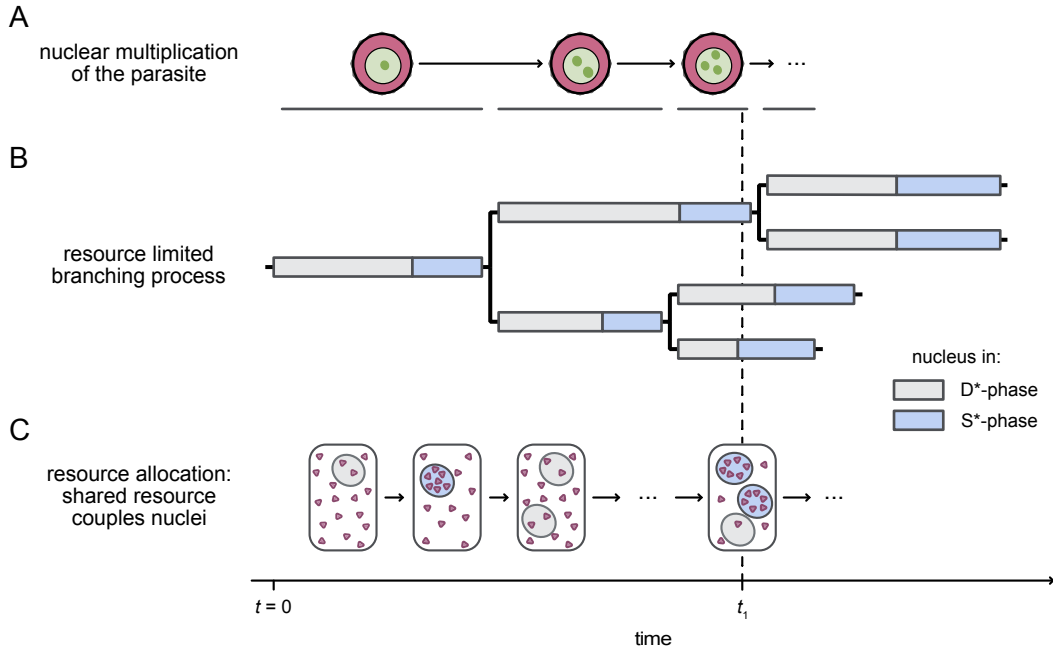


Figure 12.2 | Overview of the resource-dependent branching process with its resource allocation. (A) Schematic illustration of nuclear multiplication of the parasite. (B) Schematic illustration of the corresponding lineage tree resulting from the resource-dependent branching process. (C) Schematic illustration of resource allocation in a multinucleated cell, where two nuclei (blue) are replicating their DNA and one nucleus is in the D-phase (gray). Here, the well-mixed resource can move freely between cytoplasm and nuclei.

S- and D-phases, they are therefore annotated in the following with an asterisk. For a discussion of their differences see Subsection 12.2.3.

12.2.1 Resource-Limited S*-Phase

To keep the model simple, the progress of the S*-phase is limited by the shared resource in the sense that the progression speed depends linearly on the number of actively replicating complexes F^* . The completion of the S*-phase of the i -th of n_s nuclei $s_i \in [0, 1]$ is then described by⁵

$$\frac{ds_i}{dt} = \frac{v_{F^*}}{g} F_i^*, \quad (12.12)$$

where g introduces the length of the genome and v_{F^*} the replication speed of a single replicating complex. Here, $s = 0$ corresponds to the case that the nucleus has not started yet duplicating its DNA, and $s = 1$ corresponds to the end of S-phase where the nucleus has two copies of its DNA. After completion of DNA replication ($s = 1$), the nucleus releases all resource ($f_i = 0$) and gives birth to two daughter nuclei, each starting at its D*-phase. As each nucleus is identical, each nucleus has the same total number of complexes F_{tot} and Eq. (12.12) can be rewritten in terms of the fraction of active complexes $f_i = F_i^*/F_{\text{tot}}$ as

$$\frac{ds_i}{dt} = v_{s,\text{max}} f_i, \quad (12.13)$$

where $v_{s,\text{max}} = F_{\text{tot}} v_{F^*} / g$ defines the maximal progression speed in S-phase, corresponding to the case of full activation $f_i = 1$. The minimal S-phase duration is therefore given by $T_{s,\text{min}} = 1/v_{s,\text{max}}$. Taking the derivative of Eq. (12.13) and inserting the resource allocation model

5: Note that the reason for choosing a linear dependency in Eq. (12.12) is that it is the simplest choice that can explain the experimentally observed correlation between temporal overlap and DNA replication time, i.e. synchronous S-phases are approximately twice as long as sequential S-phases, see Section 11.2.

Eq. (12.9) yields

$$\begin{aligned} \frac{d^2 s_i}{dt^2} &= v_{s,\max} \frac{df_i}{dt}, \\ &= v_{s,\max} \left[k_b F_{\text{tot}} \left(r_{\text{tot}} - \sum_{j=1}^{n_s} f_j \right) (1 - f_i) - k_u f_i \right]. \end{aligned} \quad (12.14)$$

Let the number of nuclei in S-phase be $n_s = 2$ and the amount of resource $r_{\text{tot}} = 1$, i.e. exactly as much resource as required to replicate one nucleus at maximum speed. In the regime of high affinity, i.e. $\sum_i f_{\text{eq},i} \approx r_{\text{tot}} = 1$, equally sharing the resource results in replication at half of the maximal speed, i.e. $f_i \approx 1/2$ for $i = 1, 2$, effectively doubling their S*-phase duration. By contrast, in the case of sequential DNA replication, each nucleus replicate sequentially but with full speed ($f_i = 1, f_j = 0$ with $i, j \in (1, 2), (2, 1)$). Overall, the model can reproduce the observed prolongation of synchronous events.

12.2.2 Resource Independent D*-Phase

In contrast to the S*-phase, the D*-phase is assumed to be independent of the resource. In particular this means that nuclei are solely coupled with each other during their S*-phase, but not during their D*-phase. To break the symmetry between both daughter nuclei and to introduce some noise into the model, the D*-phase duration is assumed to be gamma distributed, i.e. $D^* \sim \Gamma(\alpha, \beta)$, where α denotes the shape parameter and β the rate parameter. The corresponding probability density function for the outcome T_d reads

$$p(T_d; \alpha, \beta) = \frac{\beta^\alpha}{\Gamma(\alpha)} T_d^{\alpha-1} e^{-\beta T_d}. \quad (12.15)$$

In the following of this chapter, the gamma distribution is parametrized by its mean value and its coefficient of variation c_v , which is defined as the ratio of the standard deviation to the mean. By using $\langle D^* \rangle = \alpha/\beta$ and $\text{Var}(D^*) = \alpha/\beta^2$, the shape and rate parameter can be rewritten as

$$\alpha = \frac{1}{c_v^2}, \quad (12.16a)$$

$$\beta = \frac{1}{\langle D^* \rangle c_v^2}. \quad (12.16b)$$

Combining all together, realizations of the resource-limited branching process are generated as follows. The process starts with a nucleus in D*-phase, drawn from the gamma distribution Eq. (12.15). Upon completion of this phase, the nucleus proceeds to the S*-phase for which the replication speed depends on the resource available. Here, the S*-phase progression [see Eq. (12.14)] is solved numerically. After completing both phases, the nucleus gives birth to two new nuclei starting again in the D*-phase. For simplicity, no distinction is made between first and second generation, as the focus here is only on understanding the resource-limited branching process.

12.2.3 Relation Between Experimental S- and D-Phase and Model S*- and D*-Phase

Next, the differences between the two phases of the model, S* and D*, and the experimentally observed phases, S and D, are discussed and demonstrated how the former are linked to the latter.

The experimentally observed S-phase is defined as the duration of PCNA1 accumulation within the nucleus, which coincides with its DNA replication. By contrast, the model predicts that if no free resource is available (for example in case when the resource is already used by other nuclei), a nucleus will still enter the S*-phase after completing its D*-phase, even though the nucleus must wait until resource becomes available to replicate its DNA. This means that while in the model this waiting time is considered to be part of the S*-phase, in the experimental framework this duration would be considered to be part of the preceding D-phase, and not the S-phase. Hence, to transform from the model to the experimental framework, a threshold activation $f_{thr} \ll 1$ can be introduced, below which a nucleus is considered to be still in D-phase and above which it is considered to be in S-phase. In particular this means, that although the D*-phase is resource independent, the corresponding transformed duration of the D-phase depends on the resource. In other words, in the resource scarcity regime, the proposed resource-limited branching process can not only describe the prolongation of S-phase, but also the delay of S-phase initiation.

It should be noted, that the capability of the model to delay S-phase initiation is crucial to reproduce active desynchronization. This is particularly important since the observed DNA-replication antibunching (see Fig. 11.1), i.e. the nuclei desynchronize more rapidly than expected for independent nuclei, is mainly introduced due to different S-phase initiation of sister nuclei, see Fig. 10.3E.

12.2.4 Lifetime of Active Complex Determines Resource-Sharing Mode

Next, the proposed resource-limited branching process is investigated. To arrive at definite results, both the binding and the unbinding timescales must be chosen. In the live-cell microscopy data, the accumulation of PCNA1 was faster than the time resolution of five minutes. Therefore, the binding time is assumed to be fast. Regarding the unbinding timescale, early experiments have shown that the replisome, the complex molecular machine that carries out DNA replication, is highly stable [268–271]. However, more recent studies revealed that for example the polymerases associated with the replisome can have a short lifetime of only tens of seconds to minutes [272–277]. Therefore, different lifetimes for the active complex are considered, ranging from much shorter to much longer than a typical S*-phase duration.

Within the first generation, in the high affinity regime, the lifetime has no effect on the nuclear lineage trees, see Fig. 12.3A. In the second generation, however, the broken symmetry between sister nuclei causes one of the two nuclei to start S*-phase slightly earlier. As the timescale for binding was chosen to be shorter than the mean difference of the two D*-phases,

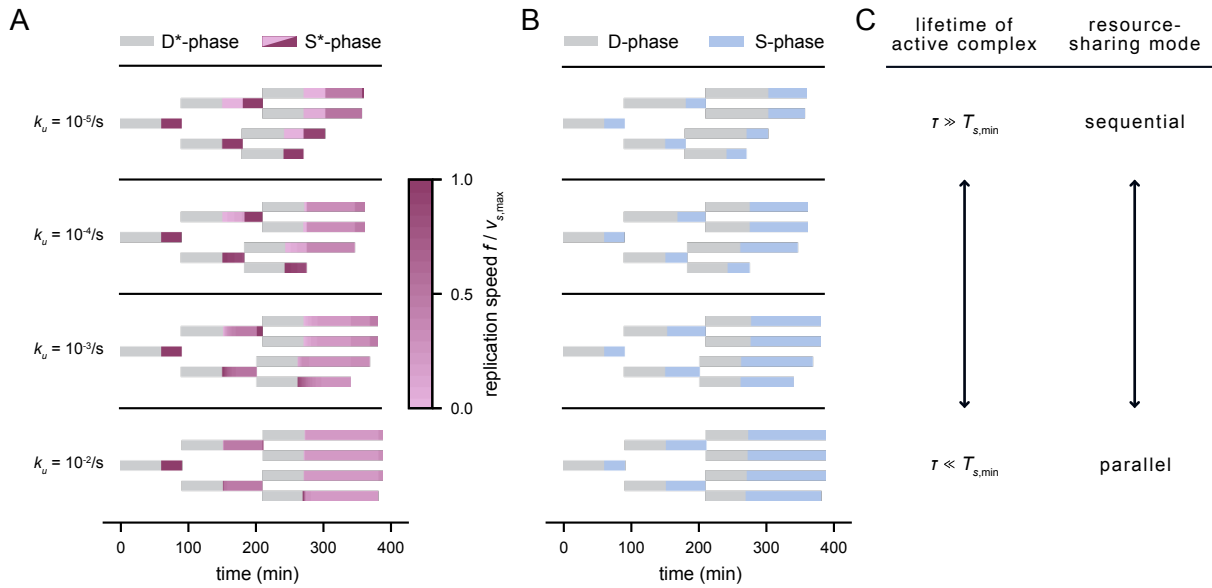


Figure 12.3 | Lifetime of active complex determines the resource-sharing mode. (A) Simulated nuclear lineage trees of the resource-limited branching process with different unbinding rates k_u . Here, the following parameter were used: $r_{tot} = 1$, $k_b F_{tot} = 100 \text{ s}^{-1}$, $c_v = 1\%$, $\langle T_d \rangle = 2T_{s,min}$ and $T_{s,min} = 30 \text{ min}$. (B) Corresponding nuclear lineage trees from A transformed to the experimental frame. Here, the activation threshold for transformation from D*- and S*-phase to D- and S-phase is set to $f_{thr} = 0.1$. (C) Schematic representation of the relationship between the lifetime of the active complex and the resulting type of resource sharing.

by the time the S*-phase of the second nucleus starts, (almost) all resource is already bound.

For lifetimes much longer than a typical S*-phase duration, this results in the nucleus, although entering S*-phase, having to wait with DNA replication until the resource is released from the first nucleus after completion of its DNA replication, see Fig. 12.3A first row. Effectively, this results in a sequential like resource-sharing mode, see Fig. 12.3B first row. Reducing the lifetime, results in faster equilibration between both nuclei. Therefore, decreasing the lifetime eventually results in a regime of relatively fast redistribution of resource, corresponding to a parallel resource-sharing mode, see Fig. 12.3AB bottom row. Note that the time at which both S-phases are finished is the same in all four cases, namely after $2T_{s,min}$.

Overall, the lifetime of the active complex determines the resource-sharing mode of the resource-limited branching process. Long-lived complexes lead to sequential resource allocation, and thus actively introduces asynchrony, whereas short-lived complexes lead to parallel resource allocation, see Fig. 12.3C.

12.3 Asymptotic Growth of Resource-Limited Branching Process

In the previous Section 12.2, it was shown that a sequential resource-sharing mode can actively introduce asynchrony, supporting the notion that the observed DNA-replication antibunching of the parasite could be caused by such a mechanism. However, a detailed understanding of how this sharing mode might be beneficial remains lacking. Next,

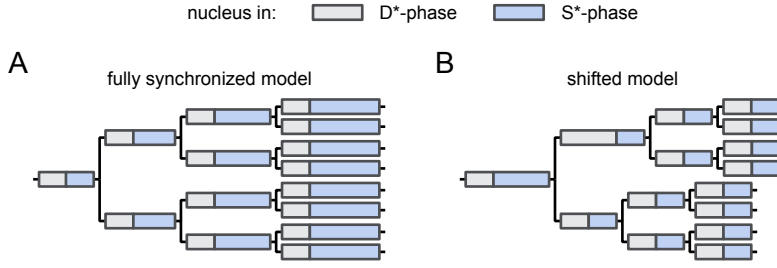


Figure 12.4 | Schematic illustration of nuclear lineage trees corresponding to (A) fully synchronized and (B) shifted toy models.

to address this open question, the asymptotic growth rate of resource-limited branching processes involving different resource allocation modes are studied.

12.3.1 Analytic Solutions of Simplified Processes

As the resource-limited branching process does not have a straightforward closed-form growth rate, in the following two simplified deterministic toy models, which nevertheless capture important properties of the more general process, are considered.

In the so-called *fully synchronized model*, it is assumed that the D*-phase is deterministic ($c_v \rightarrow 0$), and that the resource is shared equally, resulting in a step-like branching process, see Fig. 12.4A. The number of nuclei then follows a strict geometric sequence 2^k , where $k \geq 0$. In other words, the fully synchronized model is a simplified version of the resource-limited branching process with a parallel resource-sharing mode, in which the variability of the D*-phase is neglected.

The other toy model, referred to as *shifted model*, comprises two subprocesses shifted by one S*-phase duration. Here each subprocess corresponds to a fully synchronized process, see Fig. 12.4B. This process could be seen as a simplified version of a resource-limited branching process with sequential resource-sharing mode, where due to a lack of resource ($r_{\text{tot}} \leq 1$) in the second generation the second nucleus has to wait with its S*-phase until the first one has finished. The assumption that the resulting subprocesses do not dephase further corresponds to that of neglecting the variability of the D*-phase (and thus the symmetry breaking) starting from the second generation, which leads to two synchronous subprocess.

As both toy models grow exponentially, the Malthusian parameter α is used to describe their asymptotic growth rate. Using Eq. (9.16) with binary fission ($m = 2$), α is defined by the root of the equation

$$2 \int_0^{\infty} e^{-\alpha t} p(t) dt = 1, \quad (12.17)$$

where $p(t)$ describes the distribution of lifetime. In the case of both toy models, the lifetime of a nucleus is given by the duration of both phases, i.e.

$$T_{\text{tot}} = T_d + T_s, \quad (12.18)$$

where T_d and T_s describe the duration for a D*- and S*-phase, respectively. To allow a straightforward closed-form growth rate, both toy models are deterministic, i.e. they operate at the high affinity and instantaneous equilibration limit. Therefore, T_{tot} is deterministic and the distribution of lifetime reads $p(t) = \delta(t - T_{\text{tot}})$. Using this distribution, Eq. (12.17) yields

$$\alpha = \frac{\ln(2)}{T_{\text{tot}}} . \quad (12.19)$$

To arrive at finite growth rates in the case of the two toy models, the growth⁶ of the resource needs to be specified. For the sake of simplicity, it is assumed that the resource grows with the number of nuclei n , i.e.

$$r_{\text{tot}} = \zeta n , \quad (12.20)$$

where ζ introduces a scarcity factor. Since for $\zeta > 1$ there is always more resource available than can be used effectively, the range of interest is $\zeta \in (0, 1]$.

Furthermore, as a quantitative measure of resource utilization enables a better understanding of the growth rate, the resource utilization factor η is introduced, i.e.

$$\eta = \frac{\text{bound resource}}{\text{total resource}} = \frac{\sum_i f_i}{r_{\text{tot}}} . \quad (12.21)$$

Here, $\eta = 0$ ($\eta = 1$) means that the complete resource is currently (un-)used.

Fully Synchronized Model

In the fully synchronized model, in the regime of resource scarcity, all resource is bound during the S*-phase, and free during D*-phase. Therefore, the mean utilization factor reads

$$\eta_{\text{sync}} = \frac{T_s}{T_{\text{tot}}} . \quad (12.22)$$

By using η_{sync} , the asymptotic growth rate [see Eq. (12.19)] can be rewritten as

$$\alpha_{\text{sync}} = \frac{\ln(2) \eta_{\text{sync}}}{T_s} . \quad (12.23)$$

Since the resource grows with the system size n , each generation experiences the same resource shortage, resulting in the same activation $f = \zeta$. By using the fact that the duration of the S*-phase for a constant activation f reads $T_s = T_{s,\text{min}}/f$, see Eq. (12.13), the asymptotic growth rate reads

$$\alpha_{\text{sync}} = \frac{\ln(2) \zeta \eta_{\text{sync}}}{T_{s,\text{min}}} \propto \eta_{\text{sync}} . \quad (12.24)$$

Thus, for the fully synchronized model, the α_{sync} solely depends on the scarcity factor, the minimal S*-phase duration and the utilization factor. By introducing χ as the ratio of the S*-phase and D*-phase in

6: Here, a growing resource is assumed, since in the case of a constant resource, the asymptotic growth rate vanishes, as more and more nuclei have to share the same amount of resource.

resource abundance, i.e. $\chi = T_{s,\min}/T_d$, the resource utilization factor [see Eq. (12.22)] can be rewritten as

$$\eta_{\text{sync}} = \frac{1}{1 + \zeta/\chi} \leq 1. \quad (12.25)$$

Shifted Model

In the shifted model, the resource is used only by half of the current population, effectively corresponding to a doubling of resource available for each nucleus. Consequently, the relative replication speed is doubled for $\zeta \leq 1/2$ and maximal for $\zeta \geq 1/2$, i.e. $f = \zeta_{\text{eff}} \equiv \min(2\zeta, 1)$. During the lifetime of one nucleus, both subtrees complete their S^* , therefore the resource mean utilization factor is given by

$$\eta_{\text{shifted}} = \frac{2T_s}{T_{\text{tot}}} = \frac{2T_{s,\min}}{\zeta_{\text{eff}}T_{\text{tot}}}. \quad (12.26)$$

Here, for the sake of simplicity, it was assumed that the resource grows after each generation and not in between, i.e. it is assumed that the corresponding S^* -phases of both subtrees suffer the same amount of resource scarcity. Furthermore, it should be noted that for the shifted model, the regime of resource scarcity starts for $\zeta \leq 1/2$. In other words, for $\zeta \geq 1/2$, the growth rate is that of the unconstrained process with $T_{\text{tot},\min} = T_{s,\min} + T_d$. For $\zeta \leq 1/2$, i.e. the effective scarcity factor simplifies to $\zeta_{\text{eff}} = 2\zeta$, combining Eq. (12.13) and Eq. (12.26) yields

$$\alpha_{\text{shifted}} = \frac{\ln(2)\zeta\eta_{\text{shifted}}}{T_{s,\min}}, \quad (12.27)$$

where it was assumed that the two subprocesses do not overlap ($T_s \leq T_d \rightarrow \chi \leq \zeta$) and the resource utilization factor reads

$$\eta_{\text{shifted}} = \frac{2}{1 + 2\zeta/\chi}. \quad (12.28)$$

Perfectly Shifted Model Uses the Resource More Efficiently

In the resource scarcity regime, comparing the growth rates of the two toy models Eq. (12.24) and Eq. (12.27) shows that the difference in their growth rate is solely due to their difference in resource utilization, i.e.

$$\frac{\alpha_{\text{shifted}}}{\alpha_{\text{sync}}} = \frac{\eta_{\text{shifted}}}{\eta_{\text{sync}}} = \frac{\zeta + \chi}{\zeta + \chi/2} > 1, \quad (12.29)$$

where again $\chi \leq 1/2$ and $T_s \leq T_d$ were assumed. It should be noted that since α are exponential growth rates, even a small difference in α eventually results in an arbitrarily large difference in the population sizes. To illustrate this, the ratio of the two corresponding population sizes is considered, i.e.

$$\frac{n_{\text{shifted}}(t)}{n_{\text{sync}}(t)} = 2^{\zeta\Delta\eta t/T_{s,\min}}, \quad (12.30)$$

where $\Delta\eta = \eta_{\text{shifted}} - \eta_{\text{sync}}$. In other words, the time τ until the shifted model doubles relatively to the fully synchronized model reads $\tau =$

$T_{s,\min}/(\zeta\Delta\eta)$. For $\zeta = 1/2$ and $\chi = 1$, this corresponds to $\tau = 6T_{s,\min}$. Overall, the shifted model makes better use of the available resources than the fully synchronized model, which results in a faster growth. In particular, the two simple toy models demonstrate that a better resource utilization results in faster growth.

12.3.2 Simulations

Next, by simulating the full resource-limited branching process (see Section 12.2), it is investigated to what extent the results of the two toy models transfers to the more general resource-limited branching process. Accordingly, as for the two toy models, a self-supplied resource—growing linearly with the number of nuclei [see Eq. (12.20)]—is assumed.

First, a scarcity factor of $\zeta = 1/2$ is considered with a one-to-one ratio of T_d and $T_{s,\min}$, i.e. $\chi = 1$. In the regime of low D^* -phase variability ($c_v = 1\%$), the simulated branching process with parallel resource allocation reproduces the fully synchronized model, both the nuclear lineage tree (cf. Fig. 12.4 and Fig. 12.5A1) and the step-like increase in population size, corresponding to the mean-field population size of the fully synchronized model, see Fig. 12.5B1. Note that as expected, the resource scarcity ($\zeta = 1/2$ results in $f \approx 1/2$) leads to a doubling of the S^* -phase duration. Furthermore, the resource utilization factor also corresponds to the fully synchronized model, see Fig. 12.5C1. However, even a low variability leads to visible dephasing after several generations. Strikingly, this dephasing leads to an increase in η that is accompanied by an increased growth rate, see Fig. 12.5BC,1.

By contrast, for the parameters $\zeta = 1/2$ and $\chi = 1$, a sequential resource-sharing mode reproduces the shifted model, see Fig. 12.5AB,2. Here, after the initial delay of one of the nuclei of the second generation, all nuclei have enough resource subsequently ($n_s \leq r_{\text{tot}}$), i.e. the process is no longer resource-limited and grows with maximal speed. In general, also the resource utilization factor of both models is in good agreement, see Fig. 12.5C2.⁷ Comparing both resource-sharing modes shows that the sequential mode uses the resource more efficiently than the parallel mode, enabling faster growth, see Fig. 12.5D, blue curve.

Since the single-cell data of the nuclear cycling dynamics are characterized by high variability, the effect of an increase in c_v is discussed in the following. In the case of parallel resource-sharing mode, an increase in D^* -phase variability ($c_v = 20\%$) leads to a faster dephasing of generations, visible already after a few generations. Interestingly, this dephasing leads to better resource utilization and thus a faster growth rate, with the new growth rate approaching that of unconstrained growth, see Fig. 12.5BC,1 red curve. However, although variability leads to an equal growth rate of the two resource-sharing modes in the long term, the initial lead of the sequential mode remains, see Fig. 12.5D, red curve. Here, for $\zeta = 1/2$, $\chi = 1$ and $c_v = 20\%$, the population $n_{\text{sequential}}$ remains more than twice as large as n_{parallel} , i.e. $n_{\text{sequential}}(t)/n_{\text{parallel}}(t) > 2$ for sufficiently large time t .

As expected, increasing the shortage of resource results in an overall slower growth, see Fig. 12.5EF with $\zeta = 1/3$. For low variability ($c_v = 1\%$), the resource-limited branching process with a parallel resource allocation

7: The only difference between the shifted model and the simulation is that in the former new resource is produced after a generation is completed, whereas in the latter new resource is produced directly after each completed DNA replication. However, as the reduction in η in the simulation only indicates that there is more resource than can be used by the nuclei ($r_{\text{tot}} > n_s$), this is only a technical detail that has no effect on the growth rate.

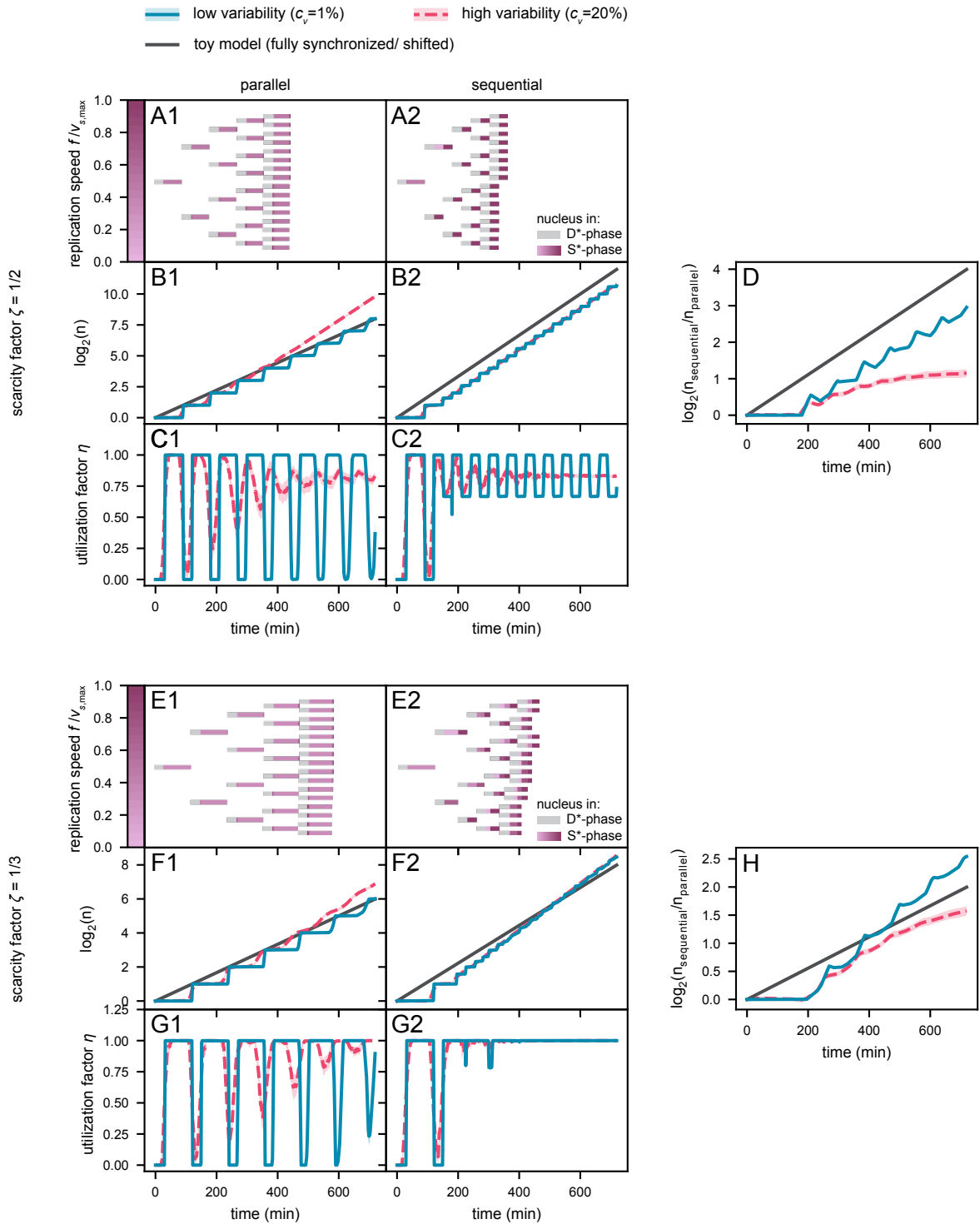


Figure 12.5 | Asymptotic behavior of resource-limited branching process with parallel (1) and sequential (2) resource allocation. (A-D) Simulated resource-limited branching processes with a moderate lack of resource $\zeta = 1/2$. (A) Lineage tree corresponding to a simulated resource-limited branching process with five generations and low D*-phase variability $c_v = 1\%$. For the sake of visualization, sister nuclei are sorted by their start of S*-phase. (B-D) Branching processes with different D*-phase variability: $c_v = 1\%$ (blue curve) and $c_v = 20\%$ (red curve). (B) Population size n vs. time. (C) Utilization factor η vs. time. (D) Ratio of population size $n_{sequential}/n_{parallel}$ vs. time. (E-H) is equivalent to A-D with reduced resource scarcity factor $\zeta = 1/3$. Here the following parameters were used: $k_b F_{tot} = 100 \text{ s}^{-1}$, $\chi = 1/2$, $T_{s,min} = 30 \text{ min}$. The unbinding rate is: sequential, $k_u = 10^{-5} \text{ s}^{-1}$; parallel, $k_u = 10^{-2} \text{ s}^{-1}$. Solid curve and band in B-D and F-H: mean (sample size 100) and bootstrapped 95% confidence interval.

is well described by the perfectly synchronized toy model, cf. Fig. 12.5E1 and Fig. 12.4A. However, in the case of a sequential resource-sharing

mode, the simulation differs from the shifted toy model, cf. Fig. 12.5E2 and Fig. 12.4B. Here, after the initial delay in the second generation, resource scarcity continues in subsequent generations, resulting in further dephasing. Interestingly, this additional dephasing enables a faster growth rate compared to the shifted model, see Fig. 12.5F2. Overall, the sequential allocation of resource utilizes the resource more efficiently, enabling a faster growth, see Fig. 12.5GH. And although the variability leads to an equal growth rate of the two resource-sharing modes in the long term, the initial lead of the sequential mode remains.

12.3.3 Mean-Field Growth Law

The exponential growth rate of the two toy models was described by the same equation, see Eq. (12.24) and Eq. (12.27). In the following, the question is addressed if this equation can also be used to describe the exponential growth rate of the more general resource-limited branching process.

For this, the number of nuclei n is approximated by the total amount of DNA, making n effectively a continuous quantity, where $n = 1$ corresponds to the amount of DNA contained in a single nucleus. The change in n is then given by the total replication speed of all replicating nuclei $v_F \sum_i F_i^*$, normalized to the length of a genome g [see Eq. (12.12) and Eq. (12.13)], i.e.

$$\frac{dn}{dt} = \frac{\ln(2)v_F^*}{g} \sum_i F_i^* = \frac{\ln(2)}{T_{s,\min}} \sum_i f_i. \quad (12.31)$$

To take into account that nuclei always go from one to two genomes and subsequently divide, the factor $\ln(2)$ was introduced. In other words, the factor $\ln(2)$ effectively means that the newly replicated DNA will only contribute to the growth in DNA itself, after the nuclear division. In a regime of limiting resources ($r_{\text{tot}} < \sum_i f_i$) and high affinity, the mean activated fraction can be described by the resource utilization factor and the total resource, i.e. Eq. (12.31) simplifies to

$$\frac{dn}{dt} = \frac{\ln(2)\eta r_{\text{tot}}}{T_{s,\min}}. \quad (12.32)$$

Assuming a self-supplied resource—growing linearly with the number of nuclei, i.e. $r_{\text{tot}} = \zeta n$ —Eq. (12.32) further simplifies to

$$\frac{dn}{dt} = \alpha n, \quad (12.33)$$

with the exponential growth rate

$$\alpha = \frac{\ln(2)\zeta\eta}{T_{s,\min}}. \quad (12.34)$$

In particular, this shows that on the mean-field level, the exponential growth rate is described by the same equation as the toy models Eq. (12.24) and Eq. (12.27).

In the regime of resource scarcity, simulating 10^4 resource-limited branching processes (that explore the reasonable parameter space of ζ, c_v, k_u

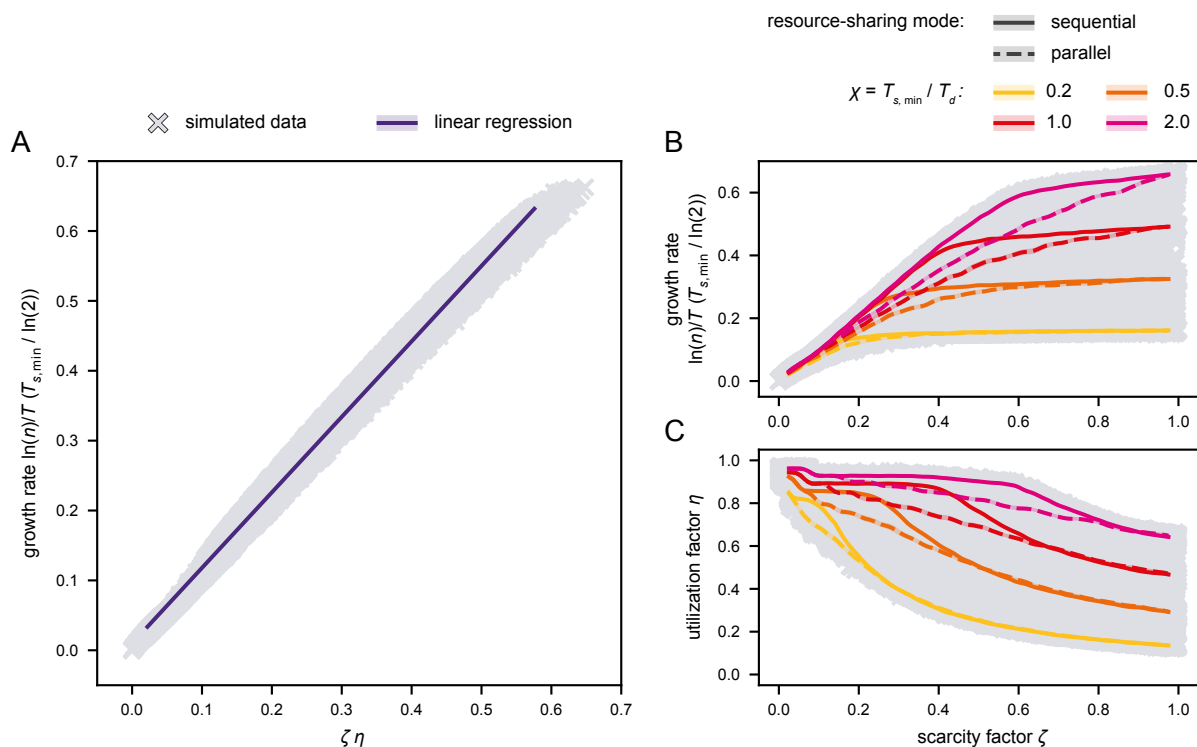


Figure 12.6 | Sequential allocation of a shared resource is a general mechanism for efficient and fast replication. (A) Simulating 10^4 different parameter sets shows that the asymptotic growth rate is proportional to the resource utilization factor and resource scarcity factor; solid line and band, linear regression and bootstrapped 95% confidence interval. The slope of 1.08 of the linear regression ($\rho = 0.992$) confirms the factor of $\ln(2)$. Here, the parameters were randomly drawn from uniform distributions with the following bounds: $c_v \in [0.05, 0.2]$, $\log_{10}(k_u s) \in [-5, -2]$, $\chi \in [0.2, 2.0]$ and $\zeta \in (0, 1]$. (BC) In regimes of resource scarcity, the sequential resource-sharing mode (solid curve) (B) grows faster and (C) has a more efficient resource utilization as the parallel mode (dashed curve). Here, curves and bands are linearly weighted moving averages of the simulated data and bootstrapped 95% confidence interval; window width is 0.05; colors highlight the different ratios of $T_{s,\min}$ to T_d , i.e. $\chi \in \{0.2, 0.5, 1.0, 2.0\}$; number of simulations is $n = 26,727$. The unbinding rate is: sequential, $k_u = 10^{-5} \text{ s}^{-1}$; parallel, $k_u = 10^{-2} \text{ s}^{-1}$. Each branching process was stopped after the duration corresponding to eleven generations in the resource abundance regime, i.e. $T(\chi) = 11(1 + 1/\chi)T_{s,\min}$. The effective binding rate is $k_b F_{\text{tot}} = 100 \text{ s}^{-1}$ and the minimal S^* -phase duration is $T_{s,\min} = 30 \text{ min}$.

and χ) confirms that the resource-limited branching process is well described by Eq. (12.34), see Fig. 12.6A. Here, the effective growth rate is estimated from each simulation using

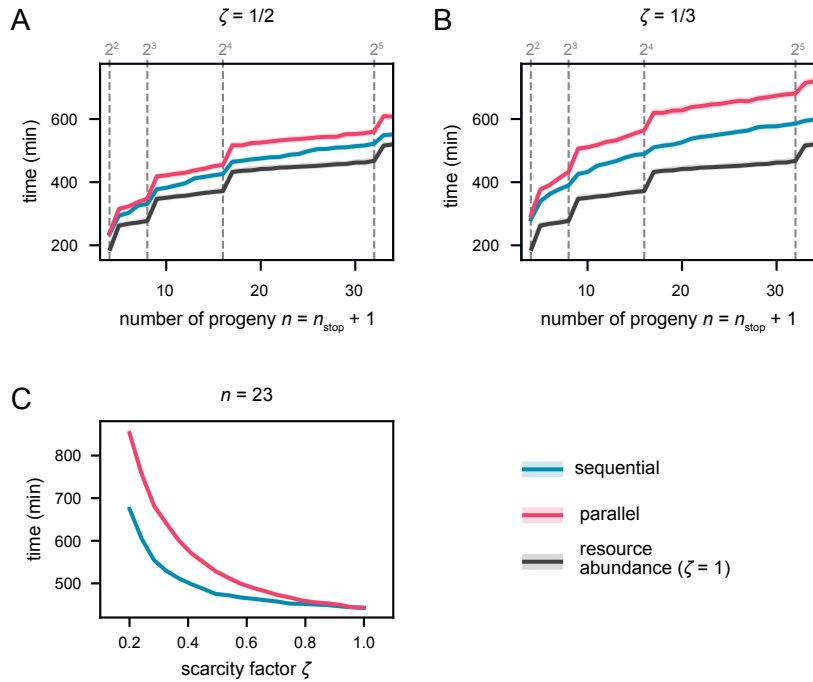
$$n(t) = 2^{\zeta\eta t/T_{s,\min}}. \quad (12.35)$$

As expected, in regimes of resource scarcity, a sequential resource-sharing mode (solid curve) yields a faster growth rate compared to a parallel mode (dashed curve), see Fig. 12.6B. The difference in their growth rate can be well explained by their differences in their resource utilization factor, see Fig. 12.6C. In summary, in the case of resource scarcity, a sequential resource allocation uses the resource more efficiently and thus allows for faster growth.

12.4 Sequential Resource-Sharing Enables Rapid Nuclear Multiplication

Until now, the two different resource allocation modes have been discussed in detail in the context of asymptotic growth rates. At the blood

Figure 12.7 | A sequential resource-sharing mode enables rapid nuclear multiplication. To reflect the parasitic nuclear multiplication, the stopping of the resource-limited branching process is regulated by a counter model. (AB) Total time vs. number of progeny for sequential (blue curve) and parallel (red curve) resource-sharing for different degrees of resource scarcity: $\zeta = 1/2$ (A) and $\zeta = 1/3$ (B). As a baseline, the time of nuclear multiplication for the regime of resource abundance is depicted ($\zeta = 1$). Here, the curve is effectively independent of the unbinding rate, i.e. sequential and parallel resource-sharing mode result in the same curve. (C) Total time to produce $n = 23$ progeny vs. resource scarcity factor for sequential (blue curve) and parallel (red curve) resource-sharing mode. Here, the unbinding rate is: sequential, $k_u = 10^{-5} \text{ s}^{-1}$; parallel, $k_u = 10^{-2} \text{ s}^{-1}$. Effective binding rate $k_b F_{\text{tot}} = 10 \text{ s}^{-1}$, D^{*}-phase variability $c_v = 10\%$, minimal S^{*}-phase duration $T_{s,\text{min}} = 30 \text{ min}$ and $\chi = 1/2$. Solid curve and band: mean (sample size 100) and bootstrapped 95% confidence interval.



stage, however, the parasite produces an average of 23 daughter parasites (see Fig. 10.3F) which corresponds to roughly four to five generations. Therefore, the question to what extent the previous results also apply to the regime of parasitic nuclear multiplication is investigated.

To account for the final multiplication phase of reaching the final number, the resource-limited branching process is extended to include a counter model that governs the stopping of the simulation, see Section 10.2. For the sake of simplicity, the counter is here implemented to count the number of initiated S^{*}-phases. Upon reaching a predefined number of S^{*}-phase initiations n_{stop} , no new S^{*}-phases are initiated, and consequently the branching process is terminated after completion of the last S^{*}-phase, resulting in exactly $n = n_{\text{stop}} + 1$ nuclei.⁸

8: By contrast, in Section 10.4 the counter was implemented slightly differently. In order to reproduce the measured distribution of the final number of nuclei, further S-phase initiations were inhibited after reaching a predefined number n_{stop} of completed S-phases, while the already initiated S-phases were allowed to finish. Consequently, the counter model of Section 10.4 for a fixed number n_{stop} nevertheless leads to some variability in the final number of nuclei.

At moderate resource scarcity, i.e. $\zeta = 1/2$, a sequential allocation of resource (blue curve) yields a faster completion of the final nuclear number compared to a parallel allocation (red curve), see Fig. 12.7A. Taking as baseline the respective duration needed in the regime of resource abundance (gray curve), the absolute prolongation due to resource scarcity is roughly twice as large in the parallel resource allocation than in the sequential one. For instance, producing 16 nuclei with a parallel resource-sharing mode takes about as long as producing 32 nuclei with a sequential mode, i.e. sequential allocation of resource yields twice as many nuclei in the same time. Note that the step-like increases in the overall time needed are due to the fact that the synchronous branching processes (parallel and resource abundance) effectively need one additional generation for producing 2^k vs. $2^k + 1$ nuclei. Furthermore, increasing the lack of resource ($\zeta = 1/3$) results in an increase in the absolute temporal advantage of the sequential resource-sharing mode, see Fig. 12.7B. Overall, sequential allocation of a shared resource is remarkably better at dealing with resource scarcity than parallel allocation. For instance, at the observed mean number of progeny $n = 23$ (see

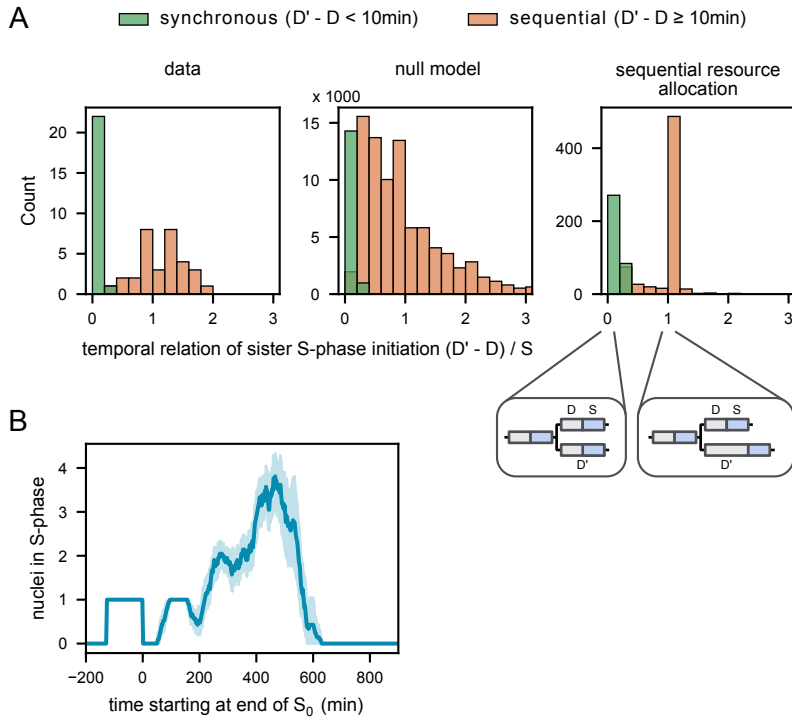


Figure 12.8 | The parasite *P. falciparum* seems to exploit a sequential resource-sharing mode. (A) The temporal relation of the second-generation sister S-phases $(D' - D)/S$, shows (left) a bimodal distribution that cannot be explained by (center) the null model of independent nuclei. However, a sequential allocation of resource can qualitatively describe the data. Here, for the resource allocation model, the following parameters were used: $r_{\text{tot}} = 1$, $k_b F_{\text{tot}} = 0.015 \text{ s}^{-1}$, $c_v = 20\%$, $f_{\text{thr}} = 0.1$. (B) Sequential allocation of the shared resource can quantitatively describe the DNA replication antibunching observed in *P. falciparum*. Here, for the simulation of the 49 realizations the following parameter were used: $\zeta = 1/3$, $k_b F_{\text{tot}} = 100 \text{ s}^{-1}$, $c_v = 25\%$, $f_{\text{thr}} = 0.1$, $\langle T_d \rangle = 2T_{s,\text{min}}$ and $T_{s,\text{min}} = 42 \text{ min}$.

Fig. 10.3F), for a given amount of resource, sequential allocation produces more nuclei in the same time as parallel allocation, see Fig. 12.7C. To put it differently, to produce a given number of nuclei within a given duration, sequential allocation requires less resource.

12.5 Does *Plasmodium falciparum* Operate in the Optimal Regime?

Does *P. falciparum* actually exploit a sequential allocation of a shared resource, limiting DNA replication? To test, for this hypothesis, the experimental data discussed in Chapter 10 are revisited. If the parasite exploits a sequential resource allocation, then a delay of DNA replication initiation should be observed in the regime of resource scarcity. As the first generation consists only of one nucleus and the data for the third generation are sparse (see Fig. 10.3A-D), the temporal relation of the S-phases of the second generation, where the parasite has two nuclei in total, are considered in the following. The temporal relation of two sister S-phases is quantified by the normalized difference of S-phase initiation, i.e. $(D' - D)/S = 0$ corresponds to a synchronous start of both nuclei and $(D' - D)/S = 1$ to the scenario, that the second nucleus starts DNA replication as soon as the first nucleus finished its S-phase, see Fig. 12.8A, inset. The experimental data show a bimodal distribution, where the lower mode corresponds to both nuclei starting at (almost) the same time and the higher mode corresponds to the case that the second nucleus waits for the first nucleus to finish its S-phase, see Fig. 12.8A left. Strikingly, this bimodal distribution can not be explained by the null model, see Fig. 12.8A center, where all phase durations D , D' and S are randomly sampled from their experimental distributions, cf. Fig. 10.3A-D. This again highlights the fact that the nuclei are coupled with each other. By contrast,

the proposed sequential allocation of a shared resource can qualitatively describe the bimodal distribution, see Fig. 12.8A right. Here, the lower mode corresponds to the case that both nuclei start at roughly the same time with their S-phases. This lack of symmetry break then results also in the so-called sequential mode in an equally sharing of resource. This means, that the model can not only reproduces the observed nuclear asynchrony but also the occasional prolonged simultaneous S-phases. Furthermore, it can quantitatively describe the observed DNA-replication antibunching, cf. Fig. 12.8B and Fig. 11.1A. Overall, all findings support the notion that *P. falciparum* evolved a sequential sharing to optimize resource allocation of replication machinery.

12.6 Conclusion

This chapter argued that the observed asynchrony of the nuclear multiplication at the blood stage in the parasite *P. falciparum* may originate from sequential sharing of replication machinery, a general mechanism for efficient and fast replication. Here, a minimal biophysical model for allocation of a shared enzyme to individual nuclei was introduced. By varying the enzyme binding kinetics, it captures parallel or sequential DNA replication. In sequential mode, the model reproduces the observed nuclear asynchrony as well as occasional prolonged simultaneous S-phases. Moreover, when the shared enzyme is limiting, sequential replication utilizes resources more efficiently, resulting in faster completion of nuclear multiplication.

Discussion - Nuclear Multiplication of *Plasmodium* *falciparum*

13

The malaria-causing pathogen *P. falciparum* is a eukaryotic parasite with a complex life cycle that includes proliferation within red blood cells. Although all clinical symptoms of malaria are caused by the rapid multiplication of parasites in the blood of patients [48, 49], it remained unknown how the asynchronous nuclear multiplication at this stage is orchestrated until recent advances in microscopy enabled it to be studied. Using a novel PCNA1-based nuclear cycle sensor system in *P. falciparum*, the resulting single cell data showed that this parasite proliferates through alternating, consecutive rounds of DNA replication and nuclear division that occurs asynchronously [2].

Using concepts of theoretical physics, the second part of this thesis investigated these single cell data and hereby provides a better understanding of nuclear multiplication. Confronting the data with different regulation mechanisms, originally proposed in the context of cell proliferation [225, 226], yielded the result that the nuclear multiplication and, consequently, the number of daughter cells are regulated by a counter mechanism. The nuclear multiplication was further investigated by using the mathematical framework of branching processes. Due to nuclear crowding, only the first two nuclear cycles, roughly corresponding to the first half of nuclear multiplication, could be extracted with confidence from the experiments. Therefore, I studied the dynamics of the unobserved second half of nuclear multiplication, revealing that after the initial increase, nuclear cycling speed slows down from the second cycle onward as nuclear multiplication continues. Including correlations to the branching processes furthermore revealed that nuclei are coupled with each other as their nuclear cycles desynchronize during multiplication more rapidly than expected for non-interacting nuclei. Combining this finding with the observation that the DNA replication speed of sister nuclei is correlated with their temporal overlap, i.e. synchronously occurring DNA replications are significantly prolonged, suggests that the coupling between the nuclei is caused by a shared resource, limiting DNA replication. To address in what way this active desynchronization might be beneficial for the parasite, a minimal biophysical model for allocation of a shared enzyme to individual nuclei was introduced. By varying the enzymatic binding kinetics, this model captures parallel or sequential DNA replication. Incorporating the resource allocation model into a branching process showed that, when the shared enzyme is limiting, the growth rate depends on how efficient the resource is used and that a sequential replication utilizes resource more efficiently, resulting in faster completion of nuclear multiplication. In sequential mode, the model reproduces the observed nuclear asynchrony as well as occasional prolonged simultaneous S-phases. Overall, all findings support the notion that *P. falciparum* evolved to optimize resource utilization by exploiting a sequential sharing of replication machinery, enabling a fast nuclear multiplication.

This study found that the relatively defined number of daughter parasites in *P. falciparum* blood stage is achieved by a counter mechanism, defying

the observed large variation in nuclear cycling dynamics. Although the counter model can describe the observed correlation in the data really well, one should keep in mind that similar correlations may be obtained from more complex modes of regulation, including those that utilize a combination of different mechanisms, like for example a timer and a counter. Indeed, recent experiments suggest that the overall duration of the whole blood-stage cycle of *P. falciparum* is maintained by an intrinsic clock [278, 279]. For experiments that perturb the initial delay beyond a certain threshold, this would indicate that the mechanism might be eventually governed by the timer of the overall blood-stage cycle. So far several *P. falciparum* proteins have been implicated in the regulation of parasite progeny number, e.g., the kinases PK7 and CRK5 [280, 281]. However, it is yet unclear how the counter operates at the molecular level. The counter could be realized by the consumption of a resource, arguably one of the simplest mechanistic models of a counter. As the parasite scavenges the red blood cell for nutrients and energy, a possible candidate could be some kind of red blood cell intrinsic resource. However, recent experiments showed that each parasite in a doubly infected red blood cells produces numbers of daughter parasites comparable to single infections [232], implying that the red blood cell resources are sufficient and do not limit the number of daughter parasites. Overall, although the concepts of timer and counter serve as useful terms to guide the way we think about the regulation of nuclear multiplication, the question of how the counter operates at the molecular level remains unanswered and can only be answered by detailed mechanistic studies.

Studying the nuclear multiplication with branching processes revealed that the nuclear multiplication in *P. falciparum* must slow down overall after the second nuclear cycle. To put a number on the degree of slowdown, a parsimonious model with a gradually slowing of the cycling dynamics showed that a slowdown by 17% per cycle described the data best and recovered both the average and the variability of the number of progeny. However, since the later stages of nuclear multiplication could not be resolved experimentally, the data cannot be used to determine the details of slowdown. For instance, the slowdown could also be accomplished by some nuclei that stop replicating earlier. To explain the data by early arrest in the third cycle, simulations showed that about 50% of nuclei would need to arrest. This would delay growth by about one generation, halving the number of generated nuclei. However, such an arrest-based slowdown is in contrast to the fact that no arrest events were observed in the first two cycles. To model slowdown in a plausible minimal way, I therefore opted for the gradual slowdown. In particular, this model is also consistent with a shared limited resource that is becoming more limited.

In the sequential mode, when the shared resource is limiting, the resource allocation model introduces asynchrony mainly by delaying the initiation of S-phase. This is in accordance with the single cell data where variability in nuclear lineages is mostly introduced in the phase before the S-phase, i.e. during the time between nuclear division and the subsequent S-phase. To compare this with other biological systems like mammalian and yeast cells, this interval shares similarities with the G₁-phase of the canonical cell cycle. Interestingly, in both mammalian and yeast cells, differences in cell cycle timing of genetically identical cells cultured in

the same environment are predominantly introduced during the G₁-phase [282–284]. Similarly, in the multinucleated cells of *A. gossypii*, nuclear asynchrony is introduced in G₁ [285]. In summary, the sequential mode can not only reproduce the asynchrony in *P. falciparum*, but even seems to capture a generic feature of asynchronous cell cycles.

In this thesis, I demonstrated that a sequentially shared diffusible cytoplasmic resource can produce asynchrony of nuclei in proximity, stressing that nucleus-intrinsic factors are not necessarily required for asynchrony in multinucleated cells. By contrast, the canonical cell cycle regulation, also based on diffusible cytoplasmic factors [187, 188], is associated with a synchronized replication. Due to the fact that in multinucleated cells all nuclei reside in the same cytoplasm, it has been argued that all nuclei receive the same signals, resulting in synchronized proliferative cycles. Indeed, the nuclei of many multinucleated cells progress synchronously through their cell cycle [194–197, 199]. Following this idea, it was argued that the asynchronous nuclear proliferation in *P. falciparum* is in contradiction to the regulation by diffusible cytoplasmic factors [206, 207], and might be established by nucleus-intrinsic factors [2]. And also in the multinucleated cells of *A. gossypii*, asynchrony is usually associated with cytoplasmic domains that are established by spatial separation of the nuclei [203, 286, 287]. Recent studies revealed that nuclei can maintain their autonomy also in proximity [286, 288], indicating that nucleus-intrinsic factors might be important to establish asynchrony. Overall, the underlying assumption that diffusible cytoplasmic factors regulating the cell cycle lead to synchronous replication is based on the notion that each nucleus receives the same signal. However, in this thesis I showed that in the case of a limited factor, sequential allocation of such a factor can also produce asynchrony, as it unequally distributes the resource between nuclei.

The shared resource, in principle, could be of two different types, either parasite-extrinsic metabolic factors or parasite-intrinsic factors such as components of the replication machinery. In *P. falciparum*, recent studies showed that the level of metabolic factors, such as glucose, in medium affects both the replication dynamics and the number of daughter parasites [289, 290]. In addition, in multinucleated human cells scarcity of nutrients increased the frequency of asynchrony [201]. However, *P. falciparum* parasites within the same medium display highly different replicating dynamics, even if they reside in close red blood cells [232], indicating that extrinsic factors are most likely not the source of the observed asynchrony in *P. falciparum*. By contrast, in this study it was shown that a sequential allocation of a shared enzymatic resource can describe the observed asynchrony in *P. falciparum*. Therefore, the model predicts that the shared resource is enzymatic-like and binds tight. As the DNA replicating complex is highly stable [268–271], the resource might be one of the individually stable components of the replication machinery. Overall, further detailed mechanistic studies would be required to answer this question conclusively.

The progression in the cell cycle in most eukaryotic cells is regulated by cytoplasmic cyclins and cyclin-dependent kinases. These proteins could be important for regulating the DNA replicating dynamics in *P. falciparum*. However, as the parasite displays a very divergent repertoire of cell cycle-related proteins, the molecular details of *P. falciparum* cell

cycle regulation remains poorly understood [165]. For example, no G₁- or S-phase cyclins could be identified by sequence homology [193]. So far, the nuclear kinase CRK4 is known to play an important role in initiating the S-phase [207, 291]. Therefore, CRK4 might be involved in generating the observed asynchrony. Yet, how the regulation of CRK4 works on a molecular level remains unknown [291].

To make sense out of the asynchronous replication in *P. falciparum*, I proposed in this thesis a minimal biophysical model for allocation of a shared enzyme to individual nuclei. Here, for sake of simplicity, it was assumed that the shared resource can diffuse freely between nuclei and cytoplasm. However, as nuclei typically tightly control the exchange of large molecules [292, 293], the shared resource might also be actively transported. To account for this possibility, in the future it might be interesting to incorporate active transport into the model. Overall, to further validate and/or adapt the suggested model, further detailed studies would be required in which possible candidates for shared resource are varied. Here, since the resource is unknown, and thus the question of active transport remains open, I opted for the simple diffusion-based model. Furthermore, due to its simplicity, in the future this model could be applied to any system which depends on a timewise needed enzymatic limiting resource. Therefore, a sequential sharing of enzymatic resource, resulting in asynchrony, could be a general mechanism for optimal resource allocation not only in *P. falciparum* but in many more biological systems.

In conclusion, by combining mathematical models with state-of-the-art experiments, this thesis contributes to the unraveling of the nuclear multiplication of *P. falciparum* and reveals laws of optimal allocation for shared enzymatic resources. Thereby, this thesis is a contribution to the body of work that shows how applying theoretical concepts, such as the question of optimal resource allocation, can contribute to decipher biological mechanisms.

APPENDIX

Author's Contribution



Part I: Cell-Cell Communication in Inflammatory Tissue

Part I is based on Ref. [1] and advanced earlier work by Nikolas Schnellbacher [50] and Nils B. Becker.

Chapter 3 and Appendix B. The local ligand concentration profiles were calculated by Nils B. Becker.

Chapter 4. The response curves of allosteric (Section 4.1), homo- and heterodimerizing (Subsection 4.2.1 and Subsection 4.2.2) receptors were already derived and investigated by Nikolas Schnellbacher. My Contribution was the derivation of the ligand-independent binding length scale (Subsection 4.2.3), the response curves including receptor turnover (Section 4.3) and the readout noise model (Section 4.4).

Chapter 6 and Appendices C–E. The underlying idea of this chapter, i.e. framing ligand discrimination as an information-theoretic task, was already established by Nikolas Schnellbacher [50]. Following this idea, I applied this concept to the IFNAR system. Therefore, I extended the task by the important *no ligand case*, and also incorporated the readout model. I furthermore derived how the discrimination power can be decomposed to the ligand type and presence sensing information. All scripts for numerical optimizations of the discrimination power were written and performed by myself.

Part II: Proliferation of Multinucleated Parasites

Part II is based on a collaboration Ref. [2] and an unpublished manuscript Ref. [3].

Chapters 10–12. All experimental data shown were generated by my collaboration partner Severina Klaus (and others see Ref. [2]). The data analysis as well as the modeling were performed by myself.

Physiological Cytokine Ligand Distribution in Higher Dimensions

B

This chapter is based on Ref. [1]. For a detailed listing of author contributions see Appendix A.

In Chapter 3, the physiological ligand distribution is derived for one spatial dimension $d = 1$ using a production-diffusion-consumption model Eq. (3.3). Following Ref. [1], this chapter extends this calculation to higher dimensions $d = 2$ and 3.

B.1 Two-Dimensional Profiles

In isotropic two-dimensional tissues such as epithelia, cytokines accumulate around producers in circular niches. For a single producer with radius r_s located in the origin $r = 0$, the radial part of Eq. (3.3) in stationary state reads

$$\mu L(r) = D \left[\frac{1}{r} \frac{\partial L(r)}{\partial r} + \frac{\partial^2 L(r)}{\partial r^2} \right], \quad (\text{B.1})$$

with the boundary conditions

$$k_s + 2\pi D r_s L'(r_s) = 0, \quad (\text{B.2a})$$

$$L(\infty) = 0. \quad (\text{B.2b})$$

Outside the producing cell ($r > r_s$), this boundary value problem has a unique solution given in terms of Bessel functions K_i of the second kind,

$$L(r) = L_0 K_0(r/\nu), \quad (\text{B.3})$$

where L_0 introduces a concentration reached roughly at half the niche radius, namely

$$L_0 = \frac{k_s}{2\pi D} \frac{1}{(r_s/\nu) K_1(r_s/\nu)}. \quad (\text{B.4})$$

For producers smaller than the niche size, the maximum concentration at the producer is

$$L(r_s) \simeq k_s / (2\pi D) \log(2\nu/r_s) \simeq L_0 \log(2\nu/r_s). \quad (\text{B.5})$$

The maximum concentration diverges for decreasing producer size, which shows that the mechanism of production, diffusion and consumption can generate very high local cytokine concentrations in two-dimensional niches. The total amount of ligand in the tissue in stationary state remains at $k_s \nu^2 / D = k_s / \mu$.

Outside the niche ($r \gg \nu$), the spatial profile $L(r)$ can be approximated

to leading order by

$$L(r) = \left[\left(\frac{r}{v} \right)^{-1/2} + O \left(\frac{r}{v} \right)^{-3/2} \right] L_0 e^{-r/v}. \quad (\text{B.6})$$

Within this approximation, the concentration distribution for a random tissue cell within a radius S of the producer can be estimated as in Eq. (3.6), yielding

$$p(L) \simeq \begin{cases} \frac{2}{W(2L_0^2/L(S)^2) - W(2)} \frac{W(2L_0^2/L^2)}{1 + W(2L_0^2/L^2)} \frac{1}{L} & \text{for } L(S) < L < L_0, \\ 0 & \text{otherwise,} \end{cases} \quad (\text{B.7})$$

where W denotes the Lambert W function. Here, in addition, the small fraction of cells within the niche, i.e. at high concentrations $L > L_0$, were neglected. Outside niches ($L \ll L_0$), it can be shown that this distribution is approximated by the limiting form $p(L) \propto 1/L$.

Together this shows that when producer cells at density $\rho_s \ll v^{-2}$ are sparse in a two-dimensional tissue, the vast majority of non-niche tissue cells is subject to a concentration distribution that is again well approximated by the scale-free distribution: $p(L) \simeq p_{sf}$ with $L_{lo} \simeq L(\rho_s^{-1/2})$ and $L_{hi} \simeq L_0 \simeq k_s/(2\pi D)$. Only for the highest concentrations, corrections that lead to some density extending up to $L(r_s)$ should be expected.

B.2 Three-Dimensional Profiles

For three-dimensional tissues with spherical niches, the radial part of Eq. (3.3) in stationary state is given by

$$\mu L(r) = D \left[\frac{2}{r} \frac{\partial L(r)}{\partial r} + \frac{\partial^2 L(r)}{\partial r^2} \right] \quad (\text{B.8})$$

with boundary conditions

$$k_s + 4\pi D r_s^2 L'(r_s) = 0, \quad (\text{B.9a})$$

$$L(\infty) = 0. \quad (\text{B.9b})$$

Here, a single producing cell with radius r_s at the origin $r = 0$ was assumed. Outside the producing cell ($r > r_s$), the solution of Eq. (B.8) is

$$L(r) = L_0 \frac{e^{-r/v}}{r/v}, \quad (\text{B.10})$$

where L_0 is attained at around half the niche radius and is defined by

$$L_0 = \frac{k_s}{4\pi D v} \frac{1}{(r_s/v + 1)e^{-r_s/v}}. \quad (\text{B.11})$$

Again, the total amount of ligand evaluates to k/μ . The maximal concentration is

$$L(r_s) = L_0 \frac{e^{-r_s/\nu}}{r_s/\nu} = \frac{k_s}{4\pi D\nu} \frac{1}{r_s/\nu + (r_s/\nu)^2}. \quad (\text{B.12})$$

For decreasing producer size, $L_0 \rightarrow k_s/(4\pi D\nu)$ and, as in two dimensions, $L(r_s)$ diverges, indicating that high local concentrations are possible around producing cells.

The comparatively simpler form of the ligand profile here allows us to evaluate the concentration distribution exactly. The result is similar to the two-dimensional case:

$$p(L) = \begin{cases} \frac{\nu}{S-r_s} \frac{W(L_0/L)}{1+W(L_0/L)} \frac{1}{L} & \text{for } L(S) < L < L(r_s), \\ 0 & \text{otherwise.} \end{cases} \quad (\text{B.13})$$

As before, outside the niche $L \ll L_0$, the factor involving the Lambert W functions tends towards 1. Thus, when producing cells are sparse at density $\rho_s \ll \nu^{-3}$, the concentration distribution is well approximated by the scale-free distribution: $p(L) \simeq p_{\text{sf}}$ with $L_{\text{lo}} \simeq L(\rho_s^{-1/3})$ and $L_{\text{hi}} \simeq L_0 \simeq k_s/(4\pi D\nu)$. Again, some density extends further up to $L(r_s)$.

B.3 Concluding Remark

In two or three dimensions, the characteristic niche size remains ν , but within the niche, the ligand profiles get steeper, reaching high concentrations at the producer cells. However, this only affect a small fraction $\rho_s \nu^d$ of tissue cells. For the vast majority of non-niche cells, the ligand profile shows small corrections to the simple exponential decay, see Fig. B.1A. Thus, most cells experience a nearly scale-free ligand distribution p_{sf} , which extends up to the niche boundary concentration L_0 . Few cells within a niche experience higher concentrations; the distribution tapers off as $L \rightarrow L(r_s)$, see Fig. B.1BC.

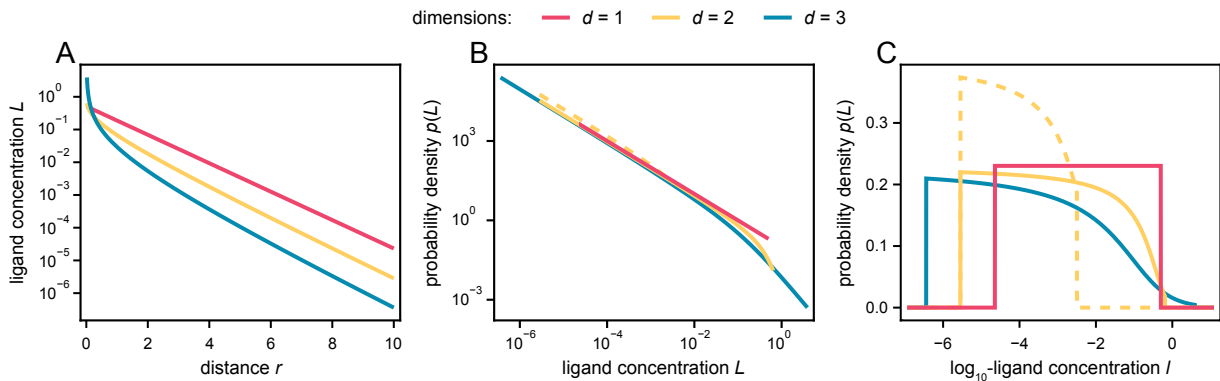


Figure B.1 | Spatial ligand profiles $L(r)$ (A) and concentration distributions $p(L)$ in (B) linear and (C) log-concentration space in different dimensions: $d = 1$, blue; $d = 2$, yellow and $d = 3$, red. The approximated distribution Eq. (B.7) outside niches for $d = 2$ is shown dashed; it differs from the numerical exact result mainly due to normalization. Note the good agreement of all distributions with the scale-free $d = 1$ form in the low-concentration regime. Parameter values: $k_s = 1$, $D = 1$, $\nu = 1$, $r_s = \nu/50$, $S = 10\nu$. Figure taken and adapted from [1].

Physical Aspects of Ligand-Receptor Binding

C

This chapter is based on Ref. [1]. For a detailed listing of author contributions see Appendix A.

In Chapter 6, the upper bound of the optimization range [see Eq. (6.18)] of the bulk and in-membrane dissociation rates, respectively, depend on the equilibrium dissociation constant K^B . Here, this upper bound is derived, and it is shown that this bound ensured that the corresponding binding rates do not exceed the diffusion-limited rates. In other words, it is demonstrated that the dependence of the upper bound on K^B reflects that the ligand-receptor interaction is not completely described by intrinsic chemical properties, but also by physical aspects such as diffusion. For a comprehensive treatment of physical aspects of ligand-receptor binding, I recommend the excellent textbook [97].

So far, the process of ligand binding to a receptor was considered as a one-step process [see for example the allosteric transmission scheme Eq. (4.2)], i.e.



where k_u describes the effective unbinding rate and k_b is the effective binding rate. However, considering the effect of diffusion, the binding of L and R is a two-step process. First, both molecules must encounter each other. Here, it is assumed that this transport step is governed by diffusion with a transport rate k_+ . Second, the step of the chemical reaction is then described by the intrinsic binding and unbinding rates k_{on} and k_{off} . In particular, this means that k_u and k_b include both the transport and reaction effects.

Ligand Binding from Bulk Solution

In 1982, David Shoup and Attila Szabo investigated the dependency of k_b on k_+ and k_{on} in the case of the binding of ligand to receptor when both are free in solution [294]. By solving the steady-state diffusion equation for the concentration of ligand molecules, they showed that k_b is described by the following combination of k_+ and k_{on} [97, 294]:

$$k_b = \frac{k_+ k_{\text{on}}}{k_+ + k_{\text{on}}}, \quad (\text{C.2})$$

where $k_+ = 4\pi Ds$ introduces the diffusion-limited binding rate, D is the sum of the ligand and receptor diffusivities and s is the encounter radius. In particular, the upper bound for the effective binding rate is given by the diffusion-limited binding rate

$$k_b \leq k_+ = 4\pi Ds. \quad (\text{C.3})$$

For a given K^B , a physically meaningful unbinding rate k_u is therefore also bounded, i.e.

$$k_u = k_b K^B \leq k_+ K^B. \quad (\text{C.4})$$

Using typical upper bounds for $D = 10^3 \mu\text{m}^2/\text{s}$ and $s = 10 \text{ nm}$ [97], one arrives at

$$k_u \leq \frac{0.06 K^B}{\text{pM s}}. \quad (\text{C.5})$$

Receptor Cross-Linking Within the Membrane

For the in-membrane dissociation rate k_d , an upper bound can also be estimated by considering a diffusion-limited association rate k_a . However, this time the diffusion-limited rates are not universal, but concentration dependent due to the two-dimensional nature of membrane binding. Therefore, the bulk membrane receptor concentration is imposed by fixing the mean free distance $2b$ of receptors in the membrane. Using a similar approach like for the case of ligand binding from bulk solution [294], it can be shown that k_a is diffusion-limited by [97]

$$k_a \leq k_+ = \frac{2\pi D}{\ln(b/s)}, \quad (\text{C.6})$$

where, D is the sum of free and ligand-bound receptor diffusivities and s is the encounter radius. For a given K^X , the upper bound of the association rate also imposes an upper bound on k_d , i.e.

$$k_d = k_a K^X \leq k_+ K^X. \quad (\text{C.7})$$

By using typical values $D = 0.1 \mu\text{m}^2/\text{s}$, $s = 10 \text{ nm}$ and $b = 100 \text{ nm}$ [97], the upper bound of in-membrane dissociation rate reads

$$k_d \leq 0.3 K^X \mu\text{m}^2 \text{s}^{-1} = \frac{2 \times 10^{-6} \lambda K^B}{\text{nm pM s}}. \quad (\text{C.8})$$

Mutual Information Decomposes for Hierarchical Probability Distributions

D

This chapter is based on Ref. [1]. For a detailed listing of author contributions see Appendix A.

In Chapter 6, the discrimination power is decomposed into the partial information about ligand presence and ligand type, see Eq. (6.3). Here, this equation is derived by showing that for hierarchical probability distribution, the mutual information can be decomposed.

Let p_i be a finite probability distribution $p_i \equiv (p_1, \dots, p_d)$. The decomposition property for the corresponding entropy then reads

$$H(p_i) = H[(p_1, 1 - p_1)] + (1 - p_1)H(p_{i|i>1}), \quad (\text{D.1})$$

where the first term denotes the entropy of the binary decision $i = 1$ vs. $i > 1$. The second term is the entropy remaining in the case $i > 1$, weighted with its probability. Applied to the variable $x \in \{\alpha, \beta, \emptyset\}$ and introducing the new variables π and τ , indicating ligand presence [$\pi(x) = \delta_{x\alpha} + \delta_{x\beta}$], and ligand type when ligand is present [$\tau(x) = x$ when $\pi(x) = 1$], respectively, this relation yields

$$\begin{aligned} H(p_x) &= H[(p_\emptyset, 1 - p_\emptyset)] + (1 - p_\emptyset)H(p_{x|x \in \{\alpha, \beta\}}) \\ &= H(p_\pi) + p_{\pi=1}H(p_{\tau|\pi=1}). \end{aligned} \quad (\text{D.2})$$

The basic relation

$$I(p_{x,n}) = H(p_x) - \langle H(p_{x|n}) \rangle, \quad (\text{D.3})$$

where the average runs over n , by applying (D.2) twice and reordering, then becomes [1]

$$\begin{aligned} I(p_{x,n}) &= H(p_\pi) + p_{\pi=1}H(p_{\tau|\pi=1}) - \langle H(p_{\pi|n}) + p_{\pi=1|n}H(p_{\tau|n,\pi=1}) \rangle \\ &= H(p_\pi) - \langle H(p_{\pi|n}) \rangle + p_{\pi=1}H(p_{\tau|\pi=1}) + \langle p_{\pi=1|n}H(p_{\tau|n,\pi=1}) \rangle \\ &= I(p_{\pi,n}) + p_{\pi=1} \left\{ H(p_{\tau|\pi=1}) - \sum_n p_{n|\pi=1}H(p_{\tau|n,\pi=1}) \right\} \\ &= I(p_{\pi,n}) + p_{\pi=1}I(p_{\tau,n|\pi=1}). \end{aligned} \quad (\text{D.4})$$

To summarize, the ligand discrimination power can be written as a weighted sum of two terms, $I = I_\pi + p_\pi I_\tau$, where I_π and I_τ introduces the partial information about ligand presence and ligand type, respectively. Note that as the results of Eq. (6.3) solely depends on the underlying hierarchical structure of the input distribution, the decomposition rule is also valid for the case of more than two ligands.

Parameter Values for Response Curves Optimally Discriminating Ligands

E

This chapter is based on Ref. [1]. For a detailed listing of author contributions see Appendix A.

The dissociation constants K and unbinding rates k used for the response curves shown in Chapter 6 are summarized in Table E.1 - E.3. The kinetic rates used for the IFN activation curve are shown in Table E.4.

Table E.1 | Dissociation constants and unbinding rates for activation curves shown in Fig. 6.3.

figure	receptor architecture	case	dissociation constants (pM)	peak activation
Fig. 6.3E	allosteric	I	$K_\alpha = 3300, K_\beta = 1.6$	$f_{\max,\alpha} = f_{\max,\beta} = 1.00$
		II	$K_\alpha = K_\beta = 28$	$f_{\max,\alpha} = f_{\max,\beta} = 1.00$
		III	$K_\alpha = K_\beta = 21$	$f_{\max,\alpha} = f_{\max,\beta} = 1.00$
Fig. 6.3G	homodimer	I	$K_\alpha^B = 2.0 \times 10^4$ $K_\beta^B = 960$	$f_{\max,\alpha} = 0.71$ $f_{\max,\beta} = 0.93$
		IV	$K_\alpha^B = K_\beta^B = 1.0 \times 10^4$	$f_{\max,\alpha} = f_{\max,\beta} = 0.78$
Fig. 6.3I	heterodimer	I	$K_{\alpha,1}^B = 9.6 \times 10^5, K_{\alpha,2}^B = 4.2$ $K_{\beta,1}^B = 3300, K_{\beta,2}^B = 1700$	$f_{\max,\alpha} = 0.21$ $f_{\max,\beta} = 0.84$
		IV	$K_{\alpha,1}^B = 1.0 \times 10^6, K_{\alpha,2}^B = 33$ $K_{\beta,1}^B = 3900, K_{\beta,2}^B = 3500$	$f_{\max,\alpha} = 0.21$ $f_{\max,\beta} = 0.81$

Table E.2 | Dissociation constants for activation curves shown in Fig. 6.7.

figure	receptor architecture	dissociation constants (pM)	peak activation
Fig. 6.7A1	allosteric	$K_\alpha = 4000, K_\beta = 3.9$	$f_{\max,\alpha} = f_{\max,\beta} = 1.00$
Fig. 6.7A2	homodimer	$K_\alpha^B = 3.0 \times 10^4, K_\beta^B = 1400$	$f_{\max,\alpha} = 0.65, f_{\max,\beta} = 0.91$
Fig. 6.7A3	heterodimer	$K_{\alpha,1}^B = 8.1 \times 10^5, K_{\alpha,2}^B = 11$	$f_{\max,\alpha} = 0.24$
		$K_{\beta,1}^B = 1600, K_{\beta,2}^B = 1400$	$f_{\max,\beta} = 0.87$
Fig. 6.7C1	allosteric	$K_\alpha = K_\beta = 22$	$f_{\max,\alpha} = f_{\max,\beta} = 1.00$
Fig. 6.7C2	homodimer	$K_\alpha^B = K_\beta^B = 6000$	$f_{\max,\alpha} = f_{\max,\beta} = 0.83$
Fig. 6.7C3	heterodimer	$K_{\alpha,1}^B = 4.5 \times 10^5, K_{\alpha,2}^B = 22$	$f_{\max,\alpha} = 0.33$
		$K_{\beta,1}^B = 8700, K_{\beta,2}^B = 1500$	$f_{\max,\beta} = 0.81$
Fig. 6.7E1	allosteric	$K_\alpha = K_\beta = 17$	$f_{\max,\alpha} = f_{\max,\beta} = 1.00$
Fig. 6.7E2	homodimer	$K_\alpha^B = K_\beta^B = 5000$	$f_{\max,\alpha} = f_{\max,\beta} = 0.84$
Fig. 6.7E3	heterodimer	$K_{\alpha,1}^B = 1.1 \times 10^6, K_{\alpha,2}^B = 12$	$f_{\max,\alpha} = 0.20$
		$K_{\beta,1}^B = 2100, K_{\beta,2}^B = 1600$	$f_{\max,\beta} = 0.86$

Table E.3 | Dissociation constants and unbinding rates for activation curves shown in Fig. 6.8.

receptor architecture	dissociation constants (K in pM) and unbinding rates (k in s^{-1})	peak activation
homodimer with turnover	$K_{\alpha}^B = 1.2 \times 10^4$ $K_{\beta}^B = 83$ $k_{u,a} = 340, k_{u,b} = 1.5 \times 10^{-4}$ $k_{d,a} = 0.012, k_{d,b} = 8.3 \times 10^{-5}$	$f_{\max,\alpha} = 0.76$ $f_{\max,\beta} = 0.94$
heterodimer with turnover	$K_{\alpha,1}^B = 1.6 \times 10^4, K_{\alpha,2}^B = 27$ $K_{\beta,1}^B = 420, K_{\beta,2}^B = 20$ $k_{u,a,1} = 1.0 \times 10^{-6}, k_{u,a,2} = 0.074$ $k_{u,b,1} = 1.0 \times 10^{-6}, k_{u,b,2} = 0.0014$ $k_{d,a,1} = 2.6 \times 10^{-5}, k_{d,a,2} = 2.7 \times 10^{-5}$ $k_{d,b,1} = 4.2 \times 10^{-4}, k_{d,b,2} = 1.0 \times 10^{-6}$	$f_{\max,\alpha} = 0.27$ $f_{\max,\beta} = 0.93$

Table E.4 | Kinetic rates used for the IFN activation curve shown in Fig. 6.9. Here, IFN α 2 serves as an example of a weak ligand and IFN β of a strong ligand. The literature values are extracted and converted from [112, 114, 137, 295].

kinetic rate	unit	IFN α 2	IFN β
$k_{b,1}$	(Ms) $^{-1}$	6.7×10^5	5.0×10^5
$k_{u,1}$	s^{-1}	1.0	1.0×10^{-2}
K_1^B	nM	1500	20
$k_{b,2}$	(Ms) $^{-1}$	2.2×10^6	1.0×10^7
$k_{u,2}$	s^{-1}	2.0×10^{-2}	1.0×10^{-3}
K_2^B	pM	9100	100
$k_{a,1}$	$\mu m^2 s^{-1}$	5.48×10^{-2}	1.67×10^{-2}
$k_{d,1}$	s^{-1}	0.40	3.3×10^{-3}
$k_{a,2}$	$\mu m^2 s^{-1}$	1.67×10^{-2}	1.67×10^{-2}
$k_{d,2}$	s^{-1}	4.4×10^{-3}	3.3×10^{-4}

Summary of all Lineage Trees of *Plasmodium Falciparum* Nuclei

F

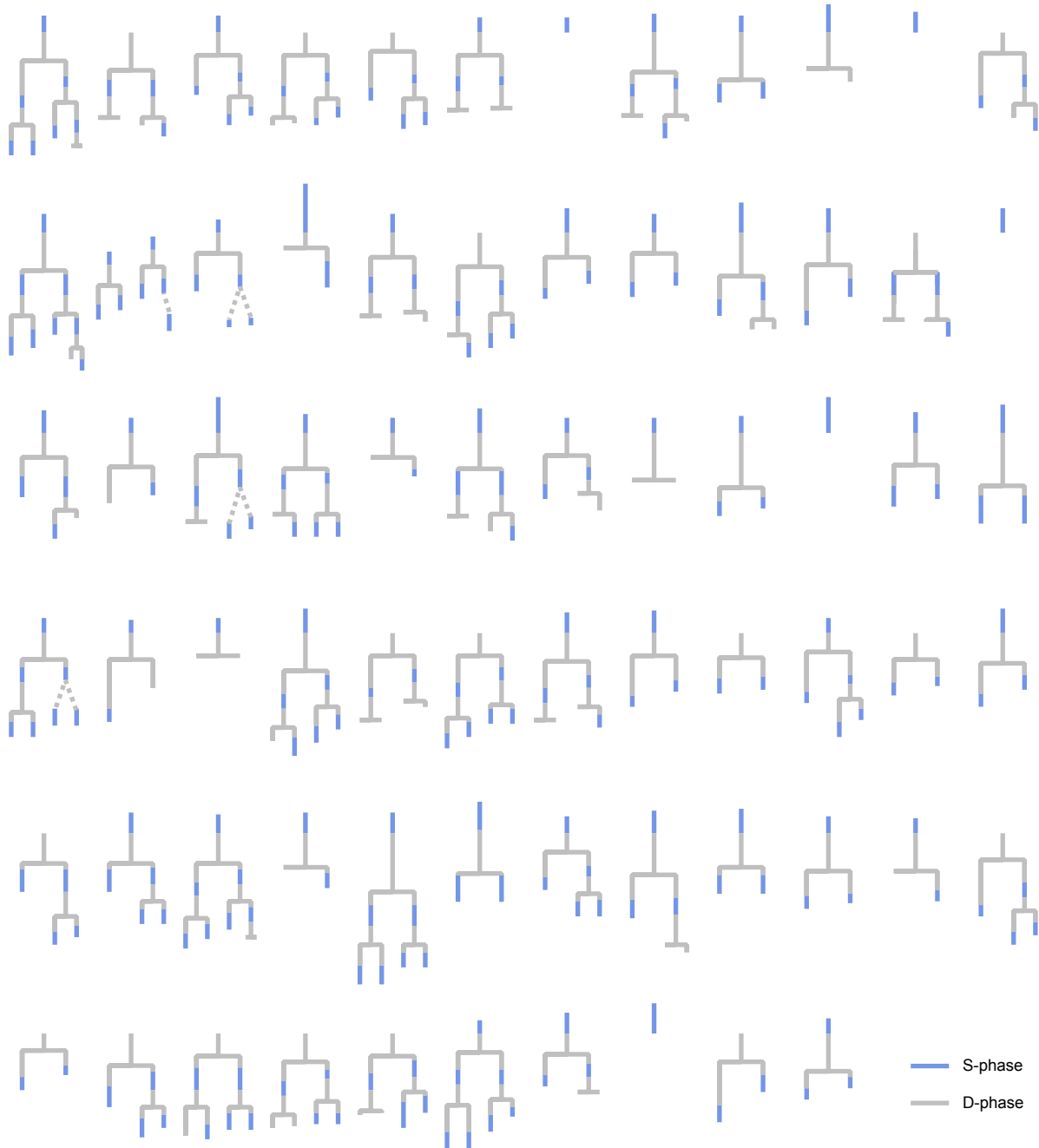


Figure F.1 | Overexpression of PCNA1::GFP allows tracing of lineage trees of *P. falciparum* nuclei. Summary of all lineage trees that were analyzed for Fig. 10.3; dashed lines, timing of nuclear division event could not be determined with confidence; timing drawn to scale. Taken and adapted from [2].

Binding Timescale of the Resource Allocation Model

G

Chapter 12 proposes a model for allocation of a shared enzymatic resource. In the case of a single nucleus, the fraction of actively DNA-replicating complexes f is described by Eq. (12.5), i.e.

$$\frac{df}{dt} = k_b F_{\text{tot}}(r_{\text{tot}} - f)(1 - f) - k_u f. \quad (\text{G.1})$$

The dynamics of this equation are described by two timescales, an unbinding timescale $\tau_u = 1/k_u$ and a binding timescale τ_b . To get an estimate of τ_b , the ordinary differential equation Eq. (12.5) is solved for the initial condition $f(t = 0) = 0$. The expected timescale of change in resource is described by the typical length of a nuclear cycle. By contrast the experiments showed that the binding time is on the timescale of minutes, i.e. the live-cell microscopy time resolution of 5 min cannot resolve the dynamics of binding. By applying the separation of timescales, which results in an effectively constant resource r_{tot} , solving Eq. (12.5) results in

$$f(t) = f_{\text{eq}} + \sqrt{\rho^2 - r_{\text{tot}}} \left\{ 1 - \tanh \left[\sqrt{\rho^2 - r_{\text{tot}}} k_u t + \tanh^{-1} \left(\frac{\rho}{\sqrt{\rho^2 - r_{\text{tot}}}} \right) \right] \right\}, \quad (\text{G.2})$$

where the steady state f_{eq} and the auxiliary parameter ρ are defined accordingly to Eq. (12.7) and Eq. (12.8), respectively. Approximating τ_{eq} as the duration of half activation, i.e. $f(\tau_{\text{eq}}) = f_{\text{eq}}/2$, yields

$$\tau_{\text{eq}} = \frac{1}{2k_b F_{\text{tot}} \sqrt{\rho^2 - r_{\text{tot}}}} \ln \left(\frac{3r_{\text{tot}} - 2\rho f_{\text{eq}}}{r_{\text{tot}}} \right). \quad (\text{G.3})$$

In the high affinity limit, i.e. $k_u/(k_b F_{\text{tot}}) \rightarrow 0$ and therefore $\rho \rightarrow (1 + r_{\text{tot}})/2$, and in the resource abundance regime $r_{\text{tot}} \gg 1$, the binding timescale can be simplified to

$$\tau_{\text{eq}} \approx \frac{\ln(2)}{k_b F_{\text{tot}} r_{\text{tot}}}. \quad (\text{G.4})$$

List of Manuscripts

The following manuscripts have been written up during the course of this thesis.

- [1] Patrick Binder, Nikolas D. Schnellbacher, Thomas Höfer, Nils B. Becker, and Ulrich S. Schwarz. 'Optimal ligand discrimination by asymmetric dimerization and turnover of interferon receptors'. In: *Proceedings of the National Academy of Sciences* 118.37 (2021) (cited on pages 4, 13, 14, 17, 28, 35, 37, 42, 44, 47, 50, 51, 53–55, 123, 125, 127, 129, 131, 133).
- [2] Severina Klaus, Patrick Binder, Juyeop Kim, Marta Machado, Charlotta Funaya, Violetta Schaaf, Darius Klaschka, Aiste Kudulyte, Marek Cyrklaff, Vibor Laketa, Thomas Höfer, Julien Guizetti, Nils B. Becker, Friedrich Frischknecht, Ulrich S. Schwarz, and Markus Ganter. 'Asynchronous nuclear cycles in multinucleated *Plasmodium falciparum* facilitate rapid proliferation'. In: *Science Advances* 8.13 (2022), eabj5362 (cited on pages 4, 75–79, 81–83, 88, 91, 95, 96, 99, 117, 119, 123, 135).
- [3] Patrick Binder, Thomas Höfer, Nils B. Becker, and Ulrich S. Schwarz. 'Sequential resource-sharing enables rapid growth in sparse environment'. unpublished (cited on pages 4, 91, 99, 123).

Bibliography

References in citation order.

- [4] Eduardo L. Yeyati and Federico Filippini. 'Social and economic impact of COVID-19'. In: *Bangladesh Institute of Development Studies* (June 2021) (cited on page 1).
- [5] Peterson K. Ozili and Thankom Arun. 'Spillover of COVID-19: Impact on the Global Economy'. In: *Managing Inflation and Supply Chain Disruptions in the Global Economy*. Hershey, PA, USA: IGI Global, 2023, pp. 41–61 (cited on page 1).
- [6] Bhaskar Bagchi et al. 'Impact of COVID-19 on Global Economy'. In: *Coronavirus Outbreak and the Great Lockdown: Impact on Oil Prices and Major Stock Markets Across the Globe*. Singapore: Springer Singapore, 2020, pp. 15–26 (cited on page 1).
- [7] John Whitfield. 'Portrait of a serial killer'. In: *Nature* (Oct. 2002) (cited on page 1).
- [8] World Health Organization. *World malaria report 2021*. World Health Organization, 2021, liv, 263 p. (Cited on pages 1, 63).
- [9] Robert Rosen. *Optimality principles in biology*. London: Butterworths, 1967, 198 p. (Cited on pages 1, 2).
- [10] Paul J. H. Schoemaker. 'The quest for optimality: A positive heuristic of science?' In: *Behavioral and Brain Sciences* 14.2 (1991), pp. 205–215 (cited on page 1).
- [11] John S. Dugdale. *Entropy and its physical meaning*. London: Taylor & Francis, 1996, IX, 198 p. (Cited on page 1).
- [12] Max Born, Emil Wolf, and Avadh Behari Bhatia. *Principles of optics. electromagnetic theory of propagation, interference and diffraction of light*. 7. (expanded) ed., reprinted with corr., 4. print. Cambridge: Cambridge University Press, 2006, XXXIII, 952 p. (Cited on page 1).
- [13] Eugene Hecht. *Optics*. 5 ed. Boston: Pearson, 2017, 722 p. (Cited on page 1).
- [14] Richard P. Feynman, Robert B. Leighton, and Matthew L. Sands. *Mainly electromagnetism and matter*. The new millennium edition, paperback first published. New York: Basic Books, 2011 (cited on page 1).
- [15] Lev D. Landau and Evgenij M. Lifšic. *Lehrbuch der theoretischen Physik. [in zehn Bänden]*. Berlin: Akad.-Verl., 19XX- (cited on page 1).
- [16] Theodosius Dobzhansky. 'Nothing in Biology Makes Sense Except in the Light of Evolution'. In: *The American Biology Teacher* 75.2 (2013), pp. 87–91 (cited on page 2).
- [17] Charles Darwin. *On the Origin of Species by Natural Selection, or the Preservation of Favoured Races in the Struggle for Life*. 6th ed. London: John Murray, 1872 (cited on page 2).
- [18] Ronald A. Fisher. *The genetical theory of natural selection*. The Clarendon Press, 1930 (cited on page 2).

- [19] Sewall Wright. 'Evolution in Mendelian populations'. In: *Genetics* 16.2 (1931), p. 97 (cited on page 2).
- [20] Sewall Wright. 'The Roles of Mutation, Inbreeding, crossbreeding and Selection in Evolution'. In: *Proceedings of the XI International Congress of Genetics* 8 (1932), pp. 209–222 (cited on page 2).
- [21] John B. Haldane. *The causes of evolution*. Vol. 5. Princeton University Press, 1990 (cited on page 2).
- [22] Theodosius Dobzhansky. *Genetics and the Origin of Species*. 11. Columbia university press, 1982 (cited on page 2).
- [23] Ernst Mayr and Susanne Warmuth. *Konzepte der Biologie*. Stuttgart: Hirzel, 2005, 247 p. (Cited on page 2).
- [24] Peter A. Corning. 'Beyond the modern synthesis: A framework for a more inclusive biological synthesis'. In: *Progress in Biophysics and Molecular Biology* 153 (2020), pp. 5–12 (cited on page 2).
- [25] Otto Warburg et al. 'The quantum efficiency of photosynthesis'. In: *Biochimica et Biophysica Acta* 4 (1950), pp. 335–348 (cited on page 2).
- [26] Denis Pelli and Colin Blakemore. 'The quantum efficiency of vision'. In: *Vision: Coding and efficiency* (1990), pp. 3–24 (cited on page 2).
- [27] Howard C. Berg and Edward M. Purcell. 'Physics of chemoreception'. In: *Biophysical Journal* 20.2 (1977), pp. 193–219 (cited on page 2).
- [28] Howard C. Berg. *Random walks in biology*. Princeton, N.J.: Princeton Univ.Pr., 1983, 142 p. (Cited on page 2).
- [29] Christopher C. Govern and Pieter Rein ten Wolde. 'Optimal resource allocation in cellular sensing systems'. In: *Proceedings of the National Academy of Sciences* 111.49 (2014), pp. 17486–17491 (cited on pages 2, 99).
- [30] Hamish Spencer. 'Optimization in Evolution, Limitations of'. In: *International Encyclopedia of the Social & Behavioral Sciences*. Ed. by Neil J. Smelser and Paul B. Baltes. Oxford: Pergamon, 2001, pp. 10882–10887 (cited on page 2).
- [31] Andrea Velenich and Jeff Gore. 'Synthetic approaches to understanding biological constraints'. In: *Current Opinion in Chemical Biology* 16.3 (2012), pp. 323–328 (cited on page 2).
- [32] Jacques Ninio. 'Kinetic amplification of enzyme discrimination'. In: *Biochimie* 57.5 (1975), pp. 587–595 (cited on page 2).
- [33] Wiktor Młynarski et al. 'Statistical analysis and optimality of neural systems'. In: *Neuron* 109.7 (2021), 1227–1241.e5 (cited on page 2).
- [34] Simon Laughlin. In: *Zeitschrift für Naturforschung C* 36.9-10 (1981), pp. 910–912 (cited on page 2).
- [35] J. H. van Hateren. 'Theoretical predictions of spatiotemporal receptive fields of fly LMCs, and experimental validation'. In: *Journal of Comparative Physiology A* 171.2 (Sept. 1992), pp. 157–170 (cited on page 2).
- [36] H. Kacser and J. A. Burns. 'The control of flux'. In: *Biochemical Society Transactions* 23.2 (May 1995), pp. 341–366 (cited on page 2).

- [37] Steven H. Orzack et al. *Adaptationism and optimality*. Cambridge University Press, 2001 (cited on page 2).
- [38] Rafael U. Ibarra, Jeremy S. Edwards, and Bernhard O. Palsson. 'Escherichia coli K-12 undergoes adaptive evolution to achieve in silico predicted optimal growth'. In: *Nature* 420.6912 (Nov. 2002), pp. 186–189 (cited on page 2).
- [39] R. McNeill Alexander. *Principles of animal locomotion*. Princeton University Press, 2003 (cited on page 2).
- [40] Joshua I. Gold and Michael N. Shadlen. 'The Neural Basis of Decision Making'. In: *Annual Review of Neuroscience* 30.1 (2007). PMID: 17600525, pp. 535–574 (cited on page 2).
- [41] G Tkacik, C G Callan, and W Bialek. 'Information flow and optimization in transcriptional regulation'. In: *Proceedings of the National Academy of Sciences of the United States of America* 105.34 (2008), pp. 12265–12270 (cited on page 2).
- [42] Atsushi Tero et al. 'Rules for Biologically Inspired Adaptive Network Design'. In: *Science* 327.5964 (2010), pp. 439–442 (cited on page 2).
- [43] Yonatan Savir et al. 'Cross-species analysis traces adaptation of Rubisco toward optimality in a low-dimensional landscape'. In: *Proceedings of the National Academy of Sciences* 107.8 (2010), pp. 3475–3480 (cited on page 2).
- [44] Wilson S. Geisler. 'Contributions of ideal observer theory to vision research'. In: *Vision Research* 51.7 (2011). Vision Research 50th Anniversary Issue: Part 1, pp. 771–781 (cited on page 2).
- [45] Liliana Mancio-Silva et al. 'Sir2a regulates rDNA transcription and multiplication rate in the human malaria parasite *Plasmodium falciparum*'. In: *Nature Communications* 4.1 (Feb. 2013), p. 1530 (cited on pages 3, 64, 75, 99).
- [46] Carolina M. Andrade et al. 'Increased circulation time of *Plasmodium falciparum* underlies persistent asymptomatic infection in the dry season'. In: *Nature Medicine* 26.12 (Dec. 2020), pp. 1929–1940 (cited on pages 3, 64, 75, 99).
- [47] Caroline S. Simon, Vanessa S. Stürmer, and Julien Guizetti. 'How Many Is Enough? - Challenges of Multinucleated Cell Division in Malaria Parasites'. In: *Frontiers in Cellular and Infection Microbiology* 11 (2021) (cited on pages 3, 64, 75, 76, 80, 99).
- [48] Arjen M Dondorp et al. 'Estimation of the Total Parasite Biomass in Acute Falciparum Malaria from Plasma PfHRP2'. In: *PLOS Medicine* 2.8 (Aug. 2005), null (cited on pages 3, 64, 75, 117).
- [49] Alan F. Cowman et al. 'Malaria: Biology and Disease'. In: *Cell* 167.3 (Oct. 2016), pp. 610–624 (cited on pages 3, 63, 64, 75, 117).
- [50] Nikolas David Schnellbacher. *Particle-based computer simulations of biological reaction-diffusion systems*. Heidelberg, 2017, 181 p. (Cited on pages 4, 123).
- [51] John T. Hancock. *Cell Signalling*. Oxford University Press, 2017 (cited on pages 7, 20).
- [52] Bruce Alberts, ed. *Molecular biology of the cell*. 6. ed. New York: Garland Science, 2015, Getr. Zählung (cited on pages 7, 100).

- [53] Satoe Takahashi and Peter M. Pryciak. 'Membrane Localization of Scaffold Proteins Promotes Graded Signaling in the Yeast MAP Kinase Cascade'. In: *Current Biology* 18.16 (Aug. 2008), pp. 1184–1191 (cited on pages 7, 35).
- [54] Michael Hinczewski and D. Thirumalai. 'Cellular signaling networks function as generalized Wiener-Kolmogorov filters to suppress noise'. In: *Physical Review X* 4.4 (2014), pp. 1–15 (cited on pages 7, 35).
- [55] Hernán E. Grecco, Malte Schmick, and Philippe I H Bastiaens. 'Signaling from the living plasma membrane'. In: *Cell* 144.6 (2011), pp. 897–909 (cited on pages 7, 35).
- [56] Nils B. Becker, Andrew Mugler, and Pieter Rein Ten Wolde. 'Optimal Prediction by Cellular Signaling Networks'. In: *Physical Review Letters* 115.25 (2015), pp. 1–5 (cited on pages 7, 35).
- [57] Andrew Mugler et al. 'Membrane clustering and the role of rebinding in biochemical signaling.' In: *Biophysical journal* 102.5 (Mar. 2012), pp. 1069–78 (cited on pages 7, 35).
- [58] Andrew Mugler, Filipe Tostevin, and Pieter Rein ten Wolde. 'Spatial partitioning improves the reliability of biochemical signaling.' In: *Proceedings of the National Academy of Sciences of the United States of America* 110.15 (Apr. 2013), pp. 5927–32 (cited on pages 7, 35).
- [59] Jacob Piehler et al. 'Structural and dynamic determinants of type I interferon receptor assembly and their functional interpretation.' In: *Immunological reviews* 250.1 (2012), pp. 317–34 (cited on pages 11, 12, 14, 24, 35, 36, 40, 57, 58).
- [60] Alick Isaacs, J. Lindenmann, and Christopher Howard Andrewes. 'Virus interference. I. The interferon'. In: *Proceedings of the Royal Society of London. Series B - Biological Sciences* 147.927 (1957), pp. 258–267 (cited on page 11).
- [61] Xiao He et al. 'Type I Interferons and Malaria: A Double-Edge Sword Against a Complex Parasitic Disease'. In: *Frontiers in Cellular and Infection Microbiology* 10 (2020) (cited on page 11).
- [62] Giorgio Trinchieri. 'Type I interferon: friend or foe?' In: *Journal of Experimental Medicine* 207.10 (Sept. 2010), pp. 2053–2063 (cited on page 11).
- [63] Laura M. Snell, Tracy L. McGaha, and David G. Brooks. 'Type I Interferon in Chronic Virus Infection and Cancer'. In: *Trends in Immunology* 38.8 (2017), pp. 542–557 (cited on page 11).
- [64] Lionel B. Ivashkiv and Laura T. Donlin. 'Regulation of type I interferon responses'. In: *Nature reviews. Immunology* 14.1 (Jan. 2014). nri3581[PII], pp. 36–49 (cited on page 11).
- [65] Finlay McNab et al. 'Type I interferons in infectious disease'. In: *Nature Reviews Immunology* 15.2 (Feb. 2015), pp. 87–103 (cited on page 11).
- [66] Katharina S. Schulz and Karen L. Mossman. 'Viral Evasion Strategies in Type I IFN Signaling – A Summary of Recent Developments'. In: *Frontiers in Immunology* 7 (2016) (cited on page 11).

- [67] Kun Chen, Juan Liu, and Xuetao Cao. 'Regulation of type I interferon signaling in immunity and inflammation: A comprehensive review'. In: *Journal of Autoimmunity* 83 (2017), pp. 1–11 (cited on page 11).
- [68] Gideon Schreiber. 'The Role of Type I Interferons in the Pathogenesis and Treatment of COVID-19'. In: *Frontiers in Immunology* 11 (2020) (cited on page 11).
- [69] Paul Bastard et al. 'Type I interferons and SARS-CoV-2: from cells to organisms'. In: *Current Opinion in Immunology* 74 (2022), pp. 172–182 (cited on page 11).
- [70] Cecile King and Jonathan Sprent. 'Dual Nature of Type I Interferons in SARS-CoV-2-Induced Inflammation'. In: *Trends in Immunology* 42.4 (2021), pp. 312–322 (cited on page 11).
- [71] Annsea Park and Akiko Iwasaki. 'Type I and Type III Interferons – Induction, Signaling, Evasion, and Application to Combat COVID-19'. In: *Cell Host & Microbe* 27.6 (2020), pp. 870–878 (cited on page 11).
- [72] Jérôme Hadjadj et al. 'Impaired type I interferon activity and inflammatory responses in severe COVID-19 patients'. In: *Science* 369.6504 (2020), pp. 718–724 (cited on page 11).
- [73] Gideon Schreiber and Jacob Piehler. 'The molecular basis for functional plasticity in type I interferon signaling'. In: *Trends in Immunology* 36.3 (Mar. 2015), pp. 139–149 (cited on pages 11, 35, 58).
- [74] Batya Cohen et al. 'Ligand-induced association of the type I interferon receptor components'. In: *Molecular and Cellular Biology* 15.8 (1995), pp. 4208–4214 (cited on page 12).
- [75] Juan L. Mendoza et al. 'Structure of the IFN γ Receptor Complex Guides Design of Biased Agonists'. In: *Nature* 567.7746 (Mar. 2019), pp. 56–60 (cited on pages 12, 57).
- [76] Jan Vilcek. 'Novel interferons'. In: *Nature Immunology* 4.1 (Jan. 2003), pp. 8–9 (cited on page 12).
- [77] Baris Atakan. *Molecular Communications and Nanonetworks*. Springer, 2016 (cited on page 13).
- [78] Georgia Perona-Wright, Katja Mohrs, and Markus Mohrs. 'Sustained signaling by canonical helper T cell cytokines throughout the reactive lymph node'. In: *Nature Immunology* 11.6 (June 2010), pp. 520–526 (cited on page 13).
- [79] Alon Oyler-Yaniv et al. 'A Tunable Diffusion-Consumption Mechanism of Cytokine Propagation Enables Plasticity in Cell-to-Cell Communication in the Immune System'. In: *Immunity* 46.4 (2017), pp. 609–620 (cited on pages 13–15, 37).
- [80] Grégoire Altan-Bonnet and Ratnadeep Mukherjee. 'Cytokine-Mediated Communication: A Quantitative Appraisal of Immune Complexity'. In: *Nature Reviews Immunology* 19.4 (Apr. 2019), pp. 205–217 (cited on pages 13, 14).
- [81] Grégoire Altan-Bonnet, Thierry Mora, and Aleksandra M. Walczak. 'Quantitative Immunology for Physicists'. In: *Physics Reports. Quantitative Immunology for Physicists* 849 (Mar. 2020), pp. 1–83 (cited on pages 13, 14).

- [82] Roberto A. Maldonado et al. 'A role for the immunological synapse in lineage commitment of CD4 lymphocytes'. In: *Nature* 431.7008 (Sept. 2004), pp. 527–532 (cited on page 13).
- [83] C. Pangault et al. 'Follicular lymphoma cell niche: identification of a preeminent IL-4-dependent TFH–B cell axis'. In: *Leukemia* 24.12 (Dec. 2010), pp. 2080–2089 (cited on page 13).
- [84] Catherine A. Sabatos et al. 'A Synaptic Basis for Paracrine Interleukin-2 Signaling during Homotypic T Cell Interaction'. In: *Immunity* 29.2 (2008), pp. 238–248 (cited on page 13).
- [85] Kevin Thurley et al. 'Three-Dimensional Gradients of Cytokine Signaling between T Cells'. In: *PLOS Computational Biology* 11.4 (Apr. 2015), pp. 1–22 (cited on page 13).
- [86] Andreas J. Müller et al. 'CD4+ T Cells Rely on a Cytokine Gradient to Control Intracellular Pathogens beyond Sites of Antigen Presentation'. In: *Immunity* 37.1 (July 2012), pp. 147–157 (cited on page 13).
- [87] Anne R. Syversveen. 'Noninformative bayesian priors. interpretation and problems with construction and applications'. In: *Preprint statistics* 3.3 (1998), pp. 1–11 (cited on page 13).
- [88] E T Jaynes and G L Bretthorst. *Probability Theory: The Logic of Science*. Cambridge University Press, Cambridge, UK, 2003 (cited on page 14).
- [89] William M. Bolstad. *Introduction to Bayesian statistics*. 2. ed. Hoboken, NJ: Wiley, 2007, XXIV, 437 p. (Cited on page 14).
- [90] James O. Berger, José M. Bernardo, and Dongchu Sun. 'The formal definition of reference priors'. In: *The Annals of Statistics* 37.2 (2009), pp. 905–938 (cited on page 14).
- [91] Harold Jeffreys. 'An Invariant Form for the Prior Probability in Estimation Problems'. In: *Proceedings of the Royal Society of London. Series A, Mathematical and Physical Sciences* 186.1007 (1946), pp. 453–461 (cited on page 14).
- [92] David J. C. MacKay. *Information theory, inference, and learning algorithms*. 10. ed. Cambridge: Cambridge University Press, 2011, XII, 628 p. (Cited on pages 14, 31, 34).
- [93] Alan S. Perelson and Charles DeLisi. 'Receptor clustering on a cell surface. I. theory of receptor cross-linking by ligands bearing two chemically identical functional groups'. In: *Mathematical Biosciences* 48.1 (Feb. 1980), pp. 71–110 (cited on pages 17, 21).
- [94] Alan S. Perelson. 'Receptor clustering on a cell surface. II. theory of receptor cross-linking by ligands bearing two chemically distinct functional groups'. In: *Mathematical Biosciences* 49.1 (May 1980), pp. 87–110 (cited on pages 17, 22, 23).
- [95] Alan S. Perelson. 'Receptor clustering on a cell surface. III. theory of receptor cross-linking by multivalent ligands: description by ligand states'. In: *Mathematical Biosciences* 53.1-2 (1981), pp. 1–39 (cited on page 17).
- [96] Alan S. Perelson and Gérard Weisbuch. 'Immunology for physicists'. In: *Reviews of Modern Physics* 69.4 (1997), pp. 1219–1268 (cited on pages 17, 21, 22).

- [97] Douglas Lauffenburger and Jennifer Linderman. *Receptors : models for binding, trafficking, and signaling*. New York: Oxford University Press, 1993 (cited on pages 17, 21, 22, 129, 130).
- [98] Ignacio Moraga et al. 'Receptor density is key to the alpha2/beta interferon differential activities.' In: *Molecular and cellular biology* 29.17 (Sept. 2009), pp. 4778–87 (cited on pages 18, 46).
- [99] Flavia Trettel et al. 'Ligand-Independent CXCR2 Dimerization'. In: *Journal of Biological Chemistry* 278.42 (Oct. 2003), pp. 40980–40988 (cited on page 18).
- [100] Samantha J. Allen, Susan E. Crown, and Tracy M. Handel. 'Chemokine: Receptor Structure, Interactions, and Antagonism'. In: *Annual Review of Immunology* 25.1 (Mar. 2007), pp. 787–820 (cited on page 18).
- [101] Jacque Monod, Jeffries Wyman, and Jean-Pierre Changeux. 'On Nature of Allosteric Transitions - a Plausible Model'. In: *Journal of Molecular Biology* 12.1 (1965), pp. 88–& (cited on page 19).
- [102] Dennis Bray and Thomas Duke. 'Conformational Spread: The Propagation of Allosteric States in Large Multiprotein Complexes.' In: *Annual review of biophysics and biomolecular structure* 33 (2004), pp. 53–73 (cited on page 19).
- [103] Carl-Henrik Heldin. 'Dimerization of Cell Surface Receptors in Signal Transduction'. In: *Cell* 80.2 (Jan. 1995), pp. 213–223 (cited on page 20).
- [104] Adrian Whitty and Christopher W. Borysenko. 'Small Molecule Cytokine Mimetics'. In: *Chemistry & Biology* 6.4 (Apr. 1999), R107–R118 (cited on page 20).
- [105] Yoshlaki Nakamura et al. 'Heterodimerization of the IL-2 Receptor β - and γ -Chain Cytoplasmic Domains Is Required for Signalling'. In: *Nature* 369.6478 (May 1994), pp. 330–333 (cited on page 20).
- [106] Brad H. Nelson, James D. Lord, and Philip D. Greenberg. 'Cytoplasmic Domains of the Interleukin-2 Receptor β and γ Chains Mediate the Signal for T-Cell Proliferation'. In: *Nature* 369.6478 (May 1994), pp. 333–336 (cited on page 20).
- [107] Sándor Damjanovich et al. 'Preassembly of Interleukin 2 (IL-2) Receptor Subunits on Resting Kit 225 K6 T Cells and Their Modulation by IL-2, IL-7, and IL-15: A Fluorescence Resonance Energy Transfer Study'. In: *Proceedings of the National Academy of Sciences* 94.24 (Nov. 1997), pp. 13134–13139 (cited on page 20).
- [108] Jesse W. Cotari et al. 'Cell-to-Cell Variability Analysis Dissects the Plasticity of Signaling of Common γ Chain Cytokines in T Cells'. In: *Science Signaling* 6.266 (Mar. 2013), ra17–ra17 (cited on page 20).
- [109] Julianna Volkó et al. 'IL-2 Receptors Preassemble and Signal in the ER/Golgi Causing Resistance to Antiproliferative Anti-IL-2R α Therapies'. In: *Proceedings of the National Academy of Sciences* 116.42 (Oct. 2019), pp. 21120–21130 (cited on page 20).
- [110] Jin Yang and William S. Hlavacek. 'Scaffold-Mediated Nucleation of Protein Signaling Complexes: Elementary Principles'. In: *Mathematical Biosciences* 232.2 (Aug. 2011), pp. 164–173 (cited on page 21).

- [111] Sepehr Fathi et al. 'Absolute Ligand Discrimination by Dimeric Signaling Receptors'. In: *Biophysical Journal* 111.5 (2016), pp. 917–920 (cited on pages 21, 22, 25, 35, 57).
- [112] Friedrich Roder et al. 'Rapid Transfer of Transmembrane Proteins for Single Molecule Dimerization Assays in Polymer-Supported Membranes'. In: *ACS Chemical Biology* 9.11 (Nov. 2014), pp. 2479–2484 (cited on pages 25, 40, 134).
- [113] Martynas Gavutis et al. 'Lateral ligand-receptor interactions on membranes probed by simultaneous fluorescence-interference detection.' In: *Biophysical journal* 88.6 (June 2005), pp. 4289–302 (cited on pages 25, 40).
- [114] Martynas Gavutis et al. 'Determination of the two-dimensional interaction rate constants of a cytokine receptor complex.' In: *Biophysical journal* 90.9 (May 2006), pp. 3345–55 (cited on pages 25, 40, 134).
- [115] Stephan Wilmes et al. 'Receptor dimerization dynamics as a regulatory valve for plasticity of type I interferon signaling'. In: *The Journal of Cell Biology* 209.4 (2015), pp. 579–593 (cited on pages 25, 40).
- [116] Nicole F. Neel et al. 'Chemokine receptor internalization and intracellular trafficking'. In: *Cytokine & Growth Factor Reviews* 16.6 (2005). Chemokines, pp. 637–658 (cited on page 26).
- [117] Korbinian Kienle et al. 'Neutrophils self-limit swarming to contain bacterial growth in vivo'. In: *Science* 372.6548 (2021), eabe7729 (cited on page 26).
- [118] Robert G. Endres and Ned S. Wingreen. 'Accuracy of direct gradient sensing by single cells'. In: *Proceedings of the National Academy of Sciences* 105.41 (2008), pp. 15749–15754 (cited on page 26).
- [119] Crispin Gardiner. *Stochastic methods*. Vol. 4. Springer Berlin, 2009 (cited on pages 30, 46).
- [120] Claude Elwood Shannon. 'A mathematical theory of communication'. In: *The Bell System Technical Journal* 27.3 (1948), pp. 379–423 (cited on page 31).
- [121] Thomas M Cover and Joy A Thomas. *Elements of information theory*. John Wiley & Sons, 2012 (cited on pages 31, 33, 35, 37).
- [122] William S. Bialek. *Biophysics. searching for principles*. Princeton; Oxford: Princeton University Press, 2012, xii, 640 p. (Cited on page 31).
- [123] Henry Pinkard and Laura Waller. *A visual introduction to information theory*. 2022. arXiv: cs.IT/2206.07867 (cited on pages 31, 34).
- [124] Gašper Tkačik and William Bialek. 'Information processing in living systems'. In: *Annual Review of Condensed Matter Physics* 7 (2016), pp. 89–117 (cited on page 31).
- [125] John J. Tyson, Katherine C. Chen, and Bela Novak. 'Sniffers, buzzers, toggles and blinkers: Dynamics of regulatory and signaling pathways in the cell'. In: *Current Opinion in Cell Biology* 15.2 (2003), pp. 221–231 (cited on page 35).

- [126] Raymond Cheong et al. 'Information Transduction Capacity of Noisy Biochemical Signaling Networks'. In: *Science* 334.6054 (Oct. 2011), pp. 354–358 (cited on page 35).
- [127] Jangir Selimkhanov et al. 'Accurate Information Transmission through Dynamic Biochemical Signaling Networks'. In: *Science* 346.6215 (Dec. 2014), pp. 1370–1373 (cited on page 35).
- [128] Christopher C. Govern and Pieter Rein ten Wolde. 'Optimal resource allocation in cellular sensing systems'. In: *Proceedings of the National Academy of Sciences* 111.49 (2014), pp. 17486–17491 (cited on page 35).
- [129] Pieter Rein ten Wolde et al. 'Fundamental Limits to Cellular Sensing'. In: *Journal of Statistical Physics* 162.5 (2016), pp. 1395–1424 (cited on page 35).
- [130] Peter B. Detwiler et al. 'Engineering Aspects of Enzymatic Signal Transduction: Photoreceptors in the Retina'. In: *Biophysical Journal* 79.6 (Dec. 2000), pp. 2801–2817 (cited on page 35).
- [131] Bruno M. C. Martins and Peter S. Swain. 'Trade-Offs and Constraints in Allosteric Sensing'. In: *PLOS Computational Biology* 7.11 (Nov. 2011), e1002261 (cited on page 35).
- [132] Andre Levchenko and Ilya Nemenman. 'Cellular Noise and Information Transmission'. In: *Current Opinion in Biotechnology* 28 (Aug. 2014), pp. 156–164 (cited on page 35).
- [133] Tim Maiwald et al. 'Combining theoretical analysis and experimental data generation reveals IRF9 as a crucial factor for accelerating interferon- α induced early antiviral signalling'. In: *FEBS Journal* 277.22 (2010), pp. 4741–4754 (cited on page 35).
- [134] Doron Levin et al. 'Multifaceted Activities of Type I Interferon Are Revealed by a Receptor Antagonist'. In: *Science Signaling* 7.327 (May 2014), ra50–ra50 (cited on pages 35–37).
- [135] Wiet de Ronde, Filipe Tostevin, and Pieter Rein ten Wolde. 'Multiplexing Biochemical Signals.' In: *Physical review letters* 107.4 (July 2011), p. 048101 (cited on page 35).
- [136] Irene Otero-Muras, Pencho Yordanov, and Joerg Stelling. 'Chemical Reaction Network Theory elucidates sources of multistability in interferon signaling'. In: *PLOS Computational Biology* 13.4 (2017), pp. 1–28 (cited on page 35).
- [137] Changjiang You et al. 'Receptor dimer stabilization by hierarchical plasma membrane microcompartments regulates cytokine signaling'. In: *Science Advances* 2.12 (2016), pp. 1–13 (cited on pages 35, 134).
- [138] Timothy W. McKeithan. 'Kinetic proofreading in T-cell receptor signal transduction.' In: *Proceedings of the National Academy of Sciences* 92.11 (1995), pp. 5042–5046 (cited on page 35).
- [139] Grégoire Altan-Bonnet and Ronald N Germain. 'Modeling T Cell Antigen Discrimination Based on Feedback Control of Digital ERK Responses'. In: *PLoS Biology* 3.11 (Oct. 2005). Ed. by Philippa Marrack, e356 (cited on page 35).

- [140] Paul Francois et al. 'Phenotypic Model for Early T-Cell Activation Displaying Sensitivity, Specificity, and Antagonism'. In: *Proceedings of the National Academy of Sciences* 110.10 (Mar. 2013), E888–E897 (cited on page 35).
- [141] Paul François and Grégoire Altan-Bonnet. 'The Case for Absolute Ligand Discrimination: Modeling Information Processing and Decision by Immune T Cells'. In: *Journal of Statistical Physics* 162.5 (Mar. 2016), pp. 1130–1152 (cited on pages 35, 38).
- [142] Paul François and Anton Zilman. 'Physical Approaches to Receptor Sensing and Ligand Discrimination'. In: *Current Opinion in Systems Biology* 18 (Dec. 2019), pp. 111–121 (cited on pages 35, 58).
- [143] Thierry Mora. 'Physical Limit to Concentration Sensing Amid Spurious Ligands'. In: *Physical Review Letters* 115.3 (July 2015), p. 038102 (cited on page 35).
- [144] Vijay Singh and Ilya Nemenman. 'Simple Biochemical Networks Allow Accurate Sensing of Multiple Ligands with a Single Receptor'. In: *PLOS Computational Biology* 13.4 (Apr. 2017). Ed. by Alexandre V Morozov, e1005490 (cited on page 35).
- [145] Jean-Benoît Lalanne and Paul François. 'Chemodetection in Fluctuating Environments: Receptor Coupling, Buffering, and Antagonism'. In: *Proceedings of the National Academy of Sciences* 112.6 (Feb. 2015), pp. 1898–1903 (cited on pages 35, 59).
- [146] Omid Sascha Yousefi et al. 'Optogenetic Control Shows That Kinetic Proofreading Regulates the Activity of the T Cell Receptor'. In: *eLife* 8 (Apr. 2019). Ed. by Arup K Chakraborty, e42475 (cited on pages 35, 37, 58).
- [147] Alex Rhee, Raymond Cheong, and Andre Levchenko. 'The application of information theory to biochemical signaling systems'. In: *Physical Biology* 9.4 (2012), p. 045011 (cited on page 36).
- [148] Aleksandra M Walczak and Gašper Tkačik. 'Information transmission in genetic regulatory networks: a review'. In: *J. Phys. Condens. Matter* 23 (2011), 31pp (cited on page 36).
- [149] Clive G. Bowsher, Margaritis Voliotis, and Peter S. Swain. 'The Fidelity of Dynamic Signaling by Noisy Biomolecular Networks'. In: *PLoS Computational Biology* 9.3 (2013) (cited on page 36).
- [150] Piotr Topolewski and Michał Komorowski. 'Information-theoretic analyses of cellular strategies for achieving high signaling capacity—dynamics, cross-wiring, and heterogeneity of cellular states'. In: *Current Opinion in Systems Biology* 27 (2021), p. 100352 (cited on page 36).
- [151] Schaper Fred, Jetka Tomasz, and Dittrich Anna. 'Decoding cellular communication - an information theoretic perspective on cytokine and endocrine signaling'. In: *Current Opinion in Endocrine and Metabolic Research* (2022), p. 100351 (cited on page 36).
- [152] Yang Xiang et al. 'Generalized simulated annealing algorithm and its application to the Thomson model'. In: *Physics Letters A* 233.3 (1997), pp. 216–220 (cited on page 40).
- [153] Pauli Virtanen et al. 'SciPy 1.0: Fundamental Algorithms for Scientific Computing in Python'. In: *Nature Methods* 17 (2020), pp. 261–272 (cited on page 40).

- [154] Thomas B. Lavoie et al. 'Binding and activity of all human alpha interferon subtypes'. In: *Cytokine* 56.2 (2011), pp. 282–289 (cited on page 40).
- [155] Nir Friedman, Long Cai, and X. Sunney Xie. 'Linking Stochastic Dynamics to Population Distribution: An Analytical Framework of Gene Expression'. In: *Physical Review Letters* 97.16 (Oct. 2006), p. 168302 (cited on page 45).
- [156] Arren Bar-Even et al. 'Noise in Protein Expression Scales with Natural Protein Abundance'. In: *Nature Genetics* 38.6 (June 2006), pp. 636–643 (cited on pages 45, 58).
- [157] K. G. Suresh Kumar et al. 'Site-specific ubiquitination exposes a linear motif to promote interferon-alpha receptor endocytosis'. In: *Journal of Cell Biology* 179.5 (Dec. 2007). Publisher: The Rockefeller University Press, pp. 935–950 (cited on page 53).
- [158] K. G. Suresh Kumar et al. 'Basal Ubiquitin-independent Internalization of Interferon alpha Receptor Is Prevented by Tyk2-mediated Masking of a Linear Endocytic Motif'. In: *The Journal of Biological Chemistry* 283.27 (July 2008), pp. 18566–18572 (cited on page 53).
- [159] Yaron E. Antebi et al. 'Combinatorial Signal Perception in the BMP Pathway'. In: *Cell* 170.6 (Sept. 2017), 1184–1196.e24 (cited on page 59).
- [160] Christina J. Su et al. 'Ligand-receptor promiscuity enables cellular addressing'. In: *Cell Systems* 13.5 (2022), 408–425.e12 (cited on page 59).
- [161] John E. Hyde. 'Drug-resistant malaria'. In: *Trends in Parasitology* 21.11 (2005). 21 years following trends in parasitology, pp. 494–498 (cited on page 63).
- [162] Friedrich Frischknecht. *Malaria. tödliche Parasiten, spannende Forschung und keine Impfung*. Springer eBook Collection. Wiesbaden: Springer Spektrum, 2019, 1 Online-Ressource (XI, 39 p.) (Cited on page 63).
- [163] Navneet Arora, Lokhesh C. Anbalagan, and Ashok K. Pannu. 'Towards Eradication of Malaria: Is the WHO's RTS,S/AS01 Vaccination Effective Enough?' In: *Risk Manag Healthc Policy* 14 (Mar. 2021), pp. 1033–1039 (cited on page 63).
- [164] Colin J. Sutherland et al. 'Two Nonrecombining Sympatric Forms of the Human Malaria Parasite *Plasmodium ovale* Occur Globally'. In: *The Journal of Infectious Diseases* 201.10 (May 2010), pp. 1544–1550 (cited on page 63).
- [165] Holly Matthews, Craig W. Duffy, and Catherine J. Merrick. 'Checks and balances? DNA replication and the cell cycle in *Plasmodium*'. In: *Parasites & Vectors* 11.1 (Mar. 2018), p. 216 (cited on pages 63–66, 120).
- [166] Francis E. G. Cox. 'History of the discovery of the malaria parasites and their vectors'. In: *Parasites & Vectors* 3.1 (Feb. 2010), p. 5 (cited on page 63).
- [167] Francis E. G. Cox. 'History of human parasitology'. In: *Clin Microbiol Rev* 15.4 (Oct. 2002), pp. 595–612 (cited on page 63).

- [168] Georgios Pappas, Ismene J. Kiriaze, and Matthew E. Falagas. 'Insights into infectious disease in the era of Hippocrates'. In: *International Journal of Infectious Diseases* 12.4 (2008), pp. 347–350 (cited on page 63).
- [169] Robert Sallares. *Malaria and Rome. a history of malaria in ancient Italy*. Oxford: Oxford University Press, 2002, 1 online resource (xv, 341 p.) (Cited on page 63).
- [170] Ernst Hempelmann and Kristine Krafts. 'Bad air, amulets and mosquitoes: 2,000 years of changing perspectives on malaria'. In: *Malaria Journal* 12.1 (July 2013), p. 232 (cited on page 63).
- [171] Robert S. Desowitz. *The Malaria Capers (More Tales of People, Research and Reality)*. Vol. 288. 1991, p. 288 (cited on page 63).
- [172] Henry E. Shortt et al. 'The pre-erythrocytic stage of *Plasmodium falciparum*'. In: *Transactions of The Royal Society of Tropical Medicine and Hygiene* 44.4 (Feb. 1951), pp. 405–419 (cited on page 64).
- [173] Miguel Prudêncio, Ana Rodriguez, and Maria M. Mota. 'The silent path to thousands of merozoites: the *Plasmodium* liver stage'. In: *Nature Reviews Microbiology* 4.11 (Nov. 2006), pp. 849–856 (cited on page 64).
- [174] Angelika Sturm et al. 'Manipulation of Host Hepatocytes by the Malaria Parasite for Delivery into Liver Sinusoids'. In: *Science* 313.5791 (2006), pp. 1287–1290 (cited on page 64).
- [175] Alexander G. Maier et al. 'Malaria parasite proteins that remodel the host erythrocyte'. In: *Nature Reviews Microbiology* 7.5 (May 2009), pp. 341–354 (cited on page 65).
- [176] Christof Grüning et al. 'Development and host cell modifications of *Plasmodium falciparum* blood stages in four dimensions'. In: *Nature Communications* 2.1 (Jan. 2011), p. 165 (cited on page 65).
- [177] Justin A. Boddey and Alan F. Cowman. 'Plasmodium Nesting: Remaking the Erythrocyte from the Inside Out'. In: *Annual Review of Microbiology* 67.1 (2013). PMID: 23808341, pp. 243–269 (cited on page 65).
- [178] Lorena M. Coronado, Christopher T. Nadovich, and Carmenza Spadafora. 'Malarial hemozoin: From target to tool'. In: *Biochimica et Biophysica Acta (BBA) - General Subjects* 1840.6 (2014), pp. 2032–2041 (cited on page 65).
- [179] M. Read et al. 'Microtubular organization visualized by immunofluorescence microscopy during erythrocytic schizogony in *Plasmodium falciparum* and investigation of post-translational modifications of parasite tubulin'. In: *Parasitology* 106.3 (1993), pp. 223–232 (cited on pages 65, 76).
- [180] Maria E. Francia and Boris Striepen. 'Cell division in apicomplexan parasites'. In: *Nature Reviews Microbiology* 12.2 (Feb. 2014), pp. 125–136 (cited on pages 65, 85).
- [181] Luc Reininger et al. 'An essential Aurora-related kinase transiently associates with spindle pole bodies during *Plasmodium falciparum* erythrocytic schizogony'. In: *Molecular Microbiology* 79.1 (2011), pp. 205–221 (cited on pages 65, 76).

- [182] David E. Arnot, Elena Ronander, and Dominique C. Bengtsson. 'The progression of the intra-erythrocytic cell cycle of *Plasmodium falciparum* and the role of the centriolar plaques in asynchronous mitotic division during schizogony'. In: *International Journal for Parasitology* 41.1 (2011), pp. 71–80 (cited on page 65).
- [183] Caroline S Simon et al. 'An extended DNA-free intranuclear compartment organizes centrosome microtubules in malaria parasites'. In: *Life Science Alliance* 4.11 (2021) (cited on page 65).
- [184] Rachel M. Rudlaff et al. 'Three-dimensional ultrastructure of *Plasmodium falciparum* throughout cytokinesis'. In: *PLOS Pathogens* 16.6 (June 2020), pp. 1–21 (cited on pages 65, 75, 85).
- [185] Frank Hawking. 'The Clock of the Malaria Parasite'. In: *Scientific American* 222.6 (1970), pp. 123–131 (cited on page 65).
- [186] Célia R. S. Garcia, Regina P. Markus, and Luciana Madeira. 'Tertian and Quartan Fevers: Temporal Regulation in Malarial Infection'. In: *Journal of Biological Rhythms* 16.5 (2001). PMID: 11669417, pp. 436–443 (cited on page 65).
- [187] K. A. Schafer. 'The Cell Cycle: A Review'. In: *Veterinary Pathology* 35.6 (1998). PMID: 9823588, pp. 461–478 (cited on pages 65, 119).
- [188] Diego Martínez-Alonso and Marcos Malumbres. 'Mammalian cell cycle cyclins'. In: *Seminars in Cell & Developmental Biology* 107 (2020), pp. 28–35 (cited on pages 65, 119).
- [189] David G. Johnson and Cheryl L. Walker. 'Cyclins and cell cycle checkpoints'. In: *Annual Review of Pharmacology and Toxicology* 39.1 (1999). PMID: 10331086, pp. 295–312 (cited on page 66).
- [190] Andrew Murray. 'Cell cycle checkpoints'. In: *Current Opinion in Cell Biology* 6.6 (1994), pp. 872–876 (cited on page 66).
- [191] Marcos Malumbres et al. 'Cyclin-dependent kinases: a family portrait'. In: *Nature Cell Biology* 11.11 (Nov. 2009), pp. 1275–1276 (cited on page 66).
- [192] John J. Tyson, Attila Csikasz-Nagy, and Bela Novak. 'The dynamics of cell cycle regulation'. In: *BioEssays* 24.12 (2002), pp. 1095–1109 (cited on page 66).
- [193] Magali Roques et al. 'Plasmodium P-Type Cyclin CYC3 Modulates Endomitotic Growth during Oocyst Development in Mosquitoes'. In: *PLOS Pathogens* 11.11 (Nov. 2015), pp. 1–29 (cited on pages 66, 120).
- [194] Robert T. Johnson and Potu N. Rao. 'Nucleo-cytoplasmic interactions in the achievement of nuclear synchrony in DNA synthesis and mitosis in multinucleate cells'. In: *Biological Reviews* 46.1 (1971), pp. 97–155 (cited on pages 66, 91, 119).
- [195] Sina M. Adl et al. 'Revisions to the Classification, Nomenclature, and Diversity of Eukaryotes'. In: *Journal of Eukaryotic Microbiology* 66.1 (2019), pp. 4–119 (cited on pages 66, 91, 119).
- [196] Jeffrey A. Farrell and Patrick H. O'Farrell. 'From Egg to Gastrula: How the Cell Cycle Is Remodeled During the *Drosophila* Mid-Blastula Transition'. In: *Annual Review of Genetics* 48.1 (2014). PMID: 25195504, pp. 269–294 (cited on pages 66, 91, 119).

- [197] Laurence Calzone et al. 'Dynamical modeling of syncytial mitotic cycles in *Drosophila* embryos'. In: *Molecular Systems Biology* 3.1 (2007), p. 131 (cited on pages 66, 91, 119).
- [198] John R. Masters. 'HeLa cells 50 years on: the good, the bad and the ugly'. In: *Nature Reviews Cancer* 2.4 (Apr. 2002), pp. 315–319 (cited on page 66).
- [199] Potu N. Rao and Robert T. Johnson. 'Mammalian Cell Fusion : Studies on the Regulation of DNA Synthesis and Mitosis'. In: *Nature* 225.5228 (Jan. 1970), pp. 159–164 (cited on pages 66, 119).
- [200] A. Westerveld and Maria A. Freeke. 'Cell cycle of multinucleate cells after cell fusion'. In: *Experimental Cell Research* 65.1 (1971), pp. 140–144 (cited on page 67).
- [201] S. Ghosh, N. Paweletz, and I. Ghosh. 'Mitotic asynchrony of multinucleate cells in tissue culture'. In: *Chromosoma* 65.4 (Dec. 1978), pp. 293–300 (cited on pages 67, 119).
- [202] Amy S. Gladfelter. 'Nuclear anarchy: asynchronous mitosis in multinucleated fungal hyphae'. In: *Current Opinion in Microbiology* 9.6 (2006). Growth and development, pp. 547–552 (cited on page 67).
- [203] ChangHwan Lee et al. 'Protein Aggregation Behavior Regulates Cyclin Transcript Localization and Cell-Cycle Control'. In: *Developmental Cell* 25.6 (June 2013), pp. 572–584 (cited on pages 67, 119).
- [204] Cori A. Anderson et al. 'Nuclear Repulsion Enables Division Autonomy in a Single Cytoplasm'. In: *Current Biology* 23.20 (2013), pp. 1999–2010 (cited on page 67).
- [205] Huaiying Zhang et al. 'RNA Controls PolyQ Protein Phase Transitions'. In: *Molecular Cell* 60.2 (2015), pp. 220–230 (cited on page 67).
- [206] D E Arnot and K Gull. 'The *Plasmodium* cell-cycle: facts and questions'. In: *Ann. Trop. Med. Parasitol.* 92.4 (June 1998), pp. 361–365 (cited on pages 67, 76, 119).
- [207] Markus Ganter et al. '*Plasmodium falciparum* CRK4 directs continuous rounds of DNA replication during schizogony'. In: *Nature Microbiology* 2.5 (Feb. 2017), p. 17017 (cited on pages 67, 119, 120).
- [208] Peter Jagers. *Branching processes with biological applications*. Wiley series in probability and mathematical statistics. London: Wiley, 1975, XIII, 268 p. (Cited on pages 69, 75).
- [209] Marek Kimmel and David E. Axelrod. *Branching Processes in Biology*. 2nd ed. Springer eBook Collection. New York, NY: Springer, 2015, Online-Ressource (XX, 280 p. 69 illus., 3 illus. in color, online resource) (cited on pages 69, 73–75).
- [210] Inés M. del Puerto et al., eds. *Branching Processes and Their Applications*. Lecture Notes in Statistics - Proceedings ; 219. Cham: Springer, 2016, Online-Ressource (XVI, 332 p. 29 illus., 4 illus. in color, online resource) (cited on pages 69, 74).
- [211] Patsy Haccou, Peter Jagers, and Vladimir A. Vatutin. *Branching Processes: Variation, Growth, and Extinction of Populations*. Cambridge Studies in Adaptive Dynamics. Cambridge University Press, 2005 (cited on page 69).

- [212] Krishna B. Athreya, Peter E. Ney, and Peter Ney. *Branching processes*. Die Grundlehren der mathematischen Wissenschaften in Einzeldarstellungen ARRAY(0x557a3040bf38). Berlin: Springer, 1972, XI, 287 p. (Cited on pages 69, 83).
- [213] Theodore E. Harris. *The theory of branching processes*. Die Grundlehren der mathematischen Wissenschaften in Einzeldarstellungen ARRAY(0x55692e58c288). Berlin ; Göttingen ; Heidelberg: Springer, 1963, XIV, 230 p. (Cited on page 69).
- [214] Johannes Pausch, Rosalba Garcia-Millan, and Gunnar Pruessner. 'Time-dependent branching processes: a model of oscillating neuronal avalanches'. In: *Scientific Reports* 10.1 (Aug. 2020), p. 13678 (cited on page 69).
- [215] William Feller, ed. 3. ed., rev. print. Wiley series in probability and mathematical statistics. New York, NY: Wiley, 1968, XVIII, 509 p. (Cited on page 69).
- [216] William Feller, ed. 2. ed. New York, NY: Wiley, 1971, XXIV, 669 p. (Cited on page 69).
- [217] Henry William Watson and Francis Galton. 'On the probability of the extinction of families'. In: *The Journal of the Anthropological Institute of Great Britain and Ireland* 4 (1875), pp. 138–144 (cited on page 69).
- [218] David G. Kendall. 'Branching Processes Since 1873'. In: *Journal of the London Mathematical Society* s1-41.1 (Jan. 1966), pp. 385–406 (cited on page 69).
- [219] Richard Bellman and Theodore E. Harris. 'On the Theory of Age-Dependent Stochastic Branching Processes'. In: *Proceedings of the National Academy of Sciences* 34.12 (1948), pp. 601–604 (cited on pages 72, 73).
- [220] Willy Feller. 'On the Integral Equation of Renewal Theory'. In: *The Annals of Mathematical Statistics* 12.3 (1941), pp. 243–267 (cited on page 73).
- [221] B. A. Sevastyanov and A. M. Zubkov. 'Controlled Branching Processes'. In: *Theory of Probability & Its Applications* 19.1 (1974), pp. 14–24 (cited on page 74).
- [222] Miguel González Velasco, Inés María Del Puerto García, and George Petrov Yanev. *Controlled branching processes*. John Wiley & Sons, 2017 (cited on page 74).
- [223] Miguel González et al. 'Controlled branching processes with continuous time'. In: *Journal of Applied Probability* 58.3 (2021), pp. 830–848 (cited on page 74).
- [224] Paul-Christian Burda et al. 'A *Plasmodium* plasma membrane reporter reveals membrane dynamics by live-cell microscopy'. In: *Scientific Reports* 7.1 (Aug. 2017), p. 9740 (cited on page 75).
- [225] Giuseppe Facchetti, Fred Chang, and Martin Howard. 'Controlling cell size through sizer mechanisms'. In: *Current Opinion in Systems Biology* 5 (2017), pp. 86–92 (cited on pages 75, 80, 117).
- [226] Nicholas Rhind. 'Cell-size control'. In: *Current Biology* 31.21 (Nov. 2021), R1414–R1420 (cited on pages 75, 80, 117).

- [227] Marek Kimmel. 'Cellular population dynamics. I. Model construction and reformulation'. In: *Mathematical Biosciences* 48.3 (1980), pp. 211–224 (cited on page 75).
- [228] Marek Kimmel. 'Cellular population dynamics. II. Investigation of solutions'. In: *Mathematical Biosciences* 48.3 (1980), pp. 225–239 (cited on page 75).
- [229] Marek Kimmel. 'The point-process approach to age- and time-dependent branching processes'. In: *Advances in Applied Probability* 15.1 (1983), pp. 1–20 (cited on page 75).
- [230] Richard Cowan. 'Branching Process Results in Terms of Moments of the Generation-Time Distribution'. In: *Biometrics* 41.3 (1985), pp. 681–689 (cited on page 75).
- [231] Richard Cowan and Valerie B. Morris. 'Cell population dynamics during the differentiative phase of tissue development'. In: *Journal of Theoretical Biology* 122.2 (1986), pp. 205–224 (cited on page 75).
- [232] Severina Klaus. *Deciphering the spatiotemporal organization and regulation of Plasmodium falciparum schizogony*. Heidelberg, 2022 (cited on pages 75, 118, 119).
- [233] Ashish Gupta, Parul Mehra, and Suman Kumar Dhar. 'Plasmodium falciparum origin recognition complex subunit 5: functional characterization and role in DNA replication foci formation'. In: *Molecular Microbiology* 69.3 (2008), pp. 646–665 (cited on page 76).
- [234] Chris J. Janse et al. 'DNA synthesis in *Plasmodium berghei* during asexual and sexual development'. In: *Molecular and Biochemical Parasitology* 20.2 (1986), pp. 173–182 (cited on page 76).
- [235] T.H. Leete and H. Rubin. 'Malaria and the cell cycle'. In: *Parasitology Today* 12.11 (1996), pp. 442–444 (cited on page 76).
- [236] Hewson H. Swift. 'The Desoxyribose Nucleic Acid Content of Animal Nuclei'. In: *Physiological Zoology* 23.3 (1950). PMID: 15440320, pp. 169–198 (cited on page 76).
- [237] Jonas Bucevičius et al. 'Rhodamine-Hoechst positional isomers for highly efficient staining of heterochromatin'. In: *Chem. Sci.* 10 (7 2019), pp. 1962–1970 (cited on page 76).
- [238] Nathan C. Shaner et al. 'Improved monomeric red, orange and yellow fluorescent proteins derived from *Discosoma* sp. red fluorescent protein'. In: *Nature Biotechnology* 22.12 (Dec. 2004), pp. 1567–1572 (cited on page 76).
- [239] Katherine N. Choe and George-Lucian Moldovan. 'Forging Ahead through Darkness: PCNA, Still the Principal Conductor at the Replication Fork'. In: *Molecular Cell* 65.3 (2017), pp. 380–392 (cited on pages 77, 100).
- [240] Elspeth A. Bruford et al. 'HUGO Gene Nomenclature Committee (HGNC) recommendations for the designation of gene fusions'. In: *Leukemia* 35.11 (Nov. 2021), pp. 3040–3043 (cited on page 77).
- [241] Pallabi Mitra et al. 'Functional dissection of proliferating-cell nuclear antigens (1 and 2) in human malarial parasite *Plasmodium falciparum*: possible involvement in DNA replication and DNA damage response'. In: *Biochemical Journal* 470.1 (Aug. 2015), pp. 115–129 (cited on page 77).

- [242] Khadija Banu et al. 'Role of tyrosine residue (Y213) in nuclear retention of PCNA1 in human malaria parasite *Plasmodium falciparum*'. In: *FEMS Microbiology Letters* 365.17 (July 2018). fny182 (cited on page 77).
- [243] Asako Sakaue-Sawano et al. 'Visualizing Spatiotemporal Dynamics of Multicellular Cell-Cycle Progression'. In: *Cell* 132.3 (2008), pp. 487–498 (cited on page 78).
- [244] Angharad R. Jones, Leah R. Band, and James A.H. Murray. 'Double or Nothing? Cell Division and Cell Size Control'. In: *Trends in Plant Science* 24.12 (Dec. 2019), pp. 1083–1093 (cited on page 80).
- [245] Shicong Xie and Jan M. Skotheim. 'A G1 Sizer Coordinates Growth and Division in the Mouse Epidermis'. In: *Current Biology* 30.5 (Mar. 2020), 916–924.e2 (cited on page 80).
- [246] Marco D'Ario et al. 'Cell size controlled in plants using DNA content as an internal scale'. In: *Science* 372.6547 (2021), pp. 1176–1181 (cited on page 80).
- [247] Andrej Ondracka, Omayya Dudin, and Iñaki Ruiz-Trillo. 'Decoupling of Nuclear Division Cycles and Cell Size during the Coenocytic Growth of the Ichthyosporean *Sphaeroforma arctica*'. In: *Current biology : CB* 28.12 (June 2018). S0960-9822(18)30546-3[PII], 1964–1969.e2 (cited on page 80).
- [248] H. J. Kimble and L. Mandel. 'Theory of resonance fluorescence'. In: *Phys. Rev. A* 13 (6 June 1976), pp. 2123–2144 (cited on page 92).
- [249] H. J. Kimble, M. Dagenais, and L. Mandel. 'Photon Antibunching in Resonance Fluorescence'. In: *Phys. Rev. Lett.* 39 (11 Sept. 1977), pp. 691–695 (cited on page 92).
- [250] David Stoler. 'Photon Antibunching and Possible Ways to Observe It'. In: *Phys. Rev. Lett.* 33 (23 Dec. 1974), pp. 1397–1400 (cited on page 92).
- [251] H. Paul. 'Photon antibunching'. In: *Rev. Mod. Phys.* 54 (4 Oct. 1982), pp. 1061–1102 (cited on page 92).
- [252] Yung L. Tong. *The multivariate normal distribution*. Springer series in statistics. New York: Springer, 1990, XIII, 271 p. (Cited on page 94).
- [253] Richard Cowan and Robert Staudte. 'The Bifurcating Autoregression Model in Cell Lineage Studies'. In: *Biometrics* 42.4 (1986), pp. 769–783 (cited on page 94).
- [254] Robert G. Staudte. 'A bifurcating autoregression model for cell lineages with variable generation means'. In: *Journal of Theoretical Biology* 156.2 (1992), pp. 183–195 (cited on page 94).
- [255] Erika E. Kuchen et al. 'Hidden long-range memories of growth and cycle speed correlate cell cycles in lineage trees'. In: *eLife* 9 (2020). Ed. by Naama Barkai, e51002 (cited on page 94).
- [256] Anne Goelzer and Vincent Fromion. 'Resource allocation in living organisms'. In: *Biochemical Society Transactions* 45.4 (July 2017), pp. 945–952 (cited on page 99).
- [257] Mariusz Cichon. 'Evolution of longevity through optimal resource allocation'. In: *Proceedings of the Royal Society of London. Series B: Biological Sciences* 264.1386 (1997), pp. 1383–1388 (cited on page 99).

- [258] Wendy Rauw. 'Immune response from a resource allocation perspective'. In: *Frontiers in Genetics* 3 (2012) (cited on page 99).
- [259] Fakhri A. Bazzaz and John Grace. *Plant resource allocation*. Elsevier, 1997 (cited on page 99).
- [260] Pål Axel Olsson, Iver Jakobsen, and Håkan Wallander. 'Foraging and Resource Allocation Strategies of Mycorrhizal Fungi in a Patchy Environment'. In: *Mycorrhizal Ecology*. Ed. by Marcel G. A. van der Heijden and Ian R. Sanders. Berlin, Heidelberg: Springer Berlin Heidelberg, 2003, pp. 93–115 (cited on page 99).
- [261] Ben C. Sheldon and Simon Verhulst. 'Ecological immunology: costly parasite defences and trade-offs in evolutionary ecology'. In: *Trends in Ecology & Evolution* 11.8 (1996), pp. 317–321 (cited on page 99).
- [262] A. Goelzer and V. Fromion. 'Bacterial growth rate reflects a bottleneck in resource allocation'. In: *Biochimica et Biophysica Acta (BBA) - General Subjects* 1810.10 (2011). Systems Biology of Microorganisms, pp. 978–988 (cited on page 99).
- [263] Erez Dekel and Uri Alon. 'Optimality and evolutionary tuning of the expression level of a protein'. In: *Nature* 436.7050 (July 2005), pp. 588–592 (cited on page 99).
- [264] Sanjay A. Desai, Donald J. Krogstad, and Edwin W. McCleskey. 'A nutrient-permeable channel on the intraerythrocytic malaria parasite'. In: *Nature* 362.6421 (Apr. 1993), pp. 643–646 (cited on page 99).
- [265] Stefan Baumeister et al. 'The malaria parasite *Plasmodium falciparum*: cell biological peculiarities and nutritional consequences'. In: *Protoplasma* 240.1 (Apr. 2010), pp. 3–12 (cited on page 99).
- [266] James D. Watson. *Molecular biology of the gene*. 7. ed. Always learning. Boston: Pearson, 2014, XXXIV, 872 p. (Cited on page 100).
- [267] Philip Nelson and Marko Radosavljevic. *Biological physics. energy, information, life*. New York: Freeman, 2004, XXVI, 598 p. (Cited on page 101).
- [268] B. M. Alberts et al. 'Studies on DNA Replication in the Bacteriophage T4 a-.gif System'. In: *Cold Spring Harbor Symposia on Quantitative Biology* 47 (1983), pp. 655–668 (cited on pages 105, 119).
- [269] Farid A. Kadyrov and John W. Drake. 'Conditional Coupling of Leading-strand and Lagging-strand DNA Synthesis at Bacteriophage T4 Replication Forks *'. In: *Journal of Biological Chemistry* 276.31 (Aug. 2001), pp. 29559–29566 (cited on pages 105, 119).
- [270] Zeger Debyser, Stanley Tabor, and Charles C. Richardson. 'Coordination of leading and lagging strand DNA synthesis at the replication fork of bacteriophage T7'. In: *Cell* 77.1 (1994), pp. 157–166 (cited on pages 105, 119).
- [271] Sungsub Kim et al. ' τ Couples the Leading- and Lagging-strand Polymerases at the *Escherichia coli* DNA Replication Fork'. In: *Journal of Biological Chemistry* 271.35 (Aug. 1996), pp. 21406–21412 (cited on pages 105, 119).

- [272] Jingsong Yang et al. 'The dynamic processivity of the T4 DNA polymerase during replication'. In: *Proceedings of the National Academy of Sciences* 101.22 (2004), pp. 8289–8294 (cited on page 105).
- [273] Donald E. Johnson et al. 'Exchange of DNA polymerases at the replication fork of bacteriophage T7'. In: *Proceedings of the National Academy of Sciences* 104.13 (2007), pp. 5312–5317 (cited on page 105).
- [274] Joseph J. Loparo et al. 'Simultaneous single-molecule measurements of phage T7 replisome composition and function reveal the mechanism of polymerase exchange'. In: *Proceedings of the National Academy of Sciences* 108.9 (2011), pp. 3584–3589 (cited on page 105).
- [275] Chiara Indiani et al. 'A Sliding-Clamp Toolbelt Binds High- and Low-Fidelity DNA Polymerases Simultaneously'. In: *Molecular Cell* 19.6 (2005), pp. 805–815 (cited on page 105).
- [276] Chiara Indiani et al. 'Translesion DNA polymerases remodel the replisome and alter the speed of the replicative helicase'. In: *Proceedings of the National Academy of Sciences* 106.15 (2009), pp. 6031–6038 (cited on page 105).
- [277] James E. Kath et al. 'Polymerase exchange on single DNA molecules reveals processivity clamp control of translesion synthesis'. In: *Proceedings of the National Academy of Sciences* 111.21 (2014), pp. 7647–7652 (cited on page 105).
- [278] Filipa Rijo-Ferreira et al. 'The malaria parasite has an intrinsic clock'. In: *Science* 368.6492 (2020), pp. 746–753 (cited on page 118).
- [279] Lauren M. Smith et al. 'An intrinsic oscillator drives the blood stage cycle of the malaria parasite *Plasmodium falciparum*'. In: *Science* 368.6492 (2020), pp. 754–759 (cited on page 118).
- [280] Dominique Dorin-Semblat et al. 'Disruption of the PfPK7 Gene Impairs Schizogony and Sporogony in the Human Malaria Parasite *Plasmodium falciparum*'. In: *Eukaryotic Cell* 7.2 (2008), pp. 279–285 (cited on page 118).
- [281] Dominique Dorin-Semblat et al. 'An atypical cyclin-dependent kinase controls *Plasmodium falciparum* proliferation rate'. In: *Kinome* 1 (2013), pp. 4–16 (cited on page 118).
- [282] John L. Spudich and D. E. Koshland. 'Non-genetic individuality: chance in the single cell'. In: *Nature* 262.5568 (Aug. 1976), pp. 467–471 (cited on page 119).
- [283] Thomas O. Fox and Arthur B. Pardee. 'Animal Cells: Noncorrelation of Length of G1 Phase with Size after Mitosis'. In: *Science* 167.3914 (1970), pp. 80–82 (cited on page 119).
- [284] A Zetterberg and O Larsson. 'Kinetic analysis of regulatory events in G1 leading to proliferation or quiescence of Swiss 3T3 cells.' In: *Proceedings of the National Academy of Sciences* 82.16 (1985), pp. 5365–5369 (cited on page 119).
- [285] Dhanalakshmi R. Nair et al. 'A conserved G1 regulatory circuit promotes asynchronous behavior of nuclei sharing a common cytoplasm'. In: *Cell Cycle* 9.18 (2010), pp. 3795–3803 (cited on page 119).

- [286] Samantha E. R. Dundon et al. 'Clustered nuclei maintain autonomy and nucleocytoplasmic ratio control in a syncytium'. In: *Molecular Biology of the Cell* 27.13 (2016). PMID: 27193301, pp. 2000–2007 (cited on page 119).
- [287] Therese M. Gerbich et al. 'Phosphoregulation provides specificity to biomolecular condensates in the cell cycle and cell polarity'. In: *Journal of Cell Biology* 219.7 (May 2020). e201910021 (cited on page 119).
- [288] Sandrine Grava et al. 'Clustering of Nuclei in Multinucleated Hyphae Is Prevented by Dynein-Driven Bidirectional Nuclear Movements and Microtubule Growth Control in *Ashbya gossypii*'. In: *Eukaryotic Cell* 10.7 (2011), pp. 902–915 (cited on page 119).
- [289] Liliana Mancio-Silva et al. 'Nutrient sensing modulates malaria parasite virulence'. In: *Nature* 547.7662 (July 2017), pp. 213–216 (cited on page 119).
- [290] Jun-Hong Ch'ng et al. 'Enhanced virulence of *Plasmodium falciparum* in blood of diabetic patients'. In: *PLOS ONE* 16.6 (June 2021), pp. 1–17 (cited on page 119).
- [291] Marta Machado et al. '*Plasmodium falciparum* CRK4 links early mitotic events to the onset of S-phase during schizogony'. In: *bioRxiv* (2022) (cited on page 120).
- [292] Susan R. Wentz and Michael P. Rout. 'The Nuclear Pore Complex and Nuclear Transport'. In: *Cold Spring Harbor Perspectives in Biology* 2.10 (2010) (cited on page 120).
- [293] Martin Beck and Ed Hurt. 'The nuclear pore complex: understanding its function through structural insight'. In: *Nature Reviews Molecular Cell Biology* 18.2 (Feb. 2017), pp. 73–89 (cited on page 120).
- [294] David Shoup and Attila Szabo. 'Role of diffusion in ligand binding to macromolecules and cell-bound receptors.' In: *Biophysical Journal* 40.1 (Oct. 1982), pp. 33–39 (cited on pages 129, 130).
- [295] Eva Jaks et al. 'Differential receptor subunit affinities of type I interferons govern differential signal activation.' In: *Journal of molecular biology* 366.2 (Feb. 2007), pp. 525–39 (cited on page 134).

Danksagung

An dieser Stelle möchte ich mich ganz herzlich bei allen bedanken, die mich bei der Durchführung meiner Doktorarbeit unterstützt haben.

Ganz besonderer Dank gilt meinem Doktorvater Ulrich Schwarz für seine Unterstützung und Betreuung meiner Arbeit. Insbesondere bedanke ich mich auch dafür, dass er mir die Tür zur Biophysik geöffnet hat und für die Möglichkeit an den DPG-Frühjahrestagungen teilnehmen zu dürfen.

Besonders danke ich auch Thomas Höfer dafür, dass er mich in seiner Arbeitsgruppe aufgenommen hat, sowie für seine Unterstützung und Betreuung. Vielen Dank für die zahlreichen Group-Retreats, Konferenzen und die Sommerschule. Ich freue mich auf die weitere Zusammenarbeit.

Ein ganz herzliches Dankeschön gilt meinem Betreuer Nils Becker, der sich stets Zeit für all meine Fragen und Anliegen nahm und dessen Unterstützung in Form von Gesprächen und Diskussionen, Anregungen, Ideen und Feedback mir sehr viel geholfen hat. Vielen Dank dafür und für alles was noch kommen wird.

Des Weiteren möchte ich mich bei Prof. Frauke Gräter für das Interesse an und die Begutachtung meiner Arbeit bedanken.

Ein Dank geht weiterhin an die Landesgraduiertenförderung Baden-Württemberg für die Finanzierung meiner Arbeit.

Großer Dank gilt meinen Kollaborationspartnern Severina Klaus und Markus Ganter für die tolle Zusammenarbeit, die mir sehr viel Freude bereitet hat.

Vielen Dank auch all meinen Kollegen für die schöne gemeinsame Zeit.

Herzlich bedanke ich mich bei meinem Zwillingsbruder Daniel, meinem Betreuer Nils, meiner Schwägerin Maria und meiner Frau Miriam für das unermüdliche Korrekturlesen meiner Arbeit und die vielen hilfreichen Verbesserungsvorschläge.

Ein ganz besonderer Dank geht an meine lieben Eltern für ihre bedingungslose Unterstützung, an meinen Nachwuchs mit seinem beruhigenden Turnen sowie an meine Frau. Miriam, es ist schön, dass ich dich habe.